

Electrochemical cytochrome P450 enzymatic biosensors for the determination of the reactivity of TB drugs.



By

Candice Rassie

BSc Honours Chemistry (**Cum Laude**) (University of the Western Cape)
MSc Chemistry (**Cum Laude**) (University of the Western Cape)
MSc Nanoscience and Nanotechnology (Universitat Rovira I Virgili)

A thesis submitted in fulfilment of the requirements for the degree of

PHILOSOPHIAE DOCTOR

In the

**Department of Chemistry
Faculty of Science
University of the Western Cape**

Supervisor: Professor Emmanuel Iwuoha

Co-Supervisor: Professor Fanelwa Ajayi

December 2019

Abstract

Tuberculosis (TB) remains a global epidemic despite the fact that treatment has been available since the 1950's. This disease is highly contagious and spreads via transmission of the *Mycobacterium Tuberculosis* (MTB) tubercle via coughing, sneezing and spitting. The disease has various side effects including weight loss, fatigue and even death. To date no cure has been found for TB and thus optimisation of treatment is a constant focus in health related research. TB is highly prevalent in South Africa due to the increased level of patients who are co-infected with HIV. Treatment for TB consists of first line drugs including isoniazid (INH), ethambutol (ETH), pyrazinamide (PYR) and rifampicin (RIF). These drugs are highly effective but also produce many adverse drug reactions (ADR's) over the 6-month course of treatment. These reactions lead to patients not completing the course, losing quality of life and ultimately adding to the development of drug resistant strains of TB. A method of minimising these ADR's is the development of a phenotype sensor, which is able to determine the metabolic profile of patients. Metabolic profiles play a huge role in the efficacy of treatment by tailoring treatment in order for patients to stay within the therapeutic range of treatment. This would in turn minimise both toxicity and ineffective treatment. Various methods for the quantification of drugs have been developed such as high performance liquid chromatography (HPLC), mass spectrometry (MS) and ultra-violet visible spectroscopy (UV-vis). These methods have been found to be accurate but also have various drawbacks associated with them. They all require bulky laboratory based equipment, sample preparation, skilled laboratory personnel and many others. Determination of metabolic profile via drug quantification can be carried out with the use of electrochemical sensors. These systems offer an easy to use, cheap, portable and fast method of analysis, which can be used at the point of care. All of these characteristics make this technique applicable towards the detection of anti-TB drugs. Various sensors have been developed in recent years, as electrochemistry is a highly adaptable technique. This is carried out with the use of smart materials that enhance the sensitivity and

selectivity of electrochemical sensors. These materials include nanoparticles, conducting polymers, dendrimers, quantum dots, graphene and many others. Nanomaterials such as these mentioned, function by largely increasing the surface area as well as conductivity of an electrode surface. They can also be modified in order to have any other characteristics for the application such as hydrophobicity, biocompatibility etc.

In this work, a first generation copper functionalised polypropyleneimine metallodendrimer (CuPPI) was synthesised for application in a chemical sensor application towards TB drugs. Dendrimers are highly branched synthetic molecules, which consist of a core and repeating branches. Low generation dendrimers have the added advantage of having an open structure, which allows for fast electron transfer, increasing conductivity of the material. CuPPI was characterised using various techniques such as high resolution transmission electron microscopy (HRTEM), high resolution scanning electron microscopy (HRSEM) and atomic force microscopy (AFM) to determine the surface morphology. The structure was determined using Fourier transform infrared spectroscopy (FTIR), UV-vis spectroscopy and small angle X-ray scattering (SAXS). The electrochemical properties of the molecule were determined using cyclic voltammetry (CV), square wave voltammetry (SWV) and differential pulse voltammetry (DPV). The dendrimer was found to be surface confined onto the gold working electrode (Au) with a surface concentration of $9.014 \times 10^{-7} \text{ mol.cm}^{-2}$ and diffusion coefficient of $4.124 \times 10^{-5} \text{ cm}^2.\text{s}^{-1}$. CuPPI was then applied in an electrochemical sensor towards the detection of all four anti-TB drugs in 0.1 M phosphate buffer (PB). The sensor was capable of determining low nanomolar concentrations of the drugs with limits of detection (LOD) ranging from 0.022 nM to 1.16 nM. The anti-TB drugs were then detected in spiked real samples of 20 % synthetic urine and 10 % human plasma. In these matrices the LOD increased to a range of 0.153 μM to 48.52 μM . The increase in the concentration ranges were due to the interfering compounds in these two matrices as well as electrode fouling caused by plasma proteins. The linear ranges were well within the therapeutic range of each drug. Recovery studies were also carried out by dissolving the tablet forms of each

drug in the synthetic urine and plasma. The recovery for the Au|CuPPI sensor using real tablet forms on the drug was in the range of 89.27 % to 113 %.

Sensors can be further enhanced through the addition of a biological recognition element such as enzyme, DNA or antibodies. These biosensors are able to selectively react with their substrates in the presence of interferences and complex matrices found in real samples. Cytochrome P450 (CYP) enzymes are an ideal candidate for application in biosensors because of their wide variety of substrates. These enzymes are found in a variety of organisms and are capable of carrying out different types of reactions. In humans, CYP's are typically monooxygenases, which act on their substrates via a hydroxylation reaction in the presence of molecular oxygen. CYP3A4 in particular is a part of this group of enzymes and is responsible for the metabolism of 50 % of prescribed drugs. CYP3A4 was therefore incorporated into a biosensor via electrostatic attachment to a CuPPI modified gold electrode to form Au|CuPPI|CYP3A4. The biosensor was used to determine the four anti-TB drugs discussed in 0.1 M PB. In this media, the LOD ranged from 0.02244 nM to 0.1072 nM. The lower detectable concentration range was due to the increased sensitivity of the CYP enzyme. In order to apply this biosensor in real life conditions, synthetic real samples were prepared using the same method as the chemical sensor. The resulting calibration curves all showed typical Michaelis-Menten enzyme kinetics, as did the calibration curves in 0.1 M PB. The detection in synthetic urine and plasma yielded LOD in the range of 0.165 μ M to 0.884 μ M. Recovery studies using real tablet drugs were also carried out using the Au|CuPPI|CYP3A4 with excellent results in the range of 91.5 % to 108.5 %.

The results obtained from the sensor and biosensor affords us two options for the detection of anti-TB drugs. The chemical sensor (Au|CuPPI) has successfully been found to detect these drugs in both plasma and synthetic urine as high as 1000 μ M. It also has the added benefit of clearly distinguishing between each anti-TB drug since each has its own unique electrochemical signature. The biosensor allows us to go down to concentrations of 0.165 μ M, which shows excellent sensor capabilities in terms of sensitivity. This study was thus successful in developing both a chemical

sensor and biosensor towards INH, ETH, PYR and RIF in phosphate buffer, synthetic urine and human plasma.



Keywords

Biosensor

Cytochrome P450

CYP3A4

Drug Metabolism

Ethambutol

Isoniazid

Metallo dendrimer

Phenotype

Polypropyleneimine

Pyrazinamide

Real Samples

Rifampicin

Tuberculosis



Acronyms and abbreviations

3-DMC	3-demethylated colchicine
5-OH-PA	5-hydroxypyrazinoic acid
5-OH-PZA	5-hydroxypyrazinamide
6-DEB	6-deoxyerthronolide B
ADR	Adverse drug reaction
AdR	Adrenodoxin Reductase
Adx	Ferredoxin adrenodoxin
AFM	Atomic force microscopy
AgNP's	Silver Nanoparticles
CE	Capillary electrophoresis
CO	Carbon Monoxide
CPR	Cytochrome P450 reductase
CuPPI	Copper poly(propyleneimine)
CV	Cyclic Voltammetry
CYP	Cytochrome P450
DNA	Deoxyribonucleic acid
DPV	Differential Pulse Voltammetry
EC'	Electrochemical catalytic reaction
EDX	Energy dispersive X-ray spectroscopy
EG-NHS	Ethylene glycol bis(succinic acid N-hydroxysuccinimide ester)
E_{pa}	Anodic peak potential
E_{pc}	Cathodic peak potential
EPG	edge plane pyrolytic graphite electrode
ETH	Ethambutol

ETO	Ethionamide
FAD	Flavin Adenine Dinucleotide
Fdr	Ferredoxin Reductase
Fdx	Ferredoxin
FeS	Flavin Mononucleotide
FTIR	Fourier Transform Infrared Spectroscopy
G1	First Generation
GCE	Glassy Carbon Electrode
HPLC	High Performance Liquid Chromatography
HR-SEM	High Resolution Scanning Electron Microscopy
HR-TEM	High Resolution Transmission Electron Microscopy
INH	Isoniazid
I_{pa}	Anodic Peak Current
I_{pc}	Cathodic Peak Current
IUPAC	International Union Of Pure And Applied Chemistry
LOD	Limit Of Detection
LOQ	Limit Of Quantification
MDR	Multi-Drug Resistant
MOF	Metal Organic Framework
MTB	Mycobacterium Tuberculosis
MWCNT	Multi-Walled Carbon Nanotubes
NADH	Nicotinamide Adenine Dinucleotide Hydrogen
NADPH	Nicotinamide Adenine Dinucleotide Phosphate Hydrogen
PA	Pyrazinoic Acid
PAMAM	Polyamidoamine
PANSA	Poly (8-Anilino-1-Naphthalene Sulfonic Acid)
PAS	Para-Aminosalicylic Acid

PB	Phosphate Buffer
PDDF	Pair Distance Distribution Function
POC	Point Of Care
PPI	Poly(propyleneimine)
PVP	Polyvinylpyrrolidone
PYR	Pyrazinamide
PZA	Pyrazinamide
RIF	Rifampicin
SA	di-Succinimidyl Octanedioate
SAM	Self-Assembled Monolayers
SAXS	Small Angle X-Ray Scattering
SD	Size Distribution
SWV	Square Wave Voltammetry
TB	Tuberculosis
TDR	Total Drug Resistant
UV-vis	Ultra-Violet Visible Spectroscopy
WHO	World Health Organisation
XDR	Extreme Drug Resistant

Declaration

I declare that “***Electrochemical cytochrome P450 enzymatic biosensors for the determination of the reactivity of TB drugs.***” is my own work, that it has not been submitted before for any degree or examination in any other university, and that all the sources I have used or quoted have been indicated or acknowledged as complete references.



UNIVERSITY *of the*
WESTERN CAPE



SIGNED

Candice Rassie

Date: December 2019

Dedication

This work is dedicated to

My son, **Matai Franke**

Jeremiah 1:5

Before I formed you in the womb I knew you,

Before you were born I set you apart;

I anointed you as a prophet to the nations.



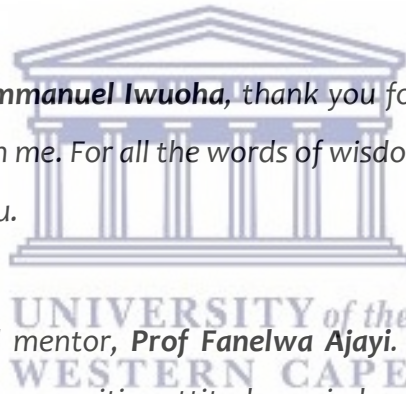
UNIVERSITY *of the*
WESTERN CAPE

Acknowledgements

To the **Lord God almighty**, you have carried me through the most trying of times and will continue to carry me through the most glorious ones. Without God I would have never been able to complete this work. Thank you for your grace, this achievement is only for your glory.

To my son, **Matai Franke**, my world and my light. You are my first PhD and the one I will always be proud of the most. You have brought me joy since the moment I knew of your existence. I dedicate this work to you, an achievement I got with you right at my side. I love you my son, you have given me the motivation to obtain this milestone in my career.

To my supervisor **Prof Emmanuel Iwuoha**, thank you for your patience and guidance and for never giving up on me. For all the words of wisdom I have gotten from you over the years, I appreciate you.



To my co-supervisor and mentor, **Prof Fanelwa Ajayi**. Thank you for your constant encouragement, advice, your positive attitude carried me through the most challenging times in this work. Your contribution to this period of my life is beyond measure.

To my mother, **Marion Rassie**, my rock and my stronghold. You have shown me what the meaning of a strong woman is. You have supported me through all these years of getting my education, you were a constant cheerleader and encourager whether the situation was good or bad. I would not be where I am now if it wasn't for your love and sacrifice.

To my siblings, **Grant Rassie, Cindy De Wet and Craig Daniels**. Thank you so much for being here for me, for always letting me know how proud you are of your baby sister, and for being such amazing role models to me. I love you all so much.

To my friends who became family: **Ashlin Paulsen, Nastasha Jantjies, Dr Anne Lutgarde Djoumessi, Dr Lindsay Wilson, Dr Keagan Pokpas, Dr Francis Muya and Dr Meryck Ward.** You all have walked this journey with me and seen me stumble and get up again so many times while pushing to finish this work. Thank you for being alongside to help pick me up again.

To my colleagues in Sensorlab as well as the Chemistry Department, especially **Prof Baker, Mrs Jackson, Dr Mohamed, Prof Jahed, Mr Lesch, Dr Busa, Prof Titinchi and Dr Mciteka.** For always helping me in the department and going the extra mile to push me to get this degree. Thank you so much.

Lastly I would like to acknowledge the National Research Foundation (NRF), the L'Oreal UNESCO For Women In Science Fellowship, the nGAP (next generation of academics programme) and Department of Higher Education and Training (DHET) for funding my studies as well as my development in my academic career.



List of Publications

Candice Rassie, Juanita Van Wyk, Lindsay Wilson, Nomaphelo Ntshongontshi, Anovuyo Jonnas, Usisipho Feleni, Rachel Fanelwa Ajayi, Priscilla Baker, and Emmanuel Iwuoha. **2017**. “*Electrochemical Ultra-Low Detection of Isoniazid Using a Salicylaldamine Functionalised G1-DAB-(NH₂)₄ Dendritic Sensor vs. UV-VIS Spectrophotometric Detection.*” *Journal of Nano Research* 45: 164–74. <https://doi.org/10.4028/www.scientific.net/JNanoR.45.164>.

Candice Rassie, Juanita Van Wyk, Lindsay Wilson, Hlamulo Makelane, Usisipho Feleni, Unathi Sidwaba, Selwyn Mapolie, Priscilla Baker, and Emmanuel Iwuoha. **2015**. “*Microscopy and Electroanalysis of a First Generation Copper- Poly(propyleneimine) Metallodendrimer System.*” *International Journal of Electrochemical Science* 10: 432–44.



Candice Rassie, Rasaq Olowu, Tesfaye Waryo, Lindsay Wilson, Avril Williams, Priscilla Baker, and Emmanuel Iwuoha. **2011**. “*Dendritic 7T-Polythiophene Electro-Catalytic Sensor System for the Determination of Polycyclic Aromatic Hydrocarbons.*” *International Journal of Electrochemical Science* 6: 1949–67.

Samantha Douman, Usisipho Feleni, Natasha Ross, Xolile Fuku, Rachel Ajayi, Ezo Nxusani, Nomaphelo Ntshongontshi, Unathi Sidwaba, **Candice Rassie**, Abongile Jijana, Priscilla Baker, Avril Williams and Emmanuel Iwuoha, **2016**. “*New Generation Nanoelectrochemical Biosensors for Disease Biomarkers: 1. Indium Telluride Quantum Dots Signaling of Telomerase Cancer Biomarker.*” *Journal of Nanoscience and Nanotechnology* 16 (12): 12844–50. <https://doi.org/10.1166/jnn.2016.13648>.

Mawethu Bilibana, Avril Williams, **Candice Rassie**, Christopher Sunday, Hlamulo Makelane, Lindsay Wilson, Nomaphelo Ntshongontshi, Abongile Jijana, Milua Masikini, Priscilla Baker and Emmanuel Iwuoha **2016**. “Electrochemical Aptatoxisensor Responses on Nanocomposites Containing Electro-Deposited Silver Nanoparticles on Poly(Propyleneimine) Dendrimer for the Detection of Microcystin-LR in Freshwater.” *Sensors* 16 (11): 1901. <https://doi.org/10.3390/s16111901>.

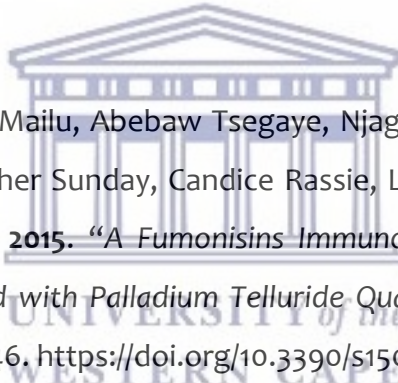
Nomaphelo Ntshongontshi, Abd Almonam Baleg, Rachel Fanelwa Ajayi, **Candice Rassie**, Ezo Nxusani, Lindsay Wilson, Usisipho Feleni, Unathi Sidwaba, Sinazo Qakala, Samantha Douman, Priscilla Baker and Emmanuel Iwuoha. **2016**. “Cytochrome P450-3A4/Copper-Poly(Propylene Imine)-Polypyrrole Star Co-Polymer Nanobiosensor System for Delavirdine - A Non-Nucleoside Reverse Transcriptase Inhibitor HIV Drug.” *Journal of Nano Research* 44 (November): 265–80. <https://doi.org/10.4028/www.scientific.net/JNanoR.44.265>.

Unathi Sidwaba, Usisipho Feleni, Hlamulo Makelane, Ezo Nxusani, Lindsay Wilson, Sinazo Qakala, **Candice Rassie**, Milua Masikini, Tesfaye Waryo, Rachel Fanelwa Ajayi, Priscilla Baker and Emmanuel Iwuoha. **2016**. “A Novel Polyaniline Nanocomposite with Doping Effects of Poly(Methyl Methacrylate) and TiO₂ Nanoparticles.” *Journal of Nano Research* 44 (November): 281–92. <https://doi.org/10.4028/www.scientific.net/JNanoR.44.281>.

Hlamulo Makelane, Suru John, Tesfaye Waryo, Abd Baleg, Noluthando Mayedwa, **Candice Rassie**, Lindsay Wilson, Priscilla Baker, and Emmanuel Iwuoha. **2016**. “AC Voltammetric Transductions and Sensor Application of a Novel Dendritic Poly(Propylene Thiophenoimine)-Co-Poly(3-Hexylthiophene) Star Co-Polymer.” *Sensors and Actuators B: Chemical* 227 (May): 320–27. <https://doi.org/10.1016/j.snb.2015.12.020>.

Lindsay Wilson, Juanita Van Wyk, **Candice Rassie**, Natasha Ross, Christopher Sunday, Hlamulo Makelane, Mawethu Bilibana, Tesfaye Waryo, Selwyn Mapolie, Priscilla Baker and Emmanuel Iwuoha. **2015**. “*Electrochemical Immunosensor Based on the Interactions between Polypyrrole and Cobalt (II) Salicylaldimine Dendrimer.*” *International Journal of Electrochemical Science* 10 (4): 3207–22.

Christopher Sunday, Milua Masikini, Lindsay Wilson, **Candice Rassie**, Tesfaye Waryo, Priscilla Baker and Emmanuel Iwuoha. **2015**. “*Application on Gold Nanoparticles-Dotted 4-Nitrophenylazo Graphene in a Label-Free Impedimetric Deoxynivalenol Immunosensor.*” *Sensors (Basel, Switzerland)* 15 (2): 3854–71. <https://doi.org/10.3390/s150203854>.



Milua Masikini, Stephen Mailu, Abebaw Tsegaye, Njagi Njomo, Kerileng M Molapo, Chinwe O Ikpo, Christopher Sunday, Candice Rassie, Lindsay Wilson, Priscilla Baker and Emmanuel Iwuoha. **2015**. “*A Fumonisin Immunosensor Based on Polyanilino-Carbon Nanotubes Doped with Palladium Telluride Quantum Dots.*” *Sensors (Basel, Switzerland)* 15 (1): 529–46. <https://doi.org/10.3390/s150100529>.

Fanelwa Ajayi, Unathi Sidwaba, Usisipho Feleni, Samantha Douman, Ezo Mxusani, Lindsay Wilson, **Candice Rassie**, Oluwakemi Tovide, Priscilla Baker, Sibulelo Vilakazi, Robert Tshikhudo and Emmanuel Iwuoha. **2014**. “*A Nanosensor System Based On Disuccinimydyl – CYP2E1 for Amperometric Detection of the Anti-Tuberculosis Drug, Pyrazinamide.*” *International Journal of Medical, Health, Biomedical, Bioengineering and Pharmaceutical Engineering* 8 (2): 67–71.

List of Conference Attendance

5th International Symposium on Electrochemistry – “Electrochemistry at Nanostructures Interfaces”

11th – 14th August **2019**, University of the Western Cape, Cape Town, South Africa

Oral Presentation: Dendritic CYP3A4 phenotype biosensor for the metabolism of first line anti-TB drugs

67th Annual meeting of the International Society of Electrochemistry

21st - 26th August **2016**, The Hague, Netherlands

Poster presentation: Electrochemical CYP2E1 enzyme phenotype-biosensor system for the determination of TB drug metabolism

66th Annual Meeting of the International Society of Electrochemistry

4th - 9th October **2015**, Taipei, Taiwan

Oral presentation: Microscopic and Electrochemical Signatures of Copper-poly(propyleneimine) Metallodendrimer System

Table of Contents

Abstract.....	i
Keywords	v
Acronyms and abbreviations.....	vi
Declaration.....	ix
Dedication	x
Acknowledgements	xi
List of Publications	xiii
List of Conference Attendance	xvi
Table of Contents	xvii
List of Figures	xxv
List of Tables.....	xxxiii
List of Schemes.....	xxxiv
1 Introduction.....	1
1.1 Background.....	1
1.2 TB disease burden.....	2
1.3 Personalisation of TB treatment	4
1.4 Current methods of anti-TB-drug detection.....	6
1.4.1 Titrimetry.....	7

1.4.2	Chromatography.....	7
1.4.3	Electrophoretic separation	8
1.4.4	Spectroscopy	8
1.5	Rationale and Motivation	9
1.6	Objectives	13
1.7	Thesis Overview	14
1.8	References.....	15
2	Literature review: Cytochrome P450 enzymes in catalytic reactions and applications in sensors.....	22
2.1	Introduction	23
2.1.1	Nomenclature.....	24
2.1.2	Human CYP's.....	24
2.1.3	Mechanism of Action and Classification.....	26
2.1.4	CYP reactions and substrates.....	27
2.2	Biosynthesis of natural products	29
2.2.1	Terpenoids/terpenes	29
2.2.2	Flavonoids	31
2.2.3	Carotenoids	32
2.2.4	Steroids.....	32
2.2.5	Erythromycin.....	33
2.2.6	Prunasin.....	33

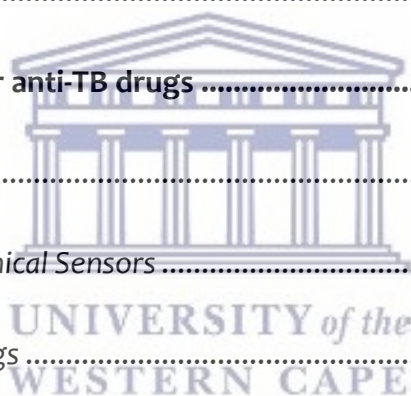


2.2.7	Indigo dyes	34
2.2.8	Anti-cancer agents	35
2.3	Biocatalysis and Bioconversion	37
2.3.1	Whole cell biocatalyst.....	37
2.3.2	Pharmaceutical agents and drugs	38
2.3.3	Steroids.....	39
2.3.4	Abiotic reactions	41
2.3.5	Large scale industrial applications.....	43
2.4	Bioremediation.....	44
2.4.1	Herbicides.....	45
2.4.2	Harmful substances.....	46
2.4.3	Insecticides.....	47
2.5	Biosensors	48
2.5.1	Carcinogens.....	49
2.5.2	Analgesics.....	50
2.5.3	Illicit drugs	51
2.5.4	Anti-retrovirals	52
2.5.5	Anti-cancer drugs.....	53
2.5.6	Anti-depressants	53
2.5.7	Antibiotics	54
2.6	Conclusion	55



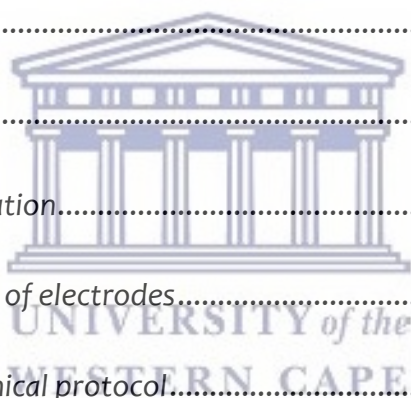
2.7	References.....	57
3	Characterisation of first generation PPI dendrimer and copper functionalised metallodendrimer	68
3.1	Introduction	69
3.2	Experimental Section.....	71
3.2.1	<i>Materials and Methods</i>	71
3.2.2	<i>Synthesis of first generation dendritic ligand and copper functionalised metallodendrimer</i>	72
3.2.3	<i>Structural and morphological characterisation of dendrimers</i>	74
3.2.3.1	<i>Fourier transform infrared spectroscopy</i>	74
3.2.3.2	<i>Ultraviolet-Visible Spectroscopy</i>	74
3.2.3.3	<i>Microscopy</i>	74
3.2.3.4	<i>Small angle X-Ray scattering</i>	75
3.2.4	<i>Preparation of electrodes</i>	75
3.2.5	<i>Electrochemical Protocol</i>	76
3.3	Results and discussion	76
3.3.1	<i>Structural and morphological characterisation of dendrimers</i>	76
3.3.1.1	<i>Fourier transform infrared spectroscopy</i>	77
3.3.1.2	<i>Ultraviolet-Visible Spectroscopy</i>	79
3.3.1.3	<i>Atomic Force Microscopy</i>	80
3.3.1.4	<i>High Resolution Transmission Electron Microscopy</i>	82

3.3.1.5	High Resolution Scanning Electron Microscopy	85
3.3.1.6	Small Angle X-Ray Scattering	88
3.3.2	Electrochemical characterisation of dendritic ligand and metallodendrimer.....	93
3.3.2.1	Electrochemical characterization of Au PPI.....	93
3.3.2.2	Electrochemical characterization of Au CuPPI.....	98
3.3.2.3	The effect of oxygen on the Au CuPPI system	103
3.4	Conclusion	110
3.5	References.....	111
4	Chemical Sensor for anti-TB drugs	117
4.1	Introduction.....	118
4.1.1	Electrochemical Sensors	119
4.1.2	Anti-TB drugs	119
4.1.2.1	Isoniazid.....	120
4.1.2.2	Ethambutol	120
4.1.2.3	Pyrazinamide	121
4.1.2.4	Rifampicin	122
4.2	Experimental	124
4.2.1	Materials	124
4.2.2	Instrumentation.....	124
4.2.3	Preparation of electrodes.....	125



4.2.4	<i>Electrochemical protocol</i>	125
4.2.5	<i>UV-Vis spectroscopic protocol</i>	126
4.3	Results and Discussion	126
4.3.1	<i>Electrochemical signatures of anti-TB drugs on bare electrodes</i>	126
4.3.1.1	<i>Isoniazid</i>	127
4.3.1.2	<i>Ethambutol</i>	129
4.3.1.3	<i>Pyrazinamide</i>	132
4.3.1.4	<i>Rifampicin</i>	134
4.3.2	<i>Electro-catalytic behaviour of Au CuPPI</i>	137
4.3.3	<i>Au CuPPI sensor for detection of anti-TB drugs</i>	139
4.3.3.1	<i>Isoniazid</i>	139
4.3.3.2	<i>Ethambutol</i>	141
4.3.3.3	<i>Pyrazinamide</i>	143
4.3.3.4	<i>Rifampicin</i>	145
4.3.4	<i>UV-Vis detection of anti-TB drugs</i>	146
4.4	Real Samples	150
4.4.1	<i>Isoniazid</i>	151
4.4.2	<i>Ethambutol</i>	154
4.4.3	<i>Pyrazinamide</i>	156
4.4.4	<i>Rifampicin</i>	157
4.4.5	<i>Recovery Studies of Au CuPPI electrode</i>	159

4.5	Conclusions.....	162
4.6	References.....	164
5	CYP3A4 biosensor system for anti-TB drugs.....	171
5.1	Introduction.....	172
5.1.1	Cytochrome P450 enzymes.....	172
5.1.2	CYP3A4 drug metabolism	174
5.1.3	CYP enzyme kinetics.....	176
5.1.4	CYP3A4 in biosensors	178
5.2	Experimental	179
5.2.1	Materials	179
5.2.2	Instrumentation.....	179
5.2.3	Preparation of electrodes.....	180
5.2.4	Electrochemical protocol.....	180
5.2.5	UV-Vis spectroscopic protocol.....	181
5.3	Results and Discussion.....	181
5.3.1	Characterisation of CYP3A4 biosensor	181
5.3.2	Au CuPPI CYP3A4 biosensor detection of anti-TB drugs	184
5.3.2.1	Isoniazid.....	186
5.3.2.2	Ethambutol.....	188
5.3.2.3	Pyrazinamide	190
5.3.2.4	Rifampicin.....	192



5.3.3	UV-Vis biosensor for detection of anti-TB drugs	194
5.4	Real Samples	197
5.4.1	Isoniazid	197
5.4.2	Ethambutol	200
5.4.3	Pyrazinamide	203
5.4.4	Rifampicin	206
5.4.5	Recovery Studies.....	209
5.5	Conclusion	211
5.6	References.....	213
6	Conclusion.....	219



List of Figures

Figure 1-1: Chemical structures of first line TB drugs	2
Figure 1-2: Estimated TB incidence in 2018, for countries with at least 100 000 incident cases	3
Figure 1-3: Graphic representation of various relative metabolism rates.....	5
Figure 2-1: Human liver cytochrome P450 content.....	25
Figure 2-2: Proposed reaction of CYP71Z18 with (S)- β -macro-carpene at C15 to form zealexin A1.....	31
Figure 2-3: CYP75B1 action at C3' on dihydroquercetin to form quercetin	32
Figure 2-4: 6-deoxyerythronolide B, a substrate of CYP107A1 which produces erythromycin.....	33
Figure 2-5: Biosynthetic pathway for the production of prunasin by <i>E. cladocalyx</i> ...	34
Figure 2-6: Colour shifts of various indigoids depending on their functional groups [59]	35
Figure 2-7: Epoxidation of epothilone D by EpoK CYP450 enzyme to form epothilone B.....	36
Figure 2-8: Hydroxylase action of CYP260B1 and CYP106A2 on DOC	40
Figure 2-9: Abiotic reactions catalysed by engineered CYP BM ₃ (A) oxidative deamination of alkyl azides (B) olefin cyclopropanation via carbene transfer (C) cyclization of carbonazidate substrates via intramolecular C-H amination (D) C-N bond formation via carbene N-H insertion [78].....	42
Figure 2-10: Bioconversion of ML-236B to provastitin using enzymes in the CYP105 family	43

Figure 2-11: Electrochemical response of CYP1A1/PB-NG/ GCE (A) (a) CV of PB-NG/GCE and (b) CYP1A1/PB- NG/GCE in 0.1 M, pH 7.4 PBS under N ₂ , (c) air saturated and (d) addition of 10 μM BaP at 100 mV s ⁻¹ (B) Current ay -0.48 V (vs. SCE) vs the concentrations of BaP (from 0.4 to 20.0 μM). Inset: CV curves of CYP1A1/PB-NG modified rotating disk electrode obtained by subtracting the back- ground before any addition of BaP [110].....	50
Figure 2-12: Cyclic voltammogram of CYP2B4 based SPCE and the detection of 1.67 mM cocaine in supporting electrolyte pH 7	52
Figure 3-1: Basic structure of a dendrimer	70
Figure 3-2: Chemical structure of poly(propyleneimine) dendritic ligand.....	77
Figure 3-3: Chemical structure of copper (II) metallodendrimer	77
Figure 3-4: (A) FTIR spectrum of PPI and CuPPI (B) Schematic representation of the functional groups responsible for the respective FTIR peaks in cm ⁻¹ , normal font are peaks assigned to PPI and bold font is attributed to CuPPI.....	78
Figure 3-5: UV-Vis spectra of PPI and CuPPI in ethanol:acetone solution	80
Figure 3-6: (A) 3-D and (B) 2-D AFM image of PPI dendrimer	81
Figure 3-7: (A) 3-D and (B) 2-D image scan of CuPPI metallodendrimer.....	82
Figure 3-8: (A) HR-TEM and (B) electron diffraction pattern of PPI dendrimer.....	83
Figure 3-9: (A) HR-TEM and (B) electron diffraction pattern of CuPPI metallodendrimer	84
Figure 3-10: HR-SEM of PPI dendrimer at (A) 5 KX and (B) 50 KX.....	86
Figure 3-11: HR-SEM of CuPPI at (A) 20 KX and (B) 100 KX	87
Figure 3-12: Pair distance distribution functions of (A) PPI and (B) CuPPI	89

Figure 3-13: Size distribution by number representations of (A) PPI in the 0 to 1 nm range (B) PPI in the 0 to 10 nm range and (C) CuPPI in the 0 to 10 nm range.....	91
Figure 3-14: Size distribution by volume representations of (A) PPI in the 0 to 100 nm range (B) CuPPI in the 0 to 100 nm range and (C) CuPPI in the 0 to 10 nm range	92
Figure 3-15: (A) Cyclic Voltammogram of Au PPI (B) CV of Au PPI run at various scan rates from 10 mV/s to 100 mV/s (C) linear plot of current vs scan rate.....	95
Figure 3-16: (A) Anodic and cathodic scan SWV of Au PPI at 10 Hz (B) anodic and (C) cathodic scans of Au PPI at various frequencies (i) 2 (ii) 5 (iii) 8 (iv) 10 (v) 15 (vi) 20 (vii) 25 and (viii) 30 Hz (D) linear plot of current vs square root of frequency for (a) anodic SWV and (b) cathodic SWV of Au PPI	97
Figure 3-17: Cyclic Voltammogram of CuPPI on gold electrode at 100 mV/s	99
Figure 3-18: (A) CV of Au CuPPI run at various scan rates from 10 mV/s to 100 mV/s (B) Linear plot of current vs scan rate and (C) current vs square root of scan rate for (a) E_{pa} and (b) E_{pc} of Au CuPPI	100
Figure 3-19: (A) Anodic and cathodic scan SWV of Au CuPPI at 10 Hz	103
Figure 3-20: Cyclic Voltammogram of CuPPI on gold electrode at 100 mV/s in the presence of oxygen	104
Figure 3-21: Cyclic voltammogram of CuPPI on gold electrode in the presence of oxygen and argon from -100 mV to 600 mV	105
Figure 3-22: (A) Cyclic voltammogram of Au CuPPI at various scan rates of (i) 10 mV/s to (x) 100 mV/s (B) current vs square root of scan rate for (a) E_{pa} and (b) E_{pc} of Au CuPPI in the presence of oxygen	106
Figure 3-23: Anodic and cathodic scan SWV of Au CuPPI in the presence of oxygen at 10 Hz.....	107
Figure 3-24: (A) Anodic and (B) cathodic scans of Au CuPPI in the presence of oxygen at various scan rates (i) 2 (ii) 5 (iii) 8 (iv) 10 (v) 15 (vi) 20 (vii) 25 and (viii) 30 Hz (C)	

Linear plot of current vs square root of frequency for (a) anodic SWV and (b) cathodic SWV of Au CuPPI in presence of oxygen.....	108
Figure 4-1: Chemical structure of Isoniazid.....	120
Figure 4-2: Chemical structure of ethambutol	121
Figure 4-3: Chemical structure of Pyrazinamide	122
Figure 4-4: Chemical structure of rifampicin	123
Figure 4-5: (A) CV and (B) anodic DPV of 200 μ M INH on bare GCE and (C) CV and (D) anodic DPV of 200 μ M INH on bare gold electrode from -600 mV to 600 mV of	128
Figure 4-6: (A) CV from -1500 mV to 1500 mV and (B) anodic DPV from 400 mV to 1500 mV of 200 μ M ethambutol on bare GCE electrode. (C) CV and (D) anodic DPV 0 mV to 1500 mV from of 200 μ M ETH on bare Au	131
Figure 4-7: (A) CV from -1300 mV to 600 mV and (B) DPV from -1500 mV to 0 mV of 200 μ M PYR on bare GCE (C) CV from -1500 mV to -500 mV of and (D) anodic and cathodic DPV from -1500 mV to -200 mV of 200 μ M PYR on bare Au.....	134
Figure 4-8: (A) CV and (B) anodic DPV from -1500 mV to 1500 mV of 200 μ M RIF on bare GCE (C) CV and (D) anodic DPV from 0 mV to 1500 mV of 200 μ M RIF on bare Au	136
Figure 4-9: Mechanism of rifampicin oxidation via loss of electrons to form rifampicin quinone.....	137
Figure 4-10: Catalytic effect of copper metallodendrimer in the oxidation of 500 nM isoniazid at bare and modified gold electrode surfaces in pH 7 phosphate buffer..	138
Figure 4-11: (A) DPV detection of 20, 40, 60, 80, 100, 120, 160 and 200 nM isoniazid at Au CuPPI electrode surface in PB pH 7.4 at (B) linear calibration plot of current vs concentration of INH in PB pH 7.4	141

Figure 4-12: DPV detection of 20, 40, 60, 80, 100, 120, 160 and 200 nM ETH at Au CuPPI electrode surface in PB pH 7.4 (B) Linear calibration plot of current vs concentration of ETH in PB pH 7.4	142
Figure 4-13: (A) DPV detection of 20, 40, 60, 80, 100, 120, 160 and 200 nM PYR at Au CuPPI electrode surface in PB pH 7.4 (B) Linear calibration plot of current vs concentration of PYR in PB pH 7.4.....	144
Figure 4-14: (A) DPV detection of 20, 40, 60, 80, 100, 120, 160 and 200 nM RIF at Au CuPPI in PB pH 7.4 (B) Linear calibration plot of current vs concentration of RIF in PB pH 7.4	146
Figure 4-15: UV-Vis of anti-TB drugs on their own, and in a mixture containing all four: ETH, INH, PYR and RIF in 0.1 M PB pH 7.4.....	148
Figure 4-16: UV-Vis detection of RIF in 0.1 M PB pH 7.4 at concentrations of 20, 40, 60, 80 and 100 μ M (B) : Calibration curves for UV-Vis detection of INH, PYR and RIF in 0.1 M PB pH 7.4	149
Figure 4-17: Au CuPPI behaviour in pH 7 0.1 PB, 20 % synthetic urine and 10 % plasma diluted with 0.1 M PB.....	151
Figure 4-18: (A) CV detection of 10, 20, 30, 40, 50, 60, 70, 80, 90 and 100 μ M INH at Au CuPPI (B) linear calibration plot of I_{pa} vs concentration of INH in 20 % synthetic urine.....	152
Figure 4-19: (A) CV detection of 10, 20, 30, 40, 50, 60, 70, 80, 90 and 100 μ M INH at Au CuPPI (B) linear calibration plot of I_{pa} vs concentration of INH in 10 % human plasma	153
Figure 4-20: (A) DPV detection of 1, 2, 3, 4, 5, 6, 7, 8, 9 and 10 μ M ETH and (B) linear calibration plot of I_{pa} vs concentration of ETH in 20 % synthetic urine	154
Figure 4-21: (A) DPV detection of 100, 200, 300, 400, 500, 600, 700, 800, 900 and 1000 μ M ETH at Au CuPPI and (B) linear calibration plot of I_{pa} vs concentration of ETH in 10 % human plasma	155

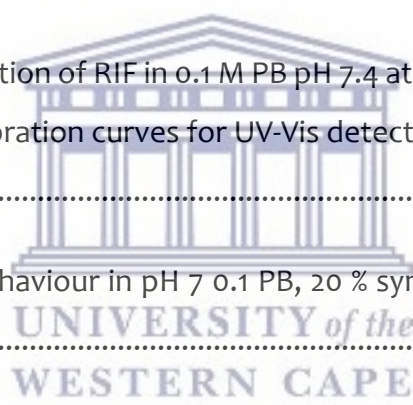


Figure 4-22: DPV detection of 10, 20, 30, 40, 50, 60, 70, 80, 90 and 100 μM PYR in (A) 20 % synthetic urine and (B) 10 % plasma and (C) calibration plot of I_{pa} vs concentration of PYR	157
Figure 4-23: (A) CV detection of concentrations of 0.5, 1, 1.5, 2, 2.5, 3, 3.5, 4, 4.5 and 5 μM	158
Figure 4-24: (A) CV detection of concentrations of 50, 150, 250, 350, 450, 550 and 650 μM RIF at Au CuPPI and (B) linear calibration plot of I_{pa} vs concentration of RIF in 10 % human plasma	159
Figure 5-1: Simplified structure of a heme centre i.e. iron protoporphyrin IX [4].....	173
Figure 5-2: Crystal structure of Cytochrome P450 3A4 [7]	174
Figure 5-3: Michaelis-Menten kinetics indicating the dependence of reaction rate on substrate concentration	177
Figure 5-4: Electrochemical activity of Au CYP3A4 under anaerobic conditions at 0.05 V/s	182
Figure 5-5: Electrochemical activity of Au and Au CYP3A4 under aerobic conditions at 0.05 V/s	183
Figure 5-6: CV of Au, Au CuPPI and Au CuPPI CYP3A4 electrode systems from -1 V to 1V at 0.1 V/s	184
Figure 5-7: Enzymatic reduction of 5 nM INH at Au CuPPI CYP3A4 biosensor electrode in 0.1 M PB pH 7.4.....	185
Figure 5-8: Most energetically favoured mechanistic pathway for the biocatalysis of INH by CYP's in the body [40]	186
Figure 5-9: (A) DPV detection of 0.2, 0.4, 0.8, 1, 2, 3, 4 and 5 nM INH in 0.1 M PB pH 7.4 at Au CuPPI CYP3A4 (B) exponential calibration plot of I_{pc} vs concentration of INH in PB pH 7.4 from 0 to 5 nM with linear region inset from 0 to 1 nM	187

Figure 5-10: (A) DPV detection of 0.2, 0.4, 0.8, 1, 2, 3, 4 and 5 nM ETH in 0.1 M PB pH 7.4 at Au CuPPI CYP3A4 (B) exponential calibration plot of I_{pc} vs concentration of ETH in PB pH 7.4 from 0 to 5 nM with linear region inset from 0 to 0.8 nM	189
Figure 5-11: Structures of ethambutol, its aldehyde intermediate and dicarboxylic acid product of CYP metabolism	190
Figure 5-12: (A) DPV detection of 0.2, 0.4, 0.8, 1, 2, 3, 4 and 5 nM PYR in 0.1 M PB pH 7.4 at Au CuPPI CYP3A4 (B) Exponential calibration plot of I_{pc} vs concentration of PYR in PB pH 7.4 from 0 to 5 nM with linear region inset from 0 to 1 nM	191
Figure 5-13: Structures of rifampicin, its formyl intermediate and carboxylic acid product of CYP metabolism	192
Figure 5-14: (A) DPV detection of 0.2, 0.4, 0.8, 1, 2, 3, 4 and 5 nM RIF in 0.1 M PB pH 7.4 at Au CuPPI CYP3A4 (B) exponential calibration plot of I_{pc} vs concentration of RIF in PB pH 7.4 from 0 to 5 nM with linear region inset from 0 to 1 nM	193
Figure 5-15: UV-Vis spectra of 5 μ M CYP3A4 enzyme, 20 μ M isoniazid and a combination of these in 0.1 M PB at pH 7.4.....	195
Figure 5-16: (A) Time study of 5 μ M CYP3A4 enzyme reaction with 20 μ M INH up to 24 hours (B) UV-Vis absorbance of CYP3A4 and INH mixture vs time from 0 to 24 h (inset) from 0 to 60 min	196
Figure 5-17: (A) DPV detection of 1, 2, 3, 4, 5, 6, 7, 8, 9 and 10 μ M INH at Au CuPPI CYP3A4 (B) I_{pc} vs concentration of INH in 20 % synthetic urine	198
Figure 5-18: (A) DPV detection of 1, 2, 3, 4, 5, 6, 7 and 8 μ M INH at Au CuPPI CYP3A4 (B) I_{pc} vs concentration of INH in 10 % plasma.....	200
Figure 5-19: (A) DPV detection of 1, 2, 3, 4, 5, 6, 7, 8, 9 and 10 μ M ETH at Au CuPPI CYP3A4 (B) I_{pc} vs concentration of ETH in 20 % synthetic urine.....	201
Figure 5-20: (A) DPV detection of 1, 2, 3, 4, 5, 6, 7 and 8 μ M ETH at Au CuPPI CYP3A4 (B) I_{pc} vs concentration of ETH in 20 % synthetic urine	203

Figure 5-21: (A) DPV detection of 1, 2, 3, 4, 5, 6, 7, 8, 9 and 10 μM PYR at Au|CuPPI|CYP3A4 (B) I_{pc} vs concentration of PYR in 20 % synthetic urine..... 204

Figure 5-22: (A) DPV detection of 1, 2, 3, 4, 5, 6, 7 and 8 μM PYR at Au|CuPPI|CYP3A4 (B) I_{pc} vs concentration of PYR in 10 % plasma 205

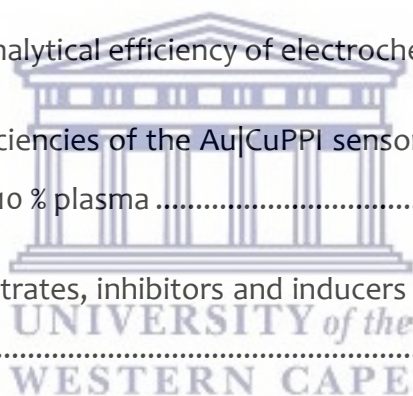
Figure 5-23: (A) DPV detection of 0.5, 1, 1.5, 2, 2.5, 3, 3.5, 4, 4.5 and 5 μM RIF at Au|CuPPI|CYP3A4 (B) I_{pc} vs concentration of RIF in 20 % synthetic urine..... 207

Figure 5-24: (A) DPV detection of 1, 2, 3, 4, 5 and 6 μM RIF at Au|CuPPI|CYP3A4 (B) I_{pc} vs concentration of RIF in 10 % plasma 208



List of Tables

Table 2-1: 57 Human enzymes according to their major substrate class [25], [26]	26
Table 2-2: General characteristics of cytochrome P450 enzymes [35], [36], [27].....	28
Table 3-1: FTIR peaks of dendritic ligand and copper (II) metallodendrimer	78
Table 3-2: EDX results of PPI and CuPPI.....	84
Table 3-3: Summary of electrochemical characteristics of PPI and CuPPI	109
Table 4-1: Electrochemical signatures of anti-TB drugs on bare electrodes.....	137
Table 4-2: UV-Vis absorption bands of anti-TB drugs.....	148
Table 4-3: Summary of analytical efficiency of electrochemistry vs UV-Vis	150
Table 4-4: Analytical efficiencies of the Au CuPPI sensor towards of anti-TB drugs in 20 % synthetic urine and 10 % plasma	160
Table 5-1: A list of 7 substrates, inhibitors and inducers of the CYP3A4 enzyme [14], [15]	176
Table 5-2: Summary of analytical efficiency of Au CuPPI CYP3A4 biosensor in 0.1 M PB at pH 7.4	194
Table 5-3: Analytical efficiency of Au CuPPI CYP3A4 biosensor towards anti-TB drugs in 20 % synthetic urine and 10 % plasma	210



List of Schemes

Scheme 2-1: Graphical abstract for Chapter 2 [3].....	23
Scheme 2-2: CYP450 system in (A) typical class I bacterial CYP system (B) a typical class II eukaryotic membrane bound CYP reductase system (CPR) consisting of FMN/FAD (C) fused self-sufficient CYP system with CPR	27
Scheme 2-3: Bioremediation mechanisms of an MES system [92]	45
Scheme 2-4: Immobilised CYP71B1 reductase fusion catalytic cycle for chlortoluron N-monodemethylation [93].....	46
Scheme 2-5: Biosensor components.....	48
Scheme 3-1: Graphical abstract for Chapter 3	69
Scheme 3-2: Synthesis of first generation poly(propyleneimine) dendritic ligand....	72
Scheme 3-3: Synthesis of copper (II) metallodendrimer	73
Scheme 4-1: Graphical abstract for chapter 4.....	117
Scheme 4-2: Oxidation mechanism of isoniazid [43].....	129
Scheme 4-3: Oxidation and reduction mechanism of pyrazinamide	134
Scheme 4-4: Representation of EC' mechanism occurring at metallodendrimer modified electrode surface	139
Scheme 5-1: Graphical abstract for Chapter 5	171
Scheme 5-2: CYP450 enzyme mechanism of action.....	175

Chapter 1

1 Introduction

1.1 **Background**

In the year 1905 Robert Koch was awarded the Nobel Prize for Medicine for his work for the ultimate discovery of the tubercle bacillus. Before this discovery, tuberculosis was proven to be a contagious disease spread by sputum inhalation and through other methods as depicted by various researchers between 1650 and 1880. Koch embarked on a journey to discover the micro-organism responsible for the disease in 1881. It was on the 24th of March, 1882 that Koch announced the discovery of the tubercle bacillus at a monthly meeting of the Berlin Physiological Society. He presented his techniques and novel methods that resulted in him being acclaimed the founder of science in bacteriology [1]. Since Koch's discovery of tubercle bacillus there have been countless instances of research on the bacterium and despite this discovery many years ago, a cure for the disease associated with the bacterium has not been found.

Tuberculosis (TB) is a common and infectious disease caused by the tubercle i.e. *Mycobacterium tuberculosis* (MTB) [2]. The infection is spread as exhaled drops in coughs, spits or sneezes from infected individuals. MTB primarily attacks the lungs causing pulmonary TB but it can also affect the lymphatic system, central nervous system, the genitourinary system, the circulatory system, the gastrointestinal system, joints, bones and even the skin [3]. This tubercle (MTB) is said to be a slow-growing pathogen which has the unusual propensity to shut down its metabolism during adverse conditions such as starvation or immune stress [4]. Symptoms of TB include a cough that lasts more than three weeks, weight loss, fatigue and when left untreated, even death [5].

TB is treated using a variety of drugs which can be separated into their various classes and/or their lines of treatment. First line drugs used to combat TB are usually administered to those who are being treated for TB for the first time. This group of drugs include isoniazid (INH), rifampicin (RIF), ethambutol (ETH) and pyrazinamide (PYR). The chemical structures of these drugs are as shown in Figure 1-1. These drugs are usually administered as a multi-drug combination or “cocktail” to treat drug susceptible tuberculosis over a period of six months. The first two months are very intensive and all four drugs are taken together. For the remaining four months only rifampicin and isoniazid are taken [6] [7].

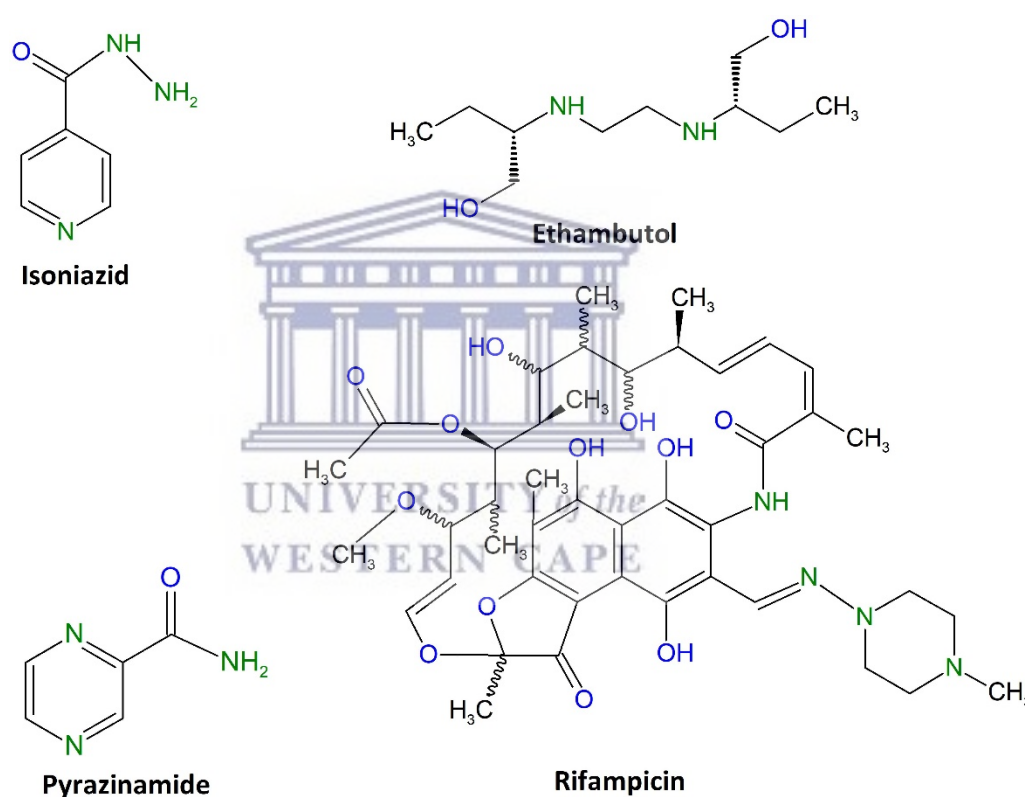


Figure 1-1: Chemical structures of first line TB drugs

1.2 TB disease burden

Although treatment for the disease has been available for decades, as far back as the 1950's, TB continues to be a global epidemic with roughly 10 million new TB cases reported worldwide in 2018. Of these cases, roughly 1.5 million people died due to TB related causes, including 250 000 deaths among patients co-infected with HIV [8].

What is concerning to us is that 25 % of these new cases occurred in Africa as illustrated by the World Health Organisation (WHO). A map indicating global TB burden in 2018 is as shown in Figure 1-2. South Africa has one of the 30 highest incidence rates of TB in the world, with an estimated 567 infected per 100 000 population per year. These statistics were extracted from the latest Global Tuberculosis Report of 2019 of the World Health Organisation (WHO) [9].

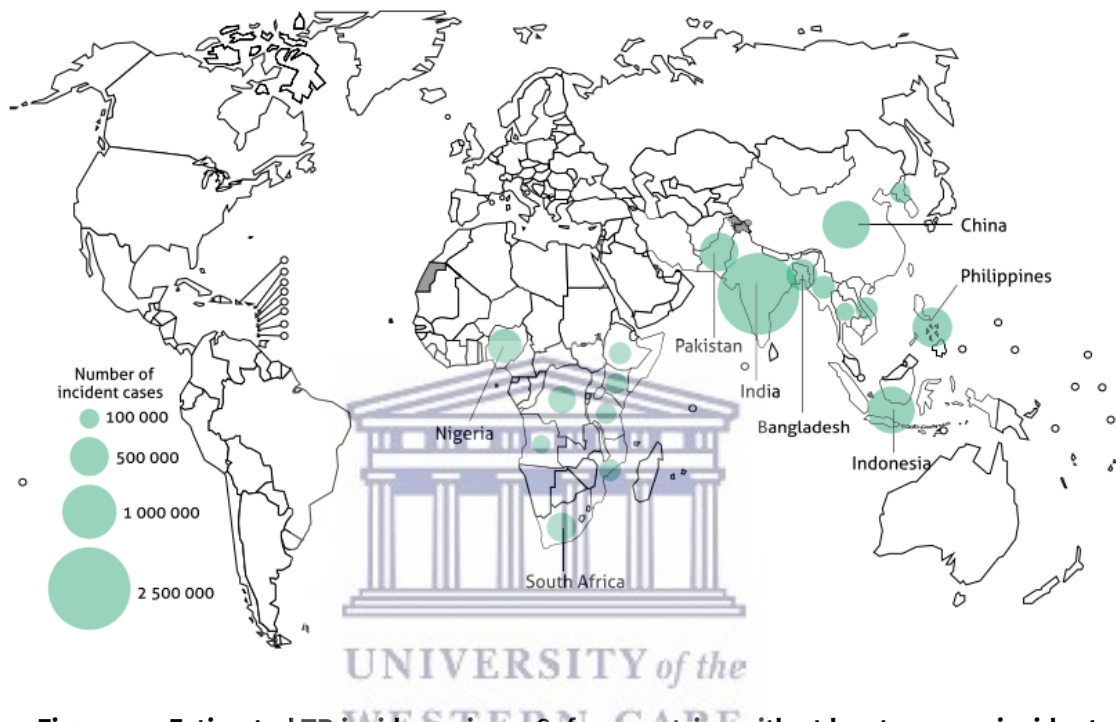


Figure 1-2: Estimated TB incidence in 2018, for countries with at least 100 000 incident cases

Incidences of TB globally are gradually decreasing; however, death due to TB complications could be avoided by efficient treatment of the disease. Incomplete implementation of the TB treatment has been a major cause of the high occurrences of the drug resistant strains of the tubercle i.e. MTB. This stems from the fact that patients with fully susceptible TB develop secondary resistance during their treatment [10]. Many factors assist the formation of drug resistant TB such as inappropriate dosing of drugs, inadequate treatment, not taking the prescribed regimen appropriately or using low quality medication. Another possible reason for the development of drug resistant TB is the metabolic profile of TB patients which vary according to genotype or phenotype [11], [12]. Multi drug resistant (MDR) TB is

defined as the resistance to two of the first line TB drugs i.e. isoniazid and rifampicin [13]. This would thus lead to the necessity to use second line drugs which include streptomycin, ofloxacin, kanamycin, capreomycin, amikacin, ethionamide, para-aminosalicylic acid (PAS) and cycloserine [14]. In more advanced cases, extreme drug resistant (XDR) TB also exists which is known as MDR-TB with an additional resistance to flouroquinolones and to any of the second-line injectable agents: amikacin, capreomycin or kanamycin [15]. To date, there have even been cases reported with resistance to all available anti-TB drugs within South Africa and a few other countries, these cases are known as totally drug resistant (TDR) TB [16].

Treatment of any form of TB is complicated further by the onset of adverse drug reactions (ADR's) caused by the combination of various drugs as well as extended treatment time. These ADR's include neurotoxicity, dermatological and hypersensitivity reactions, hepatitis or hepatotoxicity which can sometimes be fatal, [17]. The prevalence of adverse drug reactions have previously been extensively studied in hospitalised patients in the United states of America and it was found that 6-7 % of these TB patients suffer from serious ADRs and 0.32 % of these patients developed fatal ADRs thus resulting in 100 000 deaths annually in the US [18]. These numbers would obviously be much greater in areas with a larger level of TB incidence such as Africa and Southern Asia. ADR's therefore play a major role in the patient's unwillingness to finish their course of treatment for their disease, as well as contributing to the TB related death toll.

1.3 Personalisation of TB treatment

The spread of TB and development of resistance to anti-TB drugs is a very daunting battle to fight which requires millions of dollars in research and development [19]. One method of fighting TB via minimising ADR's that would be easier to achieve, is the personalisation of TB treatment. The rate at which drugs are metabolised vary from patient to patient, and thus the treatment they consume are absorbed at different time intervals [20]. This can lead to either inadequate treatment for fast

metabolisers or toxicity for slow metabolisers. A graph representing these types of metabolisers is as shown in Figure 1-3.

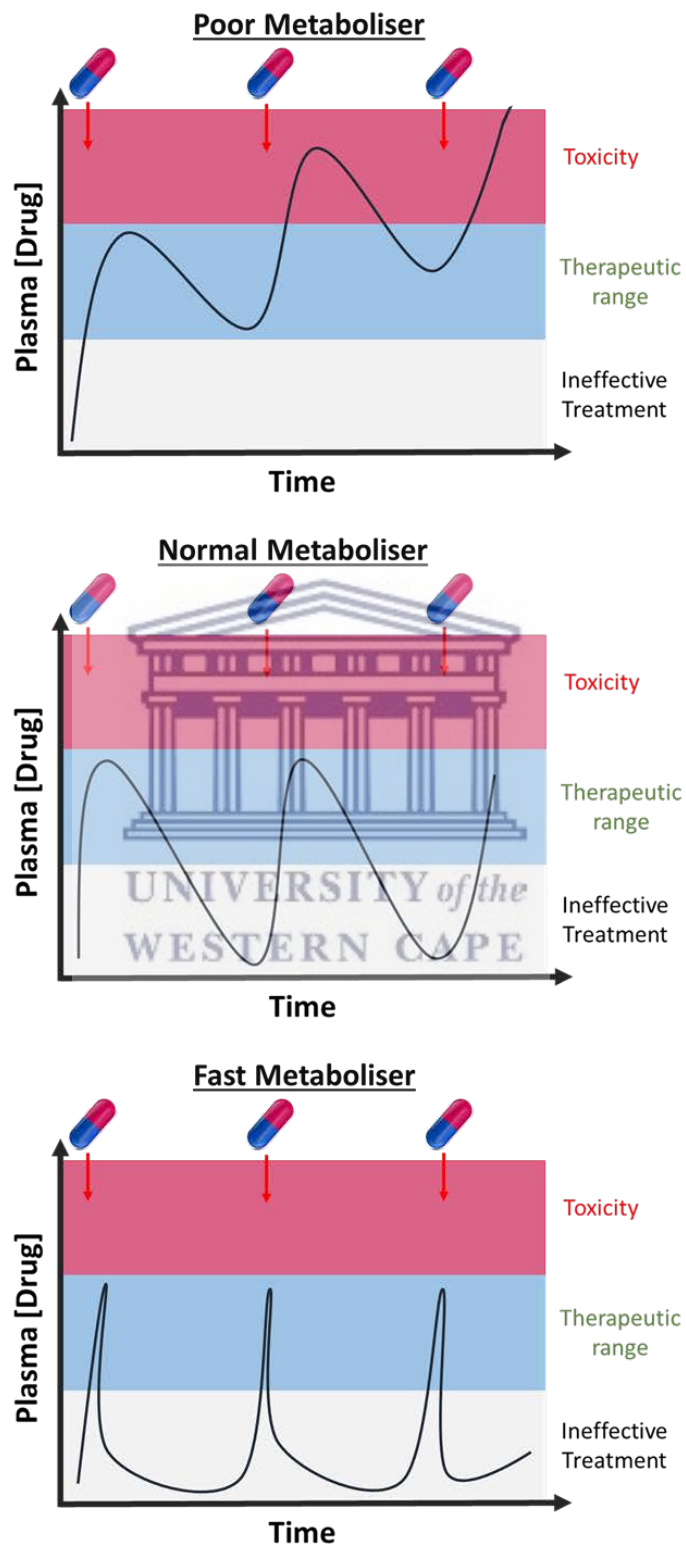
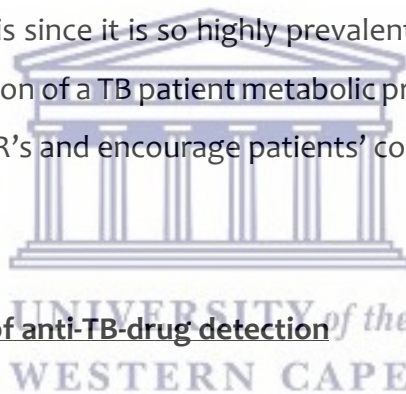


Figure 1-3: Graphic representation of various relative metabolism rates

A poor metaboliser would take a dose of a TB treatment drug and be within the therapeutic range i.e. the dosage at which treatment is effective [21] however, when another dose of drug is administered the level of drug in the body is so high that it becomes toxic. This results in adverse drug reaction such as those mentioned previously. A patient with normal metabolism would use up the administered dose in time for it to be depleted by the time the next dose is administered. A fast metaboliser on the other hand, would use up the drugs so fast that most of the time the treatment would be ineffective [22].

Africans in particular have been found to have a greater genetic diversity and variability in genes encoding drug metabolising enzymes such as cytochrome P450. These genetic variations largely contribute to the high numbers of adverse drug reactions experienced by Africans [23]. Thus, personalisation of care is vital in treatment of tuberculosis since it is so highly prevalent in this area. A cost effective and efficient determination of a TB patient metabolic profile towards TB drugs would greatly reduce these ADR's and encourage patients' completion of the treatment.



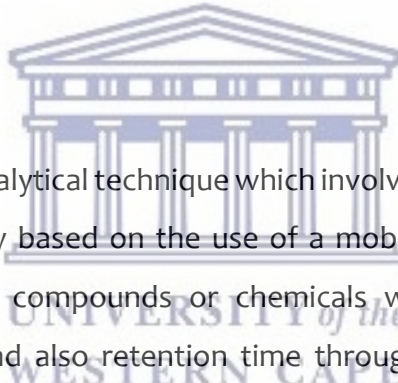
1.4 **Current methods of anti-TB-drug detection**

One way to monitor the metabolism of TB patients is to determine the amount of un-metabolised anti-TB drugs in their urine [24], or the amount of drug in their blood or plasma after a pre-determined time [25]. There are currently various methods of determining the amount of drug present in a particular medium. Most of these analytical techniques are limited to the laboratory setting. Laboratory based techniques require bulky equipment which are not mobile including a qualified technician to operate the sophisticated machinery and analyse the results obtained from them. The costs of laboratory analysis therefore include extensive sample preparation, cost of running equipment, bulk solvents required, technician labour as well as extended time [26]. Some of the techniques used for the detection of these anti-TB drugs are listed below.

1.4.1 Titrimetry

Titration, also known as titrimetry is a laboratory method of chemical analysis which uses volume measurements to determine concentration of a known analyte. Titrimetric detection of chemicals is considered one of the earliest forms of quantitative chemical analysis. One of the most common types is acid-base titrimetry where an acid-base indicator is used to determine the end point of the reaction and thus determine the concentration of the unknown [27]. Isoniazid has been successfully detected using titrimetry in previous years. One method uses o-dianisidine or p-ethoxychrysoidine as indicator [28] and another uses starch [29]. Titrimetry does not require complex machinery or instruments. However, it requires large volumes of solvent and is not environmentally friendly.

1.4.2 Chromatography

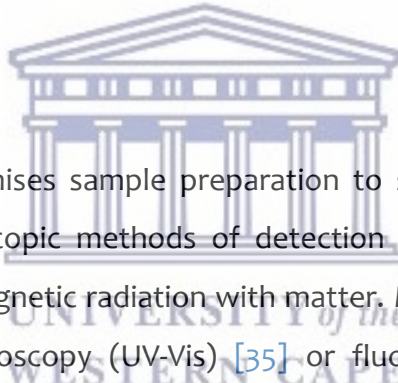


Chromatography is an analytical technique which involves the separation of a mixture of chemicals. It is mostly based on the use of a mobile and stationary phase. The differentiation between compounds or chemicals would thus depend on their movement or elution and also retention time through the different phases [30]. Pyrazinamide and its metabolites namely 5-hydroxypyrazinamide (5-OH-PZA), pyrazinoic acid (PA) and 5-hydroxypyrazinoic acid (5-OH-PA) were detected using high performance liquid chromatography (HPLC) [31]. Pyrazinamide has also been successfully identified using HPLC in a complex matrix such as human plasma [32]. HPLC is also capable of identifying and quantifying four constituents (pyrazinamide, isoniazid, rifampicin and ethambutol hydrochloride) in an anti-tuberculosis fixed dose combination tablet. Extensive sample preparation and organic solvents were needed for the analysis in this case [33]. The advantages of HPLC analysis includes high specificity, precision and accuracy. The drawbacks however are large solvent volumes, high cost and laboratory setting which is required. Although this method shows good results for detection, the time and effort associated for sample preparation is a downside for this type of detection or monitoring.

1.4.3 Electrophoretic separation

Another method of drug detection utilises capillary electrophoresis (CE) coupled with a detection method such as UV-vis or electrochemiluminescence. Capillary electrophoresis is based on the separation of charged analytes through a thin capillary using an electrolyte under the influence of a magnetic field. Here the analytes are perceived as peaks as they pass through a detector. The area of that peak is a function of the concentration present. Ethambutol and methoxyphenamine were separated via CE and detected using electrochemiluminescence [34]. The positive aspect of CE is the small sample volume required as well as the shorter time of analysis required. The disadvantage here is the necessity of a separate method of detection, which can sometimes be difficult to incorporate into a mobile device.

1.4.4 Spectroscopy



One method that minimises sample preparation to some extent is the use of a spectrometer. Spectroscopic methods of detection in this context analyses the interaction of electromagnetic radiation with matter. Methods of detection include ultraviolet-visible spectroscopy (UV-Vis) [35] or fluorescence spectroscopy [36] among others. In this type of analysis, a chromophore or fluorophore is necessary for detection methods respectively. If one of these are not present in the analyte, an indicator is required for detection. Isoniazid was successfully detected directly using UV-Vis spectroscopy in its tablet form [37]. INH has also been determined indirectly via the formation of an optical sensor which was formed by the reaction of INH with Fe(III) in the presence of PDT (3-(2-pyridyl)-5,6-diphenyl-1,2,4-triazine) [38]. Ethambutol however does not contain a chromophore and is thus not capable of being detected using UV-Vis without the addition of another chemical. Ethambutol has successfully been quantified via the quenching of a sensitive fluorescent probe [39]. Advantages of this form of analysis are decreased time as well as low labour consumption with high precision. The drawbacks however are the necessity of a laboratory setting, expensive equipment and the necessity of either a chromophore/flourophore or a label.

1.5 **Rationale and Motivation**

There is a great need to minimise all of the negative aspects and challenges associated with anti-TB drug detection described above. This is especially true when dealing with a disease such as tuberculosis since it is most prevalent in regions that experience high levels of unemployment and poverty [40]. South Africa for instance is experiencing both a record high unemployment rate as well as a high prevalence of both HIV and TB [41]. This research is in line with the Department of Health's strategic plan 2016-2020, the vision of which is for a long and healthy life for all South Africans. Its mission is to improve health status through the prevention of illness, disease and the promotion of healthy lifestyles and to consistently improve the health care delivery system by focusing on access, equity, efficiency, quality and sustainability [42].

It is thus clear that a more cost effective and efficient method to combat TB is needed, such as the monitoring metabolic profiles or phenotypes and thereby personalising TB treatment for patients. A modern and sensitive method of detection is electrochemical sensing of various anti-TB drugs. This involves either the oxidation or reduction of the analyte at a working electrode surface.

The working electrode has a relatively small surface area in the region of a few millimetres in diameter typically. Solid electrode surfaces are usually made of silver, platinum, gold and glassy carbon amongst many others. Electrochemical sensors converts the chemical reaction occurring at the surface of the electrode into an analytical useful electronic signal which can be read by the user [43]. The surface of the working electrode is usually modified in order to increase the conductivity, surface area, specificity or selectivity of the sensor.

Smart materials used to modify an electrode surface include conductive polymers [44], nanoparticles [45], quantum dots, dendrimers and carbon based materials such as graphene [46]. Dendrimers are a type of macromolecules that can also be described as dendritic polymers. They consist of highly branched and roughly spherical repeating units. Their conductivity can also be increased by the inclusion of

a metal centre and are thus ideal for applications in electrochemical sensors. They can be easily synthesised and provide a simple and effective electro-catalytic platform which increases the sensitivity of the sensor [47]. A first generation copper functionalised polypropyleneimine based dendrimer was developed and used in this work.

Many different types of electrochemical techniques are used for analysis such as voltammetry [48], amperometry, electrochemical impedance spectroscopy [49] and others. Electrochemical sensors have commonly been used in the detection of drugs and found to be hugely successful [50]. An example is the simple electrochemical determination of isoniazid (INH). A rhodium modified glassy carbon electrode detected INH by linear sweep voltammetry. Sample preparation is minimal for electrochemical detection with the standard samples being dissolved in pH 7 phosphate buffer 30 minutes before analysis. Human urine sample were centrifuged and the supernatant diluted with the same buffer. No further treatment of samples were needed for analysis. The electrochemical sensor was highly sensitive towards isoniazid in the presence of other interferences with a detection limit of $0.13 \mu\text{M}$ [51]. Pyrazinamide (PYR) was detected more recently at even lower detection limits of $4.31 \times 10^{-8} \text{ M}$ using a graphene-zinc oxide carbon paste electrode. The pyrazinamide was detected in pharmaceutical formulations, urine samples and blood serum. No pre-treatment of samples were necessary for the laboratory samples, these were only cleaned by filtering through a $0.22 \mu\text{m}$ PVDF (polyvinylidene fluoride) syringe and dissolving in buffer [52]. An electrochemical sensor for the determination of rifampicin was also developed in 2013. Here a glassy carbon electrode was modified with a nano-hybrid film of nickel hydroxide nanoparticle and reduced graphene oxide nano-sheets. Tablets of rifampicin prepared in human blood serum were subsequently detected. The serum was vortexed and the proteins separated by centrifugation, diluted and then spiked with rifampicin. The electrocatalytic analysis of rifampicin was carried out by linear sweep voltammetry with a detection limit of 4.16 nmol/L found for this method [53]. Simultaneous detection of anti-TB drugs are also possible and much more feasible with electrochemical sensors since each drug has a unique electrochemical signature. In one such case, pyrazinamide and

ethionamide (ETO) was detected together on a poly-L-cysteine modified glassy carbon electrode. Stock solutions of ETO and PYR were diluted either in urine or serum. As is protocol, the serum was first allowed to precipitate and centrifuged to separate the supernatant. Simultaneous detection of ETO and PYR were carried out and the limit of detection were determined to be 0.531 and 0.113 $\mu\text{mol/L}$ respectively [54].

Biosensors are analytical devices which consist of a biological element such as an enzyme [55] [56], DNA [57] or antigens [48], which is attached to a transducer surface. This biosensor produces a signal due to a bio-recognition event when in the presence of a specific analyte [58]. IUPAC (International Union of Pure and Applied Chemistry) defines a biosensor as a device that uses specific biochemical reactions mediated by isolated enzymes, immunosystems, tissues, organelles or whole cells to detect chemical compounds usually by electrical, thermal or optical signals [59] [60]. Electrochemical biosensors thus have an electrochemical transducer in use.

Quite a few biosensors have been developed for TB via detection of the tubercle itself [61], or in other cases, where the TB biomarkers [62] are detected. However, not many have been developed for the specific detection of TB drugs. Amongst the very few biosensors for TB drug detection are those carried out by Ajayi et al. In this study for instance, an electroactive nanocomposite was used consisting of poly (8-anilino-1-naphthalene sulfonic acid) (PANSA) and silver nanoparticles (AgNP's) stabilized in polyvinylpyrrolidone (PVP). The nanocomposite was used in conjunction with a CYP450-2E1 enzyme to develop a biosensor for the detection of first line drugs. Ethambutol was successfully detected using chronoamperometry within a linear range of 2-12 μM and a detection limit of 0.7 μM [63]. In another application, a modified form of the CYP2E1 enzyme was used for the detection of rifampicin. The enzyme was modified with ethylene glycol bis(succinic acid N-hydroxysuccinimide ester) to produce an EG-modified CYP2E1 biosensor with the same nanocomposite base. Amperometric detection was carried out and a linear range of 2-14 μM was achieved along with a detection limit of 0.05 μM . This biosensor also showed excellent reproducibility, stability as well as sensitivity [64]. Another method of CYP2E1 enzyme modification carried out by the same author was carried out with di-

succinimidyl octanedioate (SA). The modified enzyme biosensor was used to detect pyrazinamide with a similar linear range and a detection limit of $0.044 \mu\text{M}$ [65].

The benefit of electrochemical sensors and biosensors thus include the fact that one can minimise sample preparation drastically. The analysis time is also limited to a large extent in comparison to standard techniques. Electrochemical sensors and biosensors have gained attention since they offer easy to use, low cost and an at point-of-care (POC) alternative to other analytical techniques. POC analysis is considered an on-site diagnostic tool using a mobile device that is accessible to patients at their point of need or location [66]. These sensors are also highly sensitive and selective and can be easily miniaturised. They thus allow for mobility and efficient analysis to be carried out at the point of care of patients. Various electrochemical sensors have been developed to combat TB via DNA based detection of MTB [67], immunosensors for detection of the tubercle itself [61] and even enzymatic biosensors for TB drug detection [65]. Phenotype biosensors however, have not been studied extensively in order to personalise TB treatment and thus, this was the focus of this study in order to assist with the End TB strategy [68]. The End TB strategy was developed by the World Health Organisation and approved by the 67th World Health Assembly in 2014. This strategy aims to achieve a health related target under the UN sustainable development goal 3, which calls to end the TB epidemic [69].

In this work, a first generation polypropyleneimine based dendrimer was synthesised along with its copper functionalised counterpart. Both dendrimers were characterised using microscopic, spectroscopic and electrochemical techniques. Surface morphology was investigated using high resolution transmission electron microscopy (HRTEM), high resolution scanning electron microscopy (HRSEM) and atomic force microscopy (AFM). The size and shape of the samples were determined using small angle X-ray scattering (SAXS) and their structure and optical properties were determined using fourier transform infrared spectroscopy (FTIR) and ultraviolet-visible spectroscopy (UV-vis). The dendrimers were then immobilised on the surface of gold working electrodes for the detection of the four anti-TB drugs, namely isoniazid, ethambutol, pyrazinamide and rifampicin in standard solutions and

complex matrices. This was followed by the incorporation of cytochrome P450 (CYP) 3A4 enzymes into the dendrimer modified working electrode surfaces in order to form simple biosensors. CYP enzymes are responsible for the metabolism of a large variety of compounds, with TB drugs being a part of their substrates. The inclusion of the biological recognition element into the sensor system enhanced their sensitivity and selectivity towards these four drugs and its effects were investigated and compared to the additionally developed chemical sensors.

1.6 Objectives

- To synthesise and characterise polypropyleneimine based dendrimer and copper functionalised first generation metallodendrimer
- Characterisation of the abovementioned materials will be carried out in order to determine its structure, morphology, size, shape and electrochemical properties. Characterisation methods include HRTEM, HRSEM, AFM, FTIR, UV-Vis, SAXS and electrochemical methods such as cyclic voltammetry (CV) and differential pulse voltammetry (DPV).
- To fabricate biosensors using the copper metallodendrimer and cytochrome p450 3A4 enzymes as the biological element
- To use the biosensors to detect various concentrations of each of the four first line anti-TB drugs i.e. INH, ETH, PYR and RIF
- To use the electrochemical biosensors to detect drugs in synthetic urine, plasma or serum samples
- To model the biosensor responses to relate to metabolic profile of TB patients.

1.7 Thesis Overview

CHAPTER 1: This is the introduction chapter, which introduces the topic of the thesis as well as give the background and motivation of the study.

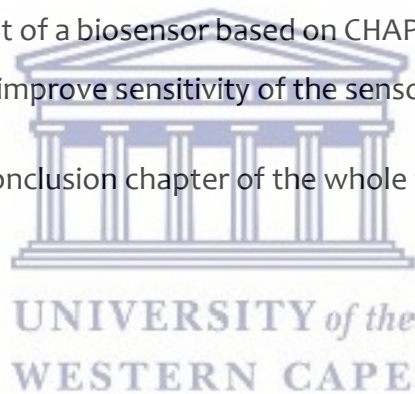
CHAPTER 2: This is the literature review covering the use of CYP 450 enzymes in catalysis and their application in sensors.

CHAPTER 3: The first experimental chapter includes the characterisation of a first generation dendrimer and its copper functionalised counterpart.

CHAPTER 4: This describes the application of the copper metallodendrimer in an electrochemical sensor for the detection of four anti-TB drugs

CHAPTER 5: Development of a biosensor based on CHAPTER 4 with the incorporation of a CYP 3A4 enzyme to improve sensitivity of the sensor.

CHAPTER 6: This is the conclusion chapter of the whole thesis including future works and recommendations



1.8 References

- [1] A. Sakula, "Robert Koch: centenary of the discovery of the tubercle bacillus, 1882.," *The Canadian Veterinary Journal. La revue vétérinaire canadienne*, vol. 24, pp. 127–31, 1983.
- [2] D. Castagnolo, M. Radi, F. Dessì, F. Manetti, M. Saggi, R. Meleddu, A. De Logu, and M. Botta, "Synthesis and biological evaluation of new enantiomerically pure azole derivatives as inhibitors of *Mycobacterium tuberculosis*," *Bioorganic & Medicinal Chemistry Letters*, vol. 19, pp. 2203–2205, 2009.
- [3] W. C. Wang, J.-Y. Chen, Y.-K. Chen, and L.-M. Lin, "Tuberculosis of the head and neck: a review of 20 cases," *Oral Surgery, Oral Medicine, Oral Pathology, Oral Radiology, and Endodontology*, vol. 107, pp. 381–386, 2009.
- [4] T. S. S. Balganes, P. M. M. Alzari, and S. T. T. Cole, "Rising standards for tuberculosis drug development," *Trends in Pharmacological Sciences*, vol. 29, pp. 576–581, 2008.
- [5] S. K. Field, P. Escalante, D. A. Fisher, B. Ireland, R. S. Irwin, "Cough Due to TB and Other Chronic Infections: CHEST Guideline and Expert Panel Report," *Chest*, vol. 153, pp. 467–497, 2018.
- [6] A. Zumla, M. Raviglione, R. Hafner, and C. Fordham von Reyn, "Tuberculosis," *New England Journal of Medicine*, vol. 368, pp. 745–755, 2013.
- [7] A. Idaly, M. Sanchez, M. R. Bertolozzi, C. D. E. La, T. Medio, Q. U. E. Promueve, L. A. Comunicación, and I. D. E. L. A. S. Necesidades, "Beyond DOTS (Directly Observed Treatment Short-course) in Tuberculosis control: interfacing and sharing needs," *Rev Latino Am Enfermagem*, vol. 17, pp. 689–694, 2009.
- [8] P. Glaziou, K. Floyd, and M. C. Raviglione, "Global Epidemiology of Tuberculosis," *Seminars in Respiratory and Critical Care Medicine*, vol. 39, pp. 271–285, 2018.
- [9] World Health Organisation (WHO), "Global Tuberculosis Report 2019," 2019.
- [10] A. Gupta-Wright, G. S. Tomlinson, M. X. Rangaka, and H. A. Fletcher, "World TB Day 2018: The Challenge of Drug Resistant Tuberculosis," *F1000Research*, vol. 7, p. 217, 2018.
- [11] E. M. Streicher, R. M. Warren, C. Kewley, J. Simpson, N. Rastogi, C. Sola, G. D. Van Der Spuy, P. D. Van Helden, and T. C. Victor, "Genotypic and Phenotypic Characterization of Drug-Resistant *Mycobacterium tuberculosis* Isolates from Rural Districts of the Western Cape Province of South Africa," *Journal of Clinical Microbiology*, vol. 42, pp. 891–894, 2004.

- [12] R. C. Y. Chan, M. Hui, E. W. C. Chan, T. K. Au, M. L. Chin, C. K. Yip, C. K. W. AuYeang, C. Y. L. Yeung, K. M. Kam, P. C. W. Yip, and A. F. B. Cheng, "Genetic and phenotypic characterization of drug-resistant Mycobacterium tuberculosis isolates in Hong Kong," *Journal of Antimicrobial Chemotherapy*, vol. 59, pp. 866–873, 2007.
- [13] Centers for Disease Control and Prevention (CDC), "Emergence of Mycobacterium tuberculosis with extensive resistance to second-line drugs--worldwide, 2000-2004.," *MMWR. Morbidity and mortality weekly report*, vol. 55, pp. 301–5, 2006.
- [14] S. Chetty, M. Ramesh, A. Singh-Pillay, and M. E. S. Soliman, "Recent advancements in the development of anti-tuberculosis drugs," *Bioorganic and Medicinal Chemistry Letters*, vol. 27, pp. 370–386, 2017.
- [15] A. A. Velayati, M. R. Masjedi, P. Farnia, P. Tabarsi, J. Ghanavi, A. H. ZiaZarifi, and S. E. Hoffner, "Emergence of New Forms of Totally Drug-Resistant Tuberculosis Bacilli: Super Extensively Drug-Resistant Tuberculosis or Totally Drug-Resistant Strains in Iran," *Chest*, vol. 136, pp. 420–425, 2009.
- [16] A. A. Velayati, P. Farnia, and M. R. Masjedi, "The totally drug resistant tuberculosis (TDR-TB).," *International journal of clinical and experimental medicine*, vol. 6, pp. 307–9, 2013.
- [17] K. Gholami, E. Kamali, S. H. Mi, M. Hajiabdolbaghi, and G. Shalviri, "Evaluation of anti-tuberculosis induced adverse reactions in hospitalized patients," *Pharmacy Practice*, vol. 4, pp. 134–138, 2006.
- [18] H. Hug, D. Bagatto, R. Dannecker, R. Schindler, O. Horlacher, and J. Gut, "ADRIS - The Adverse Drug Reactions Information Scheme.," *Pharmacogenetics*, vol. 13, pp. 767–772, 2004.
- [19] World Health Organisation (WHO), "Global Tuberculosis Report 2016," 2016.
- [20] E. Varshney, M. Tandon, N. Saha, and S. Ali, "In vivo phenotyping of cytochrome 450 isoforms involved in the metabolism of anti-HIV and anti-tubercular drugs in human using cocktail approach: An LC–MS/MS analysis," *Journal of Pharmaceutical and Biomedical Analysis*, vol. 164, pp. 698–705, 2019.
- [21] M. Ingelman-Sundberg, "Pharmacogenetics of cytochrome P450 and its applications in drug therapy: The past, present and future," *Trends in Pharmacological Sciences*, vol. 25, pp. 193–200, 2004.
- [22] S. Ting and S. Schug, "The pharmacogenomics of pain management: Prospects for personalized medicine," *Journal of Pain Research*, vol. 9, pp. 49–56, 2016.
- [23] I. Rajman, L. Knapp, T. Morgan, and C. Masimirembwa, "African Genetic Diversity: Implications for Cytochrome P450-mediated Drug Metabolism and Drug Development," *EBioMedicine*, vol. 17, pp. 67–74, 2017.

- [24] I. Zentner, C. Modongo, N. M. Zetola, J. G. Pasipanodya, S. Srivastava, S. K. Heysell, S. Mpagama, H. P. Schlect, T. Gumbo, G. P. Bisson, and C. Vinnard, "Urine colorimetry for therapeutic drug monitoring of pyrazinamide during tuberculosis treatment," *International Journal of Infectious Diseases*, vol. 68, pp. 18–23, 2018.
- [25] J. Kuhlin, M. G. G. Sturkenboom, S. Ghimire, I. Margineanu, S. H. J. van den Elsen, N. Simbar, O. W. Akkerman, E. M. Jongedijk, R. A. Koster, J. Bruchfeld, D. J. Touw, and J. W. C. Alffenaar, "Mass spectrometry for therapeutic drug monitoring of anti-tuberculosis drugs," *Clinical Mass Spectrometry*, vol. 14. Elsevier, pp. 34–45, 19-Oct-2019.
- [26] M. R. Siddiqui, Z. A. Allothman, and N. Rahman, "Analytical techniques in pharmaceutical analysis: A review," *Arabian Journal of Chemistry*, vol. 10, pp. S1409–S1421, 2017.
- [27] O. Budevsky, "Effectivity of solvents- A new approach in non-aqueous acid-base titrimetry," *Talanta*, vol. 36, pp. 1209–1216, 1989.
- [28] K. K. Verma and S. Palod, "The Titrimetric Determination of 4-Pyridine Carboxylic Acid Hydrazide (Isoniazid) in Drug Formulations with Thallium (III)," *Analytical Letters*, vol. 18, pp. 11–19, 1985.
- [29] D. Amin and A. M. M. Al-Daher, "Titrimetric microdetermination of isoniazid by amplification reactions," *Microchemical Journal*, vol. 27, pp. 389–392, 1982.
- [30] C. Horvath, W. R. Melander, C. Horvath, and W. R. Melander, "Chapter 3 Theory of chromatography," *Journal of Chromatography Library*, vol. 22, pp. A27–A135, 1983.
- [31] A. Mehmedagic, P. Verite, S. Menager, C. Tharasse, C. Chabenat, D. Andre, and O. Lafont, "Determination of pyrazinamide and its main metabolites in rat urine by high-performance liquid chromatography," *Journal of Chromatography B*, vol. 695, pp. 365–372, 1997.
- [32] T. Sriram Siddhartha, B. Prasanthi, T. Santosh, and J. V. Ratna, "Development and validation of high performance liquid chromatographic method for the determination of pyrazinamide in human plasma," *JOPR: Journal of Pharmacy Research*, vol. 7, pp. 33–38, 2013.
- [33] H. Wang, C. Cai, C. Chu, J. Liu, and Y. Kong, "A simple and rapid HPLC/UV method for simultaneous quantification of four constituents in anti-tuberculosis 4-FDC tablets by pre-column derivatization," *Asian Journal of ...*, vol. 7, pp. 303–309, 2012.
- [34] Y.-C. Hsieh and C.-W. Whang, "Analysis of ethambutol and methoxyphenamine by capillary electrophoresis with electrochemiluminescence detection," *Journal of Chromatography A*, vol. 1122, pp. 279–282, 2006.

- [35] M. Sikder, J. R. Lead, G. T. Chandler, and M. Baalousha, "A rapid approach for measuring silver nanoparticle concentration and dissolution in seawater by UV-Vis," *Science of The Total Environment*, 2017.
- [36] M. Shamsipur, M. Sadeghi, A. Garau, and V. Lippolis, "An efficient and selective fluorescent chemical sensor based on 5-(8-hydroxy-2-quinolinylmethyl)-2,8-dithia-5-aza-2,6-pyridinophane as a new fluoroionophore for determination of iron(III) ions. A novel probe for iron speciation," *Analytica Chimica Acta*, vol. 761, pp. 169–177, 2013.
- [37] P. Y. Pawar, A. V. Lagad, S. N. Bahir, Sumedha, and R. Rathi, "Simultaneous UV spectrophotometric method for estimation of isoniazid and pyridoxine in tablet dosage form," *Der Pharma Chemica*, vol. 4, pp. 749–754, 2012.
- [38] A. Safavi and M. Bagheri, "Design of an optical sensor for indirect determination of isoniazid," *Spectrochimica Acta - Part A: Molecular and Biomolecular Spectroscopy*, vol. 70, pp. 735–739, 2008.
- [39] W.-Y. Y. Wu, J.-Y. Y. Yang, L.-M. M. Du, H. Wu, and C.-F. F. Li, "Determination of ethambutol by a sensitive fluorescent probe," *Spectrochimica Acta - Part A: Molecular and Biomolecular Spectroscopy*, vol. 79, pp. 418–422, 2011.
- [40] O. Oxlade and M. Murray, "Tuberculosis and Poverty: Why Are the Poor at Greater Risk in India?," *PLoS ONE*, vol. 7, 2012.
- [41] S. D. Lawn, L.-G. Bekker, K. Middelkoop, L. Myer, and R. Wood, "Impact of HIV Infection on the Epidemiology of Tuberculosis in a Peri-Urban Community in South Africa: The Need for Age-Specific Interventions," *Clinical Infectious Diseases*, vol. 42, pp. 1040–1047, 2006.
- [42] Department of Health Republic of South Africa, Department of Health Strategic Plan 2016-2020. 2011.
- [43] N. Yusoff, "Graphene-Polymer Modified Electrochemical Sensors," in *Graphene-Based Electrochemical Sensors for Biomolecules*, Elsevier, 2018, pp. 155–186.
- [44] C. L. Devi and S. S. Narayanan, "Poly (amido amine) dendrimer/silver nanoparticles/multi-walled carbon nanotubes/poly (neutral red)-modified electrode for electrochemical determination of paracetamol," *Ionics*, vol. 25, pp. 2323–2335, 2019.
- [45] D. E. Motaung, G. H. Mhlongo, P. R. Makgwane, B. P. Dhonge, F. R. Cummings, H. C. Swart, and S. S. Ray, "Ultra-high sensitive and selective H₂ gas sensor manifested by interface of n-n heterostructure of CeO₂-SnO₂ nanoparticles," *Sensors and Actuators B: Chemical*, vol. 254, pp. 984–995, 2018.

- [46] S. Ben Aoun, "Nanostructured carbon electrode modified with N-doped graphene quantum dots–chitosan nanocomposite: A sensitive electrochemical dopamine sensor," *Royal Society Open Science*, vol. 4, p. 171199, 2017.
- [47] G. Congur and A. Erdem, "PAMAM dendrimer modified screen printed electrodes for impedimetric detection of miRNA-34a," *Microchemical Journal*, vol. 148, pp. 748–758, 2019.
- [48] J. H. O. Owino, A. Ignaszak, A. Al-Ahmed, P. G. L. Baker, H. Alemu, J. C. Ngila, and E. Iwuoha, "Modelling of the impedimetric responses of an aflatoxin B1 immunosensor prepared on an electrosynthetic polyaniline platform," *Analytical and Bioanalytical Chemistry*, vol. 388, pp. 1069–1074, 2007.
- [49] L. Wilson, J. Van Wyk, C. Rassie, N. Ross, C. Sunday, H. Makelane, M. Bilibana, T. Waryo, S. Mapolie, P. Baker, and E. Iwuoha, "Electrochemical immunosensor based on the interactions between polypyrrole and cobalt (II) salicylaldimine dendrimer," *International Journal of Electrochemical Science*, vol. 10, pp. 3207–3222, 2015.
- [50] L. Shaw and L. Dennany, "Applications of electrochemical sensors: Forensic drug analysis," *Current Opinion in Electrochemistry*, pp. 10–15, 2017.
- [51] S. Cheemalapati, S. M. Chen, M. A. Ali, and F. M. A. Al-Hemaid, "Enhanced electrocatalytic oxidation of isoniazid at electrochemically modified rhodium electrode for biological and pharmaceutical analysis," *Colloids and Surfaces B: Biointerfaces*, vol. 121, pp. 444–450, 2014.
- [52] P. K. Kalambate, C. R. Rawool, and A. K. Srivastava, "Voltammetric determination of pyrazinamide at graphene-zinc oxide nanocomposite modified carbon paste electrode employing differential pulse voltammetry," *Sensors and Actuators, B: Chemical*, vol. 237, pp. 196–205, 2016.
- [53] S. Rastgar and S. Shahrokhian, "Nickel hydroxide nanoparticles-reduced graphene oxide nanosheets film: Layer-by-layer electrochemical preparation, characterization and rifampicin sensory application," *Talanta*, vol. 119, pp. 156–163, 2014.
- [54] B. R. L. Ferraz, F. R. F. Leite, and A. R. Malagutti, "Simultaneous determination of ethionamide and pyrazinamide using poly(L-cysteine) film-modified glassy carbon electrode," *Talanta*, vol. 154, pp. 197–207, 2016.
- [55] E. Iwuoha, R. Ngece, M. Klink, and P. Baker, "Amperometric responses of CYP2D6 drug metabolism nanobiosensor for sertraline: a selective serotonin reuptake inhibitor," *IET Nanobiotechnology*, vol. 1, p. 62, 2007.

- [56] E. Iwuoha and M. R. Smyth, "Reactivities of organic phase biosensors: 6. Square-wave and differential pulse studies of genetically engineered cytochrome P450cam (CYP101) bioelectrodes in selected solvents," *Biosensors and Bioelectronics*, vol. 18, pp. 237–244, 2003.
- [57] O. Arotiba, A. Ignaszak, R. Malgas, A. Al-Ahmed, P. Baker, S. Mapolie, and E. Iwuoha, "An electrochemical DNA biosensor developed on novel multinuclear nickel(II) salicylaldimine metallodendrimer platform," *Electrochimica Acta*, vol. 53, pp. 1689–1696, 2007.
- [58] O. Arotiba, J. Owino, E. Songa, N. Hendricks, T. Waryo, N. Jahed, P. Baker, and E. Iwuoha, "An electrochemical DNA biosensor developed on a nanocomposite platform of gold and poly(propyleneimine) dendrimer," *Sensors*, vol. 8, pp. 6791–6809, 2008.
- [59] D. R. Thvenot, K. Toth, R. A. Durst, G. S. Wilson, and C. Dudok de Wit, "Electrochemical biosensors: Recommended definitions and classification (Technical Report)," *Pure and Applied Chemistry*, vol. 71, pp. 2333–2348, 1999.
- [60] A. Florea, B. Feier, and C. Cristea, "In situ analysis based on molecularly imprinted polymer electrochemical sensors," in *Comprehensive Analytical Chemistry*, Elsevier B.V., 2019, pp. 1–42.
- [61] E. Alocilja, "Development and Validation of a Biosensor for Rapid TB Detection," in 2015 Annual Meeting Nanotechnology & Biosensors, 2015.
- [62] D. Bhattacharyya, P. K. Sarswat, and M. L. Free, "Quantum dots and carbon dots based fluorescent sensors for TB biomarkers detection," *Vacuum*, 2017.
- [63] R. F. Ngece, N. West, P. M. Ndangili, R. A. Olowu, A. Williams, N. Hendricks, S. Mailu, P. Baker, and E. Iwuoha, "A silver Nanoparticle/Poly (8-Anilino-1-Naphthalene Sulphonic Acid) Bioelectrochemical Biosensor System for the Analytical Determination of Ethambutol," *Int. J. Electrochem. Sci*, vol. 6, pp. 1820–1834, 2011.
- [64] R. Ajayi, U. Sidwaba, U. Feleni, S. Douman, O. Tovide, S. Botha, P. Baker, X. Fuku, S. Hamid, T. Waryo, S. Vilakazi, R. Tshikhudo, and E. Iwuoha, "Chemically amplified cytochrome P450-2E1 drug metabolism nanobiosensor for rifampicin anti-tuberculosis drug," *Electrochimica Acta*, vol. 128, pp. 149–155, 2014.
- [65] F. Ajayi, U. Sidwaba, U. Feleni, S. Douman, E. Mxusani, L. Wilson, C. Rassie, O. Tovide, P. Baker, S. Vilikazi, R. Tshikhudo, and E. Iwuoha, "A Nanosensor System Based On Disuccinimydyl – CYP2E1 for Amperometric Detection of the Anti-Tuberculosis Drug , Pyrazinamide," *International Journal of Medical, Health, Biomedical, Bioengineering and Pharmeceutical Engineering*, vol. 8, pp. 67–71, 2014.

- [66] D. T. N. Tram, H. Wang, S. Sugiarto, T. Li, W. H. Ang, C. Lee, and G. Pastorin, “Advances in nanomaterials and their applications in point of care (POC) devices for the diagnosis of infectious diseases,” *Biotechnology Advances*, vol. 34, pp. 1275–1288, 2016.
- [67] E. Torres-Chavolla and E. C. Alocilja, “Nanoparticle based DNA biosensor for tuberculosis detection using thermophilic helicase-dependent isothermal amplification,” *Biosensors and Bioelectronics*, vol. 26, pp. 4614–4618, 2011.
- [68] H. L. Rieder, “Reflections on the end TB strategy,” *Indian Journal of Tuberculosis*, vol. 66, pp. 167–169, 2019.
- [69] World Health Organization, “WHO’s End TB Strategy: The Essentials,” 2015.

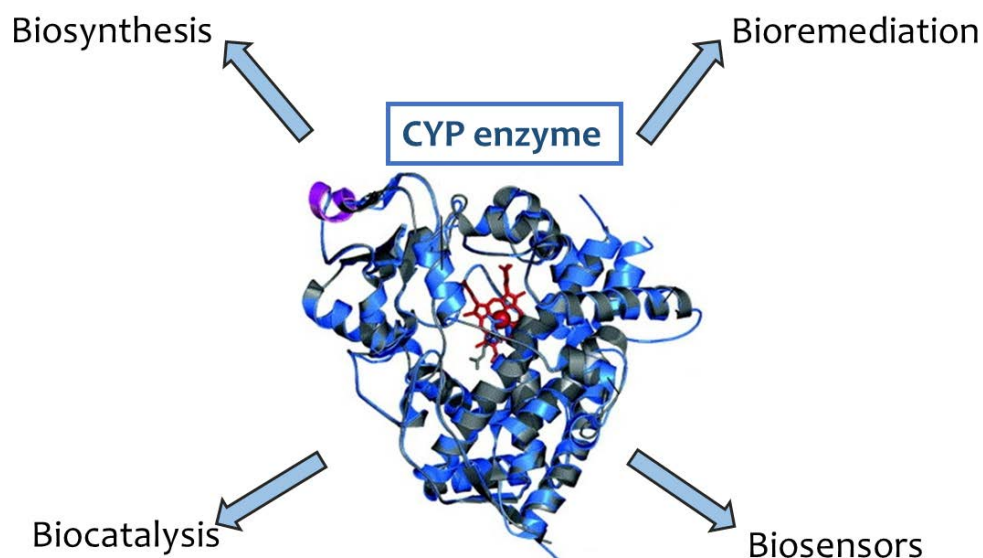


Chapter 2

2 Literature review: Cytochrome P450 enzymes in catalytic reactions and applications in sensors

Abstract

Cytochrome P450 (CYP or CYP450) enzymes are responsible for the metabolism of 75 % of drugs in the human body. CYP's in humans typically act as monooxygenases and function by hydroxylating substrates during metabolism. These enzymes are found in various other organisms, such as fungi and bacteria, with a huge variety of functions amongst them. These functions can be optimised through genetic engineering and directed evolution. The reactions CYP enzymes catalyse include not only regio-selective hydroxylation, but also epoxidation, deamination, carbene N-H insertion and others. The application of this diverse group of enzymes in industry was thus a natural route. Enzymes provide an environmentally safe method of carrying out reactions that would otherwise make use of dangerous solvents, transition metal catalysts and high temperatures and pressures. CYP's have been found to be highly regio- and stereo-selective in their reactions, which makes the application in industry more lucrative in minimising the formation of unnecessary minor products during biosynthesis and bioconversion [1]. Expressing these enzymes in microbes allow for bioremediation to take place at the site of contamination in soil or water as well. CYP's have recently been used in multiple biosensor systems acting as the biorecognition element towards various compounds. CYP's have also been found to improve the sensitivity, selectivity and detection limits of these sensors significantly and continue to be a point of research focus currently [2].



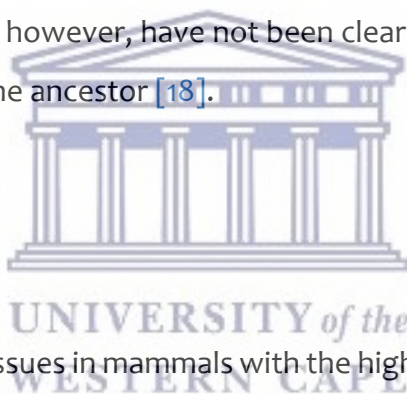
Scheme 2-1: Graphical abstract for Chapter 2 [3]

2.1 Introduction

Cytochrome P450 was first discovered in 1955 by Brodie et al [4] and Axelrod [5] who found that an enzyme system present in the liver was able to metabolise xenobiotic compounds [6]. Xenobiotics are compounds that are not normally found in the body and include drugs, pollutants and food additives etc. [7]. It was only in 1958 when another discovery was made that would give the distinctive name to this group of enzymes. A carbon monoxide (CO) binding pigment in liver microsomes was found to have a UV-Visible absorption maxima at 450 nm, which was in actuality the P450 enzyme [8], [9]. Human CYP enzymes are involved in the initial phase of metabolism of 75 % of drugs and many other compounds. The human genome contains 57 genes for P450 enzymes which are arranged into 18 families and 42 subfamilies [10] [11]. All CYP's contain a characteristic heme centre, which is a coordinated iron-porphyrin complex that is in close proximity to the active site of the enzyme. The substituents of the porphyrin ring determine the functionality of the enzyme [12].

2.1.1 Nomenclature

This group of enzymes are named according to a cytochrome P450 enzyme naming system established by the CYP nomenclature committee [13]. The name consists of the letters CYP, which represents the heme containing protein superfamily. A numeral will then denote the family, for example CYP1, CYP2 etc. A letter then follows which represents the sub-family (i.e. CYP1A). Finally, another numeral will represent the individual iso-enzyme or gene such as CYP1A1 [14]. The enzyme and mRNA are represented by normal font (CYP1A1), whereas the DNA and gene are written in italics (*CYP1A1*). Members of a CYP family are grouped according to their primary amino acid sequence with a 40 % similarity. The amino acid sequence in a subfamily are generally more than 55 % identical [15]. Clans have been developed as a higher order of grouping for CYP's due to the increased number of sequenced genomes [16]. Clan membership parameters however, have not been clearly identified [17], but they are derived from a single gene ancestor [18].



2.1.2 Human CYP's

CYP's are present in all tissues in mammals with the highest concentration in the liver and small intestine. Studies carried out in 1994 [19] and 2014 [20] revealed that 87 % of the human liver cytochrome P450 content was made up of CYP1A2, CYP2A6, CYP2B6, CYP2C, CYP2D6, CYP2E1, CYP3A and CYP4F. A pie chart representing the CYP450 content of the human liver is shown in Figure 2-1. The majority of CYP liver content i.e. 28.8 % is made up of the CYP3A sub-family whereas the highest percentage of single isozyme content is CYP1A2 at 12.7 %.

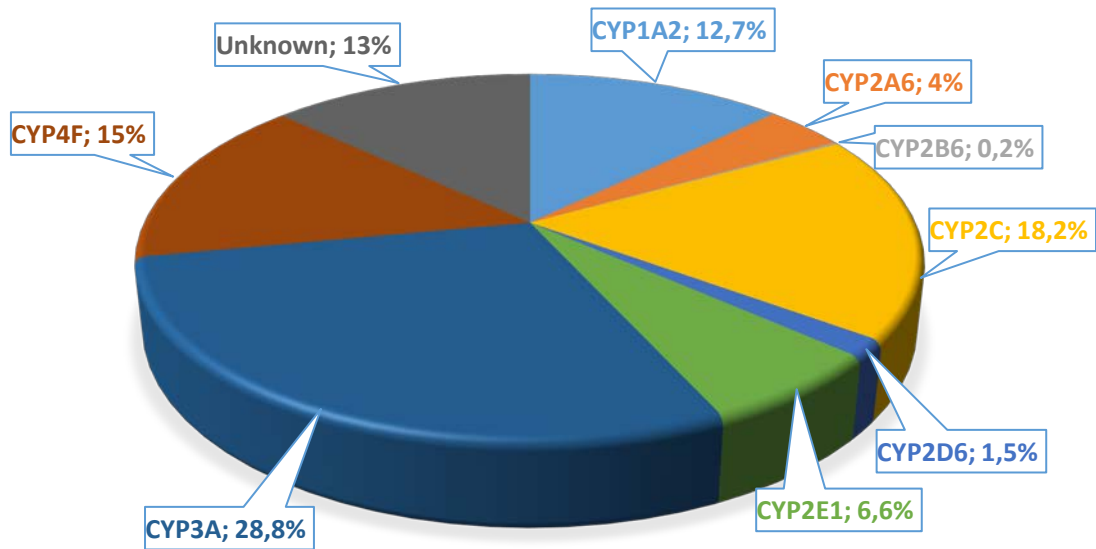


Figure 2-1: Human liver cytochrome P450 content

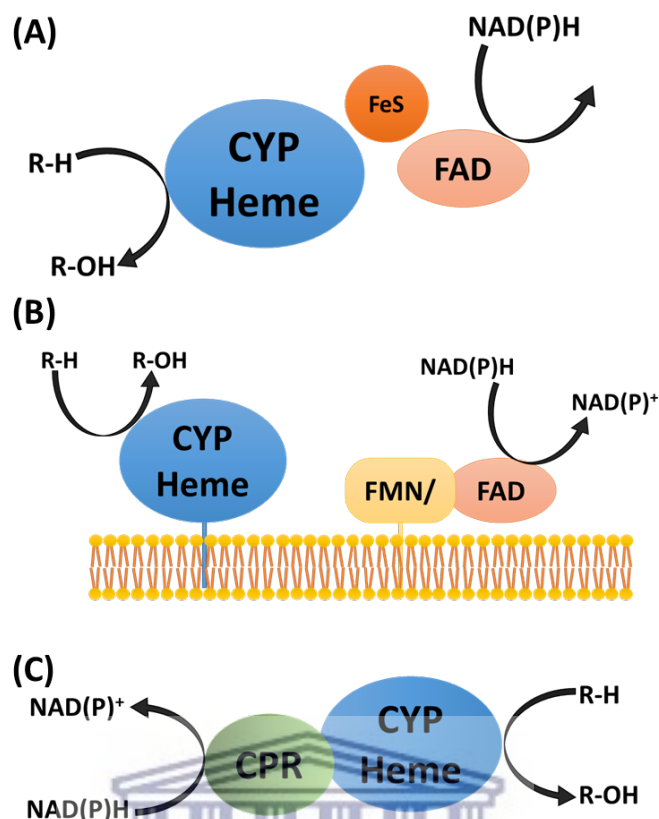
The membrane bound CYP's in humans are responsible for a variety of functions in the body depending on where they are situated. They are unique biocatalysts which undertake a variety of stereo- and regio-specific reactions in both the first and second phase of metabolism [21]. CYP's in the liver are responsible for bile acid synthesis [22] as well as metabolism of carcinogens, pollutants and drugs. Mitochondrial CYP's of steroidogenic tissues such as the ovary, adrenal cortex, testis, placenta or breasts, are involved in degradation and synthesis of endogenous steroid hormones [23]. Other functions of CYP's include metabolism of vitamins, cholesterol biosynthesis and oxidation of unsaturated fatty acids. CYP's present in the brain have been found to maintain brain cholesterol homeostasis and eliminate retinoids [24]. A table representing the 57 identified CYP enzymes in the human body and their major substrate groups are as shown in Table 2-1. It is clear that majority of these proteins act on xenobiotics and sterols as substrates. Xenobiotics are compounds that are not found in the body such as drugs, pollutants and others.

Table 2-1: 57 Human enzymes according to their major substrate class [25], [26]

Substrate Class	CYP enzyme
Vitamins	2R1, 24A1, 26A1, 26B1, 26C1, 27B1
Eicosanoids	4F2, 4F3, 4F8, 5A1, 8A1
Fatty Acids	2J2, 4A11, 4B1, 4F12
Xenobiotics	1A1, 1A2, 2A6, 2A13, 2B6, 2C8, 2C9, 2C18, 2C19, 2D6, 2E1, 2F1, 3A4, 3A5, 3A7
Sterols	1B1, 7A1, 7B1, 8B1, 11A1, 11B1, 11B2, 17A1, 19A1, 21A2, 27A1, 39A1, 46A1, 51A1
Unknown	2A7, 2S1, 2U1, 2W1, 3A43, 4A22, 4F11, 4F22, 4V2, 4X1, 4Z1, 20A1, 27C1

2.1.3 Mechanism of Action and Classification

CYP's exist in bacteria and fungus and are enormously diverse within these microbes. They have also been identified in plants, animals, protists, archaea, bacteria and even viruses [27]. Enzymes usually require co-factors like NADH or NADPH to provide electrons for the reactions they catalyse. The mechanism of action of CYP enzymes in the different organisms are defined by their redox partners or electron support system and are classified accordingly. There are two main classes i.e. I and II, as well as other subclasses. Class I consists of the bacterial system with a soluble reductase system comprising of FAD (flavin adenine dinucleotide) and FeS (iron sulphide) ferredoxin. Class II is a membrane bound system with an associated NADPH-CPR (cytochrome P450 reductase), consisting of FAD and FMN (flavin mononucleotide) [28]. A unique configuration to note is the self-sufficient CYP redox system which has a fusion protein structure with a heme domain and CPR domain consisting of FMN/FAD. This configuration is present in the CYP102A1 (CYPBM₃) enzyme, which makes this enzyme a very attractive option for application in industry. A scheme representing the molecular organisation of the classes of CYP and their redox partners are shown in Scheme 2-2. [29][30].



Scheme 2-2: CYP450 system in (A) typical class I bacterial CYP system (B) a typical class II eukaryotic membrane bound CYP reductase system (CPR) consisting of FMN/FAD (C) fused self-sufficient CYP system with CPR

FMN = Flavin mononucleotide, FAD = Flavin adenine dinucleotide, FeS = iron-sulfide cluster

2.1.4 CYP reactions and substrates

CYP's enzymes and genes are present in most eukaryotes i.e. humans and plants, but are not necessarily present in prokaryotes. Some bacteria such as *Mycobacterium smegmatis*, contain 39 genes that encode for CYP however, they are not even present in species such as *Escherichia coli*. [30]. To date there have been over 50 000 CYP's identified [31]. CYP's in humans are monooxygenases which act on the substrates by introducing one atom of oxygen into the molecule [32]. Amongst the vast range of reactions of other CYP's are aromatic hydroxylation, oxidation deamination, decarboxylation, dehydrogenation, dehydration, denitration, dehalogenation, arene and alkene epoxidation, ring formation, expansion and contraction [28], [33]. CYP's exist in plants as means of promoting growth, development and protecting plants

against stresses [34]. These enzymes also play a huge role in the adaptation of fungi to specific environments. A summary of the various types of CYP enzymes and their characteristics are shown in Table 2-2.

Table 2-2: General characteristics of cytochrome P450 enzymes [35], [36], [27]

Human Cytochrome P450			
Enzyme	Substrate reaction	Substrate	Tissue localisation
CYP1A1	Ethoxyresorufin O-deethylation	Pre-carcinogens, PAH's	Extrahepatic
CYP2D6	Dextromethorphan O-deethylation, bupuralol 1'-hydroxylation, debrisoquine 4-hydroxylation	Drugs	Liver
CYP2E1	Chlorzoxazone 6-hydroxylation	Solvents, drugs, pre-carcinogens	Liver
CYP3A4	Testosterone 6 β -hydroxylation, midazolam 1'-hydroxylation, erythromycin N-demethylase	Drugs, pre-carcinogens, dietary components	Liver, intestine
Plant Cytochrome P450			
Enzyme	Source	Metabolite	Related function
CYP75	<i>Vitis vinifera</i>	Flavonoid	Biosynthesis Of Anthocyanins
CYP85A1	<i>Oryza sativa</i>	Steroid	Biosynthesis Of Castasteron
CYP706M1	<i>Cupressus nootkatensis</i>	Terpenoids	Biosynthesis of a natural sesquiterpene ketone
Bacterial Cytochrome P450			
Bacteria	Enzyme	Function	
<i>Pseudomas putida</i>	CYP101A1	Catabolism of camphor	
<i>Bacillus megaterium</i>	CYP102A1	Fatty acid catabolism	
<i>Jeotgalicocussp. ATCC 8456</i>	CYP152A3	Decarboxylation of fatty acid	
<i>Sorangium cellulorum</i>	CYP167A1	Epothilone biosynthesis/antitumour	
Fungal Cytochrome P450			
Microbe	Enzyme	Function	
<i>Saccharomyces cerevisiae</i>	CYP51	Sterol biosynthesis (14-demethylation)	
<i>Candida tropicalis</i>	CYP52A1	Alkane and fatty acid catabolism	
<i>Rhizopus oryzae</i>	CYP509C1	Steroid 11 α -hydroxylase	
<i>Fusarium oxysporum</i>	CYP55A1	Denitrification	

Human CYP's are mostly involved in metabolism while plant CYP's are focused on biosynthesis of natural products. Bacterial and fungal CYP's are also involved in biosynthesis as well as catabolism and others. This wide range of substrates functions and reactivity's gives rise to many possible industrial applications of these enzymes. These applications include biosynthesis of natural products, biocatalysis, bioconversion/biotransformation, bioremediation and biosensors. With protein engineering becoming a more researched technique, there is a huge potential for tailoring these enzymes to produce high value products and metabolites [37]. The applications of these enzymes will therefore be discussed in this review.

2.2 **Biosynthesis of natural products**

One of the first functions of CYP enzymes for potential use in industry to be discussed, will be towards the biosynthesis of natural products. Chemical synthesis of desired products usually makes use of transition metal catalysts, dangerous solvents and sometimes high temperatures and pressures [38]. On the other hand, extraction of natural products from plants is limited to the amount of plant available, therefore to overcome this limitation, researchers have developed numerous methods of biosynthesising these products. It is possible to take advantage of the role of enzymes as well as engineering in the biosynthesis of natural products. There are multiple steps in the pathway towards the biosynthesis of groups of compounds in plants and the role of CYP's will be discussed here.

2.2.1 **Terpenoids/terpenes**

Terpenoids are an extremely diverse group of natural products which find applications in cosmetics, food and pharmaceutical industries. Terpenoids are made out of repeating isoprene units i.e. C_5H_8 and are named according to how many units they contain: monoterpenoids (10C), sesquiterpenoids (15C), diterpenoids (20C) etc. [39]. The biosynthesis of terpenoids is usually a four-stage process, with the last stage

being post modifications in which CYP's are heavily involved. Multiple issues effect the efficient biosynthesis of these compounds, which include the use of uncharacterised CYP's, slow reactions and the necessity of an additional protein partner. All of these reasons make the application in industry difficult, but recently some strategies to counteract these have been found. In order to identify CYP's which are capable of carrying out desired reactions, CYP discovery has previously focused on gene deletion/silencing and in vitro enzyme assays. Recently, one of the main solutions would be to engineer CYP's either via directed evolution [40] or rational design [41], amongst many others. CYP discovery and engineering in recent years have thus propelled the possibility of industrial applications for terpenoid biosynthesis [42].

CYP enzymes that are mostly involved in the biosynthesis of terpenoids belong to the following plant clans: CYP85, CYP71 and CYP72. Clans are a group of families within plant CYP's that are closely related and are named according to their lowest numbered family member. They might be single family or multiple family clans [43]. The CYP71 clan is mostly involved in secondary metabolism. One example is the biosynthesis of artemisinin by CYP71AV1 via the oxidation of intermediates amorpha-4,11-diene, artemisinic alcohol and artemisinic aldehyde to artemisinic acid. Artemisinin is used to treat malaria and has a lower toxicity and faster action than current anti-malarial drugs [44].

Phytoalexins, specifically zealexin, is a sesquiterpenoid antibiotic produced by maize which provides protection against fungal infections. CYP71Z18 has been identified as being involved in the initial step in the biosynthetic pathway by catalysing the oxidation of C15 in (S)- β -macro-carpene to form zealexin A1. The specific reaction of CYP450 in the pathway is shown in Figure 2-2. The group used metabolic engineering system to co-express a modified CYP71Z18 with cytochrome P450 reductase (CPR) in an *E. coli* that also produced (S)- β -macro-carpene. The oxidation reactions revealed three products, which were found to be the alcohol, aldehyde and finally the carboxylic acid form of zealexin A1. This engineered reaction was found to be successful in producing zealexin A1 [45].

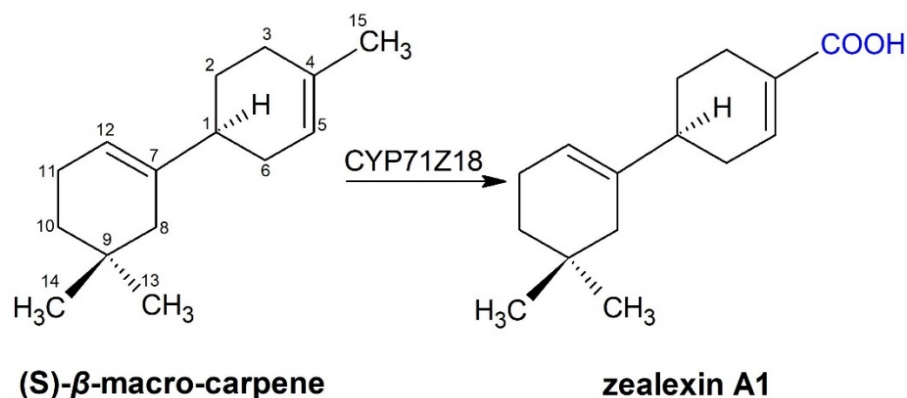


Figure 2-2: Proposed reaction of CYP71Z18 with (S)-β-macro-carpene at C15 to form zealexin A1

2.2.2 Flavonoids

Flavonoids are compounds found in plants which are known for their anti-inflammatory and antioxidant abilities. They generally consist of two C₆ aromatic rings joined by a C₃ carbon bridge which is usually a heterocyclic ring [46]. *p*-Hydroxycinnamic acid has successfully been produced from glucose in yeast. This was achieved by using phenylalanine and tyrosine ammonia lyases. The cinnamate-4-hydroxylase (C₄H-P450) and CYP450 reductase genes were also expressed from *Helianthus tuberosus* [47]. C₄H-P450 is responsible for the conversion of *trans*-cinnamic acid to *p*-coumaric acid (*p*-hydroxycinnamic acid) via a hydroxylation reaction [48].

CYP75B1, also known as flavonoid 3'-hydroxylase (F3'H) is an enzyme identified in *Arabidopsis thaliana* [49]. It acts on either dihydrokaempferol or kaempferol and converts them to dihydroquercetin and quercetin, respectively. This is done via a hydroxylation reaction occurring at the 3'-position of the B-ring in the respective flavonoid [50]. The reaction of CYP75B1 on dihydroquercetin can be shown in Figure 2-3.

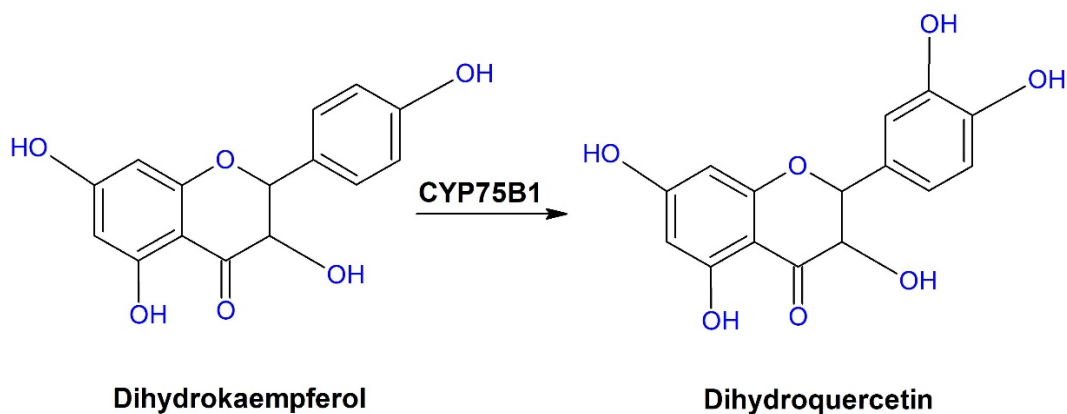


Figure 2-3: CYP75B1 action at C3' on dihydroquercetin to form quercetin

2.2.3 Carotenoids

Carotenoids are a group of pigments found in red, orange and yellow coloured fruit and vegetables. The chemical structure of these molecules determine biological functions as well as their color [51]. Carotenoids also protect against oxidative stress, play crucial roles in photoprotection and reduce risks of inflammatory diseases in humans. Recently the role of CYP's in biosynthesis of these molecules have been demonstrated in *Euglena gracilis*, a unicellular flagellate. CYP97H1 has been identified as a β -carotene monohydroxylase responsible for the hydroxylation of β -carotene to β -cryptoxanthin [52].

2.2.4 Steroids

Steroid pharmaceuticals are in high demand and the biosynthesis of these products have been investigated thoroughly. These chemicals are found in plants, fungi and animals and have a variety of functions including maintaining cell membranes, regulate blood pressure and act as sex hormones. Biosynthesis of steroid hormones in humans involve the action of six CYP enzymes. This metabolic pathway uses cholesterol as a starting material. CYP11B1 and CYP21A2 are involved in hydroxylation reactions exclusively while the others have various functions within the cycle. The other enzymes in the cycle include CYP17A1, CYP11A1, CYP19A1 and CYP21A2 [53].

The most notable products of this pathway include progesterone, testosterone and estradiol amongst others. Understanding the mechanisms of action each of these enzymes undergo, will aid in therapeutic interventions against disorders caused by deregulation of steroids in the future [54].

2.2.5 Erythromycin

Another example of biosynthesis via CYP's is the production of erythromycin. Erythromycin is an antibiotic, which is produced by *Saccharopolyspora erythraea*, an actinomycete bacterium. CYP107A1, also known as CYPeryF, is involved in the hydroxylation reactions carried out on 6-deoxyerythronolide B (6-DEB). This enzyme reacts specifically at positions 6 and 12 on a macrolide ring as shown in Figure 2-4. CYP uses two electron transport proteins; to cleave the O-O bond in molecular oxygen and to insert one oxygen atom at the 6S position of 6-DEB to form erythromycin [55].

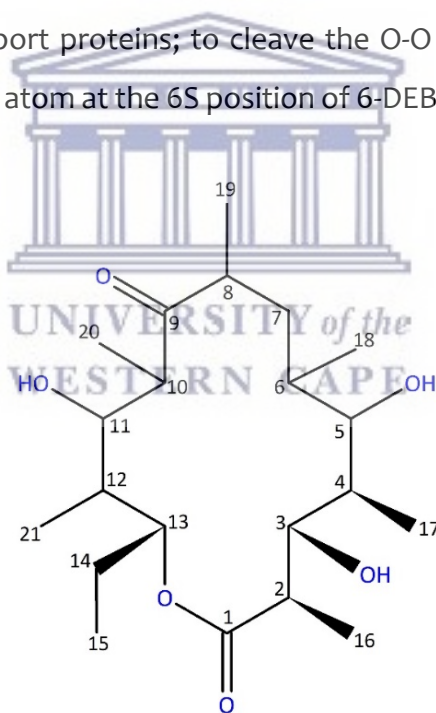


Figure 2-4: 6-deoxyerythronolide B, a substrate of CYP107A1 which produces erythromycin

2.2.6 Prunasin

Eucalyptus cladocalyx is a tree which contains a very interesting CYP functionality. This plant is cyanogenic in the sense that it releases toxic hydrogen cyanide, as a defence mechanism via the release of prunasin, a cyanogenic glucoside [56]. Prunasin is

biosynthesised via a multi-step process involving three CYP enzymes amongst others. Cyanogenic glucosides are derived from amino acids therefore prunasin is derived from phenylalanine. CYP79A125 converts phenylalanine to its corresponding aldoxime. CYP706C55 is responsible for the dehydration of phenylacetaldoxime to phenylacetonitrile. CYP71B03 then hydroxylates the compound to form mandelonitrile. The final step in the biosynthesis is carried out by UDP-glucosyltransferase to form prunasin [57]. A representation of this biosynthetic pathway is as shown in Figure 2-5.

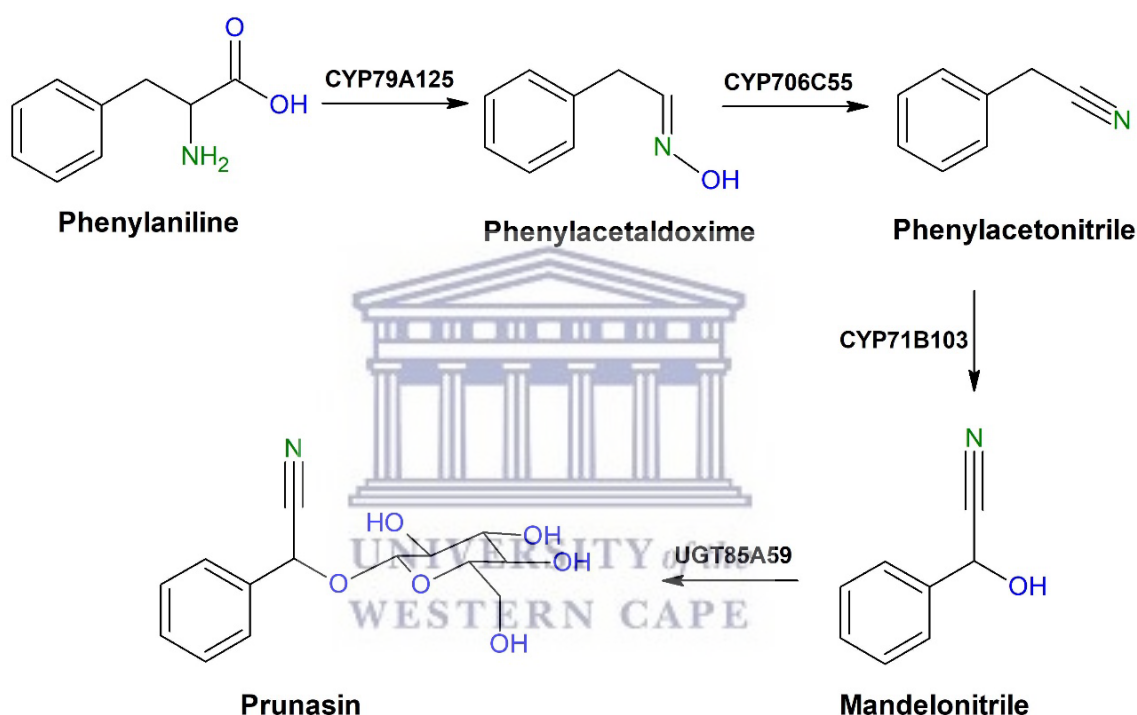


Figure 2-5: Biosynthetic pathway for the production of prunasin by *E. cladocalyx*

2.2.7 Indigo dyes

Indigo dyes are used in very large quantities throughout the world. The usual synthetic route for these dyes include the use of petrochemical resources and hazardous chemicals [58]. The biosynthesis of indigo dye and its derivatives have been carried out with the use of CYP102G4, which is obtained from *Streptomyces avermitilis*. For the experiment, the CYP was expressed in *E. coli* and used in a one pot synthesis method. L-tryptophan was used as a starting material which was modified

by tryptophan-7-halogenase and tryptophanase to form 7-chloroindole. CYP102G4 then regio-selectively hydroxylates the indole at the C3 position, activating the carbon at C2, causing dimerization to form indigo dye [59]. Various other functional groups were investigated which changed the properties of the indigo dye significantly to create dyes with different colours such as those shown in Figure 2-6.

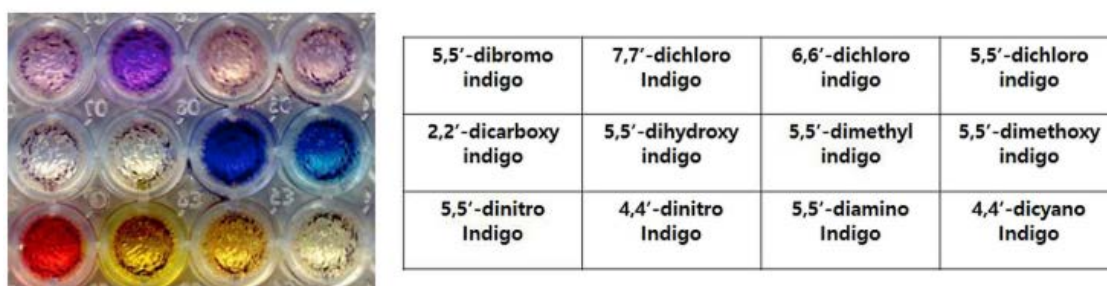


Figure 2-6: Colour shifts of various indigoids depending on their functional groups [59]

This ability to tailorise these dyes and produce them via biosynthesis is highly favourable in industry. Biosynthesis of indigo dyes have been found to be successful with CYP102A as well as other environmentally friendly routes [60].



2.2.8 Anti-cancer agents

Epothilones A and B are natural products which have been identified as highly promising anti-cancer agents. These products are isolated from *Sorangium cellulosum* and attack tumours by stabilising microtubules. Epothilones C and D have a double bond in the macrocyclic lactone ring which is converted to an epoxide group by a CYP enzyme called EpoK (CYP167A1) to produce epothilone A and B respectively [61] [62]. The activity of the epothilone can be represented by Figure 2-7.

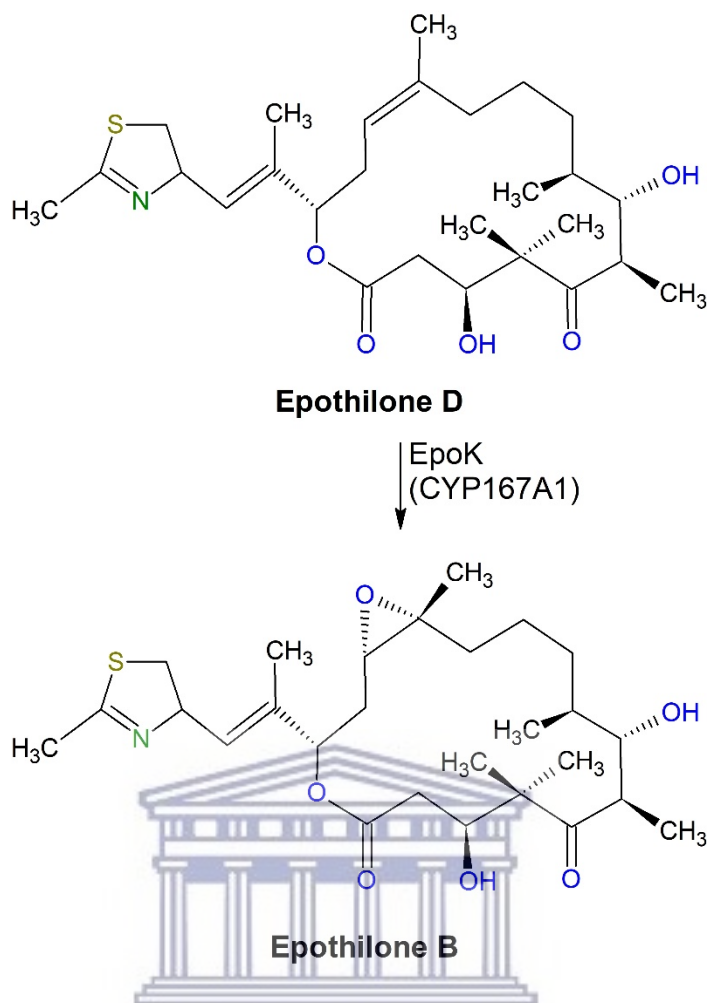


Figure 2-7: Epoxidation of epothilone D by EpoK CYP450 enzyme to form epothilone B

CYP enzymes are involved in various reactions in the synthesis of natural products. The selectivity and reactivity of these proteins will thus improve their use in producing valuable pharmaceuticals for agriculture, medicine and industry. The possibility of engineering CYP's derived from microbes to work on alternative substrates and add new functions lead to endless possibilities in drug discovery as well [63] [64].

2.3 **Biocatalysis and Bioconversion**

Biocatalysis or bioconversion refers to the use of living systems or their parts to speed up or induce chemical reactions. Natural catalysts such as enzymes, perform a tremendous number of chemical transformations which have the added benefit of being highly selective and specific under relatively mild conditions of pressure and temperature, and are thus ideal for this application. Regio- and enantio-selective hydroxylation is an ability of CYP's which make it quite attractive for the use of bioconversion. These reactions are capable of producing drugs, vitamins, fragrances, pesticides and flavours [65]. CYP's are able to selectively insert oxygen into a relatively inactive bond between carbon and hydrogen which gives it the ability to shorten long synthetic strategies [66]. In contrast to biosynthesis, bioconversion or biocatalysis is also involved in the metabolism of products, drugs and other harmful substances.



2.3.1 **Whole cell biocatalyst**

CYP's generally require a redox partner in order to initiate a reaction and this is thus one of its limitations. The solution to this is to express the enzymes within a microbe in order to mimic the reaction in nature. A whole cell biocatalyst has been developed based on CYP108N7. The enzyme was expressed in *E. coli* together with glucose dehydrogenase which supplied the reduced cofactor NADPH and redox partners. The biocatalyst was used to carry out reactions such as epoxidation, sulfoxidation, hydroxylation, demethylation and dehalogenation. These reactions were carried out on substrates such as styrene, 1-bromo-4-ethylbenzene and 4'-bromoacetophenone. This enzyme has been found to have an improved ability towards sulfoxidation reactions with an excellent enantioselectivity [67].

2.3.2 Pharmaceutical agents and drugs

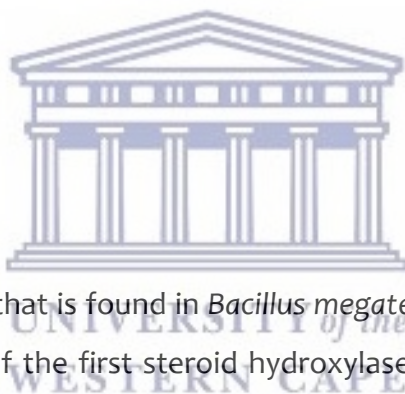
CYP's are involved in drug development by aiding in determining the metabolites and their relative adverse drug reactions. This was proven in a study recently involving ibuprofen. This drug is a very common anti-inflammatory and the enzymes involved in its metabolism in the body are CYP2C8 and CYP2C9. This process was mimicked by expressing CYP505X (from *Aspergillus fumigatus*) as well as a variant with five mutations in the yeast *Pichia pastoris*. This enzyme was successful in carrying out hydroxylation reactions to form 1- and 2-hydroxyibuprofen [68]. What is unique about this enzyme is that CYP505X is a self sufficient class VIII enzyme in that the redox partner is fused with the CYP domain, minimising the need for a separate and additional redox system [69].

A microbial CYP505X was also used for a whole cell mediated biotransformation of capsaicin. Capsaicin is a compound found in various peppers and has irritative and analgesic properties. It has also been found to have an impact on thermoregulation and adipose tissue metabolism. Capsaicin also has hypotensive, anticancer and antioxidative effects [70]. CYP505X and ten variants were expressed in *E. coli* and used as lyophilized whole cell biocatalyst. Two major metabolites were identified as a result of the respective hydroxylation and epoxidation of capsaicin. The hydroxylated product was found to be a metabolite of human CYP3A4 and CYP2C8 whereas the other major metabolite was assumed to be a product of the action of the microbial CYP. This reaction could be suitable for upscaling due to its suitable substrate concentration and reaction time [71].

Recently, a set of mutant CYP102A1 enzymes from *Bacillus megatarium* was applied for the bioconversion of polydatin to (E)-astringin. Polydatin and (E)-astringin are natural glycosides which are found in plants, wines and foods. They are both hydroxylated versions of resveratrol which has numerous beneficial pharmacological activities against inflammatory disease, cancer, obesity etc. [72], [73]. The bioconversion was carried out via a regioselective C-3' hydroxylation using CYP102A1 and found to be highly efficient. The enzyme and polydatin was dissolved in potassium phosphate buffer with an aliquot of NADPH generating system to initiate

the reactions. The synthesis of this highly valued product was beneficial because it was a mild reaction method for a complex and sensitive natural product [74].

Another chemical of great pharmaceutical value is colchicine. This chemical in its native form can be used as an anti-cancer drug, but is severely toxic. Derivatives of colchicine have thus been developed such as 3-demethylated colchicine (3-DMC) which has enhanced therapeutic characteristics. The conversion of the toxic colchicine to 3-DMC has a low yield of 45-50 % and thus bioconversion has been investigated. CYP102A1 (CYP BM3) from *Bacillus megaterium* was expressed in recombinant *E. coli* whole cells and used to convert colchicine to 3-DMC in both free and immobilized cells. The enzyme regioselectively demethylated colchicine and C3 in ring A. This experiment was successful in the environmentally friendly, mild synthesis of 3-DMC with a high selectivity and yield while offering biocatalyst reusability as well [75].



2.3.3 Steroids

CYP106A2 is an enzyme that is found in *Bacillus megaterium*, a soil bacterium. It has been identified as one of the first steroid hydroxylases in bacteria which converts progesterone to 15 β -hydroxyprogesterone. The stereo-selectivity of this enzyme has successfully been adjusted using protein design strategies in order to adapt its application in industry. The hydroxylating action of CYP102A2 has been investigated since 1975 and its use has mostly been applied selectively to steroids with hydroxylation occurring specifically at the position 15 β [41]. In-vitro CYP106A2 systems are not feasible for scaling up in industrial applications, so to circumvent this, a whole-cell biocatalyst is the best option. A group designed an *E. coli* based system using the bacterial CYP106A2 along with bovine mitochondrial electron transfer system consisting of AdR (adrenodoxin reductase) and Adx (ferredoxin adrenodoxin). The whole cell biocatalyst was successful in the conversion of 11-deoxycorticosterone (DOC) to 15 β -DOC. The average rate of the conversion was 1 mM/d in culture volume of 300 ml [76].

Another enzyme that acts on 11-deoxycorticosterone is CYP260B1 from *Sorangium cellulosum*. Recently the major product of this enzyme was identified to be the 9 α -hydroxy-11-deoxycorticosterone. A CYP260B1-T224A mutant was developed in order to minimise side reactions which increased selectivity to about 75 % compared to 60 % in the wild type. An *E. coli* whole cell biocatalyst was used with the mutant variant along with redox partners and showed great potential for upscaling [1]. The reactions on DOC by the CYP106A2 and CYP260B1 enzymes are represented in Figure 2-8. The fact that these two enzymes are able to selectively act on these inactive carbons, make them a huge benefit in organic synthesis.

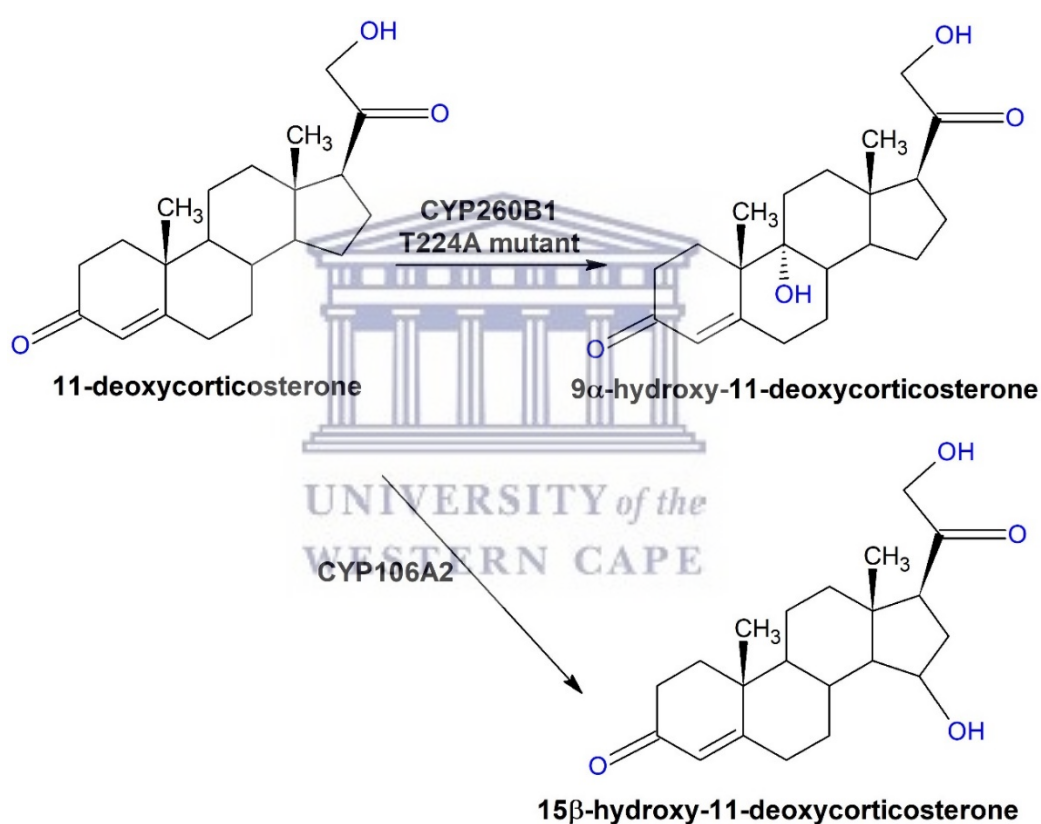


Figure 2-8: Hydroxylase action of CYP260B1 and CYP106A2 on DOC

CYP's are versatile enzymes in that they catalyse various types of reactions. Another less common way in which these enzymes have recently been proved to act is C-C cleavage of steroids. A limited number of CYPs catalyse this reaction, especially in bacteria. A CYP154C8 enzyme was expressed in *E.coli* with spinach ferredoxin reductase (Fdr) and ferredoxin (Fdx) surrogate redox partners. CYP154C8 catalyzed

C-C cleavage in steroids with hydroxyl and hydroxyacetyl functionalities at C17. It was found that a variation in redox partner affects the type and selectivity of product formed. Other redox partners investigated include Pdx and Pdr from *Pseudomonas putida* which did not produce C-C cleaved products. Substrates investigated for this reaction include cortisone, prednisone and hydrocortisone. The products of C-C cleavage via CYP are 17-ketosteroids but the exact mechanism is not yet known [77].

2.3.4 Abiotic reactions

The versatility of these CYP enzymes is further demonstrated by CYP102A1 (CYP BM₃) from *Bacillus megaterium* which has recently been engineered to perform abiotic (non-natural) reactions [78]. These include (A) oxidative deamination of alkyl azides [79], (B) olefin cyclopropanation [80], (C) intramolecular C–H amination reactions [81] (D) carbene N–H insertion [82]. These reactions by CYP BM₃ on various substrates are represented by Figure 2-9. These reactions were carried out under anaerobic conditions and using either NADPH or dithionate as reducing agents. CYP BM₃ and its engineered variants have been widely used for wide range of reactions and are still being optimised toward this goal. The fact that this single enzyme is able to work on such a range of substrates also makes it suitable for industrial application as a biocatalyst.

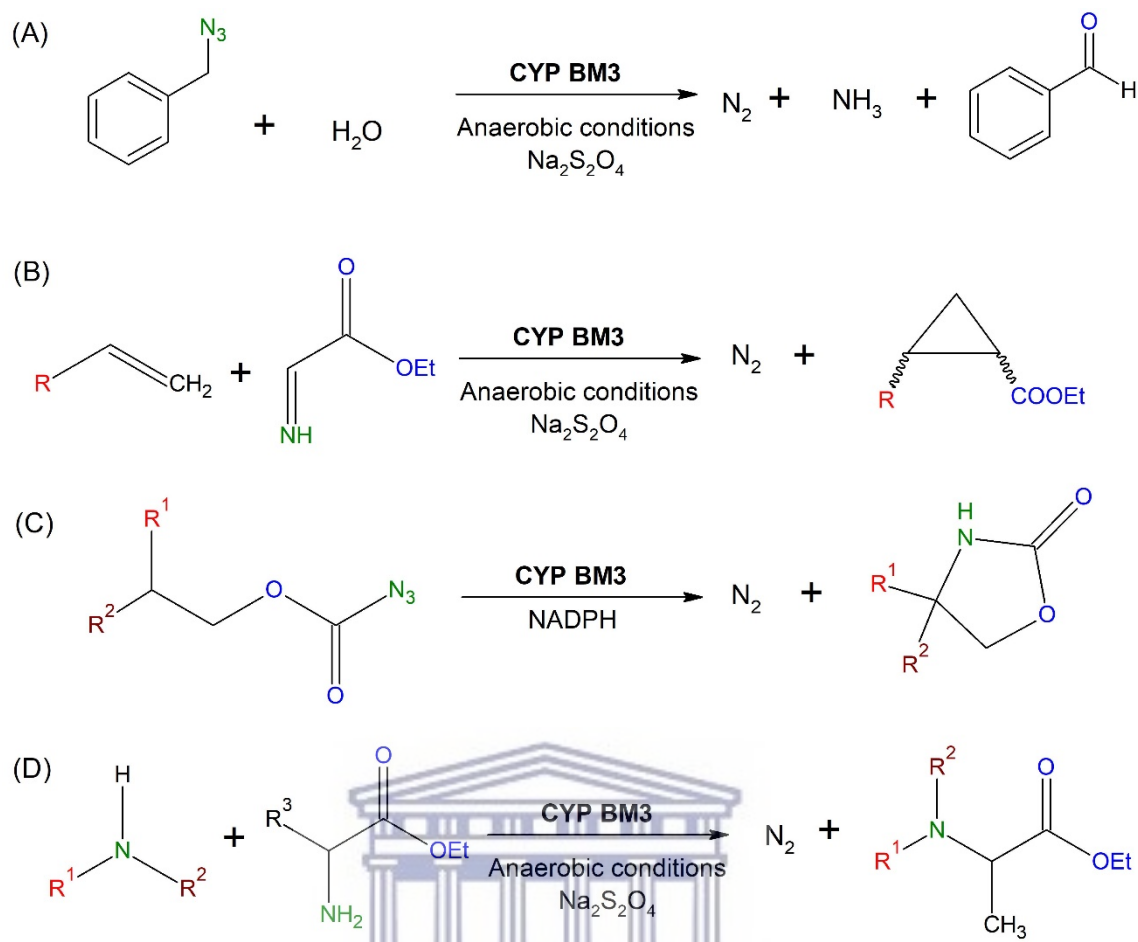


Figure 2-9: Abiotic reactions catalysed by engineered CYP BM3 (A) oxidative deamination of alkyl azides (B) olefin cyclopropanation via carbene transfer (C) cyclization of carbonazidate substrates via intramolecular C-H amination (D) C-N bond formation via carbene N-H insertion [78]

CYP enzymes have also recently been targeted in research as a method of catalysing non-natural reactions on carbene and nitrene species in the place of synthetic organic chemistry. A genetically engineered variant of CYP BM3 has been used to carry out a C-H amination reaction on a variety of starting materials. The mutated enzyme was expressed in whole *E. coli* cells and reactions carried out in anaerobic conditions. These starting materials included alkanes such as 4-ethylanisole, 4-ethyltoluene and ethylbenzene [83]. This asymmetric biocatalyst was proven to have the highest turnover number of any known chiral synthetic catalysts. The fact that CYP's have been successfully modified to act at C-H groups that are inaccessible to chemical catalysts, make it even more valuable [84].

2.3.5 Large scale industrial applications

One of the largest industrial applications of P450's is for the production of pravastatin via a bioconversion process. Pravastatin is a drug used to lower cholesterol and thereby treat coronary heart disease. This method of production was developed by Sankyo (Daiichi-Sankyo) Co, Ltd (Tokyo, Japan). *Streptomyces carbophilus* is used in the fermentation step which converts ML-236B to pravastatin [85]. It was later found that enzymes in the CYP105 family was responsible for the regio-specific hydroxylation of the 6 β -position [86]. This hydroxylation reaction is shown in Figure 2-10 below.

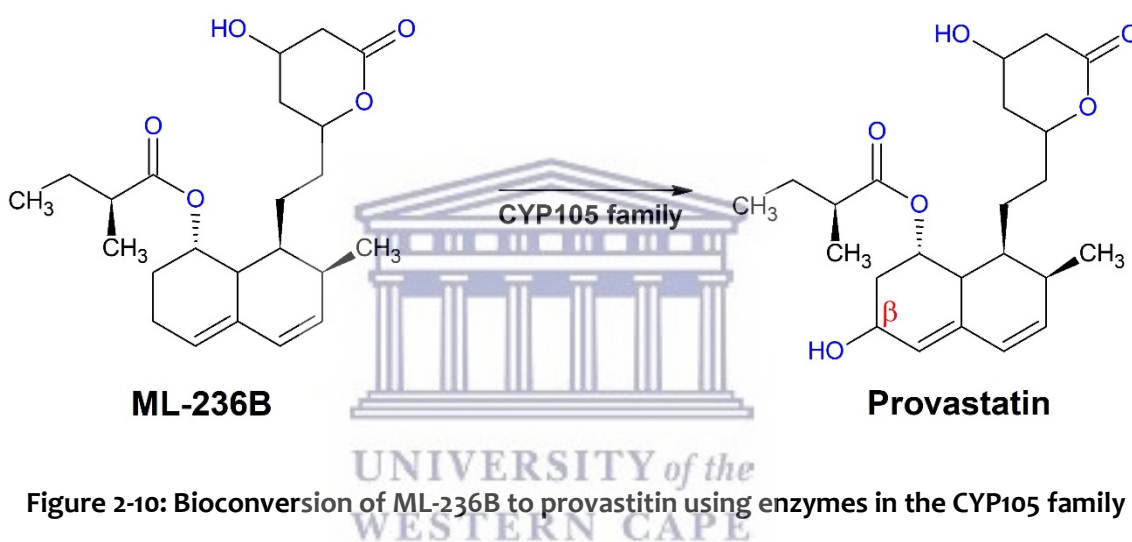
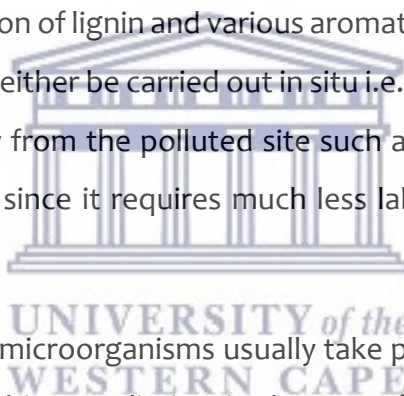


Figure 2-10: Bioconversion of ML-236B to pravastatin using enzymes in the CYP105 family

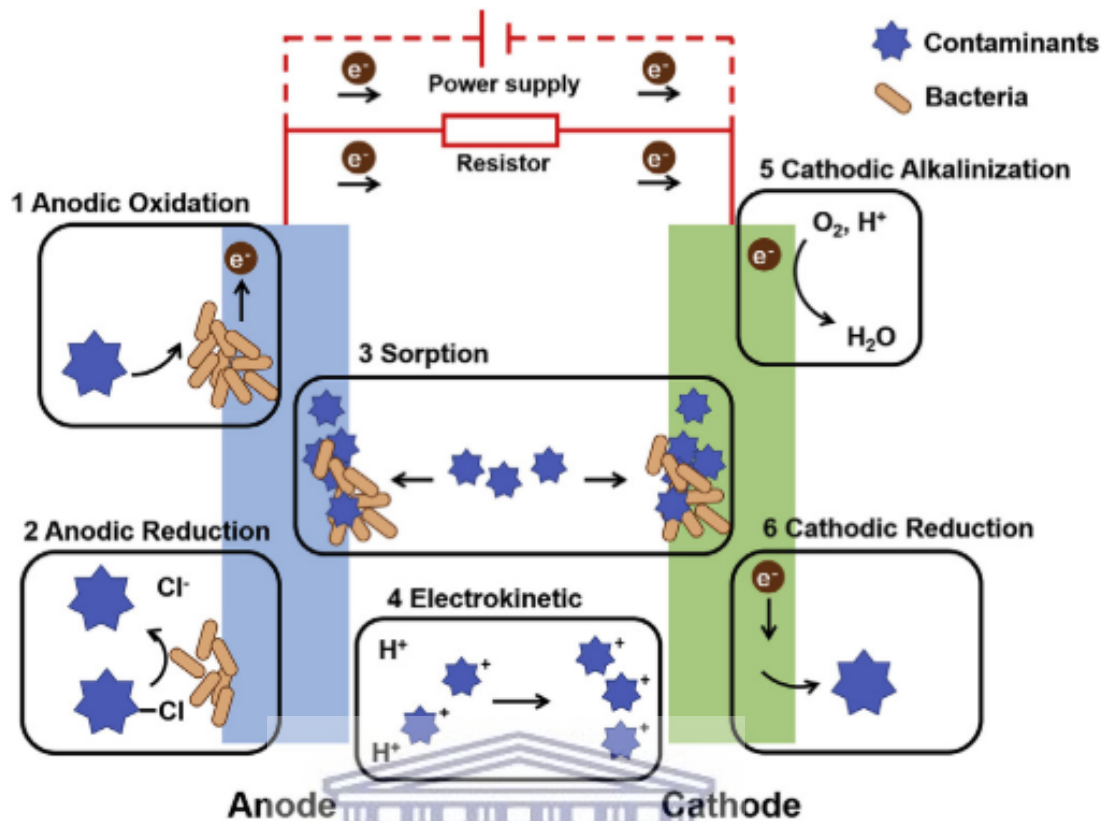
Bioconversion processes occur in bioreactors in various modes such as batch, continuous or semi-continuous and have various configurations depending on application. In each case a degree of moisture is required in order to maintain microbial activity. Other parameters such as time, media composition and pH are also optimised in each case. These biorefineries in industry are currently in use to produce various commercial products and under constant optimisation in research [87]. Biocatalysts such as enzymes have a few limitations, which include incorrect stereo- and/or regioselectivity, narrow substrate acceptance, weak robustness under operation conditions and sometimes substrate/product inhibition. However, the development of synthetic biology, metabolic engineering and directed evolution has circumvented these limitations [88].

2.4 **Bioremediation**

More effective ways of getting rid of harmful substances are always being investigated in order to preserve the environment. Bioremediation is defined as the use of a microorganism in order to degrade environmental pollutants and clean up a polluted site [89]. The use of bioremediation is attractive because microorganisms provide a quick, eco-friendly and safe alternative. It allows for the removal of dangerous toxins, pharmaceuticals and other unwanted chemicals from the environment. A number of enzymes have been found to assist with bioremediation by transforming the contaminants into a less harmful product [90]. Fungi have been found to be involved in bioremediation via laccase, lignin peroxidase (LiP), manganese peroxidases (MnP) and also CYP's. The CYP's were most likely to be involved in the degradation of lignin and various aromatic and xenobiotic compounds [91]. Bioremediation can either be carried out in situ i.e. at the polluted site, or ex situ which is at an area away from the polluted site such as a laboratory setting. In situ remediation is favoured since it requires much less labour, time, and treatment of samples.



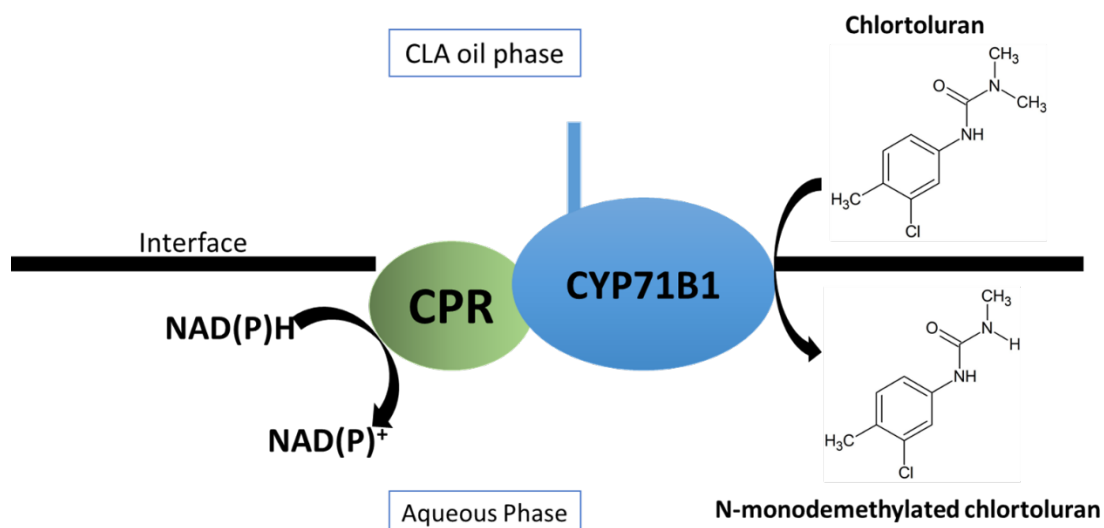
Bioremediation through microorganisms usually take place in polluted water or soil. One example of in situ bioremediation is the use of a microbial electrochemical system (MES) for bioremediation of soil. A typical MES system consists of two electrodes which are positioned in the aerobic and anaerobic zones. The mechanisms that take place in the system are summarised in Scheme 2-3. The mechanisms are (1) anodic oxidation, (2) reduction in anode, (3) electrokinetic, (4) sorption, (5) reduction in cathode and (6) cathodic alkalisation [92]. A microbial electrochemical system is in place for these remediation purposes with microbes catalysing each of the abovementioned reactions. The role of CYP enzymes in bioremediation, which can be applied in some of these mechanisms will be discussed here.



Scheme 2-3: Bioremediation mechanisms of an MES system [92]

2.4.1 Herbicides

An earlier example of bioremediation research with application in polyaphron included a plant cytochrome, CYP71B1. This enzyme was used in conjunction with a fused NADPH CYP450 reductase system for the metabolism of chlortoluran (a herbicide pollutant) and erythromycin. The process was carried out ex-situ and the issue of immobilising the enzyme onto the CLA (colloidal liquid aphrons) oil phase was addressed in this study. A polyaphron was developed using an oil in water macro-emulsion which contained a proportion of internal organic phase. The immobilised enzyme and redox partner was found to be effective in carrying out the bioremediation of chlortoluran, which was decomposed to produce N-monodemethylated chlortoluron. The researchers found that the immobilised enzyme yielded a much larger turnover than free enzyme in this study [93]. A scheme representing this study is as shown below in Scheme 2-4.



Scheme 2-4: Immobilised CYP71B1|reductase fusion catalytic cycle for chlortoluron N-monodemethylation [93]

2.4.2 Harmful substances

An ex situ degradation of triphenyl phosphate (TPHP) was investigated in order to determine the role of CYP enzymes. TPHP is largely used as a flame retardant in polyurethane foam and its accumulation in the environment is concerning due to its potential neurotoxic ability [94]. Bioremediation was carried out using a mineral salt culture containing *Brevibacillus brevis* (a bacterium) with 92.1 % efficiency obtained at 30 °C and pH 7. This microorganism's ability to degrade TPHP was however largely reduced in the presence of CYP inhibitor piperonyl butoxide (PB). This suggests that CYP's are largely responsible for degrading this contaminant via *Brevibacillus brevis*. This theory was then confirmed by the fact that the PB inhibitor significantly decreased CYP gene expression levels when present in the system [95].

A military explosive called hexahydro-1,3,5-trinitro-1,3,5-triazine or (RDX) has been found to be a source of nitrogen for soil microorganisms for many years in anaerobic [96] and aerobic conditions [97]. CYP177a1 called XplA and its partnering reductase XplB has been identified as the fused enzyme system responsible for the metabolism of this explosive. This enzyme was identified from the microbial *Rhodococcus rhodochrous* strain 11Y [98]. Various studies have been completed which have proven

the role of CYP in the bioremediation of RDX. One example would be to express the XplA in transgenic plants in order to make use of their root system to bioremediate soil. The results show that XplA expressing plants had gained biomass after being exposed to RDX for 8 weeks, whereas the wild type plants grew slower as a result of increased RDX exposure. This proves that the RDX acted as a nitrogen source for the transgenic plants [99].

2.4.3 Insecticides

Endosulfan, an insecticide has been identified as a persistent toxic pollutant (PTP) and is thus an environmental issue [100]. CYP2B6, a human cytochrome, was found to have stereo specific metabolic activity towards this molecule. A group made use of computational chemistry to investigate the similarity between CYP2B6 and CYP BM3, an enzyme encoded by *Bacillus megaterium*. An ex situ experiment was carried out with an inoculation culture of *B. megaterium* strain KKc7 and endosulfan. Results show that CYP BM3 was over-expressed fivefold in the presence of endosulfan and metabolised the molecule to endosulfan sulfate [101]. This shows huge promise as a method of bioremediation of the insecticide via CYP.

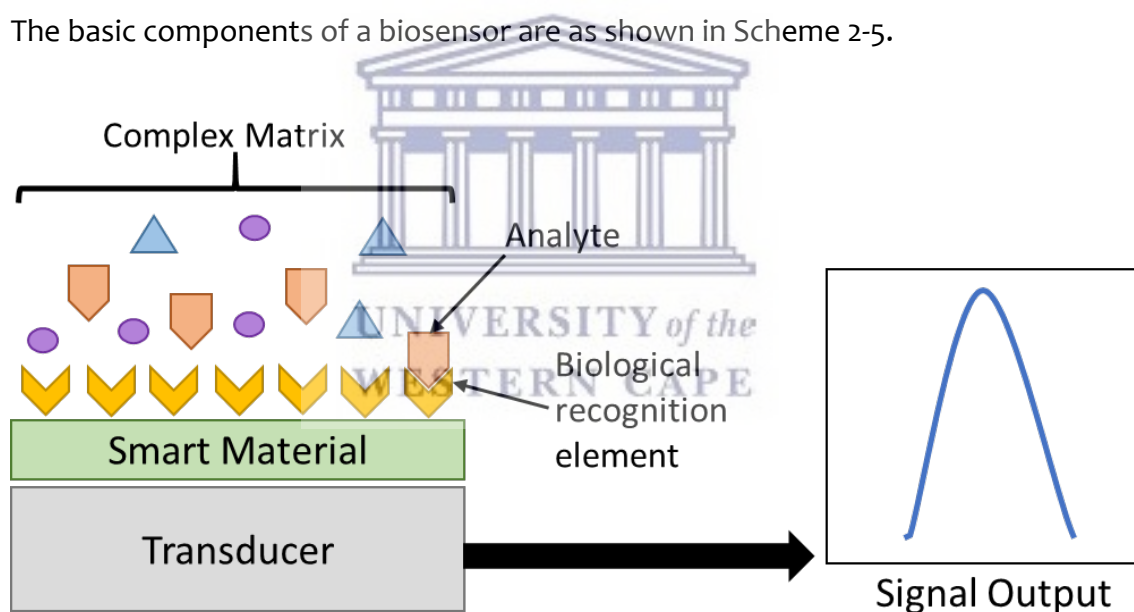
Neonicotinoid insecticides, such as acetamiprid (ACET) are used extensively in croplands since they are less harmful than older insecticides. A white rot fungus *Phanerochaete chrysosporium* (PcCYP) has been used for the bioremediation of ACET via CYP action in a cultured media for 20 day incubation period. The enzyme identified in this process was CYP5147A3, which was confirmed by an inhibition study using 1-aminobenzotriazole (ABT). *P. chrysosporium* successfully degraded ACET to IM o and ACET-c via N-dealkylation process. These metabolites were found to be much less toxic than ACET which was favourable [102].

The use of microorganisms in bioremediation strategies have been widely successful and can be attributed to the action of enzymes including CYP's. The role of CYP's in the remediation of compounds are not limited to those mentioned here but also to

dioxins [103], polyacrylamides [104], organic contaminants such as benzo(a)pyrene [105] and many other chemicals [106].

2.5 Biosensors

Cytochrome P450's have been proven to be involved in a wide variety of reactions and found numerous applications because of this flexibility. However one of the drawbacks in its application is the necessity of a redox partner and electron source such as CPR and NADPH respectively. One application, which negates this need is electrochemistry. Immobilisation of biological recognition elements onto the surface of an electrode provides a constant source of electrons for reactions to take place. The basic components of a biosensor are as shown in Scheme 2-5.



Scheme 2-5: Biosensor components

Biosensors consist of a biological recognition element which can be DNA, proteins, antibodies or enzymes etc. This element is usually used along with a smart material such as conducting polymers, nanoparticles or graphene based materials in order to enhance sensitivity. Another component is the transducer which generates the signal, and it can be in the form of an optical, calorimetric, thermal or electrochemical

transducer. The final component is the signal processing unit [107]. Enzymes have become popular as biological recognition elements due to their high reactivity, selectivity, sensitivity and fast response time makes it one of the most widely used biosensors. Enzymes by themselves are also biological catalysts in the sense that after the reaction is complete, the molecules can be re-used. The enzymes are usually incorporated with a smart material and various immobilisation strategies for the enzyme are employed. These strategies include adsorption onto bare electrodes, layer by layer adsorption, adsorption onto thin films, encapsulation into polymers and gels, covalent attachment onto self-assembled monolayers (SAM) amongst others [108]. The use of nanotechnology in biosensors has improved the limit of detection of biosensors due to various factors. The favourable characteristics of nanomaterials include high surface area to volume ratio, excellent electrical conductivity and ease of surface functionalisation [109]. The development and constant research into the area of biosensors are vital for the human population with the increased use of medications and drugs. For the purpose of this review we will focus on the recent use of CYP's in electrochemical nano-biosensors.



2.5.1 Carcinogens

Benzo[a]pyrene (BaP) is a polycyclic aromatic hydrocarbon which has the ability to cause cancer upon long term exposure. An electrochemical biosensor was developed towards the detection of BaP using a CYP 1A1 enzyme in conjunction with nitrogen-doped graphene. This graphene was further enhanced with 1-pyrene butyric acid (PBA) and used for enzyme immobilisation on a glassy carbon electrode. Human monooxygenase CYP's act on their metabolites via an overall reduction reaction taking place in the presence of oxygen which can be monitored electrochemically. The completed biosensor electrocatalytically metabolised BaP to form benzo[a]pyrene-7,8-diol within the 0.4 to 20 μM concentration range using cyclic voltammetry and as detection method as shown in Figure 2-11. This biosensor will aid in the development of drug discovery and perhaps also the prediction of toxicity [110].

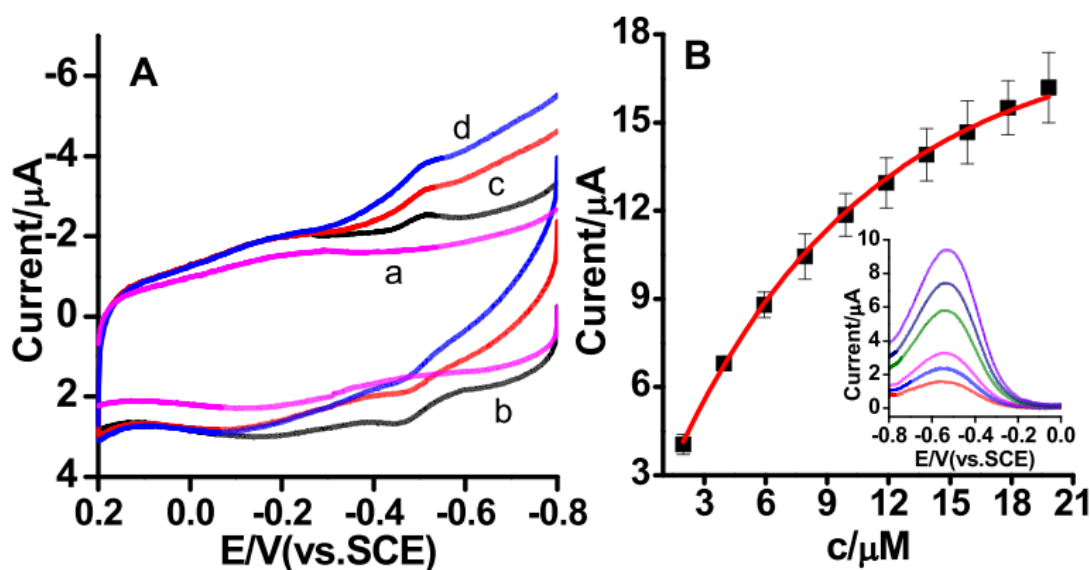


Figure 2-11: Electrochemical response of CYP1A1/PB-NG/GCE (A) (a) CV of PB-NG/GCE and (b) CYP1A1/PB-NG/GCE in 0.1 M, pH 7.4 PBS under N_2 , (c) air saturated and (d) addition of 10 μM BaP at 100 mV s^{-1} (B) Current at -0.48 V (vs. SCE) vs the concentrations of BaP (from 0.4 to 20.0 μM). Inset: CV curves of CYP1A1/PB-NG modified rotating disk electrode obtained by subtracting the background before any addition of BaP [110]

Screen printed carbon electrode (SPCE's) have the ability to be modified with smart materials such as nanoparticles for application in biosensors as proven by Hongli et al. This was achieved via electrodeposition of gold nanoparticles onto the surface of an activated SPCE. The electrode was further modified by a polyelectrolyte film of poly(diallyldimethylammonium chloride) (PDDA) and poly(sodium-p-styrenesulfonate) (PSS) via electrostatic assembly. CYP2E1 was then electrostatically attached to this charged surface and used for the detection of 4-(methylnitrosamino)-1-(3-pyridyl)-1-butanone (NNK). NNK is a group 1 carcinogen and its detection was successful via reductive metabolism through CYP2E1 in a 0 to 386 μM range [111].

2.5.2 Analgesics

A "home-made" SPCE was developed with a CYP2D6 enzyme covalently attached to the electrode surface for the detection of codeine. This pharmaceutical drug is typically used for treatment of mild pain and is metabolised into morphine via the CYP

enzyme in the liver. CYP2D6 was attached to the electrode surface using covalent bonding between N-hydroxysuccinimide (NHS) and N-(3-dimethylamino-propyl)-N'-ethylcarbodiimide hydrochloride (EDC). The researchers then made use of chronoamperometry in order to detect codeine in buffer as well as in spiked urine. The biosensor was successful in reducing codeine in both matrices in the 4.9 to 45.4 μM concentration range [112].

Recently the monooxygenase activity of CYP's was utilised by incorporating human liver microsomes (HLM) into a biosensor. In this case positively charged amine functionalised magnetic nanoparticles were used for electrostatic attachment of the HLM on an edge plane pyrolytic graphite electrode (EPG). The detection was then carried out using cyclic voltammetry and chronoamperometry to induce the hydroxylation of diclofenac, a CYP-specific non-steroidal anti-inflammatory drug (NSAID). The reaction showed Michaelis-Menten kinetics from 20 to 360 μM . Nerimetla et al thus created a successful electrocatalytic liver microsomal biofilm for enhanced metabolite production of diclofenac [113].



2.5.3 Illicit drugs

Biosensors can also be used in order to determine purity of samples such as the illicit drug, cocaine. A screen printed electrode was fabricated using a carbon based ink mixed with CYP2B4 for the working electrode surface. Chronoamperometric measurements were then carried out in the presence of cocaine which was successfully detected in the 0.2 to 1.2 mM range. Cyclic voltammograms showing the overall reduction peak monitored when using CYP enzymes is as shown in Figure 2-12. This sensor was capable of determining the purity of a street sample of cocaine which was found to be roughly [84.43 \pm 7.82]% w/w [114].

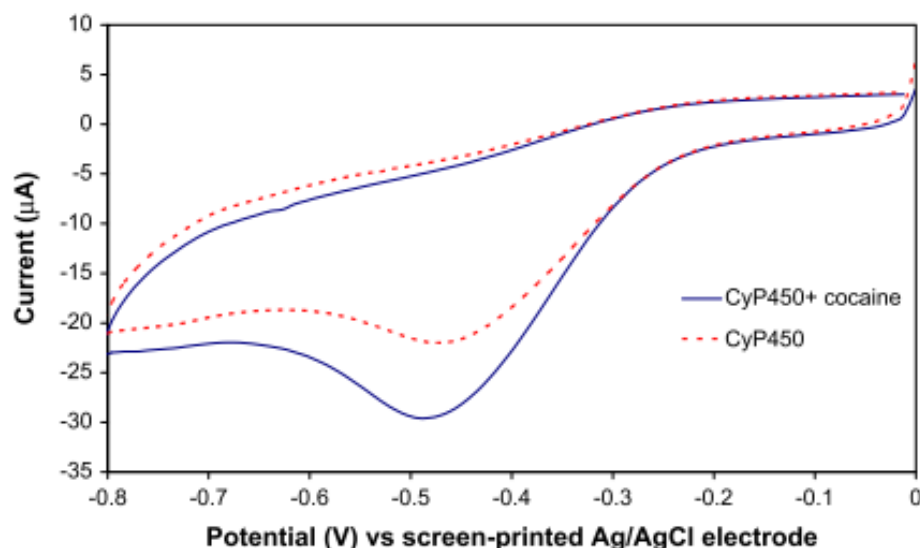


Figure 2-12: Cyclic voltammogram of CYP2B4 based SPCE and the detection of 1.67 mM cocaine in supporting electrolyte pH 7

An alternate method of enzyme immobilisation saw the CYP2B4 covalently linked onto a SPCE using EDC-NHS. The biosensor was thoroughly optimised and then used to determine very low concentrations of this drug in the 19 to 166 nM range. Chronoamperometry was the method of detection in this case and successfully used to determine the purity of cocaine street samples, which was found to be 29% \pm 3 (w/w). This purity was compared to the value obtained from HPLC which was found to be 28% \pm 2 (w/w). The biosensors developed towards cocaine was thus successful and competitive with a standard laboratory procedure such as HPLC [115].

2.5.4 Anti-retrovirals

CYP's are also known to metabolise anti-retroviral drugs such as delavirdine, which is used for treatment of HIV. A biosensor consisting of CYP3A4 was entrapped in a nano-composite i.e. dendrimeric copper generation-2 poly(propylene imine)-copolypyrrole star copolymer. The star copolymer provided a biocompatible environment for the enzyme as well as providing a highly conductive platform for the biosensors best performance. The biosensor was applied for the detection of

delavirdine using cyclic voltammetry. The detection was found to be successful in the 0.1 to 0.6 nM concentration range with a limit of detection of 0.025 nM. The development of the biosensor towards an antiretroviral is used for the determination of metabolic profile for HIV patients [116].

2.5.5 Anti-cancer drugs

Abiraterone is a prostate cancer drug which is used as a form of hormone therapy which causes suppression and shrinkage of testosterone sensitive tumor cells in the body. Since this drug is being used more frequently to treat prostate cancer, its monitoring is becoming more important for proper dosing. A CYP3A4 enzyme has been used in conjunction with multi-walled carbon nanotubes (MWCNT) on a screen printed electrode (SPE) for detection of abiraterone. Cyclic voltammetry was employed as detection method and was successful in detecting abiraterone using an inhibition method. The detection resulted in an exponential decay of the CYP3A4 peak between 0 and 1 μM and plateaued until 3 μM [117].



2.5.6 Anti-depressants

A nano-polymeric biosensor has recently been developed towards the detection of paroxetine, which is a commonly used antidepressant. A poly(8-anilino-1-naphthalene sulphonic acid) or PANSA was used as a solid phase electron mediator for the biosensor. Paroxetine acted as an inhibitor on the CYP2D6 enzyme since it is a selective serotonin reuptake inhibitor (SSRI). It was detected in the concentration range of 0.005 to 1 μM using chronoamperometry and differential pulse voltammetry (DPV) as detection method. Electrochemical Michaelis-Menten kinetics were observed and a limit of detection of 0.002 μM was obtained for the nano-biosensor [118].

2.5.7 Antibiotics

Ajayi et al has also developed phenotype biosensors for the detection of anti-TB drugs. A biosensor consisting of PANSA/silver nanoparticles was coupled to CYP2E1 for the detection of isoniazid (INH), an anti-TB drug. The nanocomposite was found to be highly electroactive and biocompatible for hosting the CYP2E1 enzyme. Differential pulse voltammetry was used for detection of INH in a dynamic linear range of 2 to 22 μM [119]. Pyrazinamide, which is also an anti-TB drug has also been determined using a similar method. In this instance the CYP2E1 was modified with disuccinimidyl octanedioate in order to increase specificity and selectivity. Using the same electrocatalytic platform, the linear range of detection 2 to 16 μM with a limit of detection of 0.044 μM [120].



2.6 Conclusion

Cytochrome P450 enzymes are a versatile group of enzymes found in most living organisms including mammals, plants, bacteria and other microorganisms. All CYP enzymes consist of an iron-heme centre and they catalyse a variety of reactions. CYP's typically require redox partners in order to provide electrons via NADPH and are classed according to these redox systems. These enzymes are typically monooxygenases in humans via a hydroxylation reaction. They have been found to be involved in other reactions in other organisms such as C-C cleavage, epoxidation, sulfoxidation and demethylation amongst many others. The functions of CYP's range from metabolism of drugs and hormone regulation to synthesis of natural products. They are regio- and stereo-selective and are thus a prime candidate for genetic engineering and synthetic biology in order to use them in industry. CYP's are able to stereo-specifically react at otherwise inactive carbons which is a huge advantage in synthesis of compounds, which would otherwise involve multiple steps and solvents to achieve. The use of enzymes in biosynthesis allows for a more environmentally friendly approach to the production of high value compounds with economic viability. CYP's are involved in the biosynthesis of steroids, indigo dyes and even anti-cancer agents. They can thus be used not only to understand mechanisms in the body but also produce industrial products. Whole cell microbial CYP's have been genetically engineered in order to be used in biocatalysis. CYPBM₃ has been the focus of many of these types of studies due to the fact that it exists as a fused heme and redox partner system, and thus does not require an additional system to provide electrons [77]. This enzyme has been engineered to biocatalyse abiotic reactions such as olefin cyclopropanation, carbene N-H insertion and intramolecular C-H amination reactions amongst others [78]. The role of CYP's in bioremediation is also an important one to note. The possibility of using plants or microbes to bioremediate soil and water is highly favourable. It allows for a natural method of cleaning up the environment and getting rid of toxic and harmful substances present in nature. CYP's have been successfully expressed in plants for this purpose and have been found to successfully remove a toxic pollutant from soil [99]. The application of CYP enzymes

in electrochemical biosensors allows for research into the metabolism and synthesis of various products without the need of an additional electron source since the electrochemical work station provides electrons constantly in order for reactions to take place. CYP's as biological recognition elements in biosensors allow for us to study the reactions which mimic bodily reactions and help to identify the effect of metabolites. CYPs also help to improve the sensitivity and selectivity of sensors with the assistance of smart nanomaterials. These nanomaterials serve to enhance surface area on which to immobilise the enzyme and act as electrocatalyst to determine ultra-low concentrations of analyte and improve biosensor performance. This niche area of research will thus be the focus of this thesis. Overall, this group of enzymes are versatile, have a broad range of substrates, are stereo- and regio-specific and synthetic biology has proven that they can be used for abiotic reactions as well. Their applications in biosynthesis, biocatalysis, bioremediation and biosensors are thus invaluable.



2.7 References

- [1] M. Litzemberger and R. Bernhardt, "CYP260B1 acts as 9 α -hydroxylase for 11-deoxycorticosterone," *Steroids*, vol. 127, pp. 40–45, **2017**.
- [2] F.-G. Banica, "Chapter 3: Enzymes and Enzymatic Sensors," in *Chemical Sensors and Biosensors: Fundamentals and Applications*, **2012**.
- [3] E. E. Scott and J. R. Halpert, "Structures of cytochrome P450 3A4," *Trends in Biochemical Sciences*, vol. 30, pp. 5–7, **2005**.
- [4] B. B. Brodie, J. Axelrod, J. R. Cooper, L. Gaudette, B. N. La Du, C. Mitoma, and S. Udenfriend, "Detoxication of drugs and other foreign compounds by liver microsomes.," *Science (New York, N.Y.)*, vol. 121, pp. 603–4, **1955**.
- [5] J. Axelrod, "The enzymatic demethylation of ephedrine.," *The Journal of pharmacology and experimental therapeutics*, vol. 114, pp. 430–438, **1955**.
- [6] P. Anzenbacher and E. Anzenbacherová, "Cytochromes P450 and metabolism of xenobiotics.," *Cellular and molecular life sciences : CMLS*, vol. 58, pp. 737–47, **2001**.
- [7] D. Twilley and N. Lall, "African Plants with Dermatological and Ocular Relevance," in *Toxicological Survey of African Medicinal Plants*, Elsevier Inc., **2014**, pp. 493–512.
- [8] M. Klingenberg, "Pigments of rat liver microsomes.," *Archives of biochemistry and biophysics*, vol. 75, pp. 376–86, **1958**.
- [9] D. Garfinkel, "Studies on pig liver microsomes. I. Enzymic and pigment composition of different microsomal fractions," *Archives of Biochemistry and Biophysics*, vol. 77, pp. 493–509, **1958**.
- [10] F. Hollmann, I. W. C. E. Arends, K. Buehler, A. Schallmey, and B. Bühler, "Enzyme-mediated oxidations for the chemist," *Green Chemistry*, vol. 13, pp. 226–265, **2011**.
- [11] A. Wiseman and D. F. V. Lewis, "57-Isoform cytochromes P450 for bioconversions," *Enzyme and Microbial Technology*, vol. 40, pp. 1469–1474, **2007**.
- [12] G. Gilardi and G. Di Nardo, "Heme iron centers in cytochrome P450: structure and catalytic activity," *Rendiconti Lincei*, vol. 28, pp. 159–167, **2017**.
- [13] A. Gaedigk, M. Ingelman-Sundberg, N. A. Miller, J. S. Leeder, M. Whirl-Carrillo, and T. E. Klein, "The Pharmacogene Variation (PharmVar) Consortium: Incorporation of the Human

- Cytochrome P450 (CYP) Allele Nomenclature Database,” *Clinical Pharmacology and Therapeutics*, vol. 103, pp. 399–401, **2018**.
- [14] B. Huang, J. Bao, Y.-R. Cao, H.-F. Gao, and Y. Jin, “Cytochrome P450 1A1 (CYP1A1) Catalyzes Lipid Peroxidation of Oleic Acid-Induced HepG2 Cells,” *Biochemistry (Moscow)*, vol. 83, pp. 595–602, **2018**.
- [15] F. P. Guengerich, M. R. Waterman, and M. Egli, “Recent Structural Insights into Cytochrome P450 Function,” *Trends in Pharmacological Sciences*, vol. 37, pp. 625–640, **2016**.
- [16] W. Chen, M.-K. Lee, C. Jefcoate, S.-C. Kim, F. Chen, and J.-H. Yu, “Fungal Cytochrome P450 Monooxygenases: Their Distribution, Structure, Functions, Family Expansion, and Evolutionary Origin,” *Genome Biology and Evolution*, vol. 6, pp. 1620–1634, **2014**.
- [17] D. R. Nelson, J. V Goldstone, and J. J. Stegeman, “The cytochrome P450 genesis locus: The origin and evolution of animal cytochrome P450s,” *Philosophical Transactions of the Royal Society B: Biological Sciences*, vol. 368, p. 20120474, **2013**.
- [18] D. Nelson and D. Werck-Reichhart, “A P450-centric view of plant evolution,” *Plant Journal*, vol. 66, pp. 194–211, **2011**.
- [19] T. Shimada, H. Yamazaki, M. Mimura, Y. Inui, and F. P. Guengerich, “Interindividual variations in human liver cytochrome P-450 enzymes involved in the oxidation of drugs, carcinogens and toxic chemicals: studies with liver microsomes of 30 Japanese and 30 Caucasians.,” *The Journal of pharmacology and experimental therapeutics*, vol. 270, pp. 414–23, **1994**.
- [20] S. Michaels and M. Z. Wang, “The revised human liver cytochrome P450 ‘Pie’ absolute protein quantification of CYP4F and CYP3A enzymes using targeted quantitative proteomics.,” *Drug metabolism and disposition: the biological fate of chemicals*, vol. 42, pp. 1241–51, **2014**.
- [21] H. Huang, D. Wang, B. Wen, J. Lv, and S. Zhang, “Roles of maize cytochrome P450 (CYP) enzymes in stereo-selective metabolism of hexabromocyclododecanes (HBCDs) as evidenced by in vitro degradation, biological response and in silico studies,” *Science of the Total Environment*, vol. 656, pp. 364–372, **2019**.
- [22] T. M. Šarenac and M. Mikov, “Bile acid synthesis: From nature to the chemical modification and synthesis and their applications as drugs and nutrients,” *Frontiers in Pharmacology*, vol. 9, Frontiers, p. 939, **2018**.
- [23] C. P. Capper, J. M. Rae, and R. J. Auchus, “The Metabolism, Analysis, and Targeting of Steroid Hormones in Breast and Prostate Cancer,” *Hormones and Cancer*, vol. 7, pp. 149–164, **2016**.

- [24] C. Ghosh, M. Hossain, J. Solanki, A. Dadas, N. Marchi, and D. Janigro, "Pathophysiological implications of neurovascular P450 in brain disorders," *Drug Discovery Today*, vol. 21, pp. 1609–1619, **2016**.
- [25] P. Manikandan and S. Nagini, "Cytochrome P450 Structure, Function and Clinical Significance: A Review," *Current Drug Targets*, vol. 19, pp. 38–54, **2017**.
- [26] F. P. Guengerich, "Human cytochrome P450 enzymes," in *Cytochrome P450: Structure Mechanism, and Biochemistry*, 3rd ed., New York: Kluwer Academic/ Plenum Press, **2005**, pp. 377–531.
- [27] J. Xu, X. Wang, and W. Guo, "The cytochrome P450 superfamily: Key players in plant development and defense," *Journal of Integrative Agriculture*, vol. 14, pp. 1673–1686, **2015**.
- [28] R. Bernhardt, "Cytochromes P450 as versatile biocatalysts," *Journal of Biotechnology*, vol. 124, pp. 128–145, **2006**.
- [29] R. Fasan, "Tuning P450 enzymes as oxidation catalysts," *ACS Catalysis*, vol. 2, pp. 647–666, **2012**.
- [30] S. L. Kelly, D. E. Kelly, C. J. Jackson, A. G. S. Warriow, and D. C. Lamb, "The Diversity and Importance of Microbial Cytochromes P450," in *Cytochrome P450: Structure, Mechanism, and Biochemistry*, P. R. Ortiz de Montellano, Ed. New York, **2007**, pp. 1–33.
- [31] D. R. Nelson, "The cytochrome P450 homepage," *Human Genomics*, vol. 4, pp. 59–65, **2009**.
- [32] D. E. Torres Pazmiño, M. Winkler, A. Glieder, and M. W. Fraaije, "Monooxygenases as biocatalysts: Classification, mechanistic aspects and biotechnological applications," *Journal of Biotechnology*, vol. 146, pp. 9–24, **2010**.
- [33] E. M. Isin and F. P. Guengerich, "Complex reactions catalyzed by cytochrome P450 enzymes," *Biochimica et Biophysica Acta - General Subjects*, vol. 1770, pp. 314–329, **2007**.
- [34] H. Ohkawa, H. Imaishi, N. Shiota, T. Yamada, H. Inui, and Y. Ohkawa, "Molecular mechanisms of herbicide resistance with special emphasis on cytochrome P450 monooxygenases," *Plant Biotechnology*, vol. 15, pp. 173–176, **1998**.
- [35] M. Ingelman-Sundberg, "Human drug metabolising cytochrome P450 enzymes: Properties and polymorphisms," *Naunyn-Schmiedeberg's Archives of Pharmacology*, vol. 369, pp. 89–104, **2004**.
- [36] S. L. Kelly and D. E. Kelly, "Microbial cytochromes P450: biodiversity and biotechnology. Where

- do cytochromes P450 come from, what do they do and what can they do for us?," *Philosophical transactions of the Royal Society of London. Series B, Biological sciences*, vol. 368, p. 20120476, **2013**.
- [37] A. W. Munro, H. M. Girvan, A. E. Mason, A. J. Dunford, and K. J. McLean, "What makes a P450 tick?," *Trends in Biochemical Sciences*, vol. 38, pp. 140–150, **2013**.
- [38] S. Taheriniya and Z. Behboodi, "Comparing Green Chemical Methods and Chemical Methods for the synthesis of titanium dioxide nanoparticles," *International journal of pharmaceutical sciences and research*, vol. 7, pp. 4927–4932, **2016**.
- [39] F. M. Schempp, L. Drummond, M. Buchhaupt, and J. Schrader, "Microbial Cell Factories for the Production of Terpenoid Flavor and Fragrance Compounds," *Journal of Agricultural and Food Chemistry*, vol. 66, pp. 2247–2258, **2018**.
- [40] E. M. J. Gillam, "Extending the capabilities of nature's most versatile catalysts: Directed evolution of mammalian xenobiotic-metabolizing P450s," *Archives of Biochemistry and Biophysics*, vol. 464, pp. 176–186, **2007**.
- [41] D. Schmitz, S. Janocha, F. M. Kiss, and R. Bernhardt, "CYP106A2—A versatile biocatalyst with high potential for biotechnological production of selectively hydroxylated steroid and terpenoid compounds," *Biochimica et Biophysica Acta (BBA) - Proteins and Proteomics*, vol. 1866, pp. 11–22, **2018**.
- [42] H. Xiao, Y. Zhang, and M. Wang, "Discovery and Engineering of Cytochrome P450s for Terpenoid Biosynthesis," *Trends in Biotechnology*, vol. 37, pp. 618–631, **2019**.
- [43] S. Bak, F. Beisson, G. Bishop, B. Hamberger, R. Höfer, S. Paquette, and D. Werck-Reichhart, "Cytochromes p450.," *The arabidopsis book*, vol. 9, p. e0144, **2011**.
- [44] X. Zheng, P. Li, and X. Lu, "Research advances on CYP450-catalysed pharmaceutical terpenoids biosynthesis in plants," *Journal of Experimental Botany*, vol. In Press, pp. 1–12, **2019**.
- [45] H. Mao, J. Liu, F. Ren, R. J. Peters, and Q. Wang, "Characterization of CYP71Z18 indicates a role in maize zealexin biosynthesis," *Phytochemistry*, vol. 121, pp. 4–10, **2016**.
- [46] K. E. Olagaray and B. J. Bradford, "Plant flavonoids to improve productivity of ruminants – A review," *Animal Feed Science and Technology*, vol. 251, pp. 21–36, **2019**.
- [47] N. Villa-Ruano, Y. Pacheco-Hernández, E. Lozoya-Gloria, C. Jonathan Castro-Juárez, C. Mosso-Gonzalez, S. Alberto Ramirez-Garcia, C. J. Castro-Juárez, C. Mosso-Gonzalez, and S. A. Ramirez-Garcia, "Cytochrome P450 from Plants: Platforms for valuable phytopharmaceuticals,"

- Tropical Journal of Pharmaceutical Research*, vol. 14, pp. 731–742, **2015**.
- [48] F. Liu, J.-R. Chen, Y.-H. Tang, H.-T. Chang, Y.-M. Yuan, and Q. Guo, “Isolation and characterization of cinnamate 4-hydroxylase gene from cultivated ramie (*Boehmeria nivea*),” *Biotechnology & Biotechnological Equipment*, vol. 32, pp. 324–331, **2018**.
- [49] C. Schoenbohm, S. Martens, C. Eder, G. Forkmann, and B. Weisshaar, “Identification of the *Arabidopsis thaliana* Flavonoid 3'-Hydroxylase Gene and Functional Expression of the Encoded P450 Enzyme,” *Biological Chemistry*, vol. 381, pp. 749–53, **2000**.
- [50] K. Saito, K. Yonekura-Sakakibara, R. Nakabayashi, Y. Higashi, M. Yamazaki, T. Tohge, and A. R. Fernie, “The flavonoid biosynthetic pathway in *Arabidopsis*: Structural and genetic diversity,” *Plant Physiology and Biochemistry*, vol. 72, pp. 21–34, **2013**.
- [51] O. Merhan, “The Biochemistry and Antioxidant Properties of Carotenoids,” in *Carotenoids*, InTech, **2017**.
- [52] S. Tamaki, S. Kato, T. Shinomura, T. Ishikawa, and H. Imaishi, “Physiological role of β -carotene monohydroxylase (CYP97H1) in carotenoid biosynthesis in *Euglena gracilis*,” *Plant Science*, vol. 278, pp. 80–87, **2019**.
- [53] A. Spinello, I. Ritacco, and A. Magistrato, “The Catalytic Mechanism of Steroidogenic Cytochromes P450 from All-Atom Simulations: Entwinement with Membrane Environment, Redox Partners, and Post-Transcriptional Regulation,” *Catalysts*, vol. 9, p. 81, **2019**.
- [54] J. T. Sanderson, “The Steroid Hormone Biosynthesis Pathway as a Target for Endocrine-Disrupting Chemicals,” *Toxicological Sciences*, vol. 94, pp. 3–21, **2006**.
- [55] J. R. Cupp Vickery and T. L. Poulos, “Structure of cytochrome P450eryF involved in erythromycin biosynthesis,” *Nature Structural Biology*, vol. 2, pp. 144–153, **1995**.
- [56] T. H. Yeats, “Setting and Diffusing the Cyanide Bomb in Plant Defense,” *Plant physiology*, vol. 178, pp. 956–957, **2018**.
- [57] C. C. Hansen, M. Sørensen, T. A. M. Veiga, J. F. S. Zibrandtsen, A. M. Heskes, C. E. Olsen, B. A. Boughton, B. L. Møller, and E. H. J. Neilson, “Reconfigured cyanogenic glucoside biosynthesis in *eucalyptus cladocalyx* involves a cytochrome P450 CYP706C55,” *Plant Physiology*, vol. 178, pp. 1081–1095, **2018**.
- [58] A. K. R. Choudhury, “Sustainable chemical technologies for textile production,” in *Sustainable Fibres and Textiles*, Woodhead Publishing, **2017**, pp. 267–322.

- [59] S. Namgung, H. A. Park, J. Kim, P. G. Lee, B. G. Kim, Y. H. Yang, and K. Y. Choi, "Ecofriendly one-pot biosynthesis of indigo derivative dyes using CYP102G4 and PrnA halogenase," *Dyes and Pigments*, vol. 162, pp. 80–88, **2019**.
- [60] H. J. Kim, S. Jang, J. Kim, Y. H. Yang, Y. G. Kim, B. G. Kim, and K. Y. Choi, "Biosynthesis of indigo in *Escherichia coli* expressing self-sufficient CYP102A from *Streptomyces cattleya*," *Dyes and Pigments*, vol. 140, pp. 29–35, **2017**.
- [61] H. Ogura, C. R. Nishida, U. R. Hoch, R. Perera, J. H. Dawson, and P. R. Ortiz De Montellano, "EpoK, a cytochrome P450 involved in biosynthesis of the anticancer agents epothilones A and B. Substrate-mediated rescue of a P450 enzyme," *Biochemistry*, vol. 43, pp. 14712–14721, **2004**.
- [62] F. Kern, T. K. F. Dier, Y. Khatri, K. M. Ewen, J.-P. Jacquot, D. A. Volmer, and R. Bernhardt, "Highly Efficient CYP167A1 (EpoK) dependent Epothilone B Formation and Production of 7-Ketone Epothilone D as a New Epothilone Derivative," *Scientific Reports*, vol. 5, p. 14881, **2015**.
- [63] L. M. Podust and D. H. Sherman, "Diversity of P450 enzymes in the biosynthesis of natural products.," *Natural product reports*, vol. 29, pp. 1251–66, **2012**.
- [64] S. Kandel, L. Wienkers, and J. Lampe, "Cytochrome P450 enzyme metabolites in lead discovery and development," *Annual Reports in Medicinal Chemistry*, vol. 49, pp. 347–359, **2014**.
- [65] K. Yasuda, H. Sugimoto, K. Hayashi, T. Takita, K. Yasukawa, M. Ohta, M. Kamakura, S. Ikushiro, Y. Shiro, and T. Sakaki, "Protein engineering of CYP105s for their industrial uses," *Biochimica et Biophysica Acta (BBA) - Proteins and Proteomics*, vol. 1866, pp. 23–31, **2018**.
- [66] T. S. Moody and S. J. C. Taylor, "Cytochrome P450 (CYP) Progress in Biocatalysis for Synthetic Organic Chemistry," in *Practical Methods for Biocatalysis and Biotransformations 3*, Chichester: John Wiley & Sons, Ltd, **2016**, pp. 31–42.
- [67] C. Guo and Z. L. Wu, "Construction and functional analysis of a whole-cell biocatalyst based on CYP108N7," *Enzyme and Microbial Technology*, vol. 106, pp. 28–34, **2017**.
- [68] C. Rinnofner, B. Kerschbaumer, H. Weber, A. Glieder, and M. Winkler, "Cytochrome P450 mediated hydroxylation of ibuprofen using *Pichia pastoris* as biocatalyst," *Biocatalysis and Agricultural Biotechnology*, vol. 17, pp. 525–528, **2019**.
- [69] R. Weis, M. Winkler, M. Schittmayer, S. Kambourakis, M. Vink, J. David Rozzell, and A. Glieder, "A diversified library of bacterial and fungal bifunctional cytochrome P450 enzymes for drug metabolite synthesis," *Advanced Synthesis and Catalysis*, vol. 351, pp. 2140–2146, **2009**.
- [70] Ł. Adaszek, D. Gadomska, Ł. Mazurek, P. Łyp, J. Madany, and S. Winiarczyk, "Properties of

- capsaicin and its utility in veterinary and human medicine,” *Research in Veterinary Science*, vol. 123, pp. 14–19, **2019**.
- [71] A. K. Migglautsch, M. Willim, B. Schweda, A. Glieder, R. Breinbauer, and M. Winkler, “Aliphatic hydroxylation and epoxidation of capsaicin by cytochrome P450 CYP505X,” *Tetrahedron*, vol. 74, pp. 6199–6204, **2018**.
- [72] E. J. Park and J. M. Pezzuto, “The pharmacology of resveratrol in animals and humans,” *Biochimica et Biophysica Acta - Molecular Basis of Disease*, vol. 1852, pp. 1071–1113, **2015**.
- [73] M. de Ligt, S. Timmers, and P. Schrauwen, “Resveratrol and obesity: Can resveratrol relieve metabolic disturbances?,” *Biochimica et Biophysica Acta - Molecular Basis of Disease*, vol. 1852, pp. 1137–1144, **2015**.
- [74] T. K. Le, H. H. Jang, H. T. H. Nguyen, T. T. M. Doan, G. Y. Lee, K. D. Park, T. Ahn, Y. H. Joung, H. S. Kang, and C. H. Yun, “Highly regioselective hydroxylation of polydatin, a resveratrol glucoside, for one-step synthesis of astringin, a piceatannol glucoside, by P450 BM3,” *Enzyme and Microbial Technology*, vol. 97, pp. 34–42, **2017**.
- [75] K. K. Dubey, A. Jawed, and S. Haque, “Enhanced bioconversion of colchicine to regiospecific 3-demethylated colchicine (3-DMC) by whole cell immobilization of recombinant *E. coli* harboring P450 BM-3 gene,” *Process Biochemistry*, vol. 48, pp. 1151–1158, **2013**.
- [76] F. Hannemann, C. Virus, and R. Bernhardt, “Design of an *Escherichia coli* system for whole cell mediated steroid synthesis and molecular evolution of steroid hydroxylases,” *Journal of Biotechnology*, vol. 124, pp. 172–181, **2006**.
- [77] B. Dangi and T. J. Oh, “Bacterial CYP154C8 catalyzes carbon-carbon bond cleavage in steroids,” *FEBS Letters*, vol. 593, pp. 67–79, **2019**.
- [78] V. B. Urlacher and M. Girhard, “Cytochrome P450 Monooxygenases in Biotechnology and Synthetic Biology,” *Trends in Biotechnology*, vol. In Press, **2019**.
- [79] S. Giovani, H. Alwaseem, and R. Fasan, “Aldehyde and Ketone Synthesis by P450-Catalyzed Oxidative Deamination of Alkyl Azides,” *ChemCatChem*, vol. 8, pp. 2609–2613, **2016**.
- [80] P. S. Coelho, E. M. Brustad, A. Kannan, and F. H. Arnold, “Olefin cyclopropanation via carbene transfer catalyzed by engineered cytochrome P450 enzymes,” *Science*, vol. 339, pp. 307–310, **2013**.
- [81] R. Singh, J. N. Kolev, P. A. Sutera, and R. Fasan, “Enzymatic C(sp³)-H amination: P450-catalyzed conversion of carbonazidates into oxazolidinones,” *ACS Catalysis*, vol. 5, pp. 1685–1691, **2015**.

- [82] Z. J. Wang, N. E. Peck, H. Renata, and F. H. Arnold, "Cytochrome P450-catalyzed insertion of carbenoids into N–H bonds," *Chem. Sci.*, vol. 5, pp. 598–601, **2014**.
- [83] C. K. Prier, R. K. Zhang, A. R. Buller, S. Brinkmann-Chen, and F. H. Arnold, "Enantioselective, intermolecular benzylic C–H amination catalysed by an engineered iron-haem enzyme," *Nature Chemistry*, vol. 9, pp. 629–634, **2017**.
- [84] Y. Wei, E. L. Ang, and H. Zhao, "Recent developments in the application of P450 based biocatalysts," *Current Opinion in Chemical Biology*, vol. 43, pp. 1–7, **2018**.
- [85] Y. Tsujita, T. Ikeda, N. Serizawa, A. Hishunuma, and T. Komai, "Pravastatin Sodium: New Clinical Aspects and Recent Progress," *Sankyō Kabushiki Kaisha Kenkyujo*, **1997**.
- [86] N. Serizawa, "Biochemical and Molecular Approaches for Production of Pravastatin, a Potent Cholesterol-Lowering Drug," in *Biotechnology Annual Review*, M. R. El-Gewely, Ed. Elsevier Science, **1996**, pp. 373–389.
- [87] C. Kennes, "Bioconversion Processes," *Fermentation*, vol. 4, p. 21, **2018**.
- [88] G. Li, J. Wang, and M. T. Reetz, "Biocatalysts for the pharmaceutical industry created by structure-guided directed evolution of stereoselective enzymes," *Bioorganic & Medicinal Chemistry*, vol. 26, pp. 1241–1251, **2018**.
- [89] J. S. Singh, "Plant Growth Promoting Rhizobacteria: Potential microbes for sustainable agriculture," *Resonance*, vol. 18, pp. 275–281, **2013**.
- [90] B. Sharma, A. K. Dangi, and P. Shukla, "Contemporary enzyme based technologies for bioremediation: A review," *Journal of Environmental Management*, vol. 210, pp. 10–22, **2018**.
- [91] M. Tuomela and A. Hatakka, "Oxidative Fungal Enzymes for Bioremediation," in *Comprehensive Biotechnology*, Academic Press, **2011**, pp. 183–196.
- [92] Y. Wu, X. Jing, C. Gao, Q. Huang, and P. Cai, "Recent advances in microbial electrochemical system for soil bioremediation," *Chemosphere*, vol. 211, pp. 156–163, **2018**.
- [93] S. B. Lamb, D. C. Lamb, S. L. Kelly, and D. C. Stuckey, "Cytochrome P450 immobilisation as a route to biomediation/biocatalysis," *FEBS Letters*, vol. 431, pp. 343–346, **1998**.
- [94] D. Canbaz, A. Logiantara, R. van Ree, and L. S. van Rijt, "Immunotoxicity of organophosphate flame retardants TPHP and TDCIPP on murine dendritic cells in vitro," *Chemosphere*, vol. 177, pp. 56–64, **2017**.
- [95] K. Wei, H. Yin, H. Peng, G. Lu, and Z. Dang, "Bioremediation of triphenyl phosphate by

- Brevibacillus brevis: Degradation characteristics and role of cytochrome P450 monooxygenase,” *Science of The Total Environment*, vol. 627, pp. 1389–1395, **2018**.
- [96] N. G. McCormick, J. H. Cornell, and A. M. Kaplan, “Biodegradation of hexahydro-1,3,5-trinitro-1,3,5-triazine,” *Applied and environmental microbiology*, vol. 42, pp. 817–23, **1981**.
- [97] N. V Coleman, D. R. Nelson, and T. Duxbury, “Aerobic biodegradation of hexahydro-1,3,5 trinitro-1,3,5-triazine (RDX) as a nitrogen source by a Rhodococcus sp., strain DN22,” *Soil Biology and Biochemistry*, vol. 30, pp. 1159–1167, **1998**.
- [98] N. S. Scrutton, “Enzymes in Synthetic Biology,” in *Methods in Enzymology*, 1st ed., N. S. Scrutton, Ed. London: Academic Press, **2018**, p. 439.
- [99] E. L. Rylott, R. G. Jackson, F. Sabbadin, H. M. B. B. Seth-Smith, J. Edwards, C. S. Chong, S. E. Strand, G. Grogan, and N. C. Bruce, “The explosive-degrading cytochrome P450 XplA: Biochemistry, structural features and prospects for bioremediation,” *Biochimica et Biophysica Acta journal*, vol. 1814, pp. 230–236, **2011**.
- [100] F. M. Mitton, M. Gonzalez, J. M. Monserrat, and K. S. B. Miglioranza, “Potential use of edible crops in the phytoremediation of endosulfan residues in soil,” *Chemosphere*, vol. 148, pp. 300–306, **2016**.
- [101] M. V. Seralathan, S. Sivanesan, A. Bafana, S. M. Kashyap, A. Patrizio, K. Krishnamurthi, and T. Chakrabarti, “Cytochrome P450 BM3 of Bacillus megaterium - A possible endosulfan biotransforming gene,” *Journal of Environmental Sciences (China)*, vol. 26, pp. 2307–2314, **2014**.
- [102] J. Wang, H. Ohno, Y. Ide, H. Ichinose, T. Mori, H. Kawagishi, and H. Hirai, “Identification of the cytochrome P450 involved in the degradation of neonicotinoid insecticide acetamiprid in Phanerochaete chrysosporium,” *Journal of Hazardous Materials*, vol. 371, pp. 494–498, **2019**.
- [103] T. Sakaki, K. Yamamoto, and S. Ikushiro, “Possibility of application of cytochrome P450 to bioremediation of dioxins,” *Biotechnology and Applied Biochemistry*, vol. 60, pp. 65–70, **2013**.
- [104] T. Song, S. Li, Y. Lu, D. Yan, P. Sun, M. Bao, and Y. Li, “Biodegradation of hydrolyzed polyacrylamide by a Bacillus megaterium strain SZK-5: Functional enzymes and antioxidant defense mechanism,” *Chemosphere*, vol. 231, pp. 184–193, **2019**.
- [105] E. M. Ostrem Loss and J.-H. Yu, “Bioremediation and microbial metabolism of benzo(a)pyrene,” *Molecular Microbiology*, vol. 109, pp. 433–444, **2018**.
- [106] S. S. Bhattacharya and J. S. Yadav, “Microbial P450 Enzymes in Bioremediation and Drug Discovery: Emerging Potentials and Challenges,” *Current Protein & Peptide Science*, vol. 19, pp.

- 75–86, **2017**.
- [107] S. GS, A. CV, and B. B. Mathew, “Biosensors: A Modern Day Achievement,” *Journal of Instrumentation Technology*, vol. 2, pp. 26–39, **2014**.
- [108] E. Schneider and D. S. Clark, “Cytochrome P450 (CYP) enzymes and the development of CYP biosensors,” *Biosensors and Bioelectronics*, vol. 39, pp. 1–13, **2013**.
- [109] C. S. Osorio-González, K. Hegde, S. K. Brar, B. Delgado-Cano, N. Gómez-Falcón, and A. Avalos-Ramírez, “Advances in protein/enzyme-based biosensors for the detection of metal contaminants in the environment,” in *Tools, Techniques and Protocols for Monitoring Environmental Contaminants*, Elsevier, **2019**, pp. 245–261.
- [110] L. Mi, F. He, L. Jiang, L. Shangguan, X. Zhang, T. Ding, A. Liu, Y. Zhang, and S. Liu, “Electrochemically-driven benzo[a]pyrene metabolism via human cytochrome P450 1A1 with reductase coated nitrogen-doped graphene nano-composites,” *Journal of Electroanalytical Chemistry*, vol. 804, pp. 23–28, **2017**.
- [111] H. Zhao, H. He, L. Shi, X. Cai, H. Li, M. Lan, and Q. Zhang, “Electrochemical detection of 4-(methylnitrosamino)-1-(3-pyridyl)-1-butanone using a cytochrome P450 2E1 decorated biosensor,” *Journal of Electroanalytical Chemistry*, vol. 816, pp. 62–67, **2018**.
- [112] L. Asturias-Arribas, M. Asunción Alonso-Lomillo, O. Domínguez-Renedo, and M. Julia Arcos-Martínez, “Cytochrome P450 2D6 based electrochemical sensor for the determination of codeine,” *Talanta*, vol. 129, pp. 315–319, **2014**.
- [113] R. Nerimetla, G. Premaratne, H. Liu, and S. Krishnan, “Improved electrocatalytic metabolite production and drug biosensing by human liver microsomes immobilized on amine-functionalized magnetic nanoparticles,” *Electrochimica Acta*, vol. 280, pp. 101–107, **2018**.
- [114] L. Asturias-Arribas, M. A. A. Alonso-Lomillo, O. Domínguez-Renedo, and M. J. J. Arcos-Martínez, “Electrochemical determination of cocaine using screen-printed cytochrome P450 2B4 based biosensors,” *Talanta*, vol. 105, pp. 131–134, **2013**.
- [115] L. Asturias-Arribas, M. A. A. Alonso-Lomillo, O. Domínguez-Renedo, and M. J. J. Arcos-Martínez, “CYP450 biosensors based on screen-printed carbon electrodes for the determination of cocaine,” *Analytica Chimica Acta*, vol. 685, pp. 15–20, **2011**.
- [116] N. Ntshongontshi et al., “Cytochrome P450-3A4/Copper-Poly(Propylene Imine)-Polypyrrole Star Co-Polymer Nanobiosensor System for Delavirdine - A Non-Nucleoside Reverse Transcriptase Inhibitor HIV Drug,” *Journal of Nano Research*, vol. 44, pp. 265–280, **2016**.

- [117] N. Aliakbarinodehi, G. De Micheli, and S. Carrara, "Enzymatic and Nonenzymatic Electrochemical Interaction of Abiraterone (Antiprostata Cancer Drug) with Multiwalled Carbon Nanotube Bioelectrodes," *Analytical Chemistry*, vol. 88, pp. 9347–9350, **2016**.
- [118] R. F. Ajayi, E. Nxusani, S. F. Douman, A. Jonnas, P. G. L. Baker, and E. I. Iwuoha, "An amperometric cytochrome P450-2D6 biosensor system for the detection of the selective serotonin reuptake inhibitors (SSRIs) paroxetine and fluvoxamine," *Journal of Nano Research*, vol. 44, pp. 208–228, **2016**.
- [119] R. F. Ajayi, E. Nxusani, S. F. Douman, A. Jonnas, N. Ntshongontshi, U. Feleni, K. Pokpas, L. Wilson, and E. I. Iwuoha, "Silver Nanoparticle-Doped Poly(8-Anilino-1-Naphthalene Sulphonic Acid)/CYP2E1 Nanobiosensor for Isoniazid - A First Line Anti-Tuberculosis Drug," *Journal of Nano Research*, vol. 44, pp. 229–251, **2016**.
- [120] F. Ajayi, U. Sidwaba, U. Feleni, S. Douman, E. Mxusani, L. Wilson, C. Rassie, O. Tovide, P. Baker, S. Vilikazi, R. Tshikhudo, and E. Iwuoha, "A Nanosensor System Based On Disuccinimydyl – CYP2E1 for Amperometric Detection of the Anti-Tuberculosis Drug , Pyrazinamide," *International Journal of Medical, Health, Biomedical, Bioengineering and Pharmeceutical Engineering*, vol. 8, pp. 67–71, **2014**.



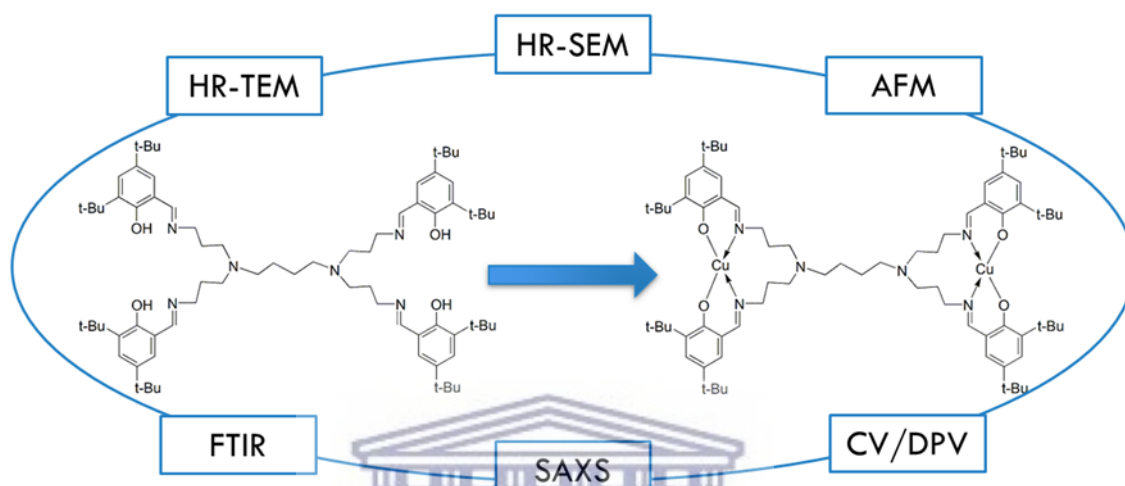
Chapter 3

3 Characterisation of first generation PPI dendrimer and copper functionalised metallodendrimer

Abstract

Dendrimers have been identified as one of the “smart materials” used in various applications in recent years. They have many favourable characteristics for their application in electrochemistry, specifically as electrocatalysts, such as their nano-size, high level of branching and high conductivity. This chapter will investigate the morphology, size, shape, internal structure as well as electrochemical behaviour of a polypropyleneimine first generation dendrimer and its copper functionalised counterpart. Techniques used for characterisation of the dendritic structures include FTIR, UV-Vis, HR-TEM, HR-SEM, AFM and SAXS. The inclusion of the metal centre was found to drastically change the morphology as well as electrochemical behaviour of the metallodendrimer. The PPI was found to be amorphous and roughly spherical whereas the CuPPI resulted in a rougher, polycrystalline ordered arrangement. The dendrimer was thus a good candidate as an electrocatalyst for sensing purposes. The PPI dendrimer showed a high capacitive current with relatively small faradaic current with regards to the oxidation and reduction processes occurring within the molecule. These were due to the cascade reaction taking place at the four hydroxyl groups on the salicylaldehyde substituents. The inclusion of the copper centre into the dendritic structure resulted in an anodic and cathodic peak appearing at 220 mV and 180 mV respectively. These reversible redox peaks were stable upon an increase in scan rate and proved that the dendrimer was surface confined. The surface concentration of

PPI on Au was calculated to be 5.095×10^{-8} mol.cm⁻² while this value increased to 9.014×10^{-7} mol.cm⁻² for Au|CuPPI. The behaviour of the metallodendrimer was investigated in the presence and absence of oxygen. The metallodendrimer maintained a good diffusion coefficient, decreasing from 4.124×10^{-5} cm²s⁻¹ to 3.29×10^{-5} cm²s⁻¹ in anaerobic and aerobic conditions respectively.



Scheme 3-1: Graphical abstract for Chapter 3

3.1 Introduction

The word dendrimer comes from the Greek word “dendro” which translates to tree. This word is used to describe a group of synthetic macromolecules, which have a roughly spherical and highly branched structure [1]. Another term used for dendrimers are cascade molecules. In 1978, Vöglte et al [2] synthesised the first structurally perfect cascade molecule via a repetitive synthetic route. These molecules can also be described as dendritic polymers, since they contain a number of monomer units which are chemically linked together [3]. Dendrimers have a basic structure, which consists of a core that can be either a single atom or a group of atoms. From this central area, dendrons or repeating units extend. Within these dendrons, wherever there is another level of branching, a different generation is formed [4] [5]. These areas representing the basic structure of a dendrimer is as shown below in Figure 3-1.

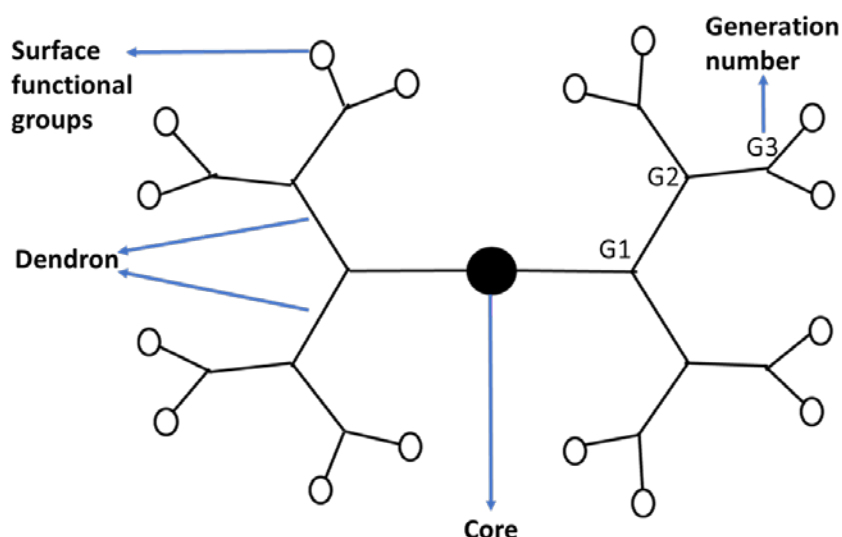


Figure 3-1: Basic structure of a dendrimer

Dendrimers have the ability to be functionalized in the core as well as on the periphery [6] [7] [8]. Therefore dendrimers that are built around a metal core for instance can be described as metal complexes of ligands which have dendritic substituents [9] [10]. These macromolecules can be synthesised via two methods, namely divergent and convergent synthesis. When the dendrimer is synthesised from the core to the periphery, it is called divergent synthesis [11]. On the other hand, when the dendritic branches are synthesised first and then linked to the core atom or molecule, this is known as convergent synthesis [12]. The ease of modification of the core, dendrons and functional groups within these molecules has resulted in countless varieties of dendrimers synthesised to date. The most common dendrimers synthesised are poly(amidoamine) or PAMAM [13] and poly(propyleneimine) or PPI [14]. The structure of dendrimers can range from generation 1 (G1) up until generation 11 (G11) for PAMAM [15], since dendrimers at a higher generation than this are energetically unstable [16]. The higher the generation the less space there is within the internal structure of the molecule, and therefore the denser the dendrimer becomes. Lower generation dendrimers have the advantage of having a more open, symmetrical structure which allows for fast electron transfer and thus have been found to be favourable in catalysis [17]. The incorporation of metals into the structure of a dendrimer is commonplace as it affects the catalytic properties of the molecule.

The metals can be incorporated into the core, as arm connectors, termini or as branching centres to form metallodendrimers [18]. Factors such as shape and size are also affected by the presence of metals [19]. These versatile molecules have proven to have various interesting and unique features and thus have found applications in gene delivery [20], drug delivery [17] [22], magnetic resonance imaging contrast agents [23] [24] as well as sensor applications [25] [26]. Other uses of dendrimers and metallodendrimers include catalysis [27] [28], models for self-assembled monolayers [29] and even as chemi-resistors [30] [31]. Dendrimers can aid in the selectivity of sensors by taking advantage of the structure of molecules, allowing only certain molecules to reach their targets [32]. Specific uses of metallodendrimers as electrocatalytic platforms for electrochemical sensors have proven to be viable [33]. Previous studies of first generation copper, cobalt and nickel poly(propyleneimine) metallodendrimers have been carried out as well [34]. Previously, this type of molecule has been applied to DNA biosensing, however an enzymatic biosensor has not yet been proven to be successful for this type of molecule.

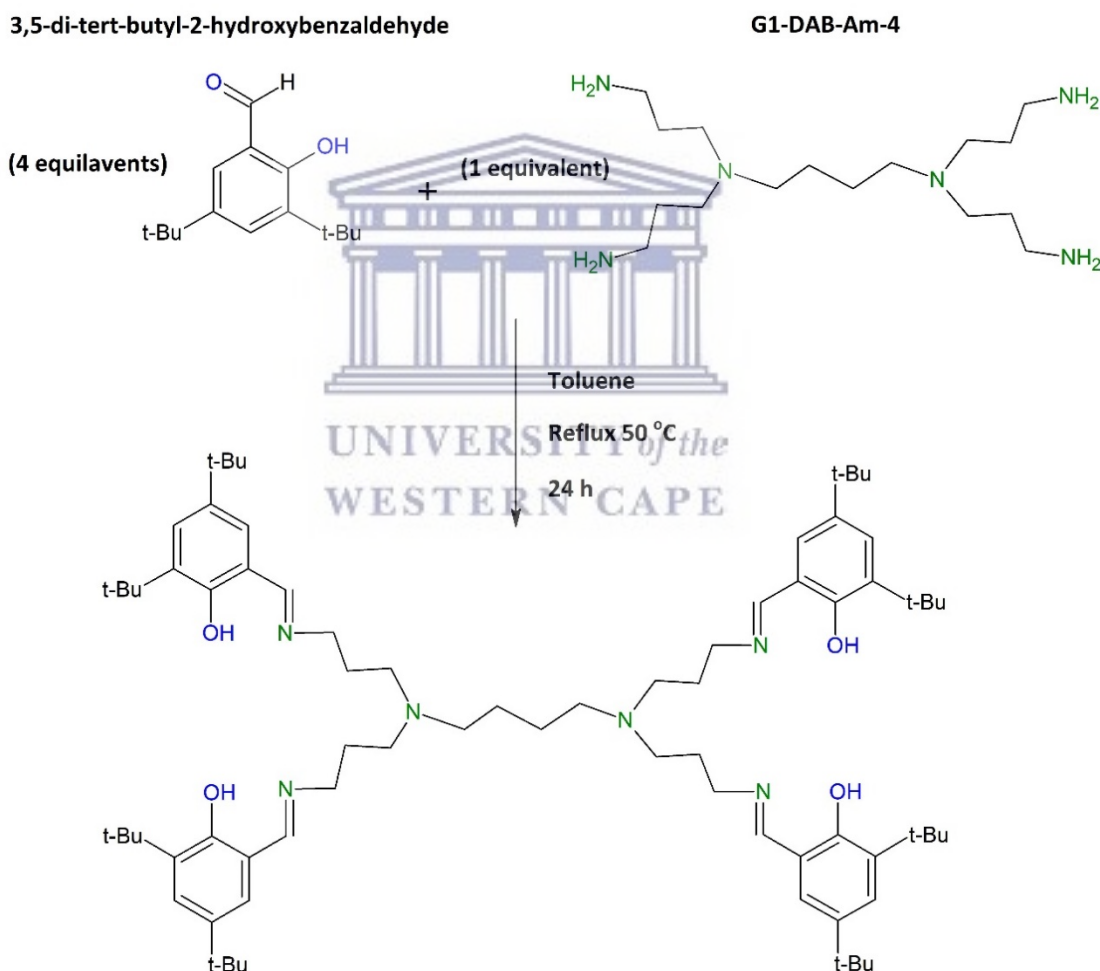
3.2 Experimental Section

3.2.1 *Materials and Methods*

Ultra-pure water purified by a Milli-Q™ system (Millipore) was used in all aqueous solutions and throughout the experiments. Sodium dihydrogen phosphate (NaH_2PO_4), disodium hydrogen phosphate (Na_2HPO_4), sodium chloride (NaCl), sulfuric acid (H_2SO_4), hydrogen peroxide (H_2O_2), ethanol and acetone were purchased from Sigma Aldrich, South Africa, and used as received. All electrochemical experiments were carried out using a 0,1 M Phosphate Buffer (PB) solution with pH of 7.4 as electrolyte. Analytical grade argon (Afrox, South Africa) was used for purging the system in anaerobic experiments. Alumina polishing pads and powder (0.05, 0.3 and 1.0 micron) were obtained from Buehler, Illinois, USA.

3.2.2 Synthesis of first generation dendritic ligand and copper functionalised metallodendrimer

The dendritic ligand and consequent metallodendrimer was synthesised using a divergent method similar to that used by Mugo et al [35]. A first generation dendrimer with a poly(propyleneimine) core was synthesised with salicylaldimine functional groups on the periphery via the following reaction steps. A 3,5-di-tert-butylsalicyldiminato group was reacted with a commercial sample of G1-DAB-(NH₂)₄ using a salicylaldimine to dendrimer ratio of 4:1. A scheme representing the synthesis of the first generation dendritic ligand is as shown in Scheme 3-2 below.

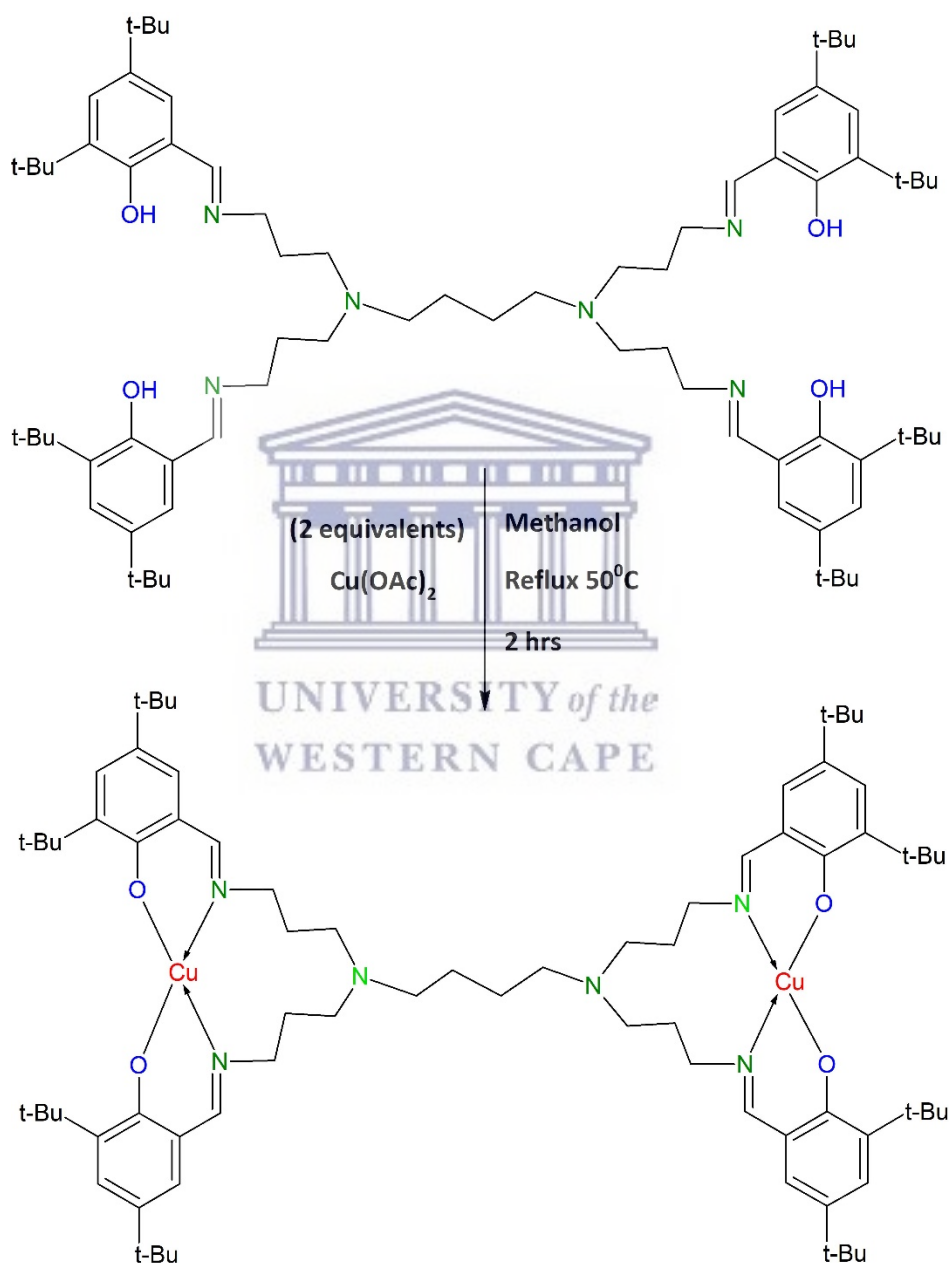


Scheme 3-2: Synthesis of first generation poly(propyleneimine) dendritic ligand

The crude product was obtained as a yellow oil which resulted in a yellow powder after extensive purification steps, i.e. extraction of dichloromethane solutions with water. The dendritic ligand was very soluble in organic solvents such as acetone,

ethanol, diethyl ether, tetrahydrofuran and dichloromethane and was stable in air. The dendritic ligand will now be referred to as PPI.

The generation 1 (G1) copper metallodendrimer was obtained by reacting the dendritic ligand with copper acetate monohydrate using stoichiometric amounts as shown in Scheme 3-3.



Scheme 3-3: Synthesis of copper (II) metallodendrimer

The resulting copper (II) metallodendrimer precipitated from the solution as a green powder with a yield of 63 – 75 %. The powder was then dissolved in a 1:1 ratio of acetone and ethanol and sonicated for 24 hours for the liquid analysis and characterisation.

3.2.3 *Structural and morphological characterisation of dendrimers*

Characterisation of the PPI dendrimer and CuPPI metallodendrimer was carried out using the methods described below.

3.2.3.1 *Fourier transform infrared spectroscopy*

Fourier transform infrared (FTIR) spectrum of the dendrimer and its copper functionalized metallodendrimer were obtained using PerkinElmer Spectrum 100-FT-IR Spectrometer in order to confirm the structure of PPI as well as the inclusion of the copper centre into the dendritic structure. The PPI dendrimer and CuPPI metallodendrimer were characterised by mixing around 1 mg of sample with potassium bromide to form a KBr pellet. The FTIR scan was run from 400 cm⁻¹ to 4000 cm⁻¹.

3.2.3.2 *Ultraviolet-Visible Spectroscopy*

Ultraviolet-Visible (UV-Vis) spectroscopy was carried out on a Nicolett evolution 100 (Thermo Electron Corporation). The dendrimers were characterised in solution within a wavelength range of 190 to 500 nm.

3.2.3.3 *Microscopy*

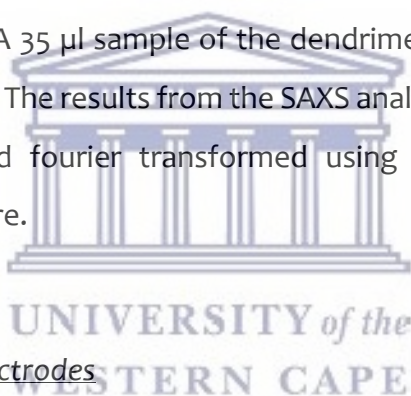
Atomic force microscopy (AFM) imaging was carried in order to determine the surface morphology of the dendrimers. The experiments were carried out on a Veeco NanoMan V model.

High resolution transmission electron microscopic (HR-TEM) analysis of dendrimer morphology was obtained using a Tecnai G2 F20 X-Twin MAT microscope. A dilute sample of either PPI or CuPPI was drop coated onto a carbon coated nickel grid which was allowed to dry completely before use.

High resolution scanning electron microscopy (HR-SEM) was carried using a Zeiss Auriga HR- SEM. The dendrimers were analysed in their powdered form and placed onto a carbon sticker. The samples were then coated in a conductive carbon film for analysis via HR-SEM.

3.2.3.4 Small angle X-Ray scattering

Small angle X-Ray scattering (SAXS) characterisation was carried out on a SAXSpace purchased from Anton Paar GmbH in order to determine the size and shape of the nano-sized dendrimers. A 35 μl sample of the dendrimers were analysed in solution for high resolution SAXS. The results from the SAXS analysis was then processed with SAXtreat, SAXquant and fourier transformed using generalised indirect fourier transform (GIFT) software.



3.2.4 Preparation of electrodes

The working electrode was gold with a diameter of 1.6 mm. The reference electrode was Ag/AgCl (3 M NaCl) and platinum wire served as the counter electrode. All electrodes were obtained from Bioanalytical Systems (BASi) in West Lafayette USA. The working electrode was cleaned before each experiment by polishing to a mirror like surface on polishing pads with alumina powder slurry of 1, 0.3 and 0.05 micron respectively. This process was followed by sonication of the electrode in ethanol and water for 5 and 10 min respectively. A 5 mM solution of dendrimer (PPI or CuPPI) was prepared using 1:1 (v/v) acetone-ethanol. A volume of 8 μL of the dendrimer solution was then drop-coated onto the surface of the clean gold electrode and left to dry for 45 min to allow for physical adsorption to take place. The surface of the electrode was then rinsed lightly with ethanol to remove any unbound dendrimer and

dried under a stream of nitrogen gas. The resulting electrode will be called Au|PPI or Au|CuPPI.

3.2.5 Electrochemical Protocol

The electrochemical experiments were carried out in a three-electrode system consisting of working, counter and reference electrodes in a 10 ml glass cell. All cyclic voltammetry (CV) and square wave voltammetry (SWV) experiments were carried out on PalmSense potentiostat (Palm Instruments BV, Netherlands). Electrochemical cleaning of the electrode was also carried out by cycling in a 1 M solution of sulfuric acid. Ten cycles were done between the potentials of -200 mV and 1500 mV or until a reproducible voltammogram was obtained. The electrodes were characterized in 0.1 M phosphate buffer pH 7.4 within a window potential of -600 mV to 600 mV using CV and SWV. The CV had an equilibration time of 5 s, E step of 10 mV and scan rate of 100 mV/s. SWV was carried out at with an E step of 20 mV, an amplitude of 50 mV and frequency of 10 Hz.



3.3 Results and discussion

3.3.1 Structural and morphological characterisation of dendrimers

The PPI and CuPPI dendrimers were investigated using various spectroscopic and microscopic methods in order to determine their structural properties. These investigations were also completed in order to confirm the incorporation of copper into the molecule and to determine their electro-catalytic properties. The resulting structures of the dendritic ligand and copper (II) metallodendrimer is shown in Figure 3-2 and Figure 3-3 below.

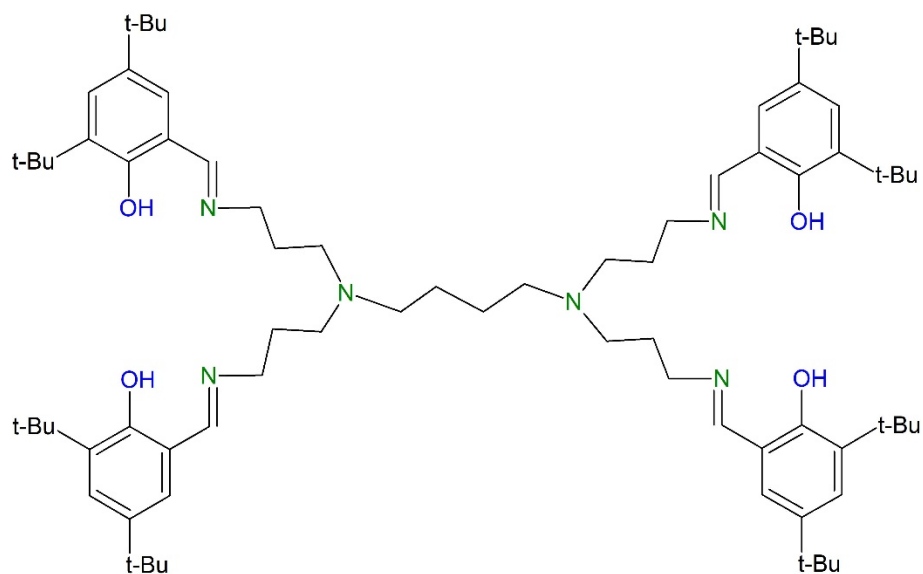


Figure 3-2: Chemical structure of poly(propyleneimine) dendritic ligand

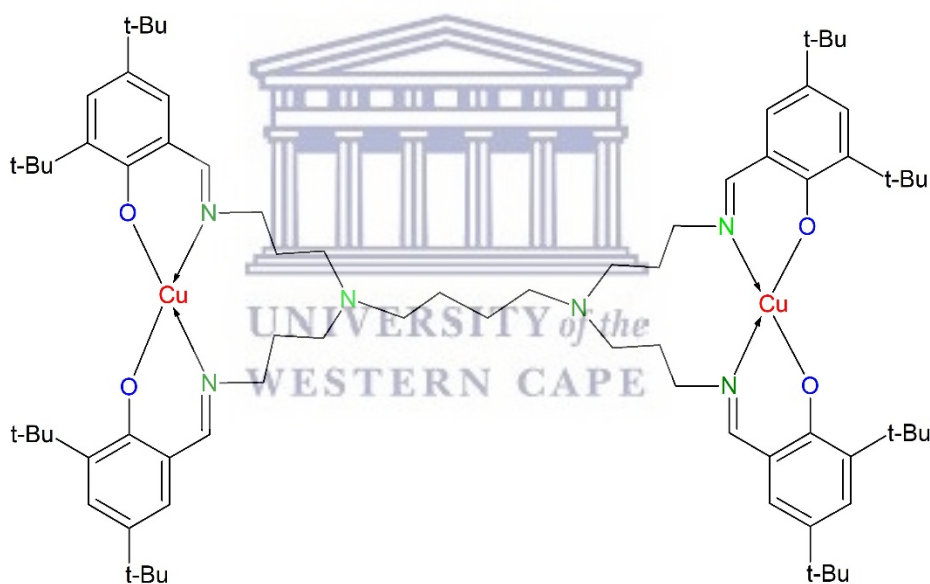


Figure 3-3: Chemical structure of copper (II) metallodendrimer

3.3.1.1 Fourier transform infrared spectroscopy

The stretching vibrations arising from the FTIR spectrum are as shown in Table 3-1 and the spectrum obtained in Figure 3-4.

Table 3-1: FTIR peaks of dendritic ligand and copper (II) metallodendrimer

Functional Group	Wavelength/ ν for PPI (cm^{-1})	Wavelength/ ν for CuPPI (cm^{-1})
Aliphatic C-H	2852	2950
C=N	1630	1625
Cu-N	-	1531
C=C	1458	1442
C-N	1254	1257
Ar-H	877	814
Cu-O	-	527, 474

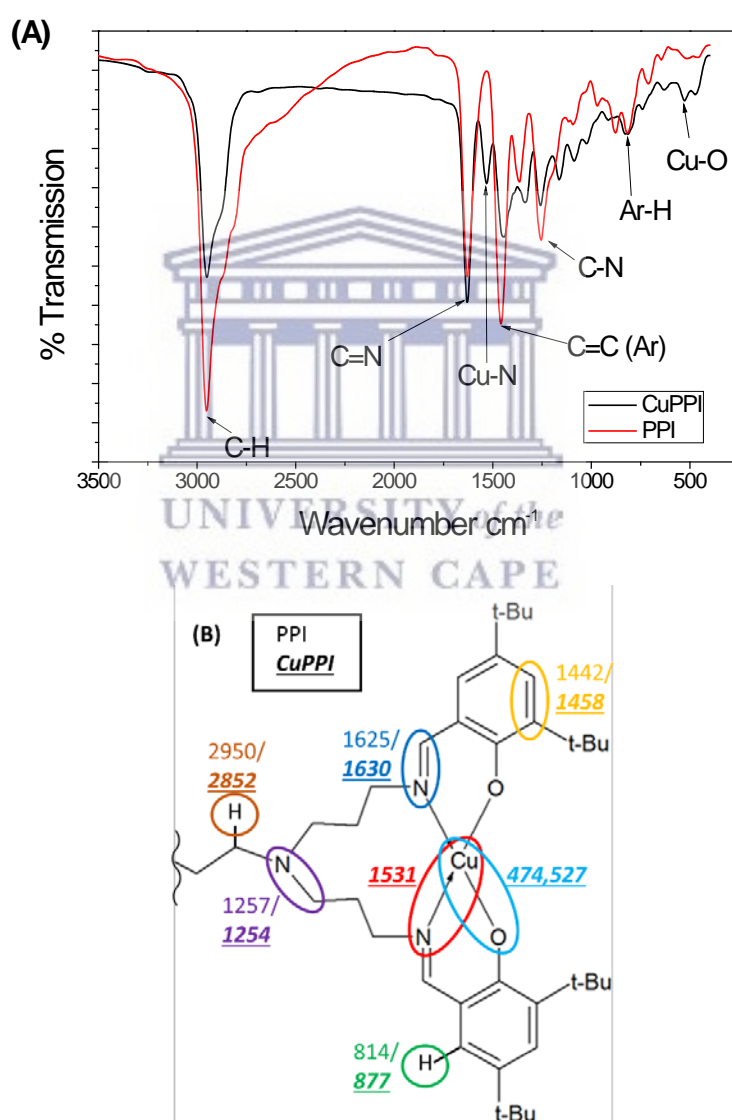
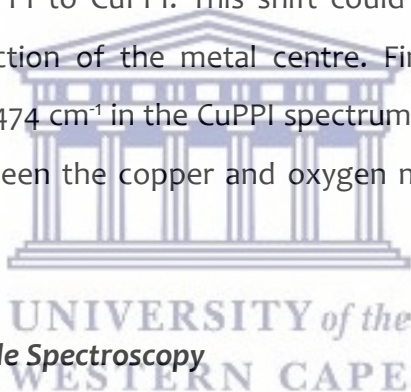


Figure 3-4: (A) FTIR spectrum of PPI and CuPPI (B) Schematic representation of the functional groups responsible for the respective FTIR peaks in cm^{-1} , normal font are peaks assigned to PPI and bold font is attributed to CuPPI

A strong peak appears around 2900 cm^{-1} which is attributed to the aliphatic C-H bonds within the poly(propyleneimine) central structure [19]. This peak is present in the spectra of both PPI and CuPPI. Another strong peak appears in the CuPPI spectrum at 1630 cm^{-1} and in the PPI spectrum at 1625 cm^{-1} . This peak is caused by the $\nu(\text{C}=\text{N})$ stretching band between the polymer branches and the salicylaldimine groups on the periphery of the dendritic structures. The shift of this peak to a higher frequency suggests the coordination between the nitrogen and the copper centre [36] [37]. A new peak appears at 1531 cm^{-1} which confirms the new coordination between copper and nitrogen $\nu(\text{Cu}-\text{N})$, since this peak is not present in the spectrum of the dendritic precursor [36]. The PPI spectrum shows a $\nu(\text{C}-\text{N})$ stretching band at 1257 cm^{-1} which shifts to 1254 cm^{-1} in the CuPPI spectrum and a decrease in peak intensity [33]. The peak attributed to aromatic hydrogens i.e. $\nu(\text{Ar}-\text{H})$ decreases from 877 cm^{-1} to 814 cm^{-1} when changing from PPI to CuPPI. This shift could be due to delocalisation of electrons upon introduction of the metal centre. Finally, the last notable peak appears at 527 cm^{-1} and 474 cm^{-1} in the CuPPI spectrum only. This peak is due to the bond which forms between the copper and oxygen molecules i.e. $\nu(\text{Cu}-\text{O})$ in the metallodendrimer [38].



3.3.1.2 Ultraviolet-Visible Spectroscopy

UV-Vis spectroscopy was carried out and the results of the scans of PPI and CuPPI in a 1:1 ethanol/acetone solution are as shown in Figure 3-5. There are three distinct absorption peaks in the spectrum of the PPI dendrimer at 248, 287 and 305 nm. The first two with an absorption maxima $\lambda_{\text{max}} = 248\text{ nm}$ and 287 nm is attributed to the intra-ligand $\pi \rightarrow \pi^*$ transition in the benzene ring of the salicylaldimine substituents [39]. The third peak at $\lambda_{\text{max}} = 305\text{ nm}$ is caused by the $n \rightarrow \pi^*$ transition of the C=N chromophore [35].

There are similar peaks in the UV-Vis spectra of CuPPI with absorption maxima $\lambda_{\text{max}} = 236, 280$ and 315 nm . The first two peaks are attributed to the $\pi \rightarrow \pi^*$ transitions which are seen to be shifted to a shorter wavelength i.e. a blue shift in the metallodendrimer caused by the inclusion of the copper metal centre into the dendritic structure. The peak at 315 nm is due to $n \rightarrow \pi^*$ transition of the C=N

chromophore. The additional peak at 380 nm in the copper metallodendrimer is caused by the metal to ligand charge transfer (MLCT) transitions [37] [40].

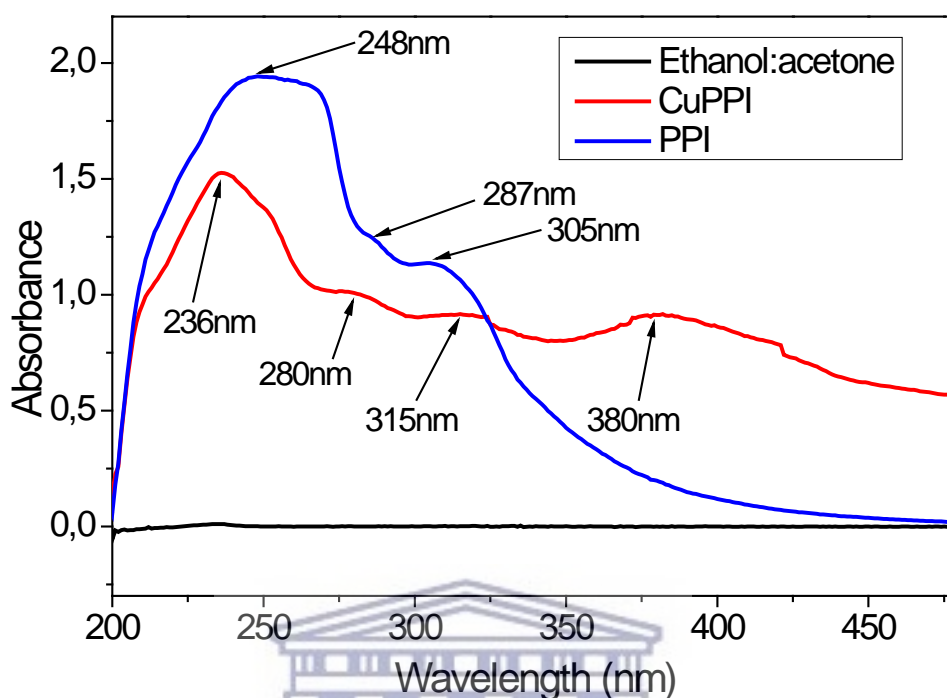


Figure 3-5: UV-Vis spectra of PPI and CuPPI in ethanol:acetone solution

3.3.1.3 Atomic Force Microscopy

We then went on to study the morphology (surface characteristics) of the dendrimer and metallodendrimer using various microscopic techniques. When studying the compounds using atomic force microscopy (AFM) the resulting images are as shown below. From the 3-dimensional image scan of the PPI dendrimer in Figure 3-6, we can see that there is an amorphous morphology with a smooth and bumpy surface. The compound has a horizontal feature in the micrometre range and vertical features in the nanometre range. This is consistent with what is expected of a first generation poly(propyleneimine) based dendrimer because of its globular structure [41] [42]. The 2-dimensional image scan of PPI in Figure 3-6 shows that the height of the PPI dendrimer is increased to 1 μm at its highest point.

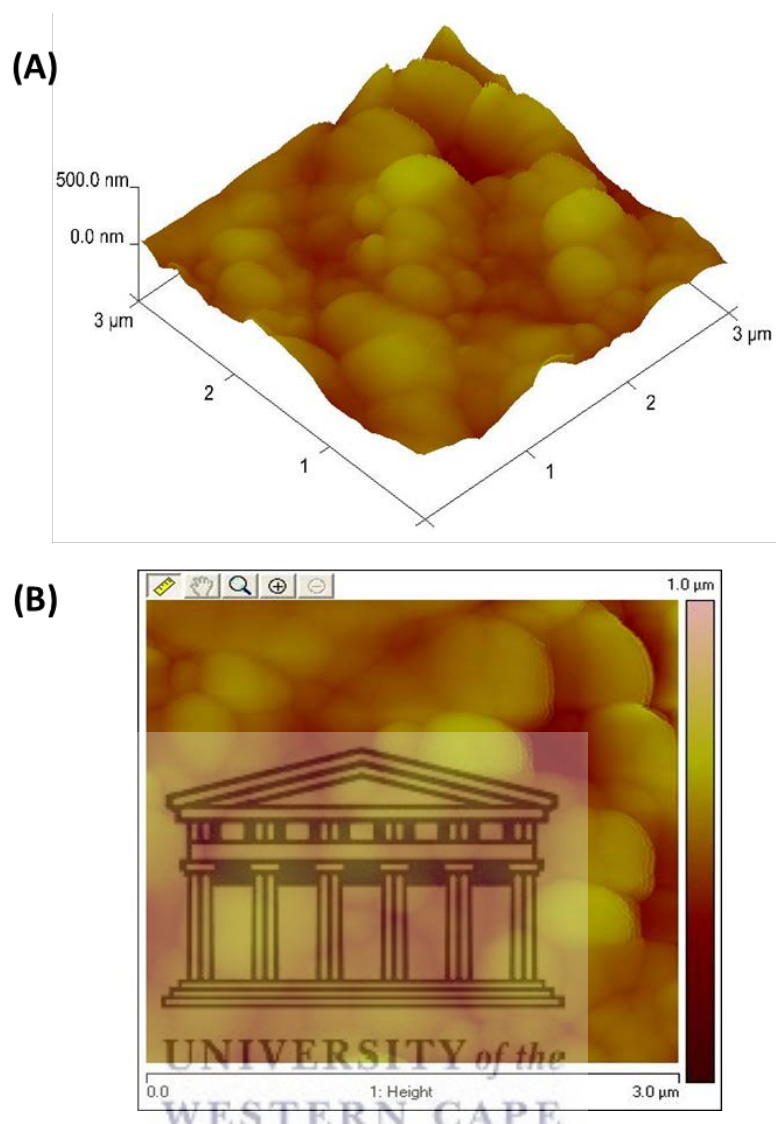


Figure 3-6: (A) 3-D and (B) 2-D AFM image of PPI dendrimer

In comparison to the PPI, the incorporation of the copper centre into the dendrimer caused a significant change to the morphology of the compound. The resulting 3-dimensional image of the CuPPI metallodendrimer is shown in Figure 3-7 (A). This image shows that the surface of the metallodendrimer is very rough and jagged. The size of the features is similar to that of the PPI dendrimer, however the difference is mostly in the roughness of the material. The jagged image is indicative of a possible crystallisation that is common in copper complexes [43]. Recent studies by Zare et al also confirm that the presence of a copper metal center in a ligand complex results in material that is more ordered and have a jagged structure similar to the results found here [44]. In order to confirm the structural changes of the metallodendrimer

we had to further investigate the morphology using a higher resolution imaging technique such as electron microscopy.

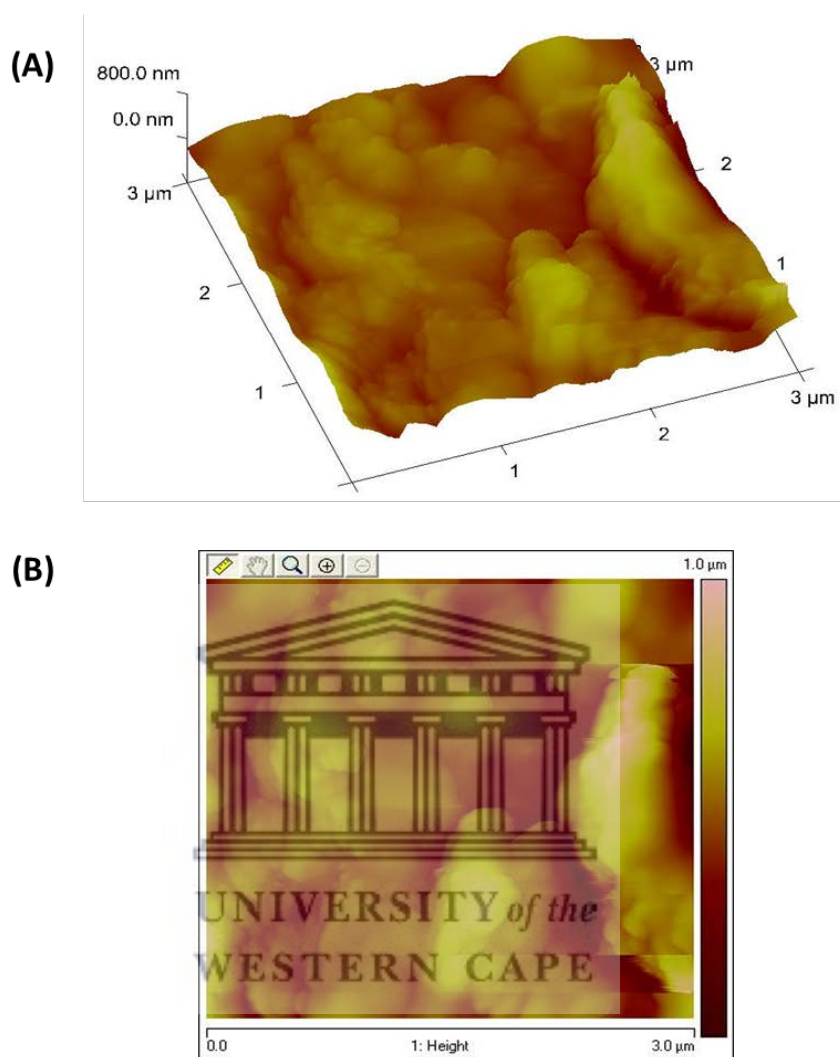


Figure 3-7: (A) 3-D and (B) 2-D image scan of CuPPI metallodendrimer

3.3.1.4 High Resolution Transmission Electron Microscopy

The characterization of the dendritic compounds via high resolution transmission electron microscopy i.e. HR-TEM are discussed next. The images obtained when investigating the dendrimer showed a globular and amorphous structure as shown in Figure 3-8. There are no distinct features visible from the high resolution image. One can also see that there are high levels of aggregation between particles with features in the 20 nm range. The HRTEM images reveal layers of particles that are less than 20 nm in diameter, stacked on top of one another. The electron diffraction pattern of

PPI shows diffuse rings which corresponds to an amorphous structure [43]. The globular shape of the PPI corresponds with what is expected of the dendrimer structure which is roughly spherical.

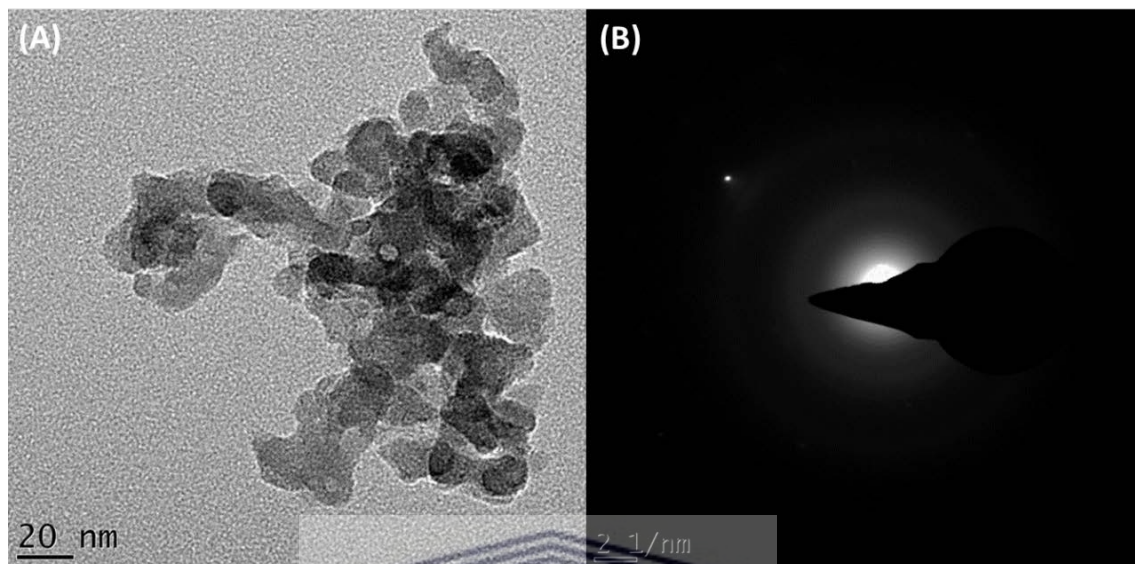


Figure 3-8: (A) HR-TEM and (B) electron diffraction pattern of PPI dendrimer

To study the effect of the copper centre on the morphology of the dendrimer, HR-TEM was carried out on the CuPPI metallodendrimer as well. The most distinct differences between the morphology of these two compounds, is the appearance of lattice fringes in CuPPI as shown in Figure 3-9. The appearance of lattice fringes, as indicated by the arrows in Figure 3-9 is an indication of the crystallinity of a material. The lattice fringe spacing is roughly $d = 0.21$ nm which corresponds to the inter-planar spacing of the Cu(111) plane of the CuPPI poly-crystalline structure [45]. The copper centre has been proven to drastically change the morphology and crystallinity of the dendrimer. Metal centred dendrimers have previously been proven to form crystalline structures [46]. The electron diffraction pattern also confirms that the metallodendrimer is crystalline, however, the multiple layers of the compound makes it difficult to form a distinct pattern using this technique. The appearance of these crystal “spots” however do confirm crystalline areas, whereas the dendrimer did not reveal any form of crystallinity from its electron diffraction pattern

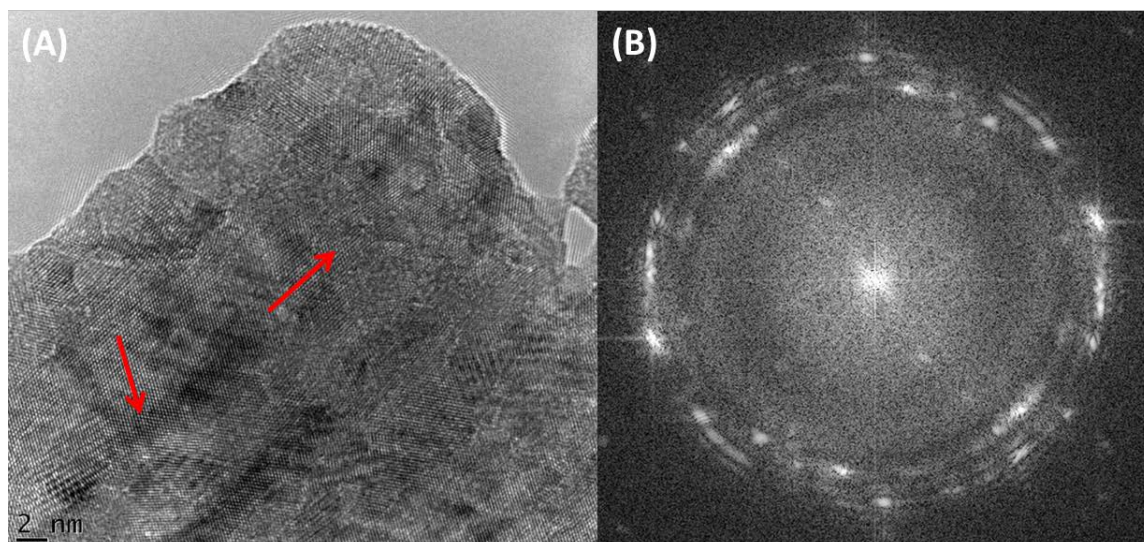


Figure 3-9: (A) HR-TEM and (B) electron diffraction pattern of CuPPI metallodendrimer

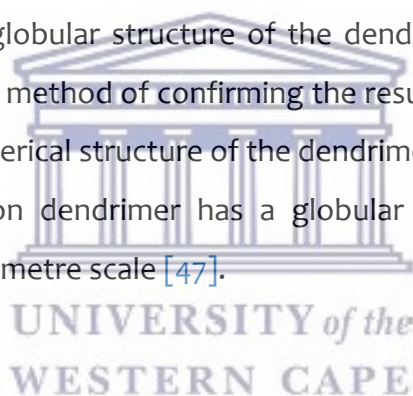
Using the HR-TEM microscope, an energy dispersive X-Ray spectroscopic or EDX analysis was also completed on both the PPI dendrimer and the CuPPI metallodendrimer. This technique gives us insight into the elemental composition of each of these compounds. The EDX results showing the relative atomic percentage of elements in each of the dendrimers are as shown in Table 3-2 below. In order to quantify the amount of copper in the metallodendrimer sample, carbon was removed from the analysis as it interfered with the accuracy of the results for the other elements. The EDX results confirm the incorporation of the copper into the structure of the dendrimer. HR-TEM analyses the internal structure of the compound and thus is a satisfactory complimentary tool to FTIR and others.

Table 3-2: EDX results of PPI and CuPPI

Elemental composition	PPI (atomic percentage)	CuPPI (atomic percentage)
C	94.76	-
N	2.92	6.52
O	2.10	39.03
Cu	-	54.43

3.3.1.5 High Resolution Scanning Electron Microscopy

High resolution scanning electron microscopic (HR-SEM) images were also taken of the PPI dendrimer and CuPPI metallodendrimer. These images are as shown in Figure 3-10 and Figure 3-11 for PPI and CuPPI respectively. The images were taken at various magnifications in order to see both the macro and micro structures of the respective dendrimers morphology. The HR-SEM results of PPI confirm the amorphous structure of the dendrimer particles, i.e. the PPI has no distinct features. In Figure 3-10 (A) we can see the bulk of the material which seems to be amorphous with some areas clumped together to form large particles. In this image the scale is at 1 μm and therefore these particles are very large and can be seen with the naked eye. When zooming in to a magnification of 50 KX one can see down to the nanoscale using the HR-SEM and this image is shown in Figure 3-10 (B) with a scale of 100 nm. In this image one can again see the globular structure of the dendrimer, which are a part of a greater particle. This is a method of confirming the results obtained by the HR-TEM, showing the roughly spherical structure of the dendrimer. We can therefore confirm that this first generation dendrimer has a globular morphology that is mostly amorphous on the micrometre scale [47].



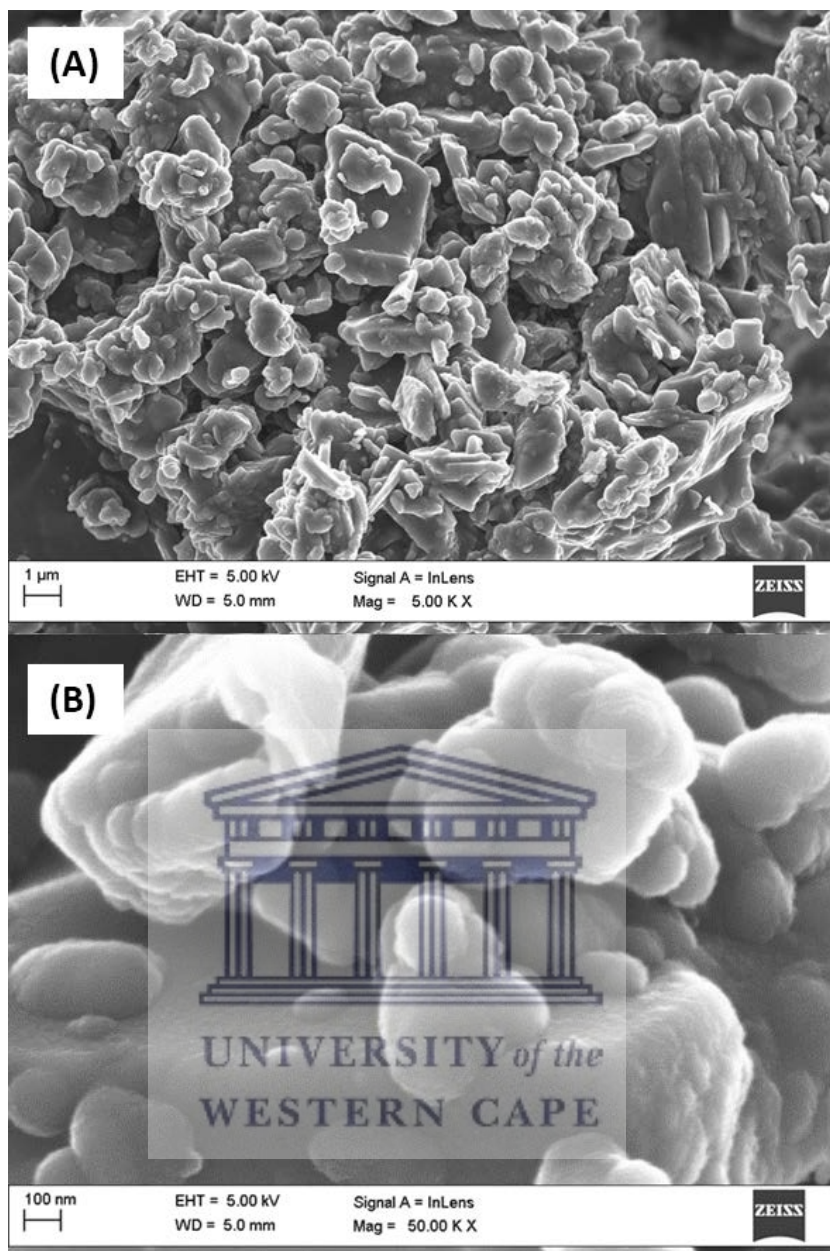


Figure 3-10: HR-SEM of PPI dendrimer at (A) 5 KX and (B) 50 KX

The comparative study was then completed by doing an HR-SEM scan of the CuPPI metallodendrimer. The images of CuPPI are as shown in Figure 3-11 (A) at a magnification of 20 KX and Figure 3-11 (B) at a magnification of 100 KX. From the HR-SEM results, one can clearly see the ordered nature of the copper metallodendrimer. There are clearly defined sheet like structures which are layered in top of one another at a scale of 1 µm. When zooming in to a scale of 200 nm, these sheet like structures are even more visible.

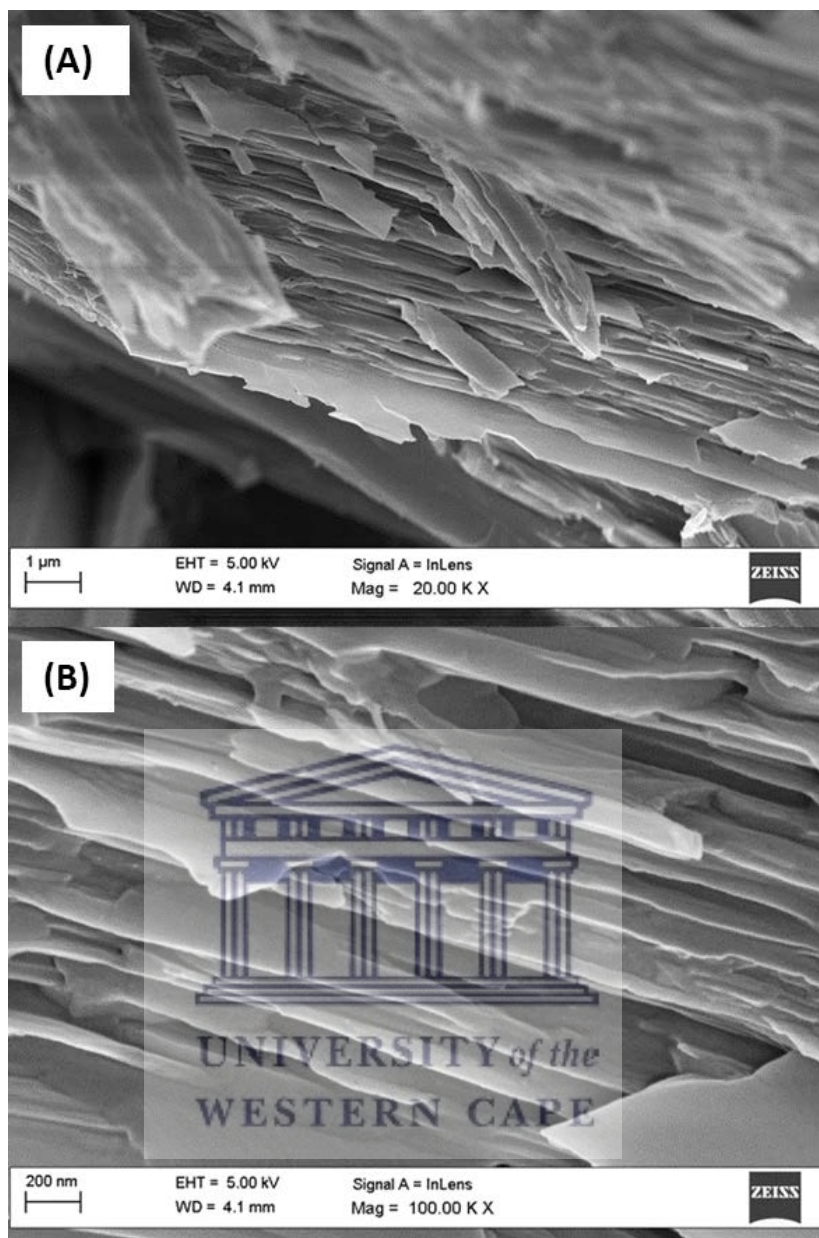


Figure 3-11: HR-SEM of CuPPI at (A) 20 KX and (B) 100 KX

These images confirm the ordered nature of a crystalline material, as well as the assumption in the HR-TEM that there are multiple layers of CuPPI on top of one another [42] [48]. A copper coordinated compound has previously been synthesised by Alturiqui et al and characterised using HRSEM, yielding similar sheet like structures shown above [49]. This type of copper based metallodendrimer has not been widely studied using microscopic methods.

The ordered nature of the copper metallodendrimer and its ability to form self-assembled layers makes it a good candidate for electrochemical sensing. It is also

clear that the thickness of these sheets are definitely in the nanometer range. Another complementary technique is required to determine the exact size of these dendrimers.

3.3.1.6 Small Angle X-Ray Scattering

Small angle X-ray scattering (SAXS) is often used to characterise hyper-branched polymers such as dendrimers. The scattering angle intensity also gives information on the arrangement of the polymeric segments and thus density of the various areas within the molecule [50]. SAXS analysis is characterised by the scattering vector, q , as shown in Equation 3-1.

$$q = \frac{4\pi}{\lambda} \sin \frac{2\theta}{2} \quad \text{Equation 3-1}$$

Where θ is the scattering angle and λ is the wavelength of the probing radiation, which in this case is Cu-K α radiation of 0.15406 nm. A fit of the scattering data gives us information on the average size of the dendrimer particles i.e. radius of gyration R_g [51]. The form factor $P(q)$ can be approximated by a Gaussian curve at small angles. According to Guinier, the curvature of the Gaussian is due to the overall size of the particle. If the structure of the particle can be assumed then the size parameter i.e. R_g , can be determined using Equation 3-2, where a_0 is the extrapolated zero-angle intensity [51].

$$P(q) \approx a_0 \cdot e^{-\left(\frac{R_g^2 q^2}{3}\right)} \quad \text{Equation 3-2}$$

The scattering curve of the dendrimer and metallodendrimer were Fourier transformed to produce a pair distance distribution function (PDDF) graph as represented by Figure 3-12. These graphs give an indication of the diameter of the particles as well as the shape [52]. The PDDF's show an average particle size of 100 nm or larger due to the shoulders at the right hand side of the curve. The PDDF's

show that there is a substantial amount of aggregation as well. The irregular shaping also indicates that the particle is poly-dispersed and has many different sized particles. There is also a distinct initial peak in both graphs at around 10 nm which indicates that there might be a large portion of the sample at this size range [53].

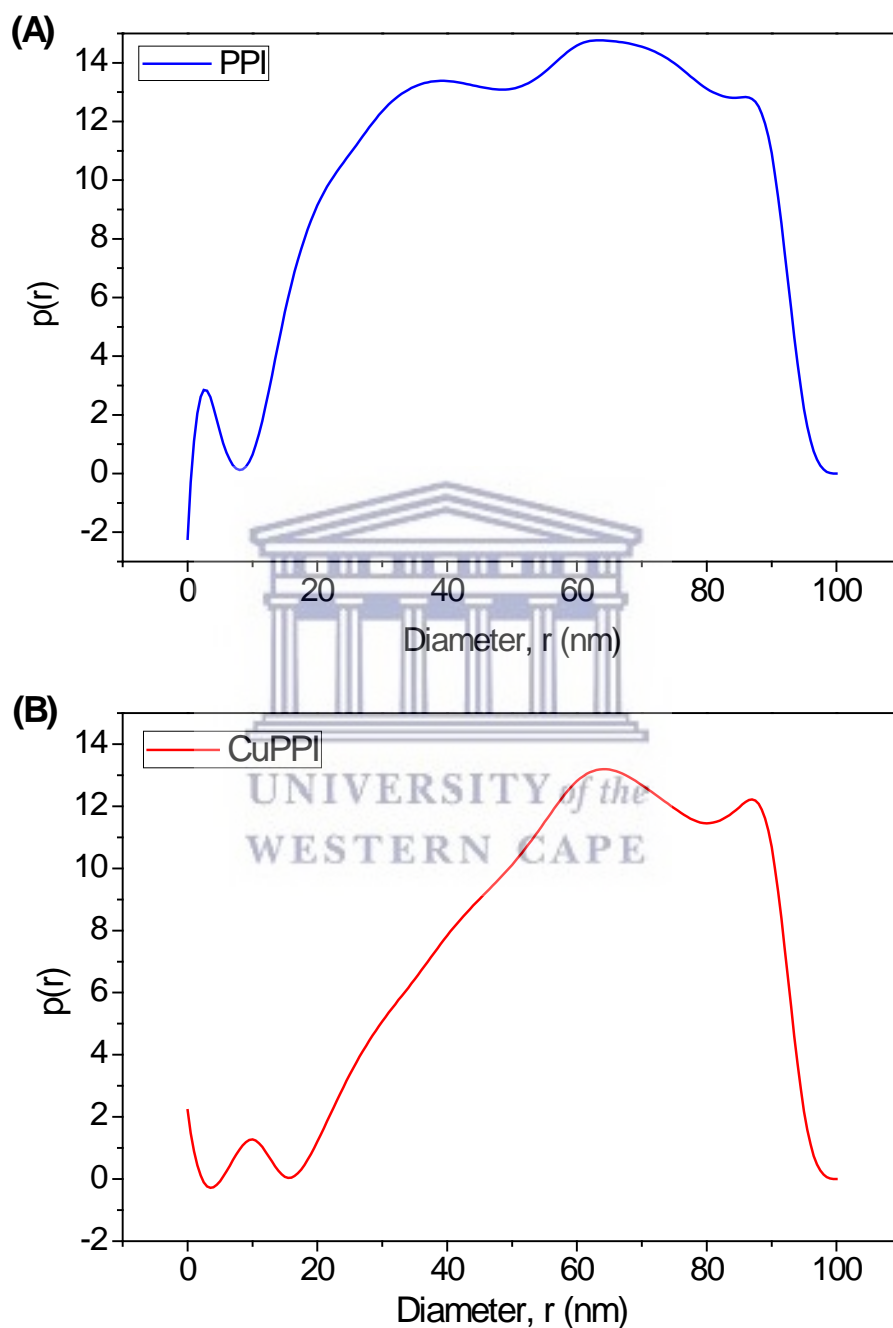


Figure 3-12: Pair distance distribution functions of (A) PPI and (B) CuPPI

Size distribution curves can be obtained via fourier transformation of scattering curves [54]. Size distribution by number (SD_{num}) curves are shown in Figure 3-13. Since SAXS takes into account the entire sample statistics, this graphs shows a relative analysis according to the number of particles in the entire sample [55]. From the microscopic analysis we are sure that there is a big amount of aggregation present in both dendrimers. The PPI shows that most of the smaller samples are around 10 nm with some of the particles being 55 and 75 nm in size. Upon analysis of the 0 – 10 nm range in the PPI SD_{num} curve we found that the specific sample size represented by this peak is at 1 nm. This is in accordance with literature as first generation PPI dendrimers without substituents on the branches have been found to be around 0.5 nm [56]. The CuPPI however shows that almost the entire number of individual particles in the sample is around 1 nm in size.

Size distribution by volume (SD_{vol}) on the other hand is a representation of the total sample volume occupied by particles of a particular size [53]. One can thus deduce that larger particles would take up a larger volume but not necessarily be the most abundant sized particle in the sample. In Figure 3-14, the SD_{vol} graph of PPI shows that the volume of 10 nm particles and 55 nm particles are almost equal and particles of the size 75 nm take up about 25 % of the volume as the 10 nm particles. This is quite useful to note as the 75 nm particles were not visible in the SD_{num} graph. We can thus deduce that the majority of particles in the sample are in the 10 nm range for both the PPI and CuPPI, with agglomerates forming in both the dendrimer and metallodendrimer.

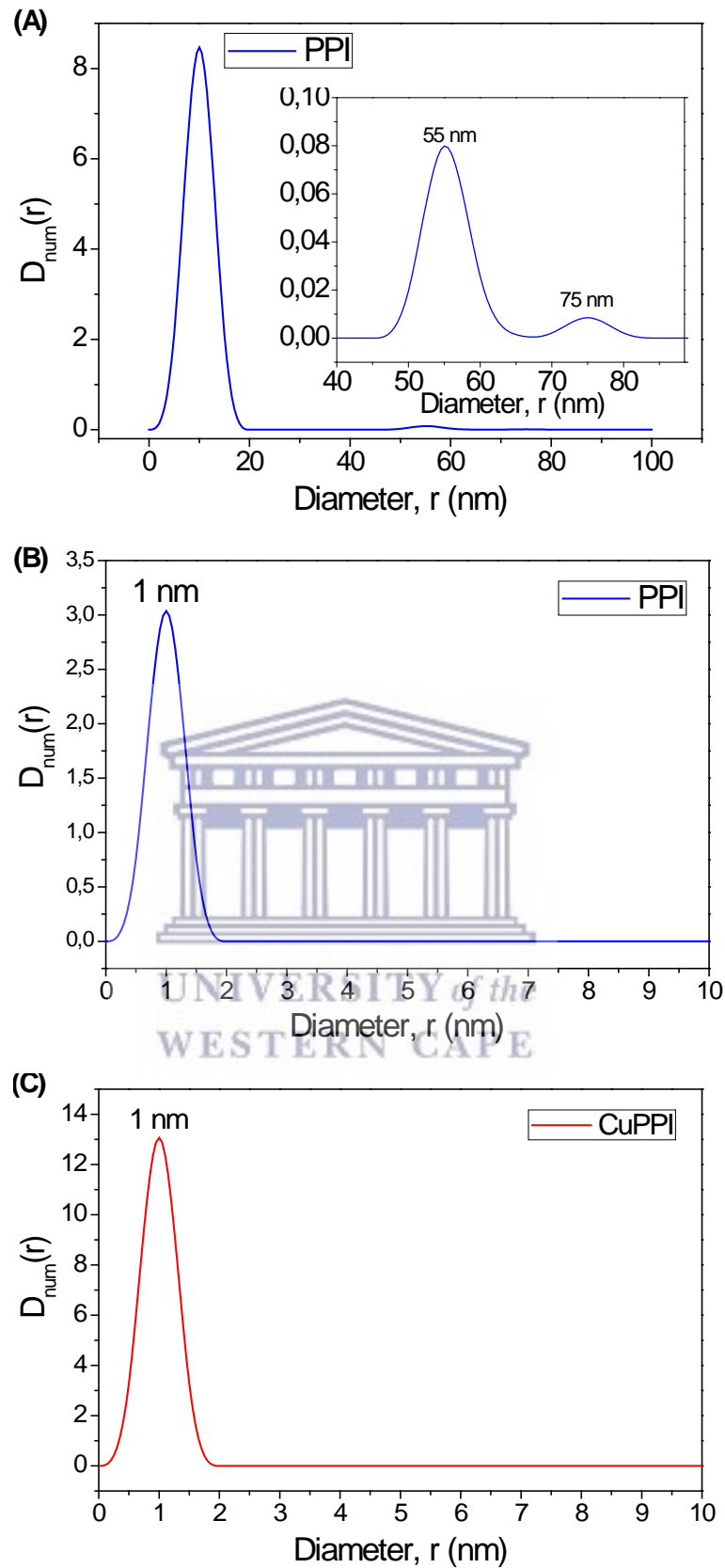


Figure 3-13: Size distribution by number representations of (A) PPI in the 0 to 1 nm range (B) PPI in the 0 to 10 nm range and (C) CuPPI in the 0 to 10 nm range

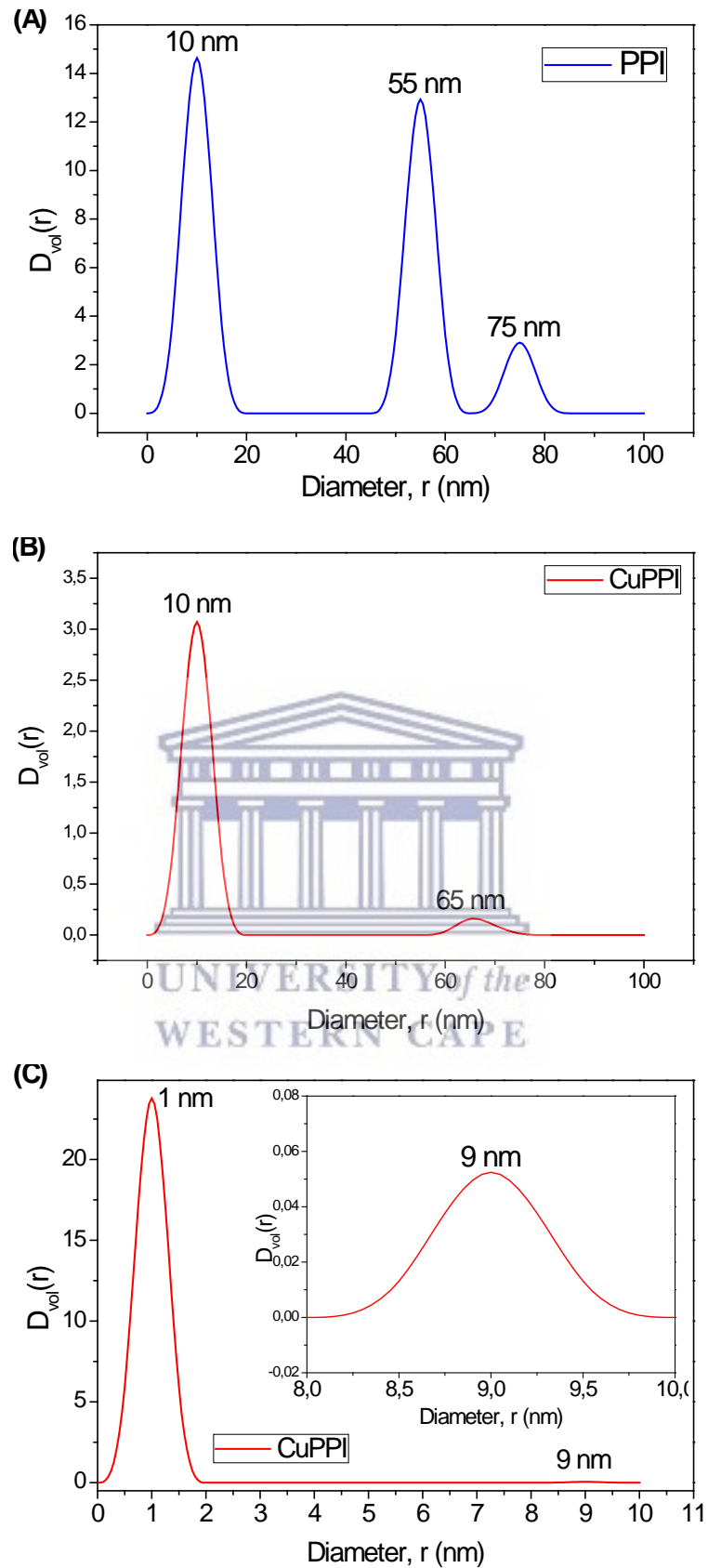


Figure 3-14: Size distribution by volume representations of (A) PPI in the 0 to 100 nm range (B) CuPPI in the 0 to 100 nm range and (C) CuPPI in the 0 to 10 nm range

3.3.2 Electrochemical characterisation of dendritic ligand and metallodendrimer

The application of the metallodendrimer for our purposes would be as an electro-catalytic platform for an electrochemical sensor. Therefore, the dendrimer and metallodendrimer were characterised using electrochemical techniques such as cyclic voltammetry and square wave voltammetry on gold electrodes. The Au|PPI and Au|CuPPI electrodes were characterised individually in order to confirm that the metallodendrimer is an ideal candidate as an electro-catalytic platform as well as the effect of the metal centre on the electrochemical behaviour of the dendrimer.

3.3.2.1 **Electrochemical characterization of Au|PPI**

The cyclic voltammogram (CV) of the first generation poly(propyleneimine) dendrimer i.e. Au|PPI under argon atmosphere is as shown in Figure 3-15 (A). The cyclic voltammogram of PPI shows some electro-activity in that it has a very different voltammogram compared to the bare gold electrode onto which it was physically adsorbed. The CV of PPI is very broad which indicates that there is a high charging (i_{ch}) or capacitive current and very low faradaic current being produced by the compound. Faradaic current is known as the current generated from oxidation or reduction of a species at the electrode surface whereas the capacitive current does not involve chemical reactions. It is due to the accumulation or removal of electric charges on the electrode or electrolyte surface near the electrode [57]. It is clear that the capacitive current of PPI is very high in the cathodic sweep of PPI. Therefore one can deduce that the oxidised form of the dendrimer has a high resistance. There are no distinct peaks visible which are attributed to PPI, but there are “shoulders” visible in the anodic scan with anodic peak potential, E_{pa} at 200 mV and 400 mV. Similar peaks were reported by Mokwebo et al [58] and Arotiba et al [59] when investigating a PPI with no functional groups on the periphery. There is also a shoulder in the cathodic scan with a cathodic peak potential, E_{pc} of 320 mV. A more sensitive technique such as square wave voltammetry makes it possible to clearly visualise these peaks as is shown in Figure 3-15 (B).

The square wave voltammogram shows peaks that are still not very pronounced but more visible than those observed in CV. There are peaks in the anodic scan at E_{pa} of 370 mV, 200 mV and a small shoulder at -130 mV. There were also four peaks visible from the anodic scan of the SWV with an E_{pc} of 480 mV, 335 mV and two smaller peaks at -60 mV and -190 mV. The peaks present in the anodic scan of the CV and SWV are attributed to the oxidation of the four hydroxyl groups in the PPI structure. This reaction occurs in a complex cascade and results in multiple peaks in the voltammograms. The peaks in the cathodic scan are due to their subsequent reduction back to its original state as shown in Figure 3-15 [34].

To determine the number of electrons transferred in the PPI dendritic system one can refer to Nernst Equation 3-3 [60].

$$\Delta E = |E_{pa} - E_{pc}| = \frac{2.3030 RT}{nF} \quad \text{Equation 3-3}$$

In this equation ΔE is the peak separation, E_{pa} and E_{pc} are the anodic and cathodic peak potentials respectively, R is the gas constant $8,314 \text{ J K}^{-1} \text{ mol}^{-1}$, n is the number of electrons transferred, T is temperature in kelvin and F is Faradays constant 96485 C mol^{-1} . The number of electrons calculated was determined to be approximately 1. This equation gives us an idea of the number of electrons transferred in the electrochemical processes occurring at the electrode surface. Therefore, for a reversible redox reaction at 25°C (298 K) with n electrons ΔE should be $0.0592/n \text{ V}$ or about 60 mV for one electron. In the case of PPI, the ΔE is equal to 80 mV. However, the reaction is quasi-reversible because $0.0592/n \text{ V}$ is more than 60 mV.

The CV was then carried out at various scan rates in order to determine the surface concentration of the dendritic ligand. The Brown Anson equation was used to determine the surface concentration where the surface area of the electrode is $A = 0.0201 \text{ cm}^2$ and n is one as in Equation 3-4. The surface concentration of PPI on the gold working electrode was calculated to be $\Gamma_0 = 5.095 \times 10^{-8} \text{ mol.cm}^{-2}$.

$$I_p = \frac{n^2 F^2}{4RT} \nu A \Gamma_0 \quad \text{Equation 3-4}$$

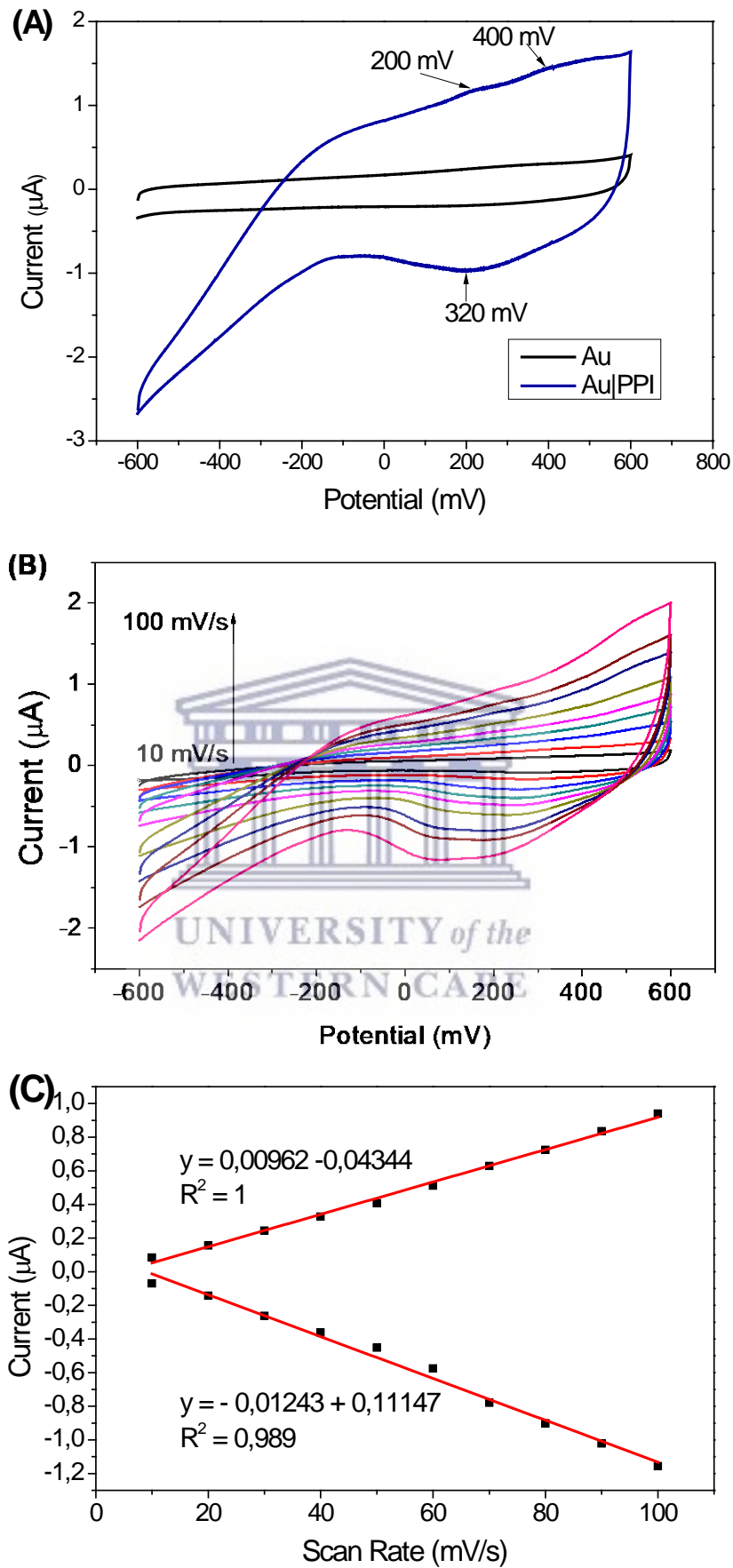
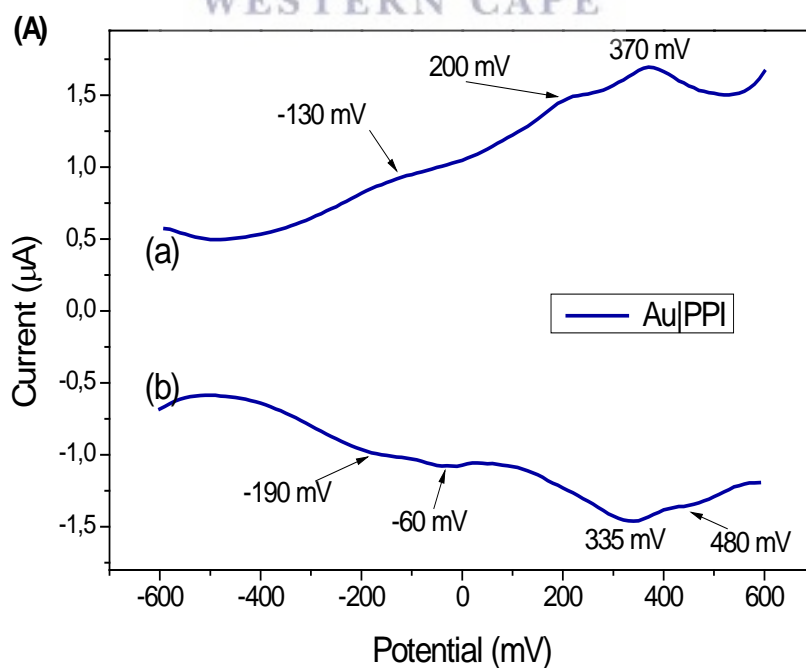


Figure 3-15: (A) Cyclic Voltammogram of Au|PPI (B) CV of Au|PPI run at various scan rates from 10 mV/s to 100 mV/s (C) linear plot of current vs scan rate

The PPI dendrimer was then characterized at various frequencies using SWV in order to determine the diffusion processes occurring at the electrode surface. The resulting voltammograms are as shown in Figure 3-16. It can be seen that at higher frequencies the shoulder peaks present at negative potentials in the anodic and cathodic scan become more prominent. This can be due to fast electron processes or transfers within the dendrimer system. There is a good linear relationship between peak current and frequency in the SWV with a correlation coefficient of 0.90 and 0.89 for the anodic and cathodic peak currents respectively according to Equation 3-5.

$$\Delta i_p = 0.665nFA \frac{D_o^{1/2}}{\pi^{1/2}} f^{1/2} \quad \text{Equation 3-5}$$

In this equation, Δi_p is the differential current obtained via SWV, n is the number of electrons transferred which we assume is 1, F is Faradays constant 96485 C mol^{-1} , $A = 0.0201 \text{ cm}^2$, $C_o^* = 0.1 \text{ M}$ and $f^{1/2}$ is the square root of frequency. According to this equation the diffusion coefficient of the Au|PPI system was determined to be $4.143 \times 10^{-4} \text{ cm}^2 \text{ s}^{-1}$.



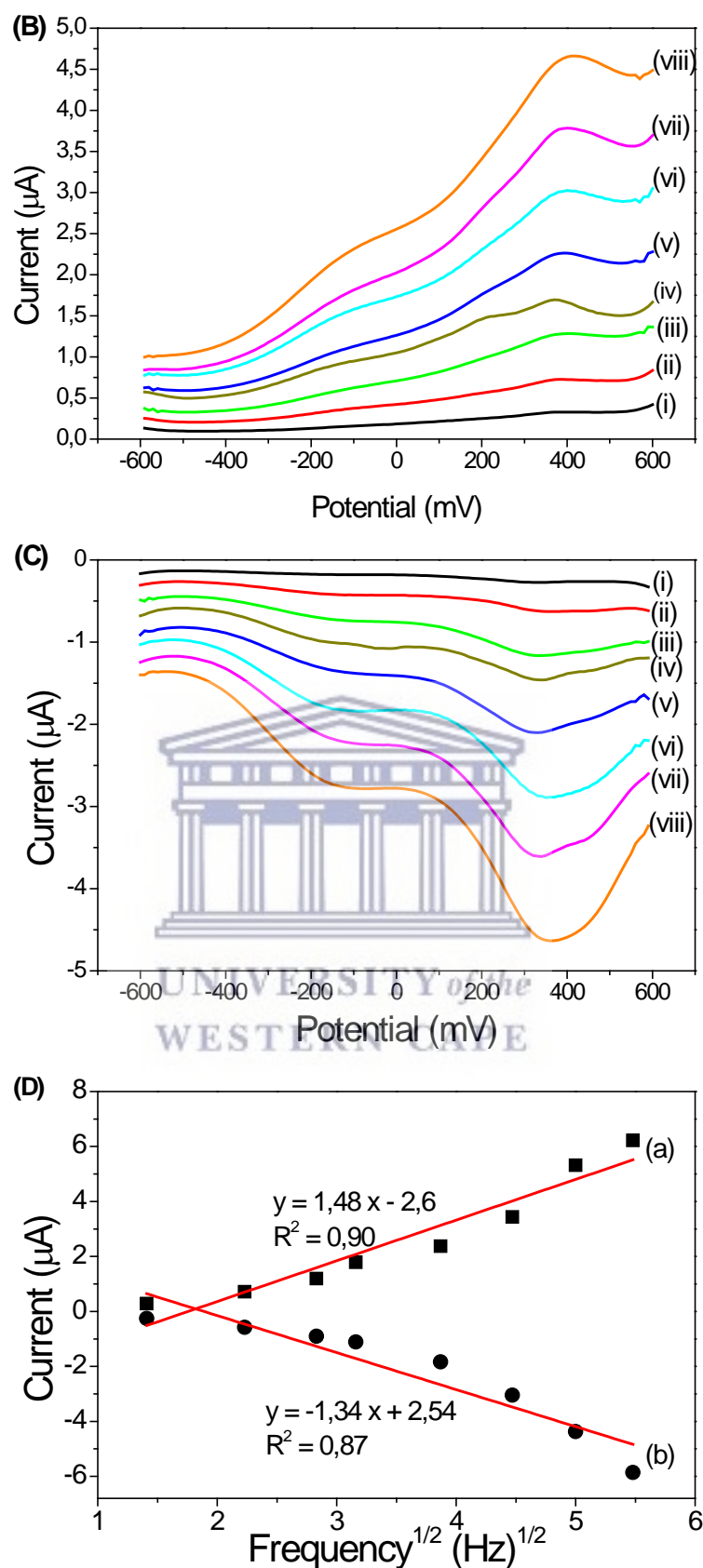


Figure 3-16: (A) Anodic and cathodic scan SWV of Au|PPI at 10 Hz (B) anodic and (C) cathodic scans of Au|PPI at various frequencies (i) 2 (ii) 5 (iii) 8 (iv) 10 (v) 15 (vi) 20 (vii) 25 and (viii) 30 Hz (D) linear plot of current vs square root of frequency for (a) anodic SWV and (b) cathodic SWV of Au|PPI

3.3.2.2 Electrochemical characterization of Au|CuPPI

The electrochemical activity of the copper metallodendrimer was investigated using CV and is as shown below in Figure 3-17. It is clear from the CV that the metallodendrimer is much more electro-active than the dendritic ligand PPI. The peaks caused by faradaic processes at the electrode surface are more pronounced. The oxidation peak was found at $E_{pa} = 220$ mV and the reduction peak at $E_{pc} = 180$ mV. These oxidation and reduction processes were found to be reversible since the peak separation ΔE is less than 60 mV i.e. it is actually 40 mV which is indicative of a fast one electron transfer process according to Equation 3.3. These major reversible peaks are attributed to the oxidation of the copper centre Cu(I) at a negative starting potential to its normal state of Cu(II) during the anodic scan. This oxidation process results in the loss of one electron. The reduction process within the metallodendrimer would then be the addition of one electron to bring the Cu(II) back to its reduced state of Cu(I) at negative potential. The background peaks here attributed to the PPI dendrimer are still visible in the CV, therefore we can be certain that these new peaks are due to oxidation and reduction of the copper centre. These peaks have now shifted, the anodic peak at 370 mV is now at 400 mV and the cathodic peak at 335 mV has shifted to 360 mV. A second cathodic peak previously at -40 mV is now shifted to -100 mV. Once again the charging current for the cathodic sweep is quite large, again indicating that the oxidized form of the dendrimer has a high resistance and thus requires a greater flow of electrons in order to reduce the compound.

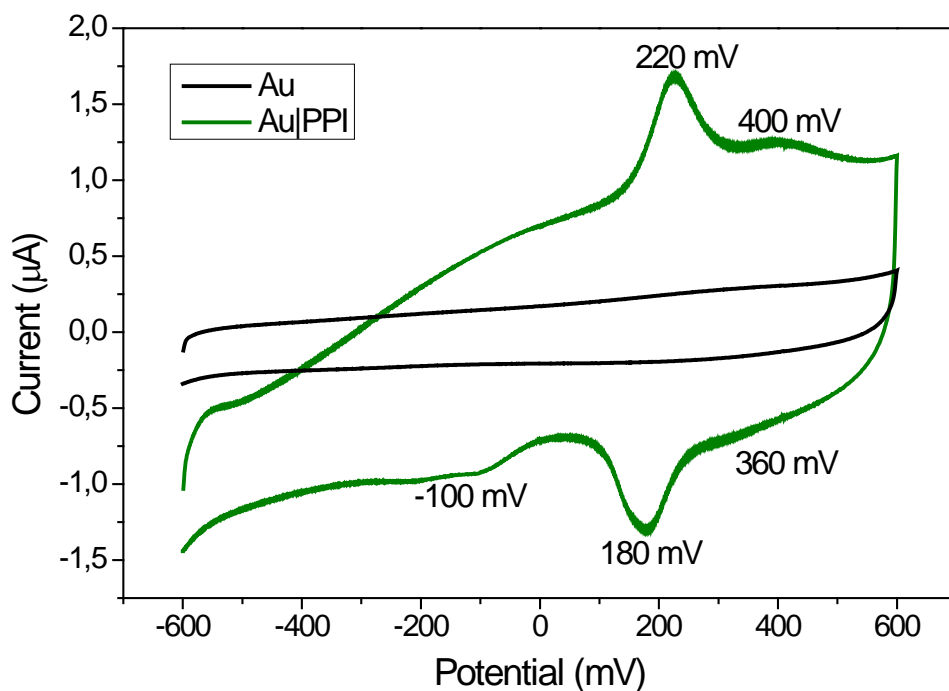


Figure 3-17: Cyclic Voltammogram of CuPPI on gold electrode at 100 mV/s

The Au|CuPPI electrode was also run at various scan rates in CV in order to determine the surface concentration of dendrimer and also to give us more information on the diffusion processes occurring at the electrode surface. The voltammogram and the linear plots is as shown in in Figure 3-18. The Au|CuPPI electrode shows good linear relationship with correlation coefficient of 0.96 between current and scan rate and 0.92 between current and square root of scan rate. The anodic peak will be analysed in order to determine the diffusion coefficient and surface concentration of the Au|CuPPI electrode system. This peak was chosen because it stays at a constant potential regardless of the scan rate. We refer to the plot of current vs scan rate in Figure 3-18 (B). From the calculation we found that the surface concentration of metallodendrimer was $\Gamma_0 = 9.014 \times 10^{-7} \text{ mol.cm}^{-2}$. This is a much larger value than what was obtained when using the PPI dendritic ligand which only yielded a surface concentration of $\Gamma_0 = 5.095 \times 10^{-8} \text{ mol.cm}^{-2}$. This shows that a generous amount of dendrimer was immobilized on the surface and that physical adsorption of dendrimer was successful. The physical adsorption of the metallodendrimer was thus stronger than that of the dendritic ligand.

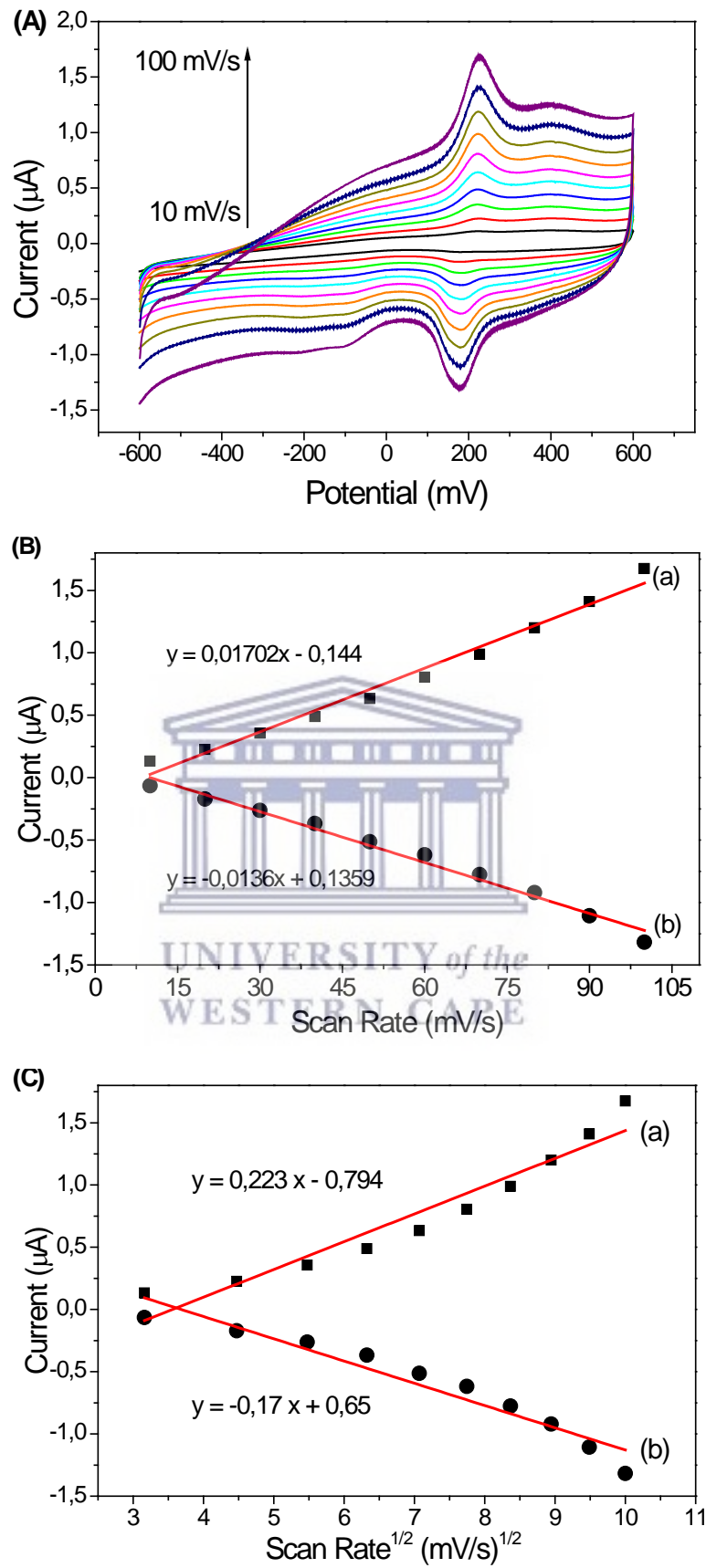


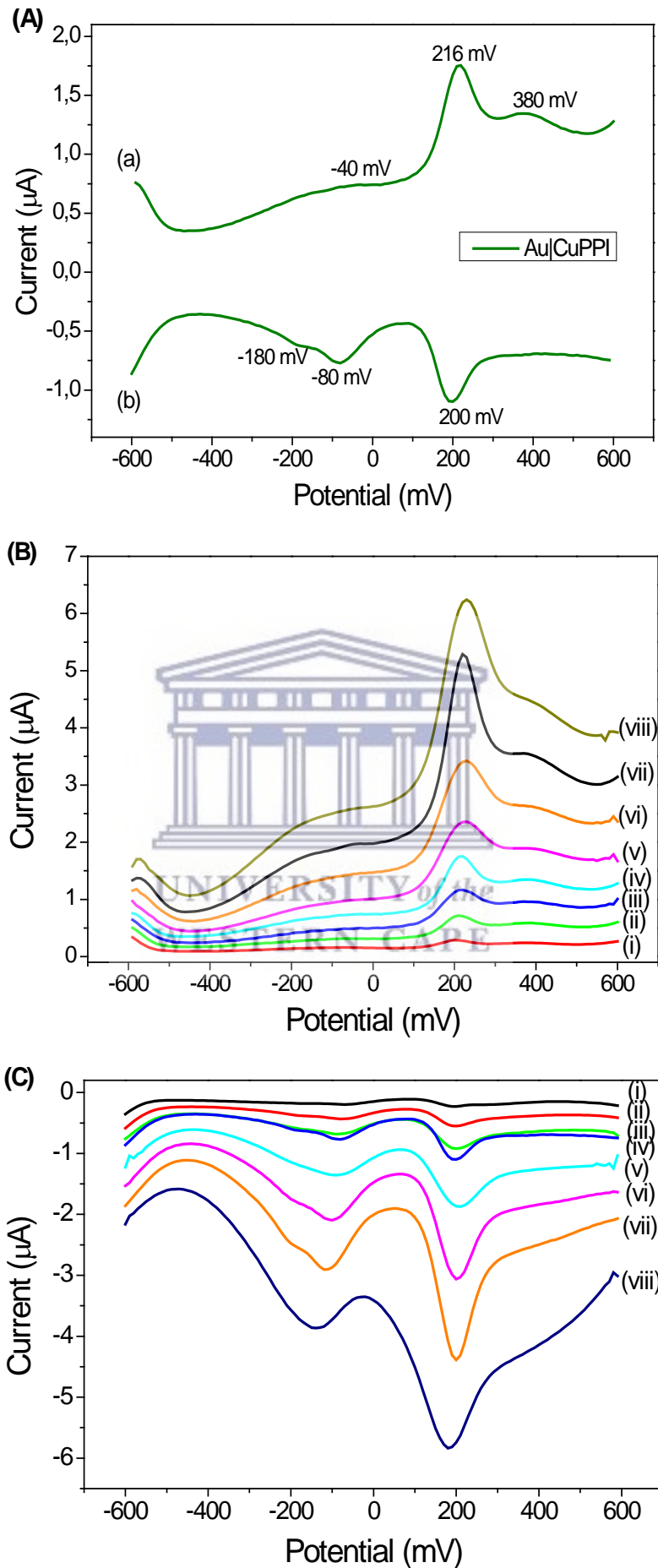
Figure 3-18: (A) CV of Au|CuPPI run at various scan rates from 10 mV/s to 100 mV/s (B) Linear plot of current vs scan rate and (C) current vs square root of scan rate for (a) E_{pa} and (b) E_{pc} of Au|CuPPI

The diffusion coefficient, **D**, was also calculated using the Randles Sevcik Equation 3-6. In this case the current vs square root of scan rate plot was used as in Figure 3-18 (C). In this case $C_0 = 0.1$ M, **n** is 1 and the surface area (**A**) of the electrode is the same. In this case the plot of current vs square root of scan rate as shown in Figure 3-18 (C).

$$I_p = 2.69 \times 10^5 n^{3/2} A D^{1/2} \nu^{1/2} C_0 \quad \text{Equation 3-6 [24]}$$

The diffusion coefficient of this CuPPI metallodendrimer system was calculated to be $D = 4.124 \times 10^{-5} \text{ cm}^2 \cdot \text{s}^{-1}$. This shows a tenfold increase in diffusion coefficient when comparing the PPI dendrimer ($4.143 \times 10^{-4} \text{ cm}^2 \text{ s}^{-1}$) and CuPPI metallodendrimer. This means that the metallodendrimer has a more favourable and faster diffusion process than the dendrimer.

A square wave voltammetry experiment of the CuPPI metallodendrimer on gold electrode was also carried out in order to verify the results obtained in the CV experiment, since it is a more sensitive technique. The SWV experiment as shown in Figure 3-19 (A) produced a major anodic peak with $E_{pa} = 216$ mV with another smaller peak with $E_{pa} = 380$ mV and a shoulder with $E_{pa} = -40$ mV. The cathodic scan of the SWV produced a major peak with $E_{pc} = 200$ mV and a smaller peak at $E_{pc} = -80$ mV with a shoulder present at $E_{pc} = -180$ mV. Again in this case it is clear that a complex cascade oxidation of the oxygen groups are taking place in the metallodendrimer with the major peaks being attributed to the oxidation of Cu(I) to Cu(II) and its subsequent reduction [42]. The Au|CuPPI metallodendrimer electrode was also run at various frequencies as shown in Figure 3-19 (B) and (C). It was found that the peaks in the negative potential region i.e. peaks at -40 mV and -80 mV in the anodic and cathodic scans respectively, were amplified and became more visible at higher frequencies as before with the PPI dendrimer.



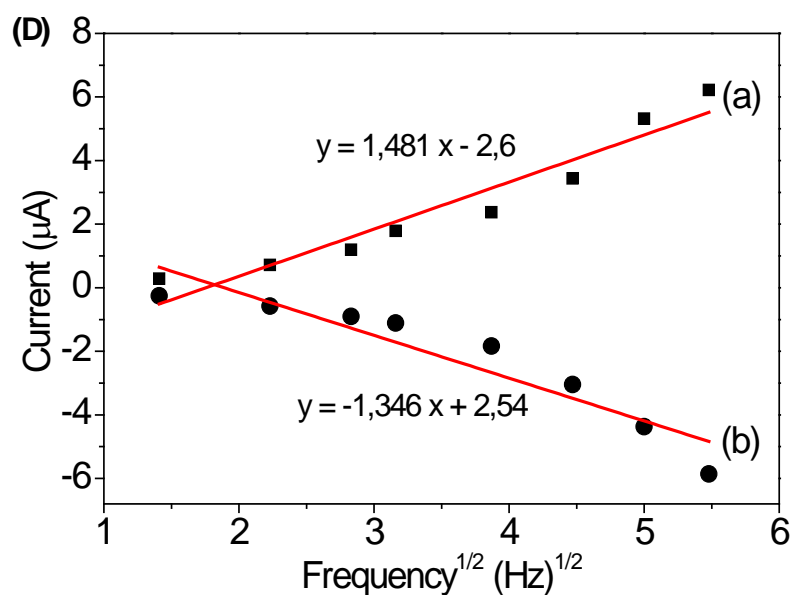


Figure 3-19: (A) Anodic and cathodic scan SWV of Au|CuPPI at 10 Hz (B) anodic and (B) cathodic scans of Au|CuPPI at various scan rates of (i) 2 (ii) 5 (iii) 8 (iv) 10 (v) 15 (vi) 20 (vii) 25 and (viii) 30 Hz (D) Linear plot of current vs square root of frequency for (a) anodic SWV and (b) cathodic SWV of Au|CuPPI

These results show that the CuPPI platform has a good linear relationship between peak current and the frequency at which the scan is carried out according to Equation 3-2. In this case a correlation coefficient of 0.90 and 0.87 were obtained for the anodic and cathodic peaks respectively as illustrated in Figure 3-19 (D).

3.3.2.3 The effect of oxygen on the Au|CuPPI system

In order for a material to be used in electrochemical sensors it is vital to understand how the material is affected by the presence of oxygen. Sensors will not only be used in an inert atmosphere but most sensors will be used in atmospheric conditions. The copper metallodendrimer was therefore electrochemically characterised in the presence of oxygen. The resulting CV of Au|CuPPI in the presence of oxygen is shown in Figure 3-20. When observing the bare Au (gold) electrode one can see a cathodic peak present at $E_{pc} = -400$ mV. We can therefore be sure that this peak is caused by the reduction of oxygen at the gold electrode surface. Once the copper metallodendrimer was adsorbed onto the gold electrode, this cathodic peak

increased considerably. It is clear that the oxygen interacts with the metallodendrimer on the surface of the electrode.

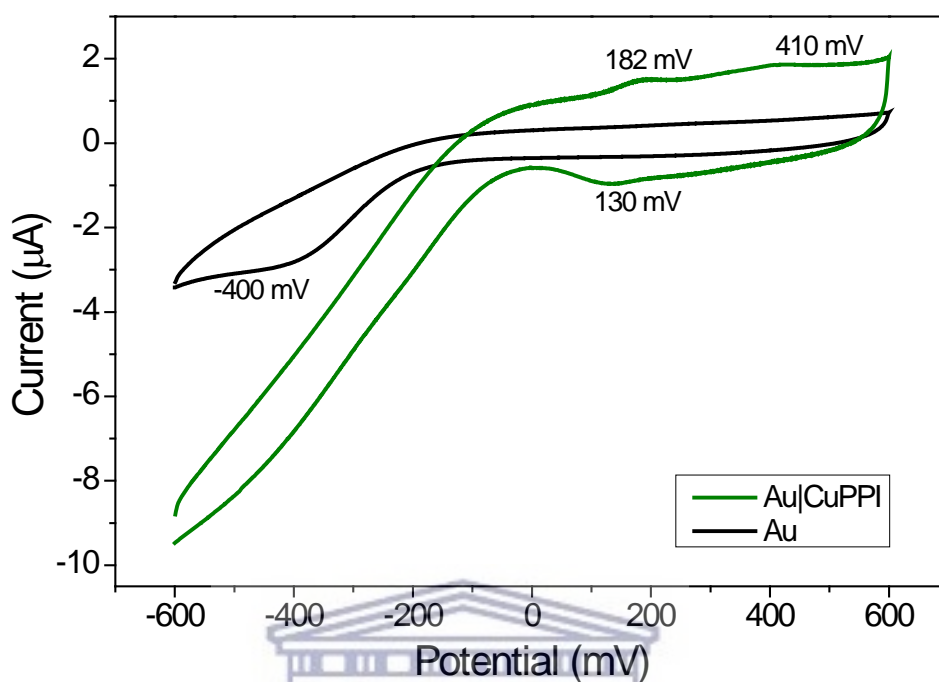


Figure 3-20: Cyclic Voltammogram of CuPPI on gold electrode at 100 mV/s in the presence of oxygen

It can also be noted that the Faradaic peak current of the metallodendrimer decreases noticeably in the presence of oxygen into the system. A comparison of reactions occurring within the system under argon atmosphere as well as in the presence of oxygen results in Figure 3-21.

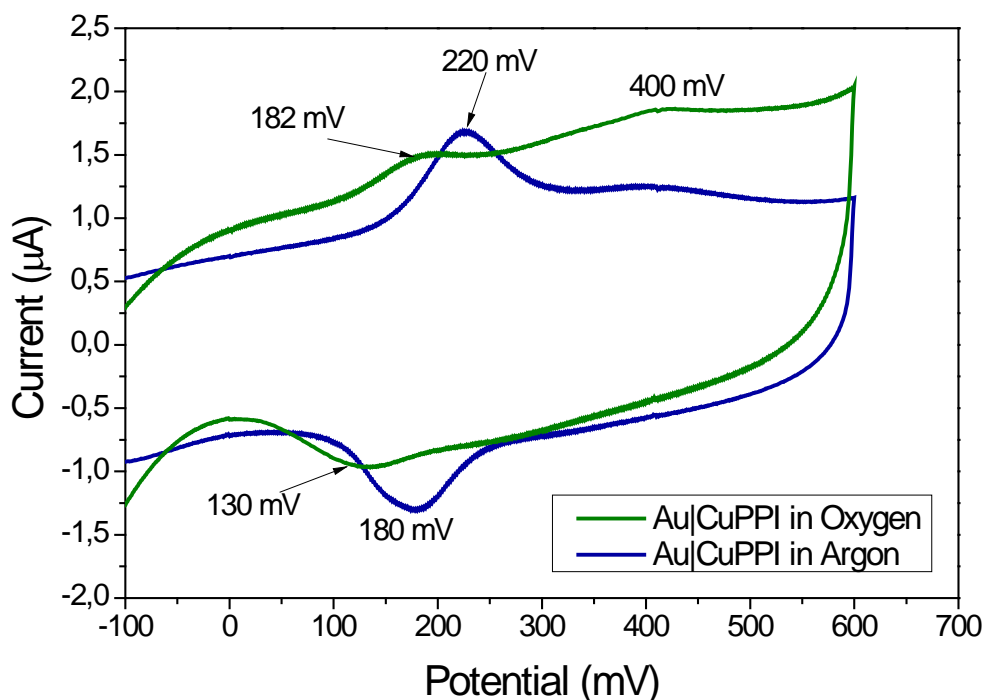


Figure 3-21: Cyclic voltammogram of CuPPI on gold electrode in the presence of oxygen and argon from -100 mV to 600 mV

From this graph, one can see that the presence of oxygen increases the capacitive current of the dendrimer system, since the CV has become slightly broader. It also increases the faradaic current of the anodic peak at 400 mV, which we can assume is the interaction or adsorption of oxygen onto the dendritic framework. The presence of oxygen also causes a shift in peaks attributed to the $\text{Cu(I)} \leftrightarrow \text{Cu(II)}$ transition to lower potentials and currents of $E_{pa} = 182 \text{ mV}$ and $E_{pc} = 130 \text{ mV}$ respectively. The oxygen does have some effect on the metallodendrimer electro-activity and the extent of its effect can be determined by the change in diffusion coefficient. The Au|CuPPI was then run at varying scan rates in the presence of oxygen in order to determine the diffusion coefficient. The CV showing the various scan rates are as shown in Figure 3-22 (A). The linear plot of current vs square root of scan rate is as shown in Figure 3-22 (B).

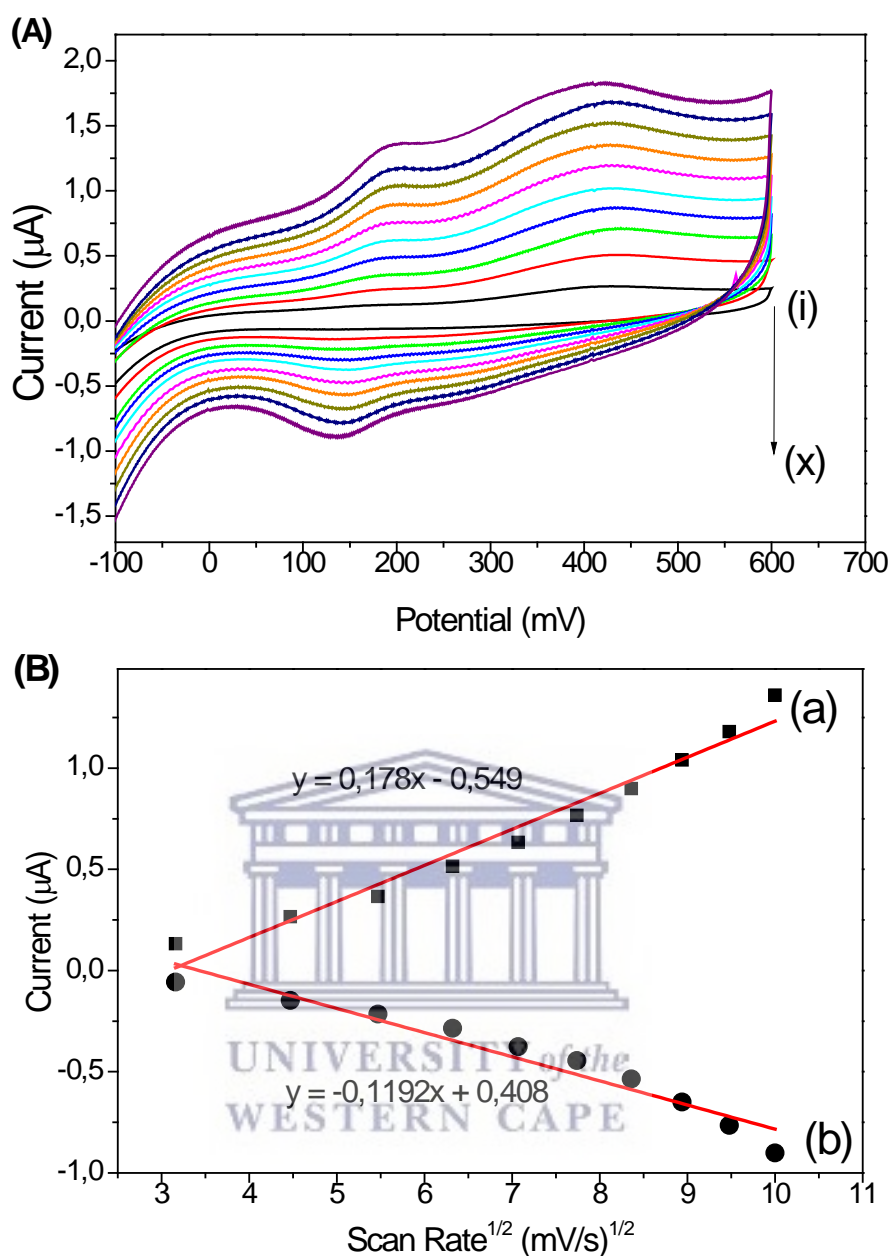


Figure 3-22: (A) Cyclic voltammogram of Au|CuPPI at various scan rates of (i) 10 mV/s to (x) 100 mV/s (B) current vs square root of scan rate for (a) E_{pa} and (b) E_{pc} of Au|CuPPI in the presence of oxygen

The diffusion coefficient D , was calculated using the Randles Sevcik Equation 3-6 and the plot of current vs square root of scan rate in Figure 3-22 (B). The value of the diffusion coefficient decreased slightly to $D = 3.29 \times 10^{-5} \text{ cm}^2 \text{ s}^{-1}$. Since the diffusion coefficient is slightly lower in the presence of oxygen we can confirm that the oxygen has some kind of interfering effect on electronic processes happening in solution and on the surface of the electrode, but this effect is negligible.

Square wave voltammetry was also carried out on Au|CuPPI in aerobic conditions. The voltammogram resulting from the anodic and cathodic scans of SWV are shown below in Figure 3-23.

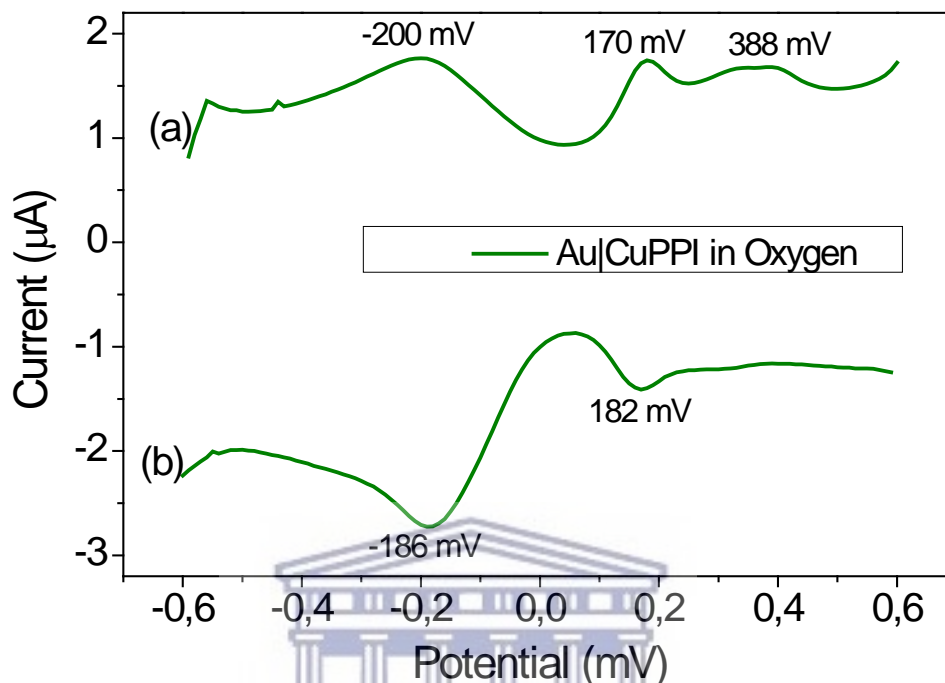


Figure 3-23: Anodic and cathodic scan SWV of Au|CuPPI in the presence of oxygen at 10 Hz

In this SWV we can see the appearance of two new peaks, $E_{pa} = -200$ mV and $E_{pc} = -186$ mV in the presence of oxygen. The peaks attributed to the copper metallodendrimer are still present i.e. $E_{pa} = 170$ mV and $E_{pc} = 182$ mV. The anodic peak at 388 mV is thus attributed to the interaction of oxygen present in the system with the metallodendrimer and the peak at $E_{pc} = -186$ mV is attributed to the reduction of oxygen at the electrode surface. The peaks at $E_{pa} = 170$ mV and $E_{pc} = 182$ mV are therefore confirmed to be characteristic of the oxidation and subsequent reduction of the CuPPI dendrimer. When increasing the frequency within square wave it was found that the peaks originating from the reduction of oxygen increase in intensity as shown in Figure 3-24 (A) and (B). This might be indicative of fast electron processes at the electrode surface. Again the peak current has good correlation with frequency in this case 0.93 and 0.93 for anodic and cathodic peaks respectively according to Equation 3-2.

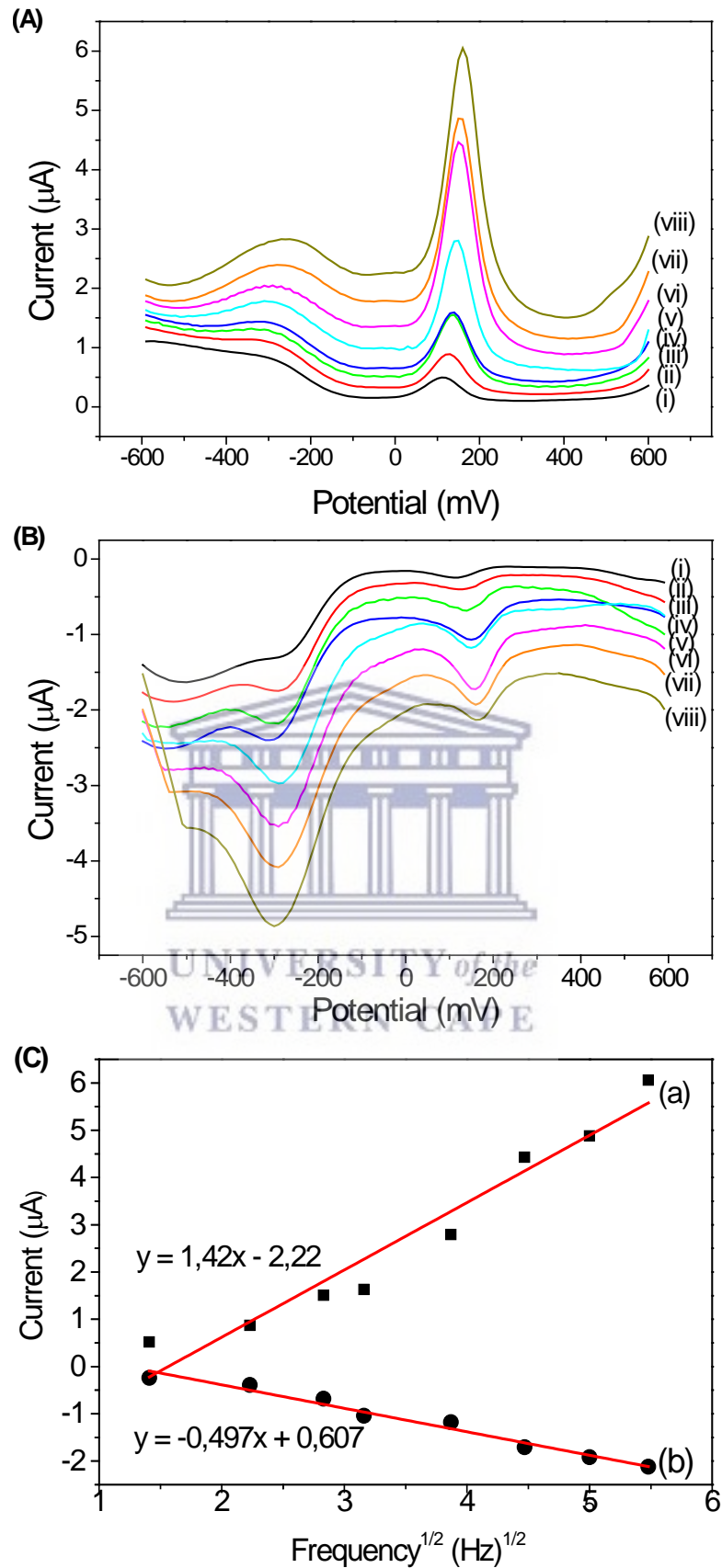


Figure 3-24: (A) Anodic and (B) cathodic scans of Au|CuPPI in the presence of oxygen at various scan rates (i) 2 (ii) 5 (iii) 8 (iv) 10 (v) 15 (vi) 20 (vii) 25 and (viii) 30 Hz (C) Linear plot of current vs square root of frequency for (a) anodic SWV and (b) cathodic SWV of Au|CuPPI in presence of oxygen

A summary of the electrochemical data of the dendrimers are as shown in Table 3-3 below. It shows that the dendritic structure of both of the molecules have a large charging or capacitive current. This means that the PPI branches can store some part of the current flowing through the structure which is why the CV of both molecules are much broader than the gold electrode they are deposited on. The charging current of the PPI dendrimer is larger than the CuPPI metallodendrimer which indicates that this structure is largely capacitive. The faradaic current (FC) of the CuPPI is much larger due to the oxidation and reduction of the copper centre within this molecule. The FC is slightly reduced in the presence of oxygen, due to interference of oxygen in solution.

Table 3-3: Summary of electrochemical characteristics of PPI and CuPPI

Electrode system	Diffusion coefficient	Capacitive current	Faradaic current	ΔE
Au PPI in Ar	$4.143 \times 10^{-4} \text{ cm}^2 \text{ s}^{-1}$	0.795	0.408	80 mV
Au CuPPI in Ar	$4.124 \times 10^{-5} \text{ cm}^2 \text{ s}^{-1}$	0.668	1.01	40 mV
Au CuPPI in O ₂	$3.29 \times 10^{-5} \text{ cm}^2 \text{ s}^{-1}$	0.739	0.807	55 mV

3.4 Conclusion

A dendrimer and copper functionalised dendrimer was synthesised and characterised using various spectroscopic, microscopic and electrochemical techniques. The techniques used to study the structure and morphology of the dendrimers were fourier transform infrared spectroscopy (FTIR), atomic force microscopy (AFM), high resolution transmission electron microscopy (HR-TEM) as well as high resolution scanning electron microscopy (HR-SEM). It was found that the inclusion of a metal centre into a first generation poly(propyleneimine) based dendrimer greatly changed the structure and morphology of the compound. The resultant metallodendrimer was more rough, jagged and also crystalline and ordered. These characteristic make the metallodendrimer a suitable candidate for use in electrochemical sensing as an electrocatalytic platform. First generation copper metallodendrimers have also found application in catalysis as proven by Mugo et al. [35]. Both dendrimers were also characterised using voltammetric techniques and both were found to be electroactive, with the copper metallodendrimer proving to be a more viable candidate for electrocatalytic purposes. This is due to the fast, reversible redox couple present in the molecule between the Cu(I) and Cu(II) electron transition. Another factor which makes this compound electrocatalytically viable is this higher retention of compound on the electrode surface shown by the increase in surface concentration of CuPPI compared to PPI, even though the electrodes were prepared in the same manner. To prove that the metallodendrimer would be a suitable candidate for biosensing application, an aerobic and anaerobic study was then carried out. We found that the presence of oxygen affects the characteristics of the CuPPI metallodendrimer. In this case it only slightly diminishes the current flow in the system since it is clear that the peaks attributed to the CuPPI action decrease in current intensity in both the anodic and cathodic sweeps of the CV. In our experiments the diffusion coefficient also slightly decreases from $4.124 \times 10^{-5} \text{ cm}^2 \text{ s}^{-1}$ in the absence of oxygen to $3.29 \times 10^{-5} \text{ cm}^2 \text{ s}^{-1}$ when oxygen was present. The copper metallodendrimer has proven to have favourable characteristics for application as an electrocatalytic platform for electrochemical biosensors according to these results.

3.5 **References**

- [1] A. Archut and F. Vogtle, "Dendritic molecules—historic development and future applications," in *Handbook of Nanostructured Materials and Nanotechnology*, Elsevier, **2000**, pp. 333–374.
- [2] E. Buhleier, W. Wehner, and F. Vögtle, "'Cascade'- and 'Nonskid-Chain-like' Syntheses of Molecular Cavity Topologies," *Synthesis*, vol. 1978, pp. 155–158, **1978**.
- [3] E. R. R. Gillies and J. M. J. M. J. Fréchet, "Dendrimers and dendritic polymers in drug delivery," *Drug Discovery Today*, vol. 10, pp. 35–43, **2005**.
- [4] E. Abbasi, S. F. Aval, A. Akbarzadeh, M. Milani, H. T. Nasrabadi, W. Joo, Y. Hanifehpour, K. Nejati-Koshki, and R. Pashaei-Asl, "Dendrimers: synthesis, applications, and properties," *Nanoschale Research Letters*, vol. 9, pp. 1–10, **2014**.
- [5] S. Choudhary, L. Gupta, S. Rani, K. Dave, and U. Gupta, "Impact of Dendrimers on Solubility of Hydrophobic Drug Molecules.," *Frontiers in pharmacology*, vol. 8, p. 261, **2017**.
- [6] J. N. . Reek, D. de Groot, G. E. Oosterom, P. C. . Kamer, and P. W. N. . van Leeuwen, "Core and periphery functionalized dendrimers for transition metal catalysis; a covalent and a non-covalent approach," *Reviews in Molecular Biotechnology*, vol. 90, pp. 159–181, **2002**.
- [7] A. S. Chauhan, "Dendrimer nanotechnology for enhanced formulation and controlled delivery of resveratrol," *Annals of the New York Academy of Sciences*, vol. 1348, pp. 134–140, **2015**.
- [8] Y.-G. Gao, X. Lin, K. Dang, S.-F. Jiang, Y. Tian, F.-L. Liu, D.-J. Li, Y. Li, Z.-P. Miao, and A.-R. Qian, "Structure–activity relationship of novel low-generation dendrimers for gene delivery," *Organic & Biomolecular Chemistry*, vol. 16, pp. 7833–7842, **2018**.
- [9] M. Venturi, S. Serroni, A. Juris, S. Campagna, and V. Balzani, "Electrochemical and Photochemical Properties of Metal-Containing Dendrimers," *Dendrimers*, pp. 193–228, **1998**.
- [10] Y. Yan, J. Zhang, L. Ren, and C. Tang, "Metal-containing and related polymers for biomedical applications," *Chemical Society Reviews*, vol. 45, pp. 5232–5263, **2016**.
- [11] B. Thomas, C. Pifferi, G. C. Daskhan, M. Fiore, N. Berthet, and O. Renaudet, "Divergent and convergent synthesis of GalNAc-conjugated dendrimers using dual orthogonal ligations," *Organic & Biomolecular Chemistry*, vol. 13, pp. 11529–11538, **2015**.
- [12] N. Dayyani, A. Ramazani, S. Khoee, and A. Shafiee, "Synthesis and Characterization of the First Generation of Polyamino-Ester Dendrimer-Grafted Magnetite Nanoparticles from 3-

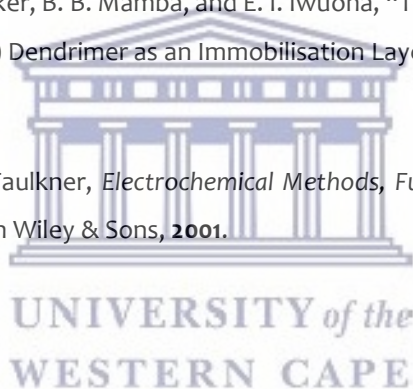
- Aminopropyltriethoxysilane (APTES) via the Convergent Approach,” *Silicon*, vol. 10, pp. 595–601, **2018**.
- [13] István J. Majoros, Andrzej Myc, Thommey Thomas, A. Chandan B. Mehta, and J. James R. Baker, “PAMAM Dendrimer-Based Multifunctional Conjugate for Cancer Therapy: Synthesis, Characterization, and Functionality,” *Biomacromolecules*, vol. 7, pp. 572–579, **2006**.
- [14] A. Szulc, L. Pulaski, D. Appelhans, B. Voit, and B. Klajnert-Maculewicz, “Sugar-modified poly(propylene imine) dendrimers as drug delivery agents for cytarabine to overcome drug resistance,” *International Journal of Pharmaceutics*, vol. 513, pp. 572–583, **2016**.
- [15] P. K. Maiti, T. Ç A In, G. Wang, and W. A. Goddard, “Structure of PAMAM Dendrimers: Generations 1 through 11,” *Macromolecules*, vol. 37, pp. 6236–6254, **2004**.
- [16] R. V. de Araújo, S. da S. Santos, E. Igne Ferreira, and J. Giarolla, “New Advances in General Biomedical Applications of PAMAM Dendrimers.,” *Molecules (Basel, Switzerland)*, vol. 23, **2018**.
- [17] C. a. Nijhuis, B. a. Boukamp, B. J. Ravoo, J. Huskens, and D. N. Reinhoudt, “Electrochemistry of ferrocenyl dendrimer - β -cyclodextrin assemblies at the interface of an aqueous solution and a molecular printboard,” *Journal of Physical Chemistry C*, vol. 111, pp. 9799–9810, **2007**.
- [18] G. R. Newkome, H. J. Kim, K. H. Choi, and C. N. Moorefield, “Synthesis of Neutral Metallodendrimers Possessing Adamantane Termini: Supramolecular Assembly with - Cyclodextrin,” *Macromolecules*, vol. 37, pp. 6268–6274, **2004**.
- [19] R. Malgas-Enus and S. F. Mapolie, “Nickel metallodendrimers as catalyst precursors in the tandem oligomerization of ethylene and Friedel–Crafts alkylation of its olefinic products,” *Inorganica Chimica Acta*, vol. 409, pp. 96–105, **2014**.
- [20] C. S. S. Braun, J. A. A. Vetro, D. A. A. Tomalia, G. S. S. Koe, J. G. G. Koe, and C. R. R. Middaugh, “Structure/Function Relationships of Polyamidoamine/DNA Dendrimers as Gene Delivery Vehicles,” *Journal of Pharmaceutical Sciences*, vol. 94, pp. 423–436, **2005**.
- [21] M. Masikini, S. N. Mailu, A. Tsegaye, N. Njomo, K. M. Molapo, C. O. Ikpo, C. E. Sunday, C. Rassie, L. Wilson, P. G. L. Baker, and E. I. Iwuoha, “A fumonisins immunosensor based on polyanilino-carbon nanotubes doped with palladium telluride quantum dots.,” *Sensors (Basel, Switzerland)*, vol. 15, pp. 529–46, **2015**.
- [22] P. Kesharwani, K. Jain, and N. K. K. Jain, “Dendrimer as nanocarrier for drug delivery,” *Progress in Polymer Science*, vol. 39, pp. 268–307, **2014**.
- [23] E. Wiener, M. W. Brechbiel, H. Brothers, R. L. Magin, O. A. Gansow, D. A. Tomalia, and P. C.

- Lauterbur, "Dendrimer-based metal chelates: A new class of magnetic resonance imaging contrast agents," *Magnetic Resonance in Medicine*, vol. 31, pp. 1–8, **1994**.
- [24] G. Zhang, R. Du, J. Qian, X. Zheng, X. Tian, D. Cai, J. He, Y. Wu, W. Huang, Y. Wang, X. Zhang, K. Zhong, D. Zou, and Z. Wu, "A tailored nanosheet decorated with a metallized dendrimer for angiography and magnetic resonance imaging-guided combined chemotherapy," *Nanoscale*, vol. 10, pp. 488–498, **2018**.
- [25] A. Bosnjakovic, M. K. Mishra, H. J. Han, R. Romero, and R. M. Kannan, "A dendrimer-based immunosensor for improved capture and detection of tumor necrosis factor- α cytokine," *Analytica Chimica Acta*, vol. 720, pp. 118–125, **2012**.
- [26] O. Finikova, A. Galkin, V. Rozhkov, M. Cordero, and Cecilia Hägerhäll, and S. Vinogradov*, "Porphyrin and Tetrabenzoporphyrin Dendrimers: Tunable Membrane-Impermeable Fluorescent pH Nanosensors," *Journal of American Chemical Society*, vol. 125, pp. 4882–4893, **2003**.
- [27] Z. Li and J. Li, "Dendrimer-Supported Catalysts for Organic Synthesis," *Current Organic Chemistry*, vol. 17, pp. 1334–1349, **2013**.
- [28] A. Blanckenberg, G. Kotze, A. J. Swarts, and R. Malgas-Enus, "Effect of nanoparticle metal composition: mono- and bimetallic gold/copper dendrimer stabilized nanoparticles as solvent-free styrene oxidation catalysts," *Journal of Nanoparticle Research*, vol. 20, p. 44, **2018**.
- [29] D. Méry and D. Astruc, "Dendritic catalysis: Major concepts and recent progress," *Coordination Chemistry Reviews*, vol. 250, pp. 1965–1979, **2006**.
- [30] Y. Daskal, R. Dittrich, J. Walter, and Y. Joseph, "Chemiresistor Sensors Based on Gold Nanoparticle Composites," *Procedia Engineering*, vol. 120, pp. 799–802, **2015**.
- [31] N. Krasteva, B. Guse, I. Besnard, A. Yasuda, and T. Vossmeier, "Gold nanoparticle/PPI-dendrimer based chemiresistors - Vapor-sensing properties as a function of the dendrimer size," *Sensors and Actuators, B: Chemical*, vol. 92, pp. 137–143, **2003**.
- [32] I. Grabchev, S. Dumas, and J.-M. Chovelon, "A polyamidoamine dendrimer as a selective colorimetric and ratiometric fluorescent sensor for Li⁺ cations in alkali media," *Dyes and Pigments*, vol. 82, pp. 336–340, **2009**.
- [33] J. Martinovic, J. van Wyk, S. Mapolie, N. Jahed, P. Baker, and E. Iwuoha, "Electrochemical and spectroscopic properties of dendritic cobalto-salicylaldimine DNA biosensor," *Electrochimica Acta*, vol. 55, pp. 4296–4302, **2010**.

- [34] J. Martinovic, A.-M. Chiorcea-Paquim, V. C. Diculescu, J. Van Wyk, E. Iwuoha, P. Baker, S. Mapolie, and A.-M. Oliveira-Brett, "Metallo-functionalized first-generation salicylaldimine poly(propylenimine) tetraamine dendrimers: Electrochemical study and atomic force microscopy imaging," *Electrochimica Acta*, vol. 53, pp. 4907–4919, **2008**.
- [35] J. N. Mugo, S. F. Mapolie, and J. L. Van Wyk, "Cu(II) and Ni(II) complexes based on monofunctional and dendrimeric pyrrole-imine ligands: Applications in catalytic liquid phase hydroxylation of phenol," *Inorganica Chimica Acta*, vol. 363, pp. 2643–2651, **2010**.
- [36] J. L. Van Wyk, S. F. Mapolie, A. Lennartson, M. Håkansson, and S. Jagner, "The catalytic oxidation of phenol in aqueous media using cobalt(II) complexes derived from N-(aryl) salicylaldimines," *Inorganica Chimica Acta*, vol. 361, pp. 2094–2100, **2008**.
- [37] E. Tas, M. Aslanoglu, M. Ulusoy, and H. Temel, "Synthesis, spectral characterization and electrochemical studies of copper(II) and cobalt(II) complexes with novel tetradentate salicylaldimines," *Journal of Coordination Chemistry*, vol. 57, pp. 677–684, **2004**.
- [38] M. Č. Vinod Vellora, Thekkae Padil, "Green synthesis of copper oxide nanoparticles using gum karaya as a biotemplate and their antibacterial application.," *International journal of nanomedicine*, vol. 8, pp. 889–98, **2013**.
- [39] M. S. Gruzdev, A. I. Alexandrov, T. V. Pashkova, and U. V. Chervonova, "Synthesis and phase behaviour of poly(propylene imine) dendromesogens of lowest generations," *Liquid Crystals*, pp. 1–15, **2018**.
- [40] S. F. Mapolie and J. L. Van Wyk, "Synthesis and characterization of dendritic salicylaldimine complexes of copper and cobalt and their use as catalyst precursors in the aerobic hydroxylation of phenol," *Inorganica Chimica Acta*, vol. 394, pp. 649–655, **2013**.
- [41] F. Zeng and S. C. Zimmerman, "Dendrimers in Supramolecular Chemistry: From Molecular Recognition to Self-Assembly," *Chemical reviews*, vol. 97, pp. 1961–1712, **1997**.
- [42] C. Rassie, J. Van Wyk, L. Wilson, H. R. Makelane, U. Feleni, U. Sidwaba, S. Mapolie, P. Baker, and E. Iwuoha, "Microscopy and Electroanalysis of a First Generation Copper- poly (propyleneimine) Metallodendrimer System," *International Journal of Electrochemical Science*, vol. 10, pp. 432–444, **2015**.
- [43] R. Selwin Joseyphus and M. Sivasankaran Nair, "Synthesis, characterization and biological studies of some Co(II), Ni(II) and Cu(II) complexes derived from indole-3-carboxaldehyde and glycyglycine as Schiff base ligand," *Arabian Journal of Chemistry*, vol. 3, pp. 195–204, **2010**.
- [44] N. Zare and A. Zabardasti, "A new nano-sized mononuclear Cu (II) complex with N,N-donor

- Schiff base ligands: sonochemical synthesis, characterization, molecular modeling and biological activity,” *Applied Organometallic Chemistry*, vol. 33, p. e4687, **2019**.
- [45] L. Thomas, A. V. Ruban, H. L. Skriver, J. Kollár, B. S. Clausen, H. Topsøe, and P. L. Hansen, “Atom-Resolved Imaging of Dynamic Shape Changes in Supported Copper Nanocrystals,” *SCIENCE*, vol. 295, pp. 2053–2055, **2002**.
- [46] S. Achar, J. J. Vittal, and R. J. Puddephatt, “Organoplatinum Dendrimers,” *Organometallics*, vol. 15, pp. 43–50, **1996**.
- [47] N. Ntshongontshi et al., “Cytochrome P450-3A4/Copper-Poly(Propylene Imine)-Polypyrrole Star Co-Polymer Nanobiosensor System for Delavirdine - A Non-Nucleoside Reverse Transcriptase Inhibitor HIV Drug,” *Journal of Nano Research*, vol. 44, pp. 265–280, **2016**.
- [48] C. Rassie, J. Van Wyk, L. Wilson, N. Ntshongontshi, A. Jonnas, U. Feleni, R. F. R. F. Ajayi, P. Baker, and E. Iwuoha, “Electrochemical Ultra-Low Detection of Isoniazid Using a Salicylaldamine Functionalised G1-DAB-(NH₂)₄ Dendritic Sensor vs. UV-VIS Spectrophotometric Detection,” *Journal of Nano Research*, vol. 45, pp. 164–174, **2017**.
- [49] A. S. Alturiqi, A. N. M. A. Alaghaz, R. A. Ammar, and M. E. Zayed, “Synthesis, Spectral Characterization, and Thermal and Cytotoxicity Studies of Cr(III), Ru(III), Mn(II), Co(II), Ni(II), Cu(II), and Zn(II) Complexes of Schiff Base Derived from 5-Hydroxymethylfuran-2-carbaldehyde,” *Journal of Chemistry*, vol. 2018, pp. 1–18, **2018**.
- [50] A. M. Caminade, C. O. Turrin, R. Laurent, A. Ouali, and B. Delavaux-Nicot, *Dendrimers: Towards Catalytic, Material and Biomedical Uses*. Wiley, **2011**.
- [51] B. J. Bauer and E. J. Amis, “Characterization of dendritically branched polymers by small Angle Neutron Scattering (SANS), Small Angle X-Ray Scattering (SAXS) and Transmission Electron Microscopy (TEM),” in *Dendrimers and Other Dendritic Polymers*, UK: John Wiley & Sons, Ltd, **2002**, pp. 255–284.
- [52] H. Liu and P. H. Zwart, “Determining pair distance distribution function from SAXS data using parametric functionals,” *Journal of Structural Biology*, vol. 180, pp. 226–234, **2012**.
- [53] H. Schnablegger and Y. Singh, *The SAXS Guide, getting acquainted with the principles*, 3rd editio. **2013**.
- [54] B. R. Pauw, C. Kästner, and A. F. Thünemann, “Nanoparticle size distribution quantification: results of a small-angle X-ray scattering inter-laboratory comparison,” *Journal of Applied Crystallography*, vol. 50, pp. 1280–1288, **2017**.

- [55] K. Chokprasombat, K. Koyvanich, C. Sirisathitkul, P. Harding, and S. Rugmai, "Investigation of Surfactant Effect on Size Distribution of FePt-based Nanoparticles by Synchrotron SAXS and TEM," *Transactions of the Indian Institute of Metals*, vol. 69, pp. 733–740, **2016**.
- [56] E. M. M. De Brabander, J. Brackman, M. Mure-Mak, H. De Man, M. Hogeweg, J. Keulen, R. Scherrenberg, B. Coussens, Y. Mengerink, and S. J. van Der Wal, "Polypropylenimine dendrimers: Improved synthesis and characterization," *Macromolecular Symposia*, vol. 102, pp. 9–17, **1996**.
- [57] F. Ciepiela and M. Jakubowska, "Faradaic and capacitive current estimation by means of Independent Components Analysis and 1 kHz sampling," *Talanta*, vol. 170, pp. 158–164, **2017**.
- [58] K. V. Mokwebo, O. S. Oluwafemi, and O. A. Arotiba, "An electrochemical cholesterol biosensor based on a CdTe/CdSe/znse quantum dots—poly (Propylene imine) dendrimer nanocomposite immobilisation layer," *Sensors*, vol. 18, pp. 1–16, **2018**.
- [59] O. A. Arotiba, P. G. Baker, B. B. Mamba, and E. I. Iwuoha, "The Application of Electrodeposited Poly(Propylene imine) Dendrimer as an Immobilisation Layer in a Simple Electrochemical DNA Biosensor," **2011**.
- [60] A. J. Bard and L. R. Faulkner, *Electrochemical Methods, Fundamentals and Applications*, 2nd Editio. New York: John Wiley & Sons, **2001**.

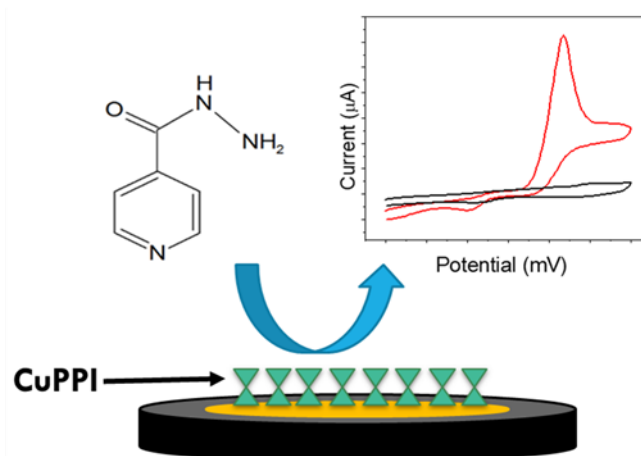


Chapter 4

4 Chemical Sensor for anti-TB drugs

Abstract

Electrochemical sensors have become one of the major trends in recent years. They have many favourable characteristics as an analytical tool since they provide higher sensitivity, selectivity and high response time. Sensors usually include a smart material to further enhance these favourable characteristics, which in this case is a first generation copper metallodendrimer. This simple chemical sensor developed in this study was applied towards the detection of four first line anti-TB drugs i.e. isoniazid, ethambutol, rifampicin and pyrazinamide. The quantification of these drugs is important in determining the metabolic profile of a patient. This allows for the adjustment of patient medication according to phenotype thus avoiding the onset of adverse drug reactions. A scheme representing the application of the sensor towards detection of isoniazid is shown in the graphical abstract in Scheme 4-1.



Scheme 4-1: Graphical abstract for chapter 4

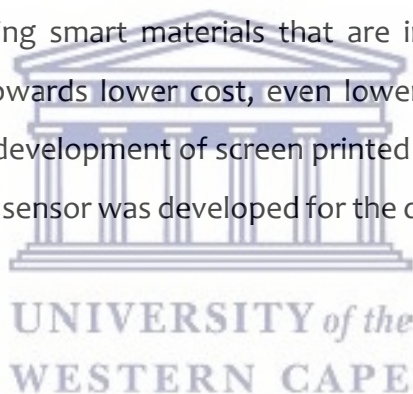
This electrochemical sensor was compared to a well-established technique such as UV-Vis with respect to limit of detection and quantification. The UV-Vis technique was compared to the electrochemical sensor using standard samples of the anti-TB drugs in pH 7 phosphate buffer. Ethambutol however does not absorb light in the UV-vis range and could thus not be detected using UV-Vis without pre-treatment. The electrochemical sensor showed a more favourable limit of detection of 0.788 nM compared to 30.1 nM using UV-vis detection of isoniazid in phosphate buffer, with similar results found for pyrazinamide and rifampicin. The LOD ranged from 0.022 nM to 1.16 nM for the dendritic sensor in 0.1 M PB for the four anti-TB drugs. The dendritic electrochemical sensor was then applied to “real samples” by spiking diluted synthetic urine and human plasma with the anti-TB drugs. The detection of standard referencing material in the complex matrix was carried out and used to form a calibration curve. The real tablet forms were then detected from two complex matrices. The LOD of the dendritic sensor ranged from 0.153 μ M to 45.52 μ M in 20 % synthetic urine and 3.33 μ M in 10 % human plasma. Recovery studies of the four drugs in real samples yielded results ranging from 89.27 to 108.89 % in either of the two matrices. The electrochemical sensor proves to be highly successful in determining accurate and ultra-low concentrations of all four anti-TB drugs in standard samples. However the matrix effects of the “real samples” increases the limit of detection substantially. The sensor was successful in obtaining excellent results for recovery and provides a viable option for the detection of anti-TB drugs in real samples such as urine and plasma.

4.1 **Introduction**

Analytical determination of chemicals are usually carried out using laboratory based equipment which are bulky, complex systems which require trained personnel to operate them. They also involve pre-treatment steps and use large volumes of solvents and other consumables. A method in which these steps could be circumvented would be to make use of electrochemical sensors.

4.1.1 Electrochemical Sensors

These analytical systems have the advantage of being portable and cheap which overcomes the obstacles associated with traditional equipment with the same capabilities [1]. Electrochemical sensors have been used for various applications, such as the detection of gases [2], biological fluids [3], polyaromatic hydrocarbons [4] and even metals [5]. Sensors in these cases consist of a transducer and receptor or chemical recognition system. Chemical reactions, such as oxidation or reduction, occur at the receptor or chemical recognition system. The transducer converts that chemical signal to an electronic readout, which can be interrogated to determine what happens within the electrochemical cell. The reaction typically occurs in a three electrode cell consisting of working, counter and reference electrodes. This systems allows for miniaturisation since electrode surfaces are well into the micrometre range, while incorporating smart materials that are in the nanometre range [6]. There is a movement towards lower cost, even lower sample volume and better reproducibility with the development of screen printed electrodes as well [7]. In this work an electrochemical sensor was developed for the determination of first line anti tuberculosis drugs.



4.1.2 Anti-TB drugs

Tuberculosis is usually treated during a six-month course consisting of a closely monitored and generalised regime of anti-tuberculosis medication. Although TB treatment is effective when used properly, the disease is still a global epidemic. Therefore, the treatment of tuberculosis needs to be more efficient as well as effective in treating the disease. The first line of defence against TB consists of isoniazid, ethambutol, rifampicin and pyrazinamide [8].

4.1.2.1 Isoniazid

Isonicotinic acid hydrazide (isoniazid) (INH) is a front line drug used to treat tuberculosis (TB) in patients who have not received treatment for TB previously and is one of the most effective drugs used to treat the disease. The chemical structure of isoniazid is as shown in Figure 4-1.

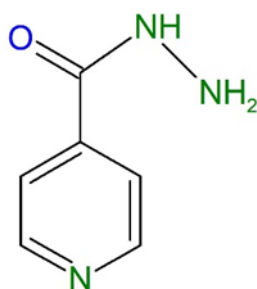


Figure 4-1: Chemical structure of Isoniazid

Isoniazid (INH) fights the growth of the mycobacterium tubercle [9] by inhibiting cell wall lipid synthesis i.e. mycolic acid synthesis as well as nucleic acid synthesis [10]. The oxidation of INH in the presence of NADH (nicotinamide adenine dinucleotide) and *InhA* (a long chain enoyl-acyl carrier protein) leads to covalent INH-NADH adducts that are powerful inhibitors of *InhA*, which is responsible for the synthesis of bacterial cell wall lipids [11]. The drugs used for TB treatment, including isoniazid have adverse side effects or drugs reactions (ADR's). The ADR's caused by isoniazid include hepatotoxicity, dizziness, abdominal pain and many others [12].

4.1.2.2 Ethambutol

Ethambutol (ETH) was discovered in 1961 by screening from a group of random synthetic compounds and was found to protect mice from a *Mycobacterium Tuberculosis* infection. ETH is a simple molecule with a diamine base that is synthesised via reaction of 1,2-dihaloethane with chirally pure (*S*)-2-amino 1-butanol. The chemical structure of ETH is as shown below in Figure 4-2 [13].

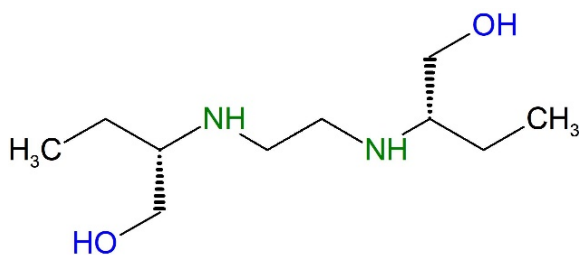


Figure 4-2: Chemical structure of ethambutol

ETH was found to have similar activity to isoniazid and was superior to streptomycin in its anti-bacterial activity. It was also found to be active towards MTB strains which were resistant to isoniazid and streptomycin in 1961 [14]. To this day ethambutol is considered one of the first line defences against TB. Ethambutol fights the MTB tubercle by inhibiting arabinosyl transferases responsible for arabinogalactan (AG) biosynthesis, a key component in cell wall synthesis [15]. The core of the cell wall is made up of a covalently linked complex of mycolic acids, the heteropolysaccharide arabinogalactan and peptidoglycan. Therefore disruption of the synthesis of any of these core components, especially AG would destroy the assembly of the cell wall [16]. The chirality of this molecule plays a huge role in its activity, the (S, S) isomer was found to be approximately 500 times more potent than the (R, R) isomer, which in fact causes blindness [17]. A few ETH analogues have also been developed with variation in the side chain groups, but none have yet been proven to enhance the activity of the molecule against TB [18]. Ethambutol is effective, but like most drugs they do have side effects or adverse drug reaction (ADR's) which include peripheral neuropathy (damage to peripheral nerves causing numbness, weakness and pain) [19], arthralgia (joint pain) [20] and hyperuricaemia (abnormally high level of uric acid in the blood) [21]. Ethambutol has also been linked to significant vision loss caused by toxic optic neuropathy [22].

4.1.2.3 Pyrazinamide

Pyrazine-2-carboxamide (pyrazinamide/PYR) has a poorly understood mechanism of action but has been shown to be active in the disruption of the bacterial membrane

[23]. Pyrazinoic acid (POA), which is the active moiety of PYR has been shown to inhibit various functions at an acidic pH in the MTB tubercle. The accumulation of POA lowers the intracellular pH to a suboptimal level that may inactivate many pathways including fatty acid synthase and membrane transport function [24]. The chemical structure of pyrazinamide is shown below in Figure 4-3.

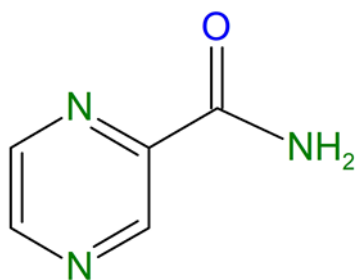


Figure 4-3: Chemical structure of Pyrazinamide

PYR has been named as one of the most fundamental elements in the treatment of tuberculosis due to its sterilizing ability. It is therefore responsible for the reduction in TB treatment time from 9 months to 6 months [25]. There are however adverse drug reactions (ADR's) associated with taking pyrazinamide. These include hepatotoxicity (liver) [26], exanthema (maculopapular rash) [27][28] and sideroblastic anemia [26]. Pyrazinamide has been proven to show more severe side effects than isoniazid and rifampicin [29].

4.1.2.4 Rifampicin

A fourth drug which also constitutes as part of the first line group is rifampicin (RIF) and is commercially known as rifampin or rifadin. This drug was discovered in 1965 and has been used since then to treat TB as well as other bacterial infections. Its mode of action is related to the inhibition of the β subunit of the bacterial RNA polymerase, thereby inhibiting gene transcription [30]. The chemical structure of rifampicin is as shown in Figure 4-4. This drug belongs to a class of macrocyclic antibiotics consisting of a naphthohydroquinone ring spanned by a aliphatic bridge which is highly substituted [31].

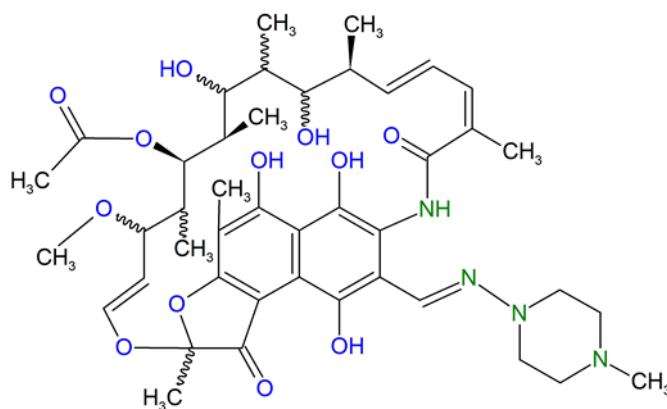


Figure 4-4: Chemical structure of rifampicin

The ADR's associated with rifampicin include dermatological issues, hypersensitivity, gastrointestinal disturbances and hepatitis. The most common side effect is a flu-like syndrome associated with RIF [32]. The huge number of ADR's associated with TB treatment is one of the main reasons TB patients fail to complete their six month treatment and in most there is an added burden of a low quality of life. Increased drug-drug interactions are also another complication to take into account. The monitoring of the levels of anti-TB drugs in patients would thus greatly help in combating TB and also hinder the development of drug resistant TB.

Analysis of drugs is not only valuable during production but also finds use in clinical trials, drug abuse and even therapeutic drug monitoring which is what our application entails. If one were to develop an electrochemical sensor for the detection of anti-TB drugs the advantages would include mobility, sensitivity, accuracy as well as minimising the sample size and time of analysis.

Electrochemical sensing or detection of TB drugs have been carried out previously with the incorporation of special materials. These materials enhance the sensitivity and selectivity of electrochemical sensors. Examples include graphene, carbon nanotubes [33], conducting polymers [34] as well as nano-materials such as nanoparticles [35]. Dendrimers such as the ones discussed in chapter 3 have also been used as platforms for electrochemical sensors. These synthetic branched structures consist of repeatedly branched components and are a type of conducting polymer [36]. The spherical, open and symmetric characteristic allows for fast

transfer of electrons which give the molecule its electro-catalytic abilities [4]. Dendrimers have been widely used as drug carriers in the past [37],[38] but their application to sensing has been limited in literature. This chapter discusses an electrochemical sensor, which was developed in order to determine ultra-low amounts of anti-TB drugs using the copper functionalised metallodendrimer in buffer as well as real samples of synthetic urine and human plasma. The electrochemical method was also compared to a spectroscopic method of detection via ultraviolet-visible spectroscopy detection.

4.2 **Experimental**

4.2.1 **Materials**

Sodium dihydrogen phosphate (NaH_2PO_4), disodium hydrogen phosphate (Na_2HPO_4), sodium chloride (NaCl), ethanol and acetone were purchased from Sigma Aldrich, South Africa and used as received. All electrochemical experiments were carried out using a 0.1 M phosphate buffer (PB) solution with pH of 7.4 as the electrolyte. Isoniazid, ethambutol, pyrazinamide and rifampicin were purchased from Sigma Aldrich and prepared by dissolving in 0.1 M PB pH 7.4. Ultra-pure water purified by a Milli-QTM system (Millipore) was used in all aqueous solutions and throughout the experiments. Synthetic urine was purchased from Sigma Aldrich containing calcium chloride, magnesium chloride, potassium chloride, sodium chloride, sodium phosphate, sodium sulfate, urea, and creatinine with sodium azide as a preservative. Human plasma was also purchased from Sigma Aldrich. The metallodendrimer used as the electrocatalytic platform was prepared as described in chapter 3.

4.2.2 **Instrumentation**

For the electrochemical analysis a three electrode setup was used consisting of a platinum wire as counter electrode, Ag/AgCl (saturated KCl) reference electrode and gold or glassy carbon as working electrodes (all purchased from BASi). A PalmSense potentiostat (Palm Instruments BV, Netherlands) was used for all electrochemical

measurements. UV-Vis was carried out on a Nicolett evolution 100 (Thermo Electron Corporation).

4.2.3 Preparation of electrodes

The gold (Au) and glassy carbon (GCE) working electrodes have a working surface area of 1.6 and 3.0 mm² respectively. The working electrodes were cleaned before each experiment by polishing to a mirror like surface on polishing pads with alumina powder slurry of 1, 0.3 and 0.05 micron respectively. This process was followed by sonication of the electrode in ethanol and water for 5 and 10 min respectively. Electrochemical cleaning of the electrode was also carried out by cycling in a 1 M solution of sulfuric acid. Ten cycles were carried out between the potentials of -200 mV and 1500 mV or until a reproducible voltammogram was obtained. Bare GCE and Au electrodes were used to characterise the electrochemical signatures of the anti-TB drugs. For modified electrodes, a 5 mM solution of CuPPI metallodendrimer was prepared using 1:1 (v/v) acetone-ethanol. A volume of 5 μ L of the dendrimer solution was then drop-coated onto the surface of the clean gold electrode and left to dry for 45 min to allow for physical adsorption to take place. The surface of the electrode was then rinsed lightly with ethanol to remove any unbound dendrimer and then dried under a stream of nitrogen gas. The resulting electrode was then called Au|CuPPI, which was activated by cycling from -2 V to 2 V before use. The modified electrode, Au|CuPPI was then used to detect various concentrations of all four anti-TB drugs in either phosphate buffer, synthetic urine (20% v/v) or plasma (10% v/v).

4.2.4 Electrochemical protocol

All measurements were carried out with 0.1 M phosphate buffer pH 7.4 as electrolyte. The cyclic voltammetry sweeps on glassy carbon electrode and gold electrodes were carried out at various potential windows, depending on the analyte. The CV had an equilibration time of 5 s and E step of 10 mV. DPV was carried out with a E step of 20

mV, an E pulse of 50 mV and t pulse of 0.02 s at a scan rate of 100 mV/s. DPV was the preferred method for detection of analytes since it has an enhanced discrimination of Faradaic currents [39]. This allows for a clearer distinction between analytes whose electrochemical signatures have an E_{pa} or E_{pc} that are close to one another.

4.2.5 UV-Vis spectroscopic protocol

As a comparative study, the electrochemical detection of the anti-TB drugs were referenced to a spectroscopic method of detection via ultraviolet-visible spectroscopy (UV-Vis). The drugs were diluted in 0.1M phosphate buffer pH 7.4. Concentrations of 20, 40, 60, 80 and 100 μ M were detected/measured using UV-Vis detection between 190 and 700 nm.



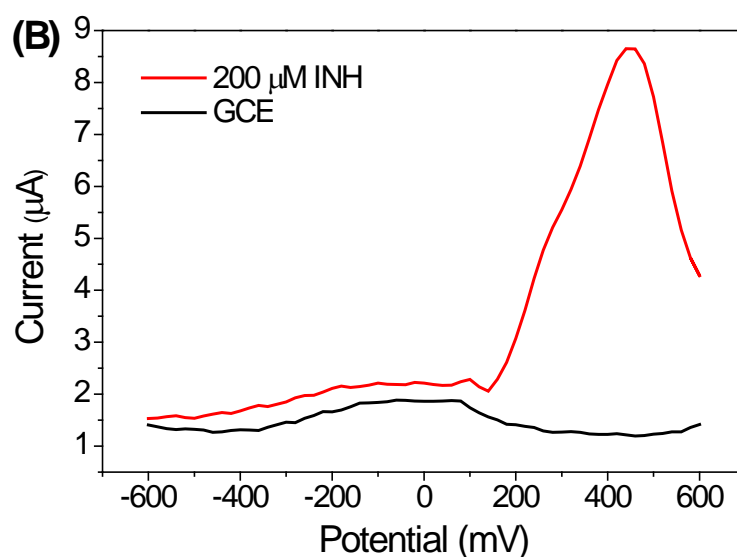
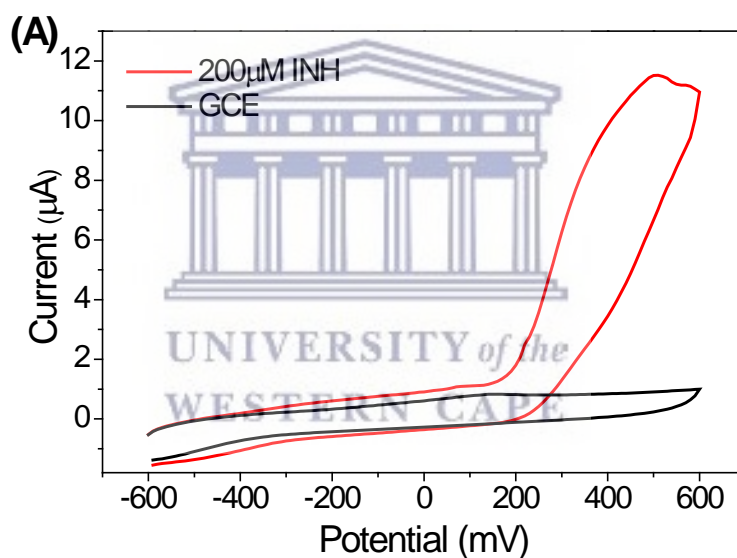
4.3 Results and Discussion

4.3.1 Electrochemical signatures of anti-TB drugs on bare electrodes

In order to assign the electrochemical signatures to the various anti-TB drugs, a set concentration of each one will be detected on bare glassy carbon and gold electrodes. The glassy carbon electrode (GCE) was initially used in order to clearly distinguish the peaks attributed to the anti-TB drugs instead of the peaks attributed to the electrode itself. Glassy carbon electrodes are inherently electrochemically inactive, meaning they do not produce peaks of its own in buffer [40]. Metallic working electrodes such as gold and platinum, usually have peaks that are inherent to the electrode surface itself caused by oxidation or reduction of the metal element [41]. Cyclic voltammetry and differential pulse voltammetry was employed under argon atmosphere to avoid interferences caused by oxygen molecules oxidising and reducing at the electrode surface.

4.3.1.1 Isoniazid

A final concentration of 200 μM isoniazid was added to a 5 ml electrochemical cell of 0.1 M PB. The results of the isoniazid detected on bare electrodes are as indicated in Figure 4-5. The detection on glassy carbon electrode revealed a major oxidation peak at 470 mV in the CV showed in Figure 4-5 (A). There are no visible reduction peaks present in this CV although the reduction does occur at a much greater negative potential around -1100 mV on a GCE. The reduction peak for INH was not considered for this analysis since it occurs at the same potential as the reduction of the gold electrode itself and would not be an analytically viable peak. The DPV detection of isoniazid at the glassy carbon surface shows and oxidation peak at 440 mV in Figure 4-5 (B).



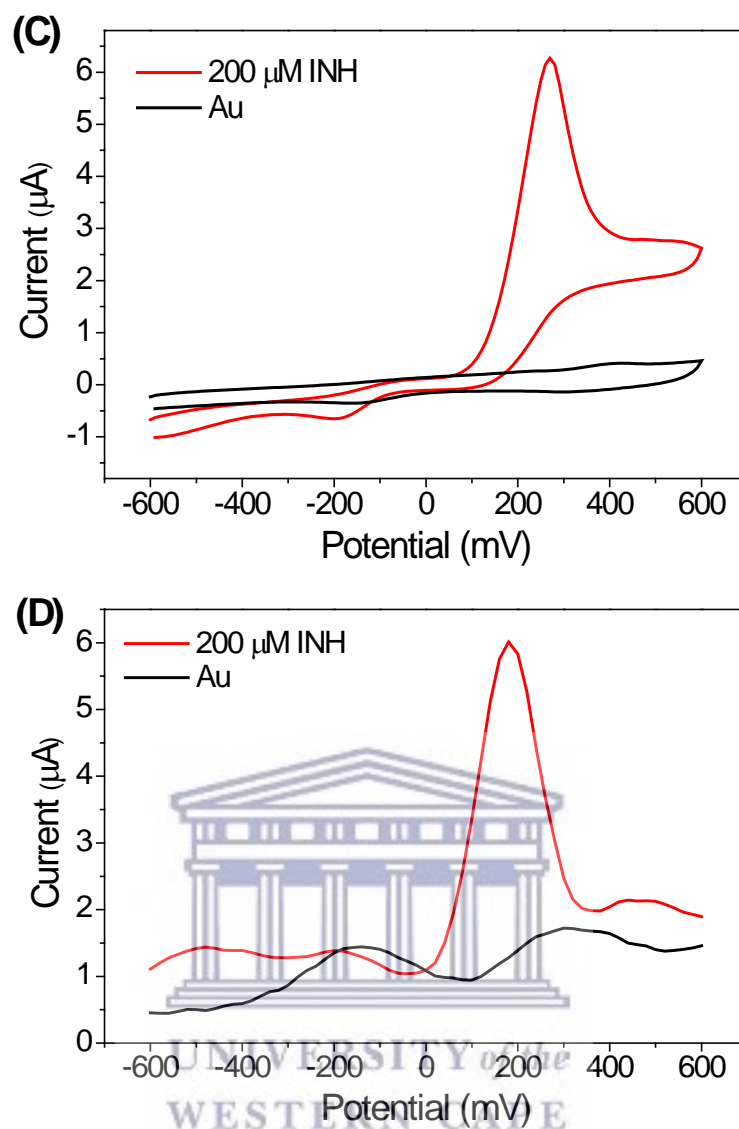
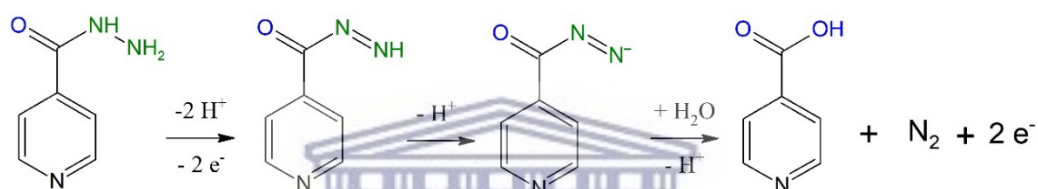


Figure 4-5: (A) CV and (B) anodic DPV of 200 μM INH on bare GCE and (C) CV and (D) anodic DPV of 200 μM INH on bare gold electrode from -600 mV to 600 mV of

The CV and DPV was carried out in a potential window -600 mV to 600 mV for detection of isoniazid on gold electrode as well. Oxidation of isoniazid at gold electrode surface is as shown in Figure 4-5 (C) and (D). The CV reveals a major oxidation peak at 230 mV while the DPV confirms this oxidation peak at 200 mV in the anodic scan. The interaction of isoniazid at the electrode surface of gold and glassy carbon are visibly different as indicated by the difference in oxidation potentials. The reaction occurs at a higher oxidation potential on glassy carbon compared to gold. This is due to the difference in the surface of the respective electrodes. Since the scan was started at -600 mV, the glassy carbon or gold electrode surface begins at a

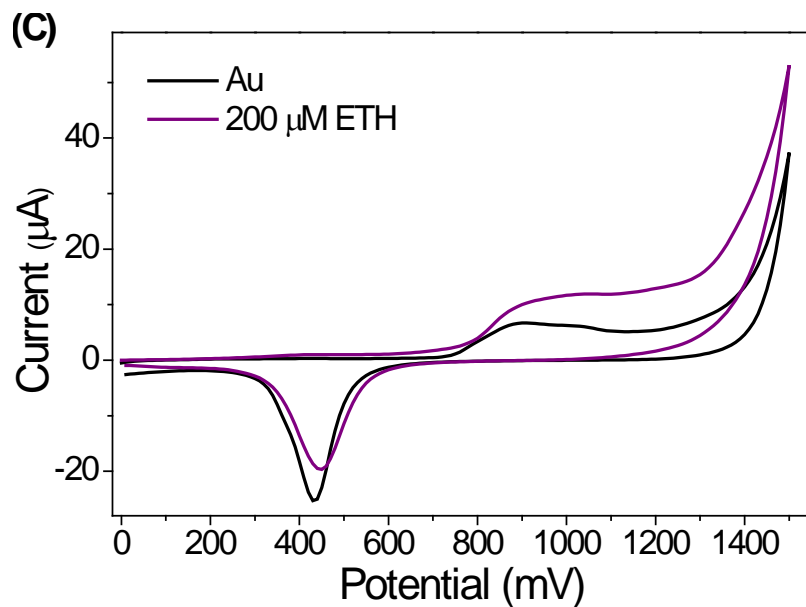
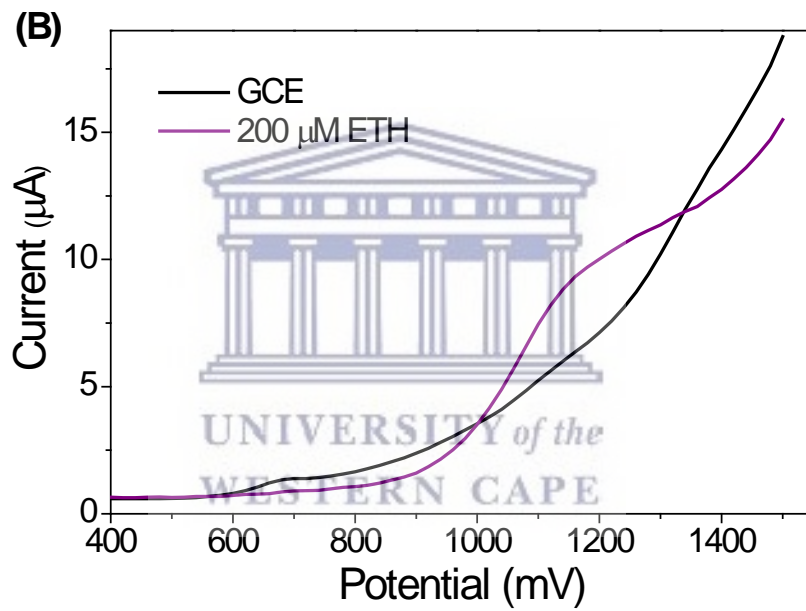
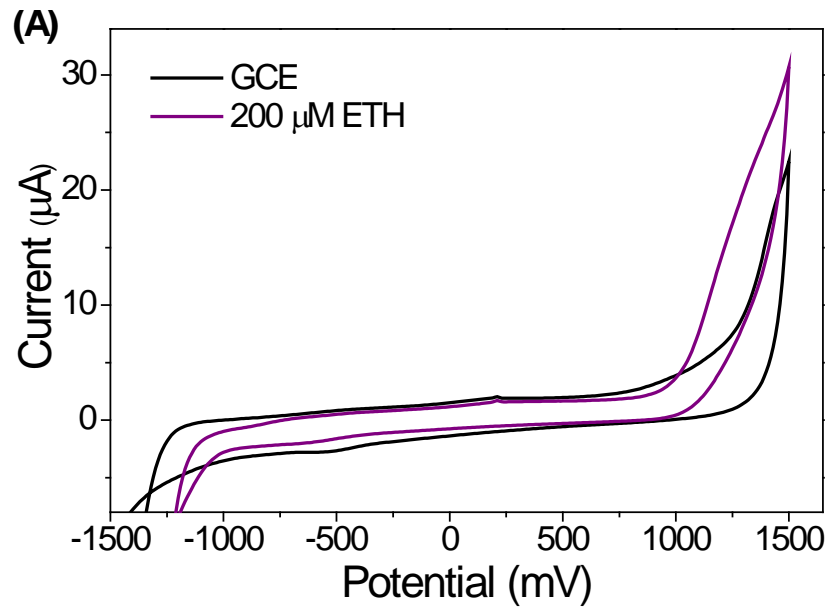
reduced state which is then oxidised as the scan continues to a positive potential. This potential scan results in the formation of oxide groups on the glassy carbon electrode surface which make it harder for the isoniazid to be oxidised at the electrode surface due to electrostatic interactions [42]. This is the reason for the potential of oxidation at glassy carbon electrode to be higher than that at the gold electrode. The oxidation of isoniazid has been previously studied and the mechanism of oxidation is as shown in Scheme 4-2 [43]. The molecule undergoes two reversible one electron transfers to produce an intermediate. The rate determining step was found to be the release of an H^+ ion from this intermediate.



Scheme 4-2: Oxidation mechanism of isoniazid [43]

4.3.1.2 Ethambutol

In order to assign the electrochemical signatures to the ETH molecule, a set concentration of ETH was detected using bare electrodes i.e. GCE and Au. The same technique was used as described above for INH. The results are as shown below with their corresponding potential ranges indicated in Figure 4-6.



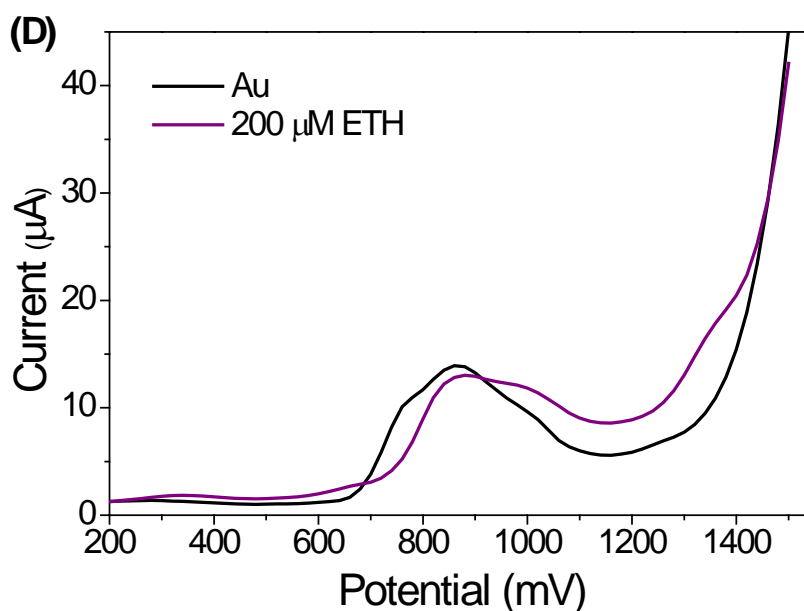


Figure 4-6: (A) CV from -1500 mV to 1500 mV and (B) anodic DPV from 400 mV to 1500 mV of 200 µM ethambutol on bare GCE electrode. (C) CV and (D) anodic DPV from 0 mV to 1500 mV from of 200 µM ETH on bare Au

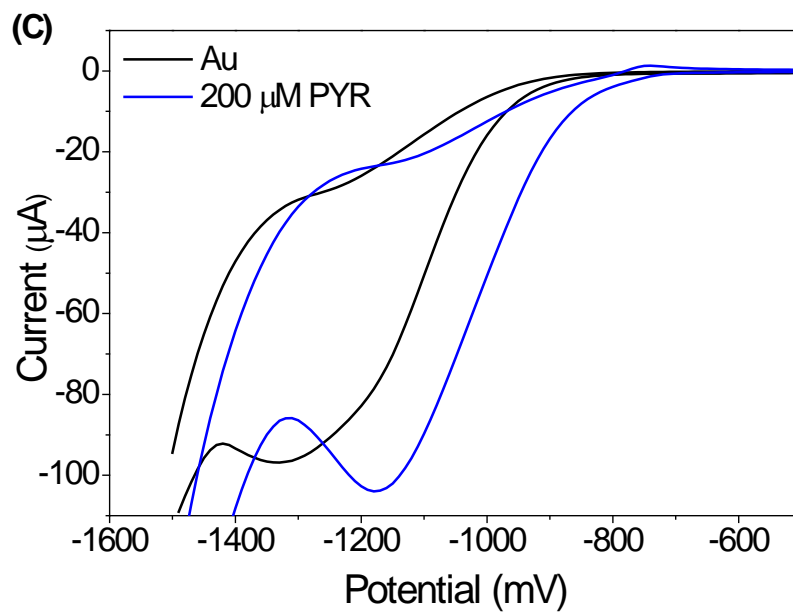
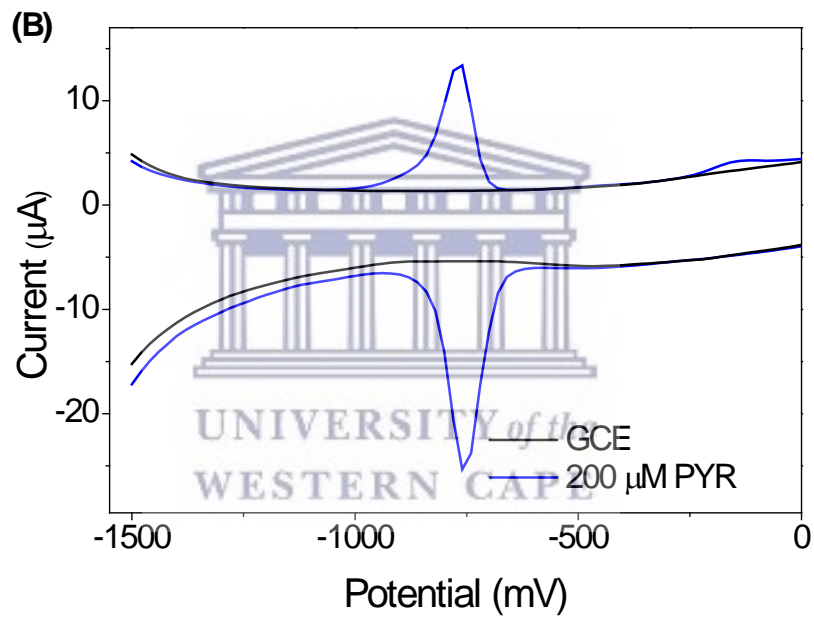
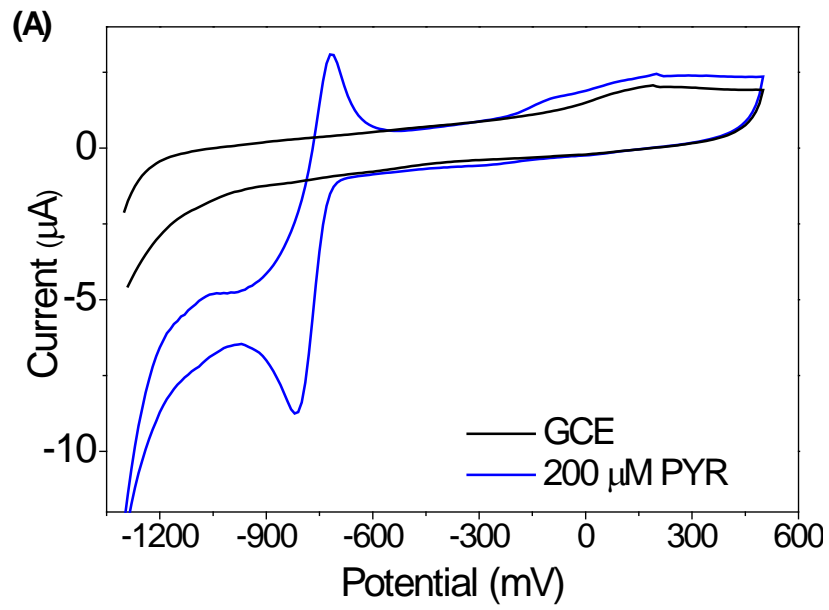
An oxidation peak was visible on a bare GCE at roughly 1200 mV in Figure 4-6 (A) during CV analysis. This oxidation peak attributed to ethambutol is consistent with those found in literature [44]. However, no clear reduction peaks are visible for ETH on the CV at any potential ranges studied using this medium. This proves that oxidation of ethambutol is irreversible or the subsequent reduction of ethambutol is difficult and requires much more energy than the potentiostat can apply. The anodic DPV scan from 400 mV to 1500 mV reveals and confirms the oxidation of ETH at the glassy carbon surface at 1150 mV in Figure 4-6 (B). The DPV analysis also did not indicate the presence of a reduction peak for ETH. For the purpose of this study we therefore chose to monitor the oxidation peak at 1200 mV for the detection of ETH.

The activity of ETH at a bare gold electrode surface was also monitored and the results shown in Figure 4-6 (C) and (D). The CV on Au was carried out from 0 mV to 1500 mV. The oxidation peak of the gold electrode was amplified at around 1000 mV due to the oxidation of ETH. The anodic DPV on Au was carried out from 0 to 1500 mV as well. Here the oxidation of ETH is seen as a shoulder at 1000 mV next to the oxidation peak inherent of the gold electrode at around 850 mV in Figure 4-6 (D). Another shoulder is present at 1350 mV as well. This is evident of two oxidation

processes occurring. These two oxidation peaks are attributed to the oxidation of the -OH and secondary amine groups (-NH) within ethambutol as shown in literature [45].

4.3.1.3 Pyrazinamide

The voltammograms representing the oxidation and reduction of 200 μM pyrazinamide on the glassy carbon electrode is as shown in Figure 4-7. From the CV, Figure 4-7 (A), one can clearly see that there are two peaks present, one oxidation and one reduction peak. The oxidation takes place in the anodic scan at a potential of $E_{pa} = -720$ mV whereas the reduction of PYR takes place in the cathodic scan at $E_{pc} = -820$ mV. The current on the cathodic peak is much larger than the current produced by the anodic peak due to further reaction of the reductive product [46]. The DPV, Figure 4-7 (B), also revealed similar results with an oxidation peak at $E_{pa} = -770$ mV for the anodic scan and a reduction peak at $E_{pc} = -750$ mV for the cathodic scan. According to the Nernst Equation 3.3, the reaction of PYR at the glassy carbon electrode surface is not reversible in that it the peak separation is more than 60 mV, ΔE is actually = 100 mV. We can thus deduce that the reaction is quasi reversible. The reaction of pyrazinamide was also carried out at the bare gold electrode surface in order to determine the interaction of PYR with the gold working electrode. The resultant CV and DPV scans are as shown in Figure 4-7 (C) and (D). Electrochemical characterisation of pyrazinamide on a bare gold electrode revealed an anodic peak at -747 mV in the CV. The cathodic peak attributed to the reduction at gold electrode was shifted from -1330 mV to -1170 mV in the presence of pyrazinamide. Similar results were observed in the DPV in Figure 4-7 (D) with a shift in the gold reduction peak from -1280 mV to -1100 mV in the cathodic scan. An additional cathodic peak was noted in the cathodic scan at -662 mV. The anodic scan revealed two oxidation peaks upon the detection of 200 μM pyrazinamide, at -1000 mV and -780 mV.



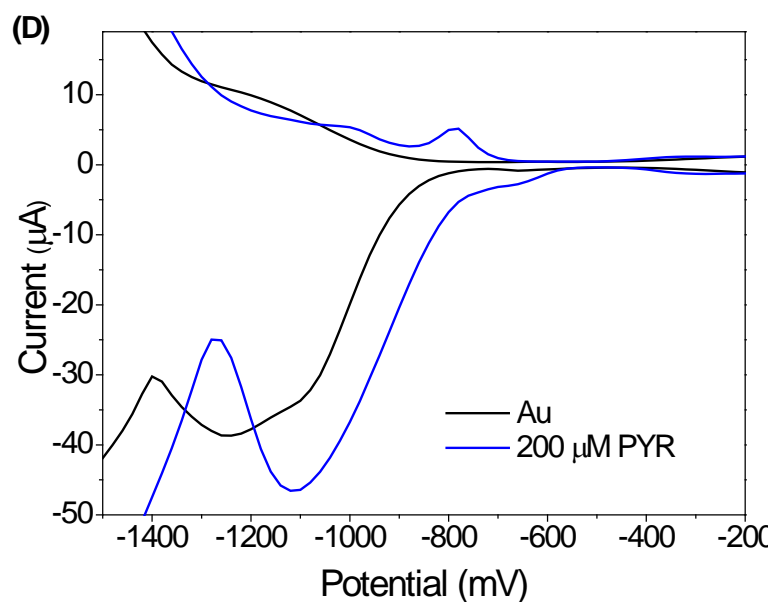
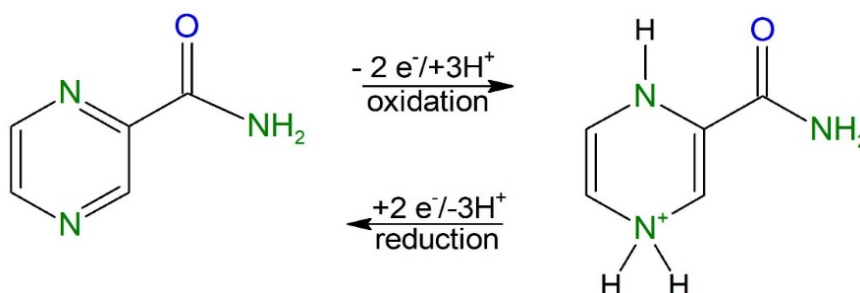


Figure 4-7: (A) CV from -1300 mV to 600 mV and (B) DPV from -1500 mV to 0 mV of 200 μM PYR on bare GCE (C) CV from -1500 mV to -500 mV of and (D) anodic and cathodic DPV from -1500 mV to -200 mV of 200 μM PYR on bare Au

The oxidation and subsequent reduction of pyrazinamide can therefore be represented by Scheme 4-3. The pyrazinamide molecule has been reported to transfer 2 electrons and 3 protons through its oxidation and subsequent reduction which is a reversible occurrence [46] [47].

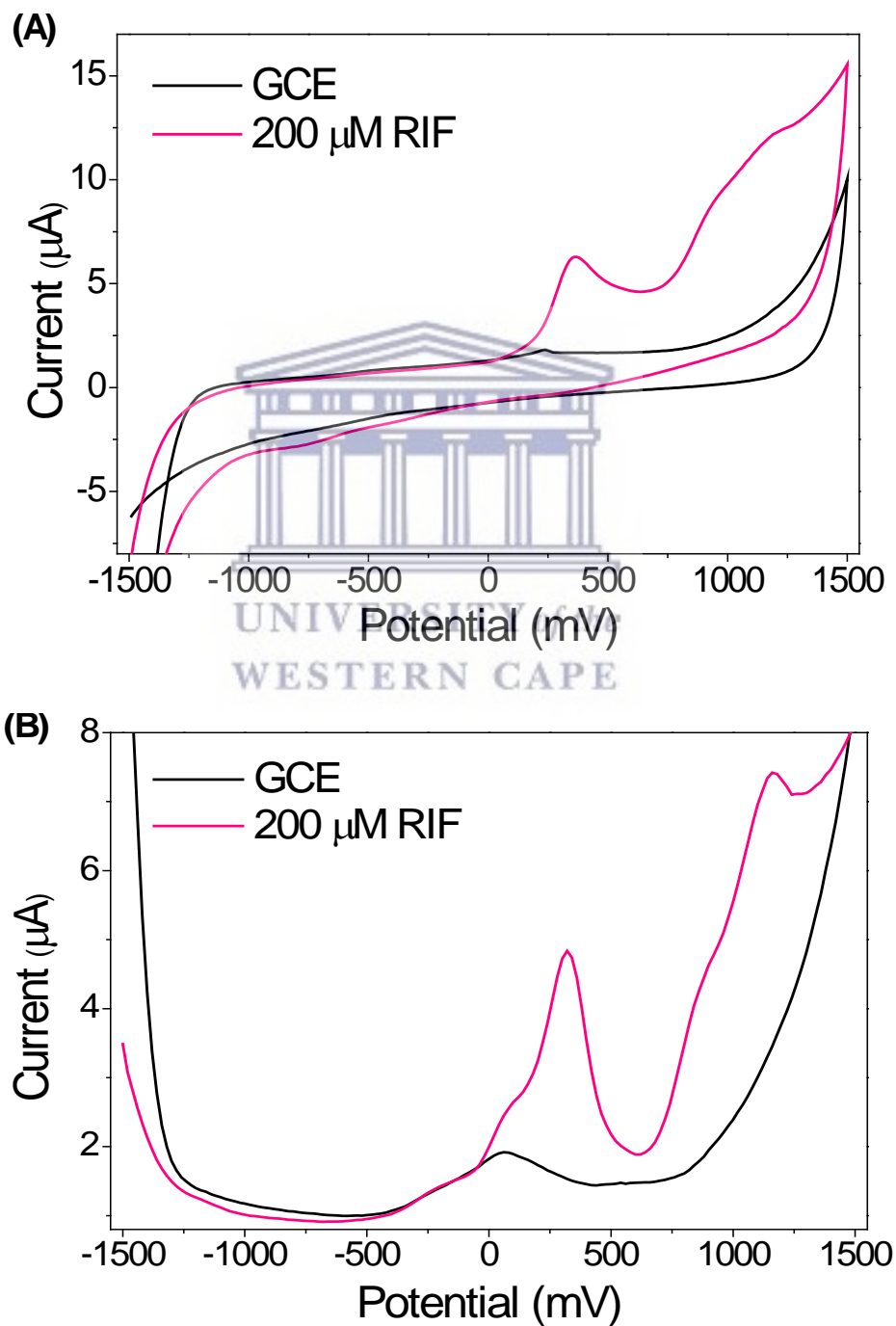


Scheme 4-3: Oxidation and reduction mechanism of pyrazinamide

4.3.1.4 Rifampicin

The electrochemical signatures of rifampicin were also determined on bare electrodes as with the other anti-TB drugs. RIF on a bare GCE revealed two oxidation peaks in the anodic scan of both CV and DPC. These two peaks are visible at 370 mV

and 1180 mV using CV and they shift to 320 mV and 1160 mV respectively when characterising using DPV as shown in Figure 4-8. In DPV, there are no distinctive cathodic peaks when analysing RIF on GCE or Au electrodes. This means that the two step process outline by these two anodic peaks are irreversible and are not electrochemically reduced again.



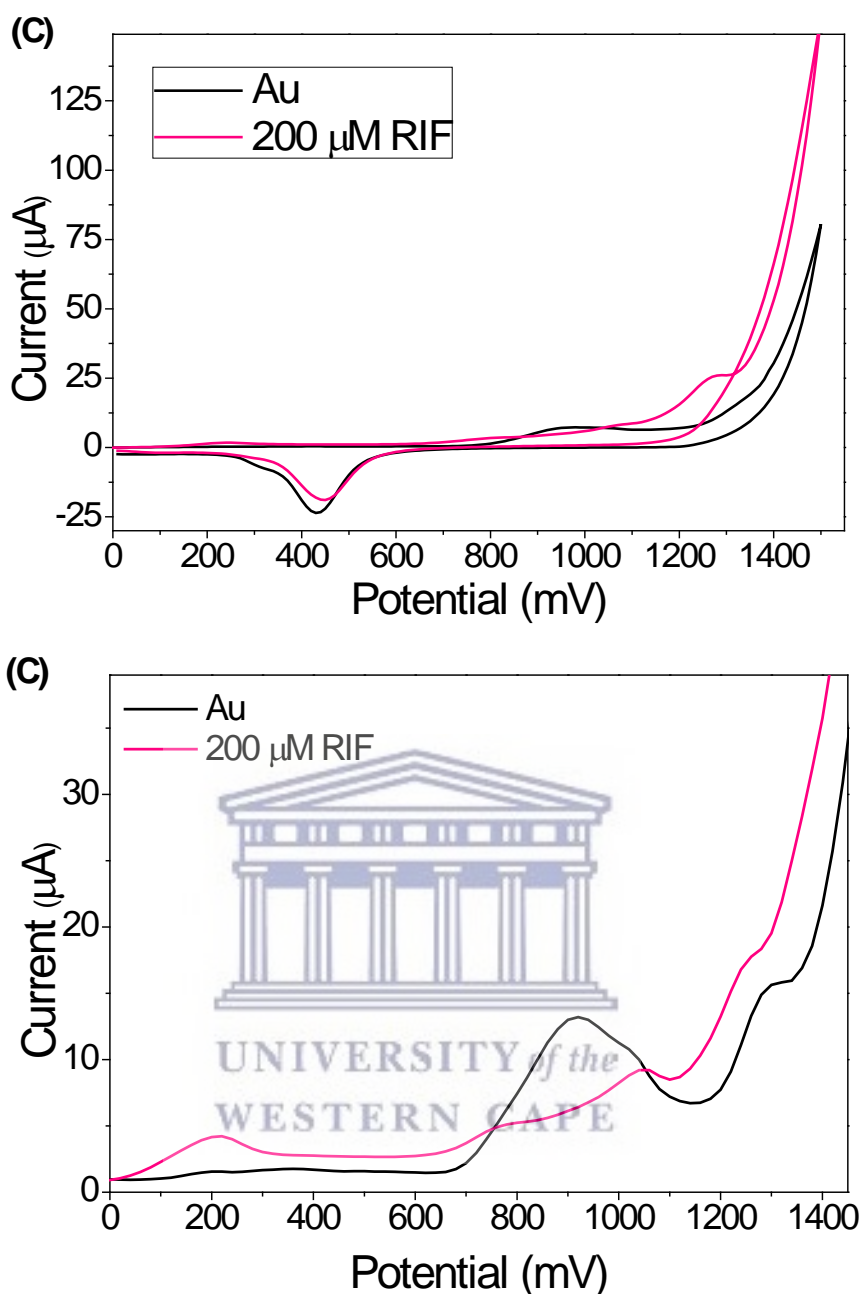


Figure 4-8: (A) CV and (B) anodic DPV from -1500 mV to 1500 mV of 200 μM RIF on bare GCE (C) CV and (D) anodic DPV from 0 mV to 1500 mV of 200 μM RIF on bare Au

RIF shows similar behaviour on a gold electrode, with distinctive oxidation peaks in the anodic scan of CV at 240, 810, 1050 and 1290 mV on a bare gold electrode. These peaks are visible in Figure 4-8 (A). The DPV shows similar potential values of 220, 760, 1040 and 126 mV. Rifampicin is a complex molecule and thus various oxidation reactions can take place within its structure. The first peak at 240 mV is attributed to the oxidation of the 6,9-dihydroxynaphthalene moiety to its corresponding naphthoquinone. This value is very close to that observed for the

hydroquinone/quinone redox system [31]. A representation of the mechanism of rifampicin oxidation to its quinone state is shown in Figure 4-9. The rest of the peaks between 810 and 1290 is thus caused by the multi-step oxidation of piperazinylimino moiety of the RIF molecule [48].

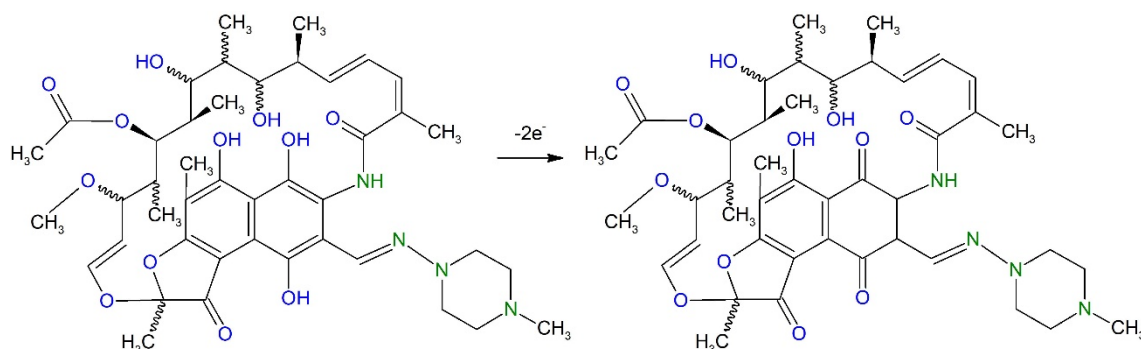


Figure 4-9: Mechanism of rifampicin oxidation via loss of electrons to form rifampicin quinone

A summary of the peaks produced by all four first line anti-TB drugs is shown in Table 4-1 on both GCE and Au electrodes using CV and DPV voltammetric techniques.

Table 4-1: Electrochemical signatures of anti-TB drugs on bare electrodes

Electrode	Method	INH	ETH	PYR		RIF
		E_{pa} (mV)	E_{pa} (mV)	E_{pa} (mV)	E_{pc} (mV)	E_{pa} (mV)
Au	CV	230	1000	-747	Au shift from -1330 to -1170	240, 810, 1050 and 1290
	DPV	200	1000 and 1350	-1000 and -780	Au shift from -1280 to -1100 and -662	220, 760, 1040 and 1260
GCE	CV	490	1200	-720	-820	370 and 1180
	DPV	440	1150	-770	-750	320 and 1160

4.3.2 Electro-catalytic behaviour of Au|CuPPI

The first generation copper metallodendrimer was then used as an electro-catalytic platform for the detection of all first line anti-TB drugs. The electrochemistry of the metallodendrimer was extensively studied in chapter 3. The electro-catalytic ability of the Au|CuPPI sensor electrode was determined by comparing the action of

isoniazid on a bare gold electrode vs. Au|CuPPI. This comparison is shown in Figure 4-10. It is clear from the voltammogram that the presence of the CuPPI on the gold electrode largely enhances the oxidation peak current and reaction of isoniazid compared to the bare electrodes tested before. Because of this large increase in peak current caused by the electrocatalytic behaviour of CuPPI, it was possible to detect a much lower concentration of analyte. A 500 nM concentration of isoniazid only produce an I_{pa} of 0.94 μA at around 400 mV on the bare gold, whereas INH on the dendrimer modified electrode yields an I_{pa} of 8.62 μA at 200 mV. The dendrimer thus acts as a highly effective electrocatalyst for the detection of INH with a current increase of nearly 10 fold. The electrocatalytic behaviour of the dendrimer could be attributed to its large surface area, its catalytic metal centre or active sites and enhanced electrical conductivity which all aid in the oxidation of INH.

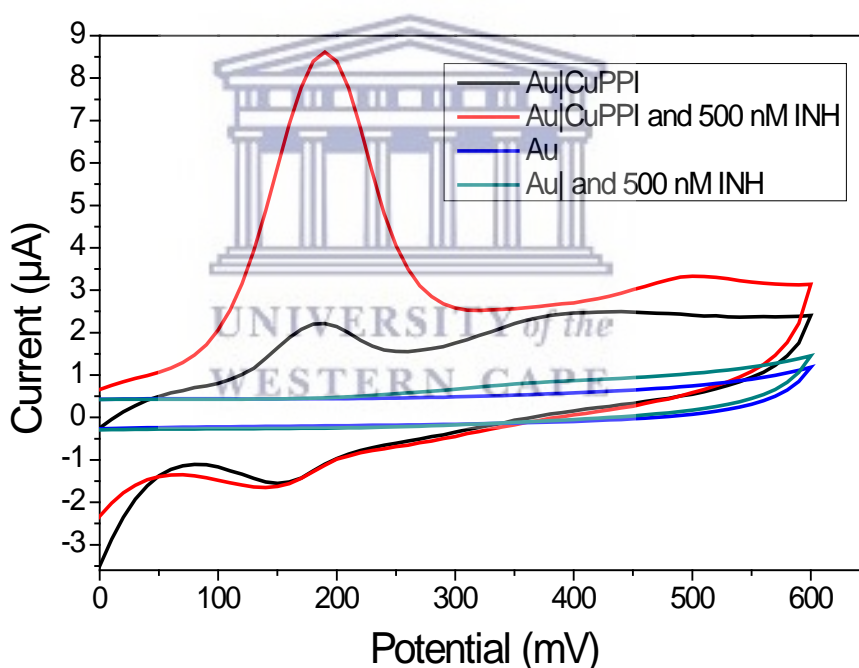
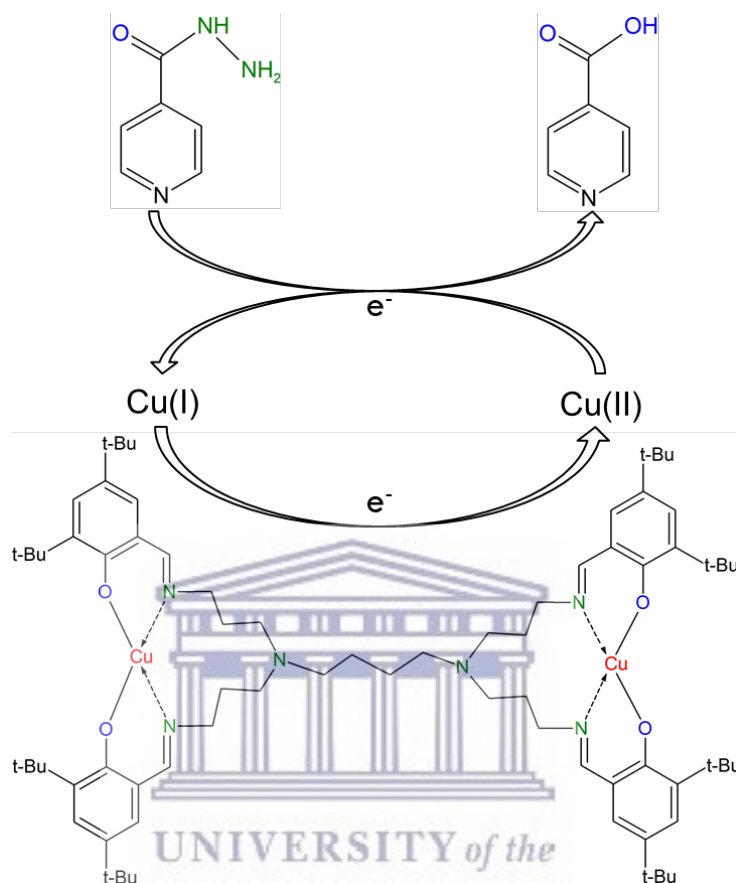


Figure 4-10: Catalytic effect of copper metallodendrimer in the oxidation of 500 nM isoniazid at bare and modified gold electrode surfaces in pH 7 phosphate buffer

The electrons transferred during the oxidation and reduction of the copper centre within CuPPI are used as catalysts in the oxidation of the analyte at modified electrode surface. A scheme representing this catalysis is shown in Scheme 4-4. The catalytic reaction occurring here is known as an EC' (electrochemical catalytic) type

mechanism [49]. The mechanism consists of a reversible reaction carried out by the electrocatalytic material which enhances the irreversible conversion of reactants to products.



Scheme 4-4: Representation of EC' mechanism occurring at metallodendrimer modified electrode surface


4.3.3 Au|CuPPI sensor for detection of anti-TB drugs

The Au|CuPPI modified electrode was then used to detect ultra-low concentrations of the anti-TB drugs in phosphate buffer pH 7.4 as electrolyte.

4.3.3.1 Isoniazid

Isoniazid was detected using cyclic voltammetry in phosphate buffer pH 7.4 as electrolyte in the presence of oxygen as shown in Figure 4-11 (A). The analysis was

carried out in the presence of oxygen in order for the system to mimic real situations in which the device could possibly be used. The anodic peak attributed to the oxidation of the metallodendrimer is present at 200 mV as shown in the DPV in Figure 4-11. During the experiments it was found that a drastically lower concentration of the analytes could be determined and the lower linear ranges were investigated. Upon the addition of 20 nM INH, the oxidation peak then appears at 140 mV, which is attributed to the drug being electrocatalysed by the dendrimer at the electrode surface. Upon additions of more INH the E_{pa} shifts to a higher potential of up to 200 mV upon addition of 200 nM INH. The resulting calibration curve is shown in Figure 4-11 (B). The detection of isoniazid was found to be linear in the range of 20 to 200 nM with a correlation coefficient of 0.96 and a sensitivity of 0.021 $\mu\text{A}/\text{nM}$. The limit of detection (LOD) and limit of quantification (LOQ) was calculated using the following equations:



$$\text{LOD} = 3.3\sigma/s \quad \text{Equation 4-1}$$

$$\text{LOQ} = 10\sigma/s \quad \text{Equation 4-2}$$

where σ is standard deviation of blank samples and s is the slope of the regression equation. The values of these limits are $\text{LOD} = 0.788 \text{ nM}$ and $\text{LOQ} = 2.37 \text{ nM}$ for the detection of INH. Similar results have been found in literature when detecting INH with a B/N co-doped mesoporous carbon film electrode which yielded a 1.5 nM limit of detection [50]. The fact that a simple and easy to produce molecule such as the G1-metallodendrimer could produce better results is highly favourable for this sensor.

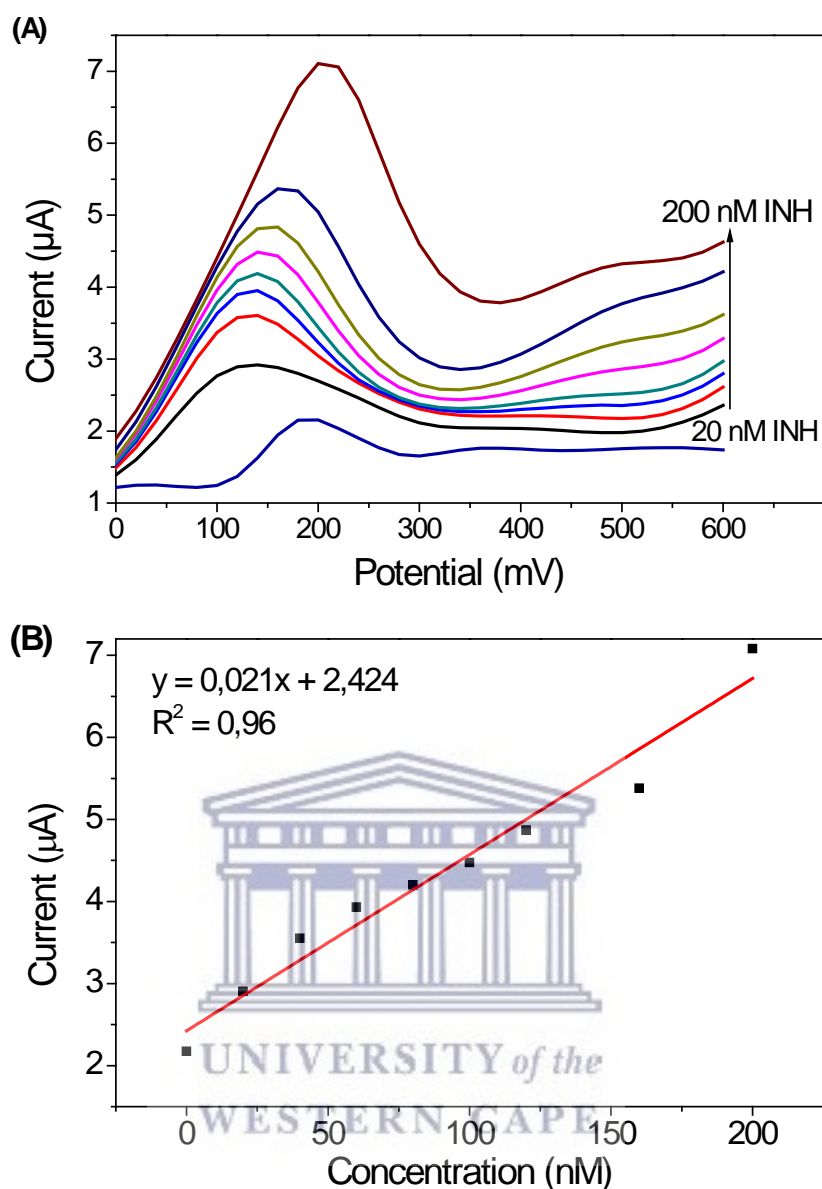


Figure 4-11: (A) DPV detection of 20, 40, 60, 80, 100, 120, 160 and 200 nM isoniazid at Au|CuPPI electrode surface in PB pH 7.4 at (B) linear calibration plot of current vs concentration of INH in PB pH 7.4

4.3.3.2 Ethambutol

The Au|CuPPI was then used for the detection of ethambutol in solution via DPV. A wide potential range was studied and the voltammogram representing additions of ETH to the electrochemical cell is as shown in Figure 4-12 (A). The action of ethambutol on the surface of Au|CuPPI (modified electrode) was similar to that on the bare gold electrode, with an oxidation peak appearing around 1000 mV, however the peak was enhanced due to the electrocatalytic behaviour of the CuPPI

metallo-dendrimer. The linear calibration plot of the ETH additions/detection is shown below in Figure 4-12 (B). The ETH produced a single anodic peak at around 900 mV at lower concentrations. However, this peak split up to 825 mV and 1000 mV after 60 nM ETH was added to the electrochemical cell. There is a good linear relationship between peak current and concentration with a linear regression of 0.97 from 20 to 200 nM. The sensitivity of the sensor towards ETH was found to be 0.042 $\mu\text{A}/\text{nM}$. The LOD and LOQ were calculated to be 0.394 nM and 1.18 nM respectively.

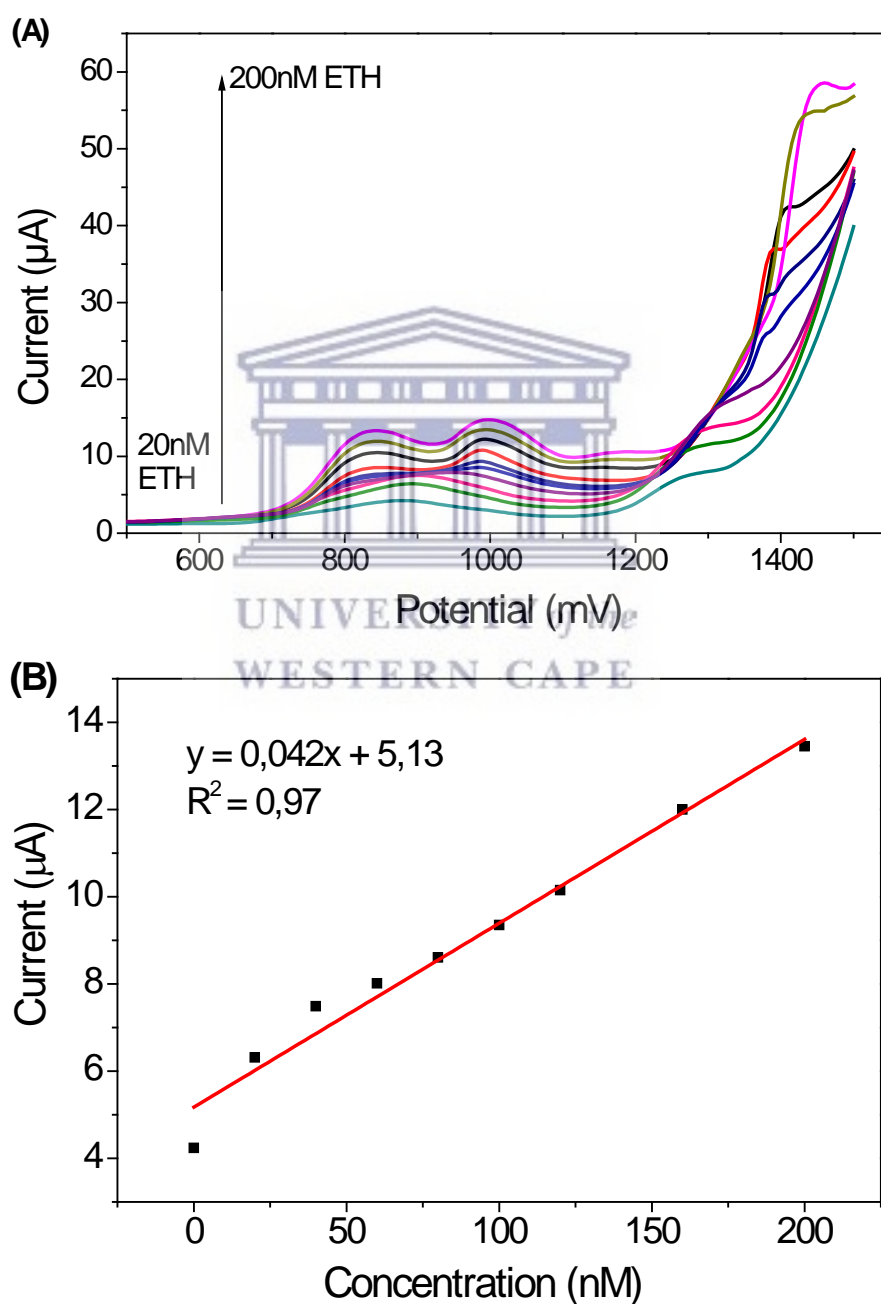


Figure 4-12: DPV detection of 20, 40, 60, 80, 100, 120, 160 and 200 nM ETH at Au|CuPPI electrode surface in PB pH 7.4 (B) Linear calibration plot of current vs concentration of ETH in PB pH 7.4

Ethambutol has previously been detected using HPLC coupled with UV or fluorescent detection, which includes many steps of sample preparation via derivatization due to the lack of an intrinsic chromophore or fluorophore [51]. This highlights the benefits of electrochemical detection or analysis of ethambutol, which decreases sample preparation, time of analysis as well as cost. Ethambutol has not been extensively detected using electrochemical techniques. Previously ETH has been studied on a glassy carbon electrode using multi walled carbon nanotubes (MWCNT's) as an electro-catalytic platform. However this method revealed a poor linear concentration range of 8-250 μM and a detection limit of 0.76 μM [52]. This Au|CuPPI chemical sensor thus has a superior performance in terms of a significantly lower limit of detection and dynamic linear range in terms of ETH detection.

4.3.3.3 Pyrazinamide

The electrochemical action of PYR on the Au|CuPPI electrode was then monitored in the 20 to 200 nM concentration range. Although both an anodic and cathodic peak is present for this molecule, the anodic peak was monitored in order to minimise the interference of the gold reduction peak in the cathodic scan. DPV analysis is shown in Figure 4-13 with an E_{pa} of -1040 mV for PYR oxidation. One can note a linear response of current vs concentration up until 100 nM. Successive additions after 100 nM resulted in a plateau in the graph. This is due to saturation of the electrode surface with PYR. The sensor had a sensitivity of 0.75 $\mu\text{A}/\text{nM}$ towards PYR. The LOD and LOQ for pyrazinamide in the linear region (200 to 100 nM) was calculated to be 0.022 nM and 0.066 nM respectively.

Pyrazinamide has previously been detected using a poly-L-methionine and electrochemically reduced graphene oxide electrode which achieved a dynamic linear range of 0.4 μM to 1129 μM and limit of detection of 0.16 μM [53]. Similar results were achieved recently when a rod-like Co based MOF (metal organic framework) was used on an electrode surface for the detection of PYR. This complex system obtained

a low linear range of 0.3 μM to 46.5 μM with a limit of detection of 0.21 μM [54]. Both of these sensors yielded good results which are in the micromolar range, however the sensor in this work is capable of obtaining results in the nanomolar range.

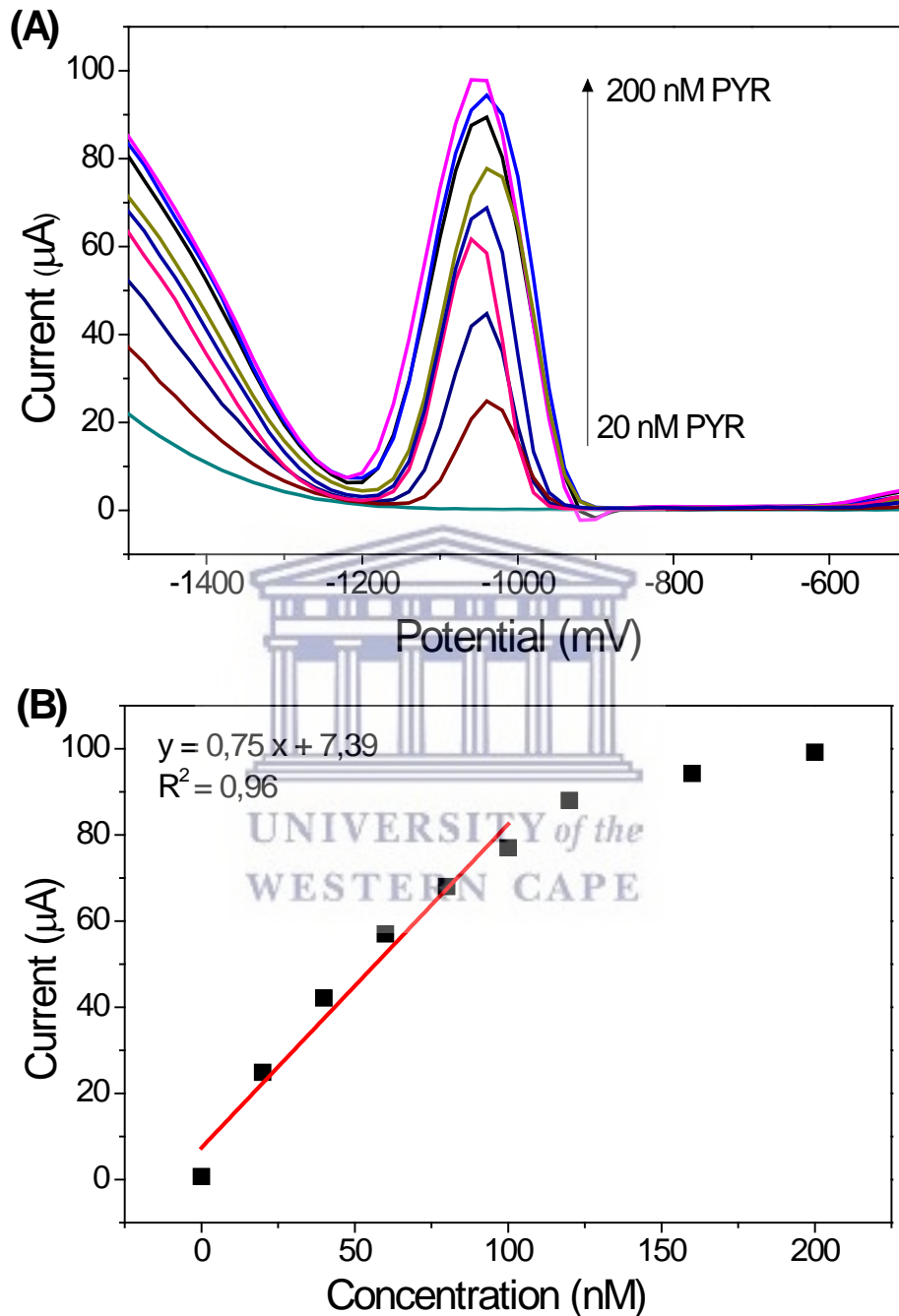


Figure 4-13: (A) DPV detection of 20, 40, 60, 80, 100, 120, 160 and 200 nM PYR at Au|CuPPI electrode surface in PB pH 7.4 (B) Linear calibration plot of current vs concentration of PYR in PB pH 7.4

4.3.3.4 Rifampicin

The dendritic sensor was also applied to the detection of rifampicin, with successive additions of the drug shown in the DPV in Figure 4-14 (A). As shown in a previous section, RIF gives rise to multiple oxidation peaks in the range of 0 to 1200 mV. For analytical purposes the peak at 445 mV was studied in order to distinguish it from the other anti-TB drugs. This oxidation peak gave a good linearity between current and concentration with a linear regression of 0.937 between 20 to 200 nM. The sensor shows a good LOD and LOQ of 1.15 nM and 3.45 nM respectively. The sensitivity of the sensor towards RIF was found to be 0.0144 $\mu\text{A}/\text{nM}$ as shown in the calibration curve in Figure 4-14 (B). Rifampicin has previously been detected using a nickel nanoparticle and nickel hexacyanoferrate modified GCE. This sensor obtained a linear analytical curve from 5 μM to 500 μM with a limit of detection of 2.6 μM . Treatment of TB with RIF tablets containing 150 to 300 mg or RIF usually result in roughly 36 to 73 μM being leftover in urine un-metabolised [55]. A complex nanoparticle in the form of a PVP capped CoFe_2O_4 magnetic core and CdSe shell was developed recently with a particularly wide linear range. The electrocatalytic activity of this nanoparticle was successful in the range of 0.1 fM to 0.1 μM and a limit of detection of 0.045 fM using square wave anodic stripping voltammetry [56]. Although these sensors obtained results which are in the correct concentration range for various phenotypes, the simplicity, stability and low cost of the dendritic sensor is still more favourable

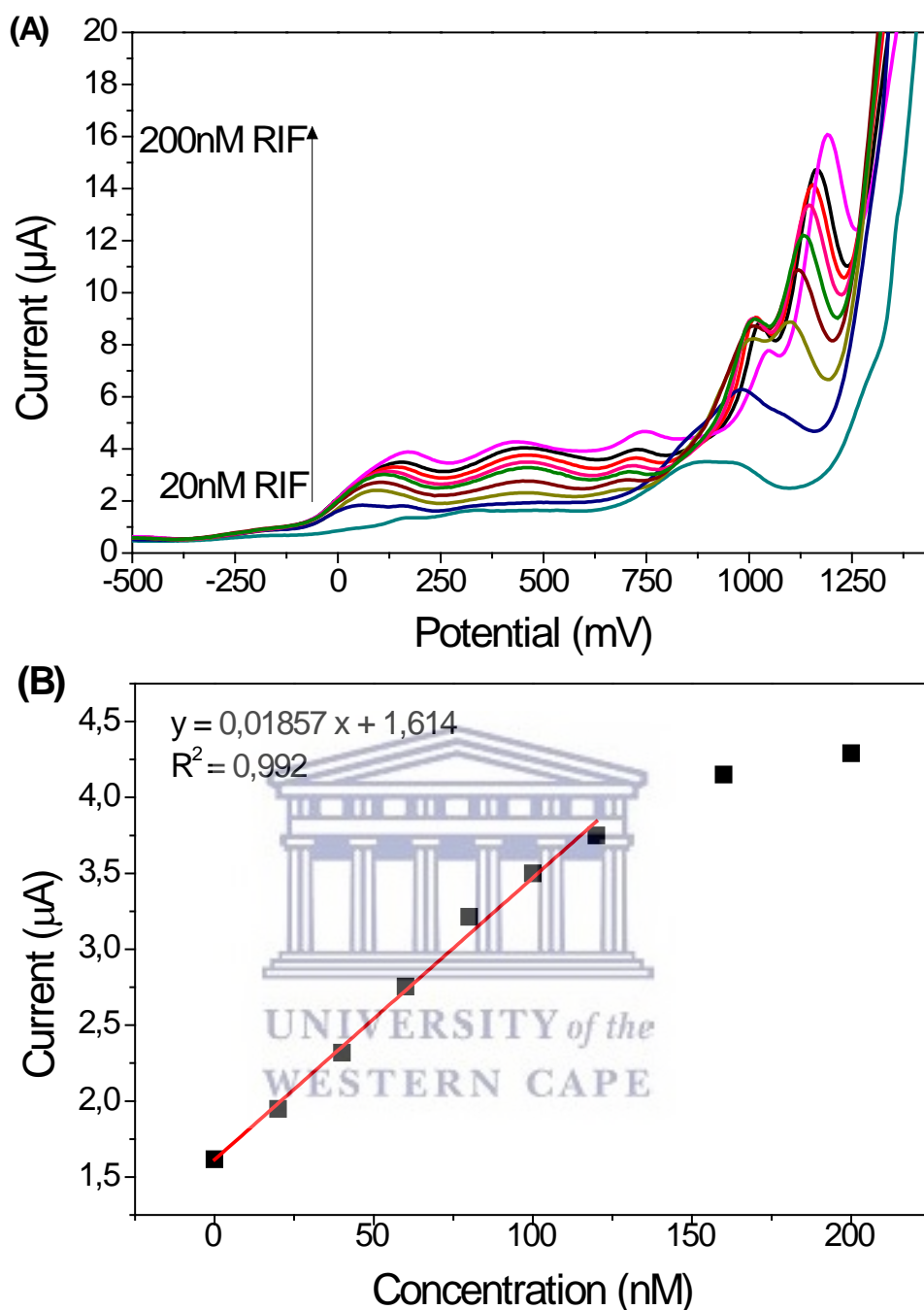
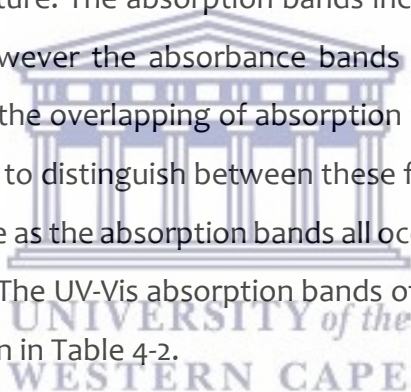


Figure 4-14: (A) DPV detection of 20, 40, 60, 80, 100, 120, 160 and 200 nM RIF at Au|CuPPI in PB pH 7.4 (B) Linear calibration plot of current vs concentration of RIF in PB pH 7.4

4.3.4 UV-Vis detection of anti-TB drugs

As a point of validation or reference, the detection of anti-TB drugs were completed using a simple UV-Vis method in order to compare this simple sensor with an established laboratory technique. In order to determine the wavelength of maximum absorption i.e. λ_{max} of the various drugs, the UV-Vis scan was carried out

from 190 nm to 700 nm. The resulting absorbance spectra for each anti TB drugs is shown in Figure 4-15, as well as a mixture of all four drugs. There are two absorption bands present for INH, one at 205 nm and an absorption maxima, λ_{max} at 263 nm. Pyrazinamide has similar absorption bands at 209 nm and λ_{max} at 268 nm. The UV-spectra of these two molecules are very similar because of the similarity in the chemical structures since both PYR and INH are substituted benzene rings. Rifampicin gives rise to multiple absorption bands at 256 nm, 333 nm and 474 nm with λ_{max} at 237 nm due to multiple chromophores. The complexity of the molecule and the existence of a bicyclic benzene gives rise to multiple peaks in the UV-Vis spectrum. Ethambutol however does not absorb light in the UV-vis range and thus gives no peaks in UV spectra. The “cocktail” containing all four of the anti-TB drugs was also measured via UV-Vis in order to determine if one could determine the quantity of the individual drugs in a mixture. The absorption bands included all those described for the individual drugs, however the absorbance bands between 200 and 300 were largely increased due to the overlapping of absorption maxima of PYR, INH and RIF. It would thus be difficult to distinguish between these four compounds using UV-Vis as an analytical technique as the absorption bands all occur in the same region, or not at all in the case of ETH. The UV-Vis absorption bands of each of the drugs as well as the combination is shown in Table 4-2.



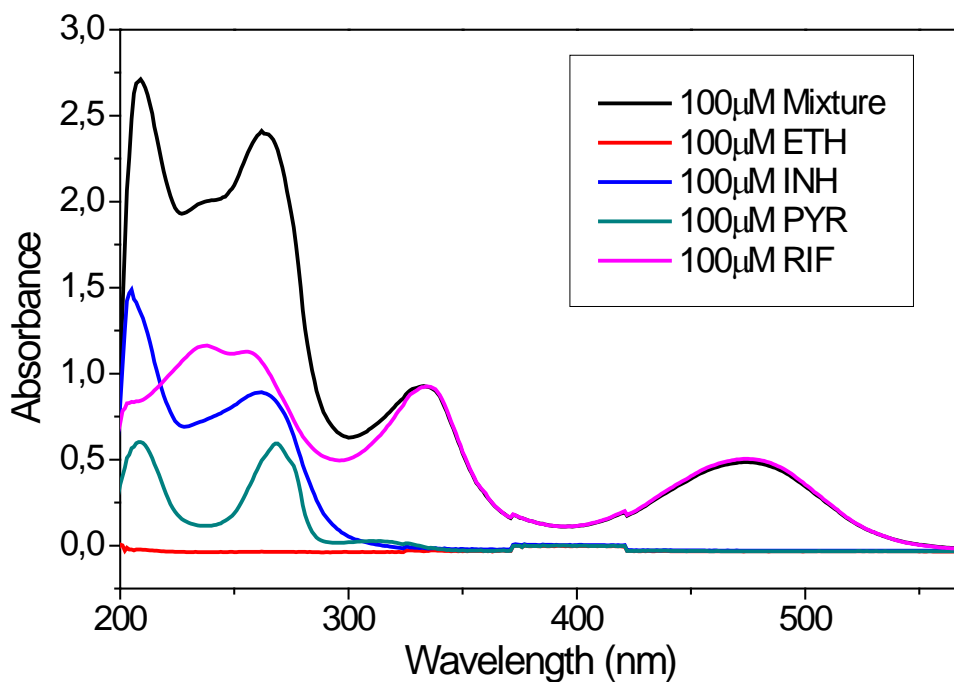


Figure 4-15: UV-Vis of anti-TB drugs on their own, and in a mixture containing all four: ETH, INH, PYR and RIF in 0.1 M PB pH 7.4

Table 4-2: UV-Vis absorption bands of anti-TB drugs

Anti-TB drug	λ (nm)	λ_{max} (nm)	Reference
Isoniazid	205	263	[57]
Ethambutol			[58]
Pyrazinamide	209	268	[59]
Rifampicin	256, 333 and 474	237	[60]
Mixture	209, 237, 333, 474	262	This work

The spectrophotometric detection of individual drugs was successful and showed linearity between λ_{max} absorbance vs concentration. The UV spectrum representing the detection of increasing concentrations of rifampicin is shown in Figure 4-16. The same method of detection was carried out for INH and PYR as well, with a steady increase in absorbance upon an increase in concentration. The resulting calibration curves of all three drugs are as shown in Figure 4-16. The LOD and LOQ for UV-Vis detection was calculated using Equation 4.1 and 4.2 respectively. UV-Vis showed a good linearity between absorbance and concentration with all three analytes, and LOD's ranging from 24.3 to 54.7 nM as detailed in Table 4-2.

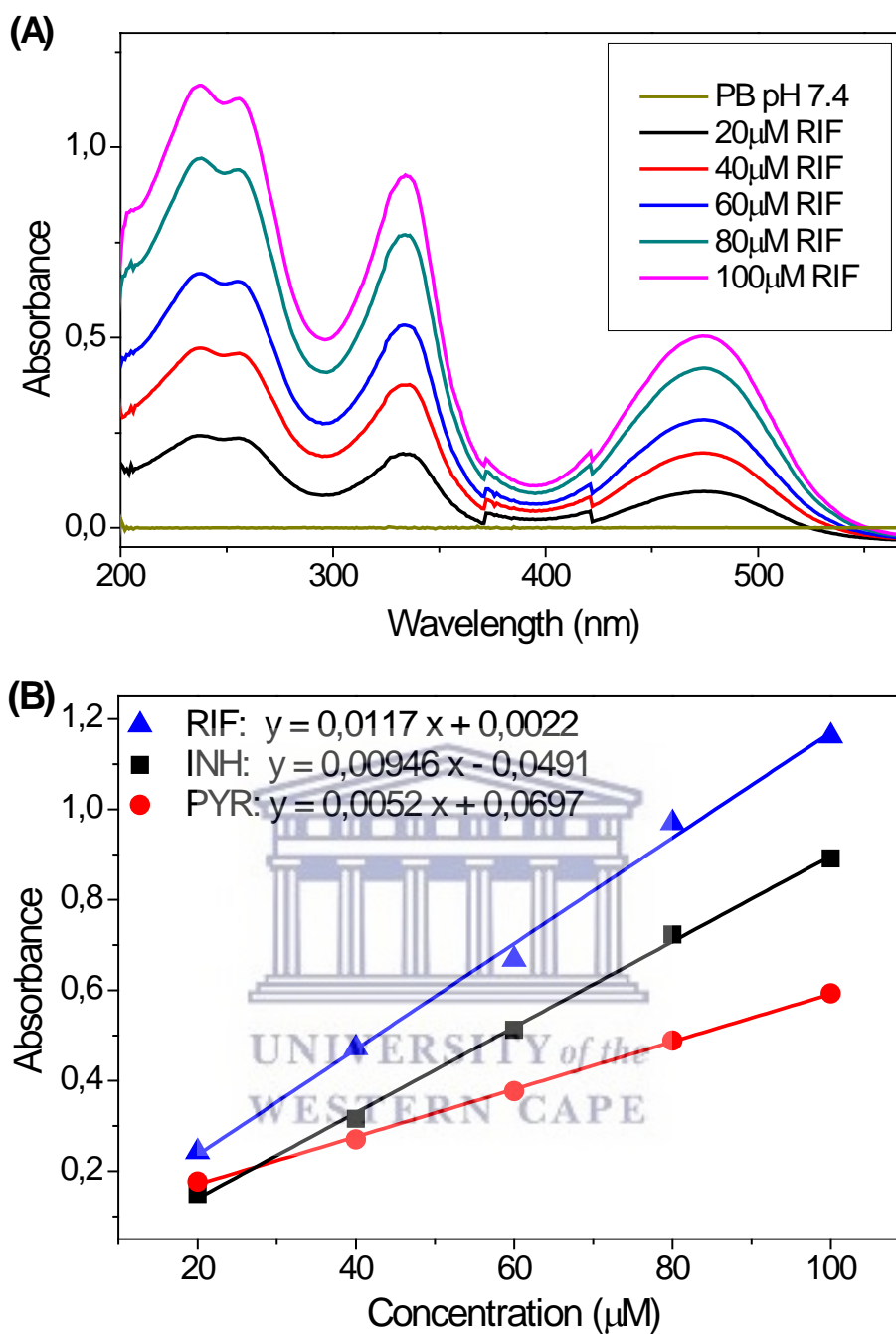


Figure 4-16: UV-Vis detection of RIF in 0.1 M PB pH 7.4 at concentrations of 20, 40, 60, 80 and 100 μM (B): Calibration curves for UV-Vis detection of INH, PYR and RIF in 0.1 M PB pH 7.4

UV-Vis can be used as a tool for the detection of three out of the four drugs used to treat TB without any major sample preparation. The fact that some molecules do not absorb light in the UV-vis range is one of the downsides of this analytical technique. Ethambutol is one of these molecules and cannot be detected using UV-Vis without pre-treatment, such as complexing it with dyes [61] in order to make the resulting

complex UV-vis active. UV-Vis also requires a laboratory setting in order for experiments to be carried out. The other issue which exists when using this technique is the effect of complex matrices. A recent study showed that a specificity of only 60 % was possible when detecting rifampicin in serum when the concentration was less than 8 mg/l [62]. Electrochemistry on the other hand requires no pre-treatment step and all four of the drugs can be detected using this technique as described above, with clear distinction between each of them. Electrochemistry also has the ability to be portable and requires very small sample volume. A comparison of analytical values such as sensitivity, limit of detection and limit of quantification is shown below in Table 4-3 between our Au|CuPPI chemical sensor and a well-established laboratory technique such as UV-Vis.

Table 4-3: Summary of analytical efficiency of electrochemistry vs UV-Vis

Anti-TB drug	Electrochemical Detection			UV-Vis Detection		
	Sensitivity ($\mu\text{A/nM}$)	LOD (nM)	LOQ (nM)	Sensitivity (abs/ μM)	LOD (nM)	LOQ (nM)
Isoniazid	0.021	0.788	2.37	0.00946	30.1	91.2
Ethambutol	0.042	0.394	1.18	-	-	-
Pyrazinamide	0.75	0.0220	0.0660	0.0052	54.7	165
Rifampicin	0.0142	1.16	3.49	0.0117	24.3	73.7

4.4 Real Samples

The Au|CuPPI chemical sensor was then applied in the detection of the four anti-TB drugs in more complex matrices such as synthetic urine and plasma. Various concentrations of each drug were detected in 20 % synthetic urine and 10 % plasma. These would mimic real samples whose only preparation step would be to dilute the samples in pH 7 phosphate buffer in a 1:5 and 1:10 ratio for synthetic urine and plasma respectively. These dilutions allowed for the matrix to become conductive by adding the PB while still maintaining the integrity of the “real sample”. The dendrimer modified electrode i.e. Au|CuPPI behaves differently in the more complex media

compared to the pure buffer as shown in Figure 4-17. From the CV's shown here it is clear that matrix effects are an issue which affects the CuPPI. Noticeable changes in the CV of the synthetic urine is the shift in the cathodic peak (E_{pa}) which is now at 40 mV instead of 160 mV in pure buffer. In 10% plasma the anodic and cathodic peaks from CuPPI are masked by other molecules in the plasma with an anodic peak occurring at 350 mV. Factors contributing to these matrix effects include interfering substances (uric acid, salicylic acid, ascorbic acid etc.), fouling of the electrode (caused by plasma proteins), non-specific binding as well as pH [63] [64]. The molecules present in these matrices thus interact on the dendrimer surface. Each of the anti-TB drugs were then detected using this dendrimer in urine and plasma.

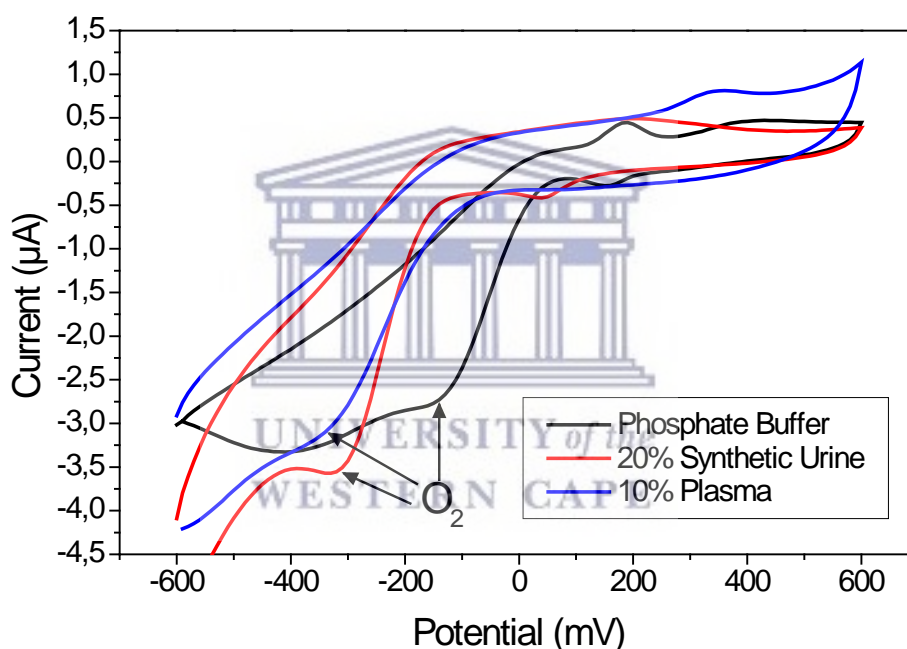


Figure 4-17: Au|CuPPI behaviour in pH 7 0.1 PB, 20 % synthetic urine and 10 % plasma diluted with 0.1 M PB

4.4.1 Isoniazid

The detection of isoniazid was first carried out in 20 % synthetic urine and successful in the concentration range of 10 to 100 μ M. Lower concentrations than 10 μ M resulted in erratic responses which were not analytically viable. The dynamic linear range was much higher in the case of synthetic urine and plasma since these matrices had a significant effect on the sensitivity of the Au|CuPPI sensor. The CV's of the addition of INH to Au|CuPPI in synthetic urine is shown in Figure 4-18 (A). The anodic

peak attributed to CuPPI appears around 170 mV in synthetic urine. Upon addition of 10 μM INH, a peak appears at 270 mV which shifts upon an increase in concentration up to 350 mV when 100 μM INH is added. The calibration curve of showing the linear response between concentration and peak height is shown in Figure 4-18 (B).

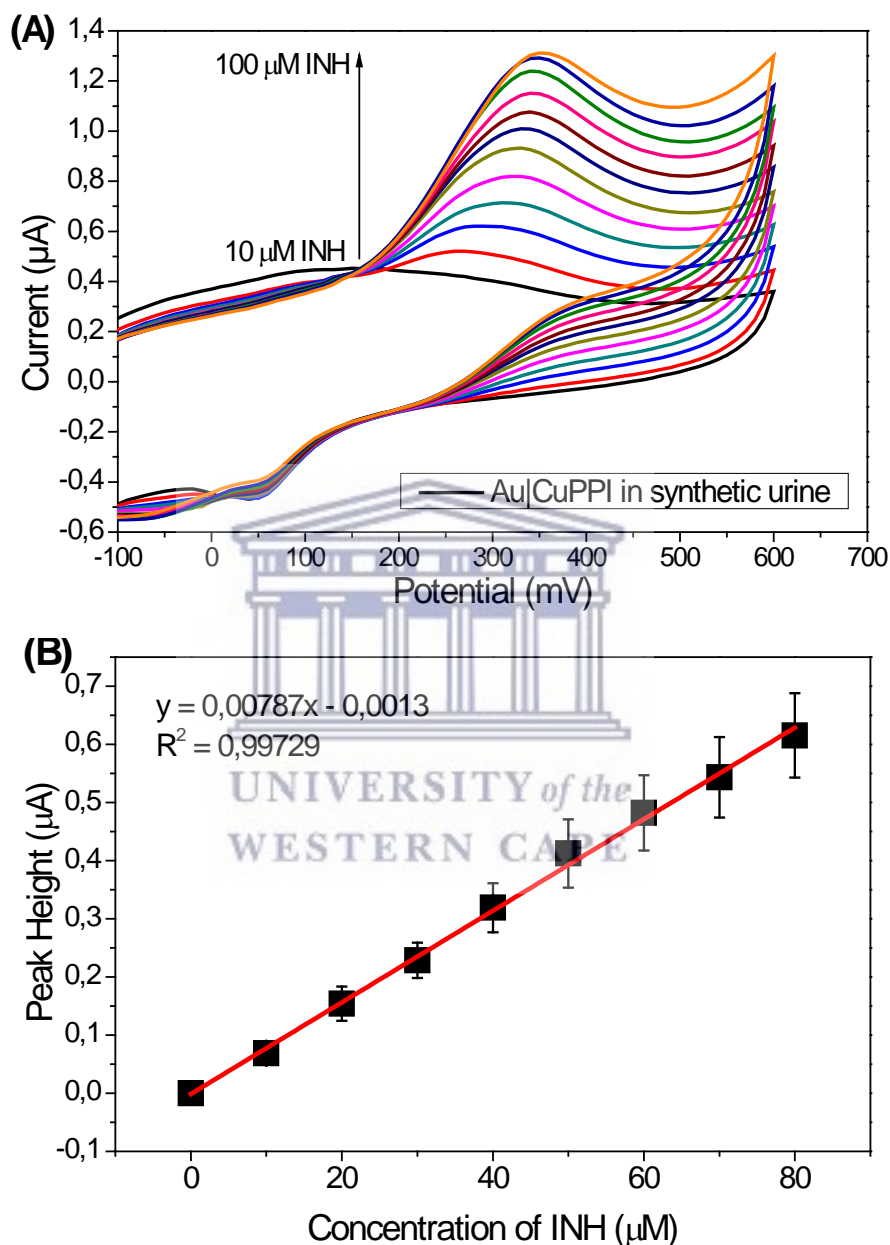


Figure 4-18: (A) CV detection of 10, 20, 30, 40, 50, 60, 70, 80, 90 and 100 μM INH at Au|CuPPI (B) linear calibration plot of I_{pa} vs concentration of INH in 20 % synthetic urine

The effect of the synthetic urine on the linear range of detection is quite vast compared to pure phosphate buffer. The amount of drug detectable in PB is in the nanomolar range, but shifts to the micromolar range in synthetic urine. One can also

note that the error increases with an increase in concentration for INH. The limit of detection for the Au|CuPPI chemical sensor was found to be $3.23 \mu\text{M}$ and limit of quantification is $10.78 \mu\text{M}$. The same experiment was carried out in 10 % plasma when detecting INH on Au|CuPPI. The INH interacted at the dendrimer surface slightly differently in this case by oxidising at 280 mV which remains constant upon an increase in concentration of INH as can be seen in Figure 4-19 (A). The linear calibration plot can be seen in Figure 4-19 (B). The LOD for the sensor in plasma was found to be $3.3 \mu\text{M}$ and LOQ of $10.99 \mu\text{M}$.

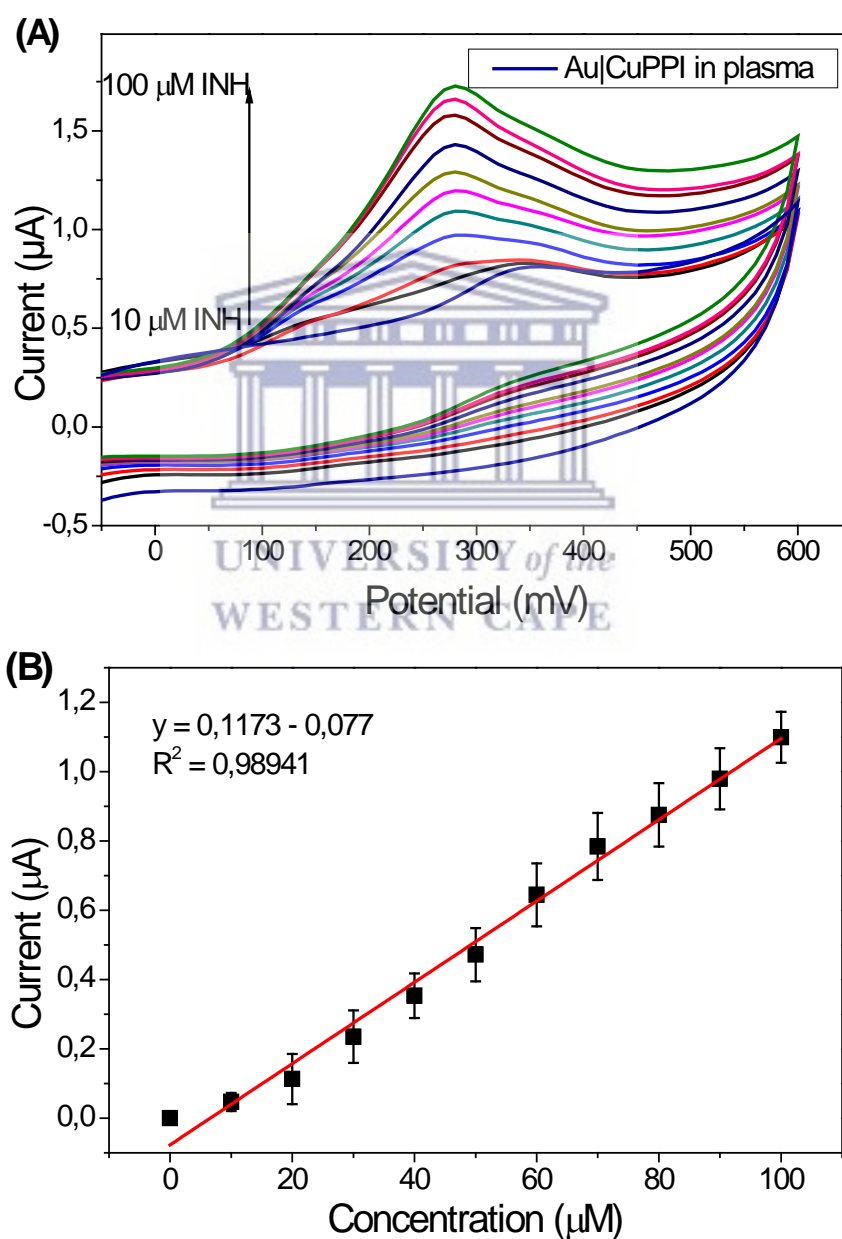


Figure 4-19: (A) CV detection of 10, 20, 30, 40, 50, 60, 70, 80, 90 and 100 μM INH at Au|CuPPI (B) linear calibration plot of I_{pa} vs concentration of INH in 10 % human plasma

4.4.2 Ethambutol

Some components in synthetic urine reacts at the Au|CuPPI surface at roughly 1000 mV, which is the same potential at which ethambutol oxidises at the electrode surface. This resulted in the ethambutol interacting with the synthetic urine components which both oxidise at the same potential, resulting in a linear range at a lower concentration of 1 μM and 4 μM with a LOD of 0.811 μM and LOQ of 2.704 μM . After 4 μM ETH is added to the system the calibration curve plateaus, which could be a result of electrode fouling or saturation as shown in Figure 4-21 (A).

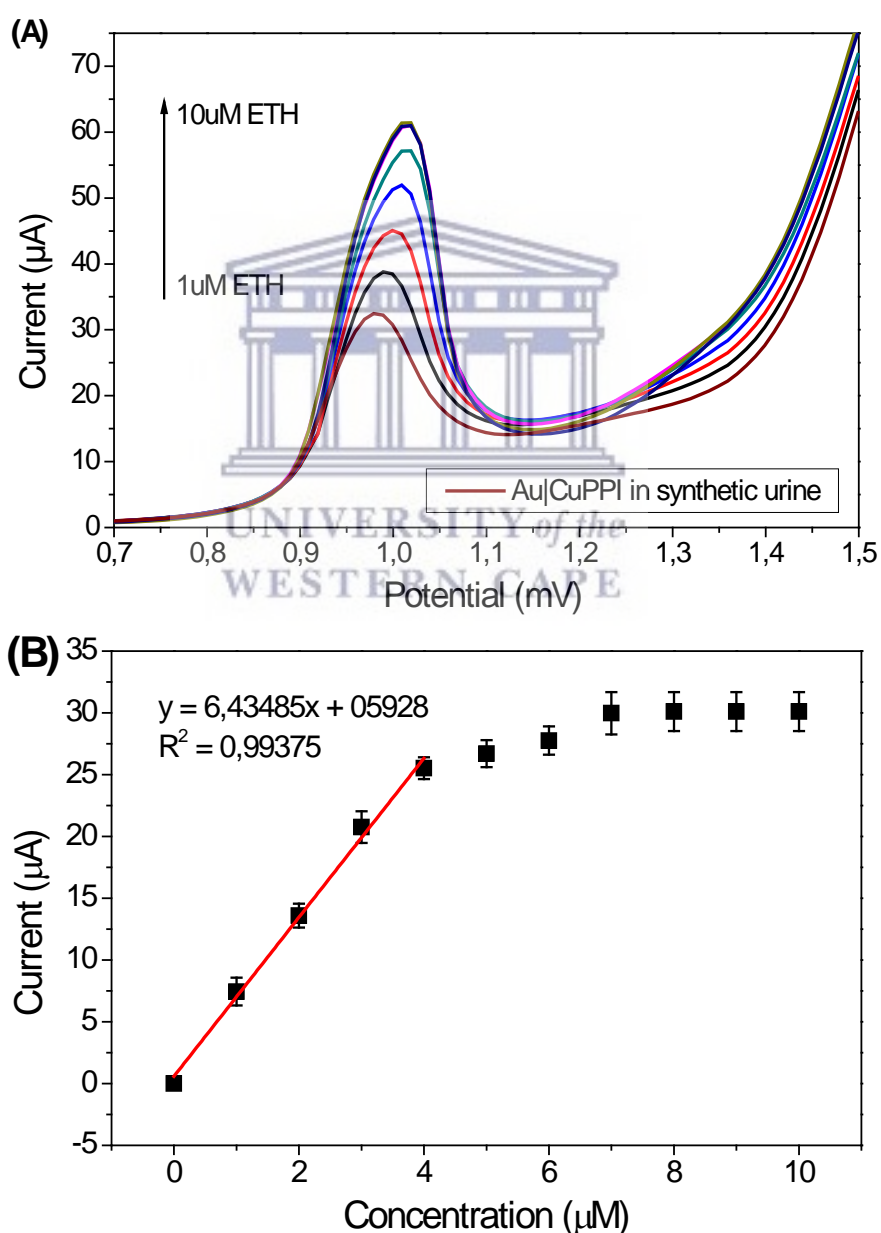


Figure 4-20: (A) DPV detection of 1, 2, 3, 4, 5, 6, 7, 8, 9 and 10 μM ETH and (B) linear calibration plot of I_{pa} vs concentration of ETH in 20 % synthetic urine

The complexity of the matrix and its components are a huge factor in this saturation. The detection of ETH was then carried out in the 10 % human plasma matrix and the resulting calibration curve is shown in Figure 4-21 (B). The oxidation of ETH at the electrode surface resulted in a peak appearing at 900 mV which was monitored for analytical purposes. A linear range was obtained from 100 μM to 1000 μM with a LOD of 48.52 μM and LOQ of 161.76 μM . The matrix effects in plasma does not allow for lower concentrations of ETH to be determined.

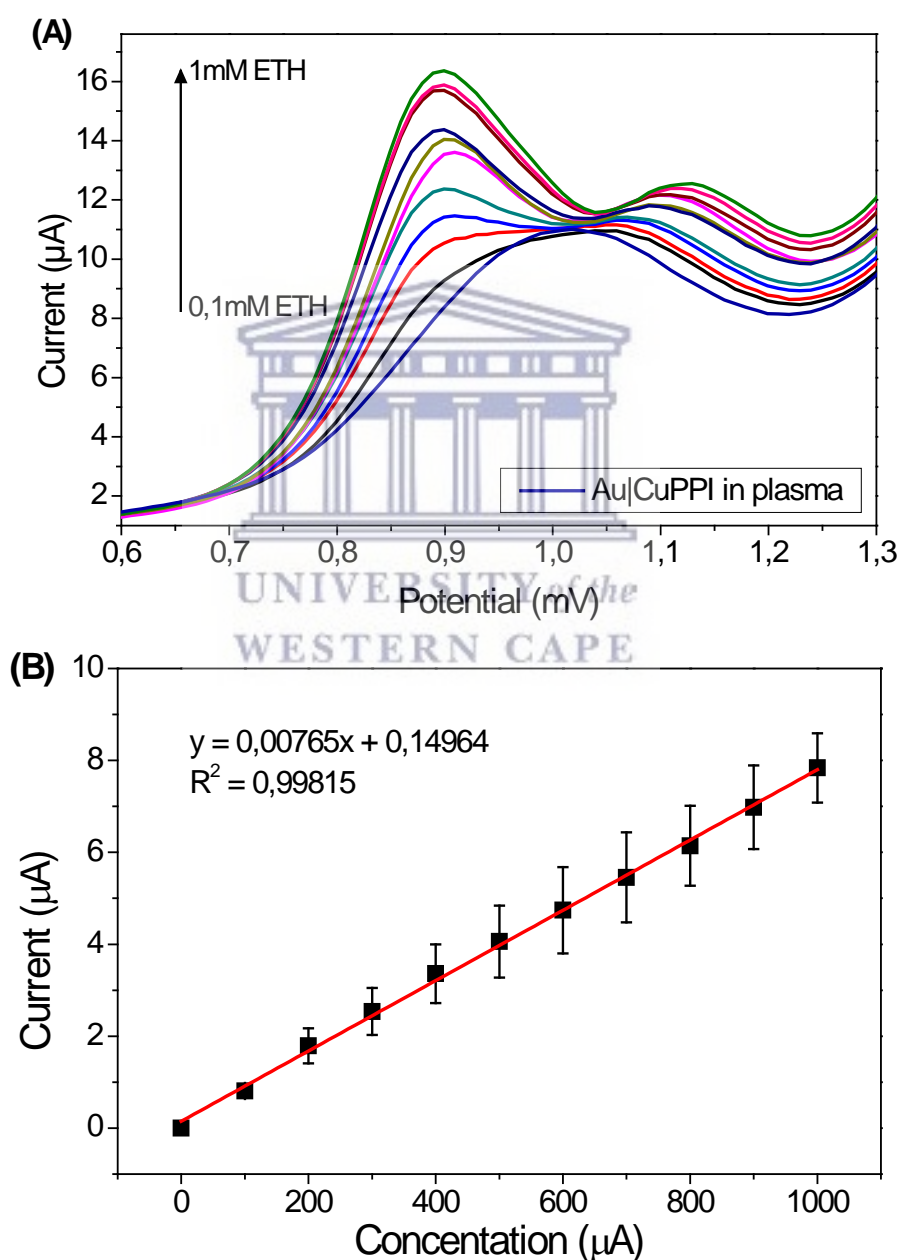
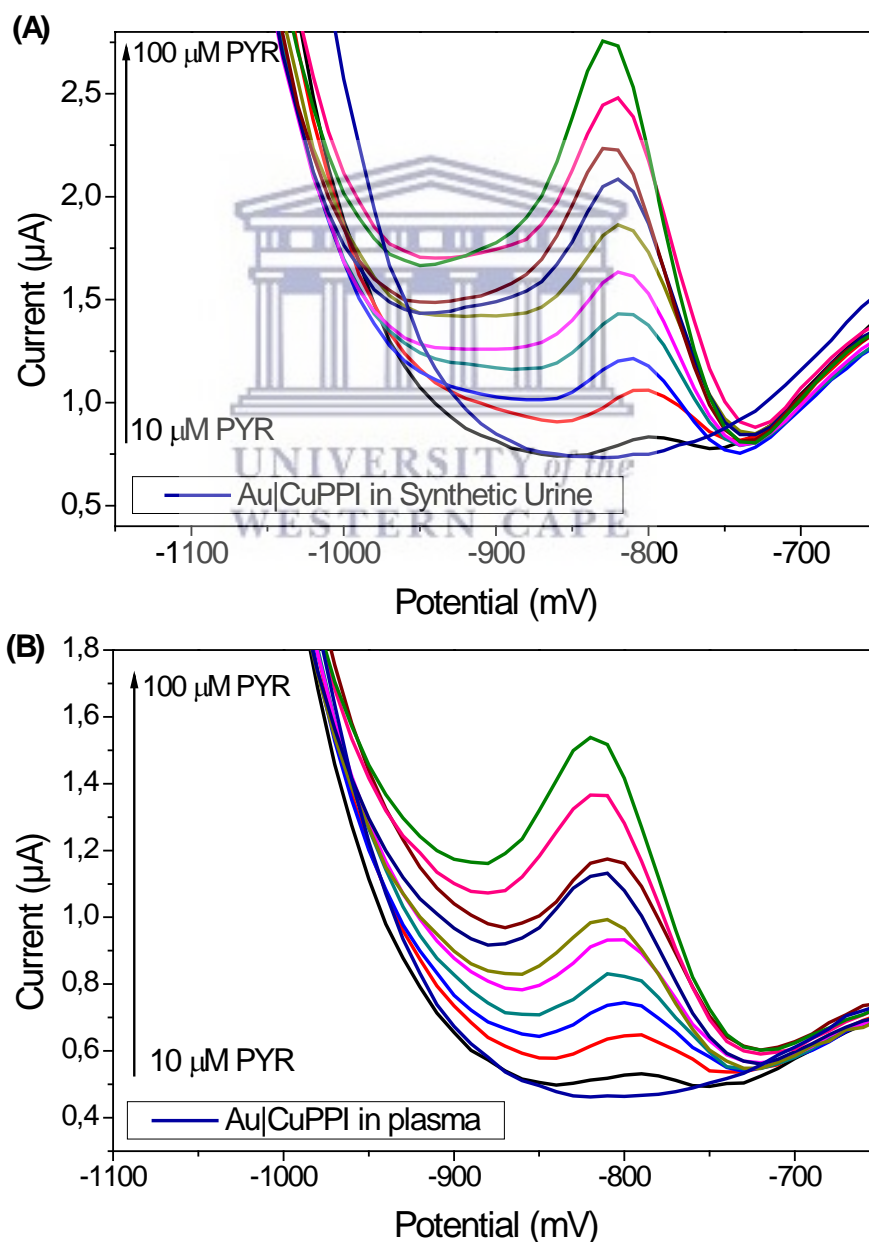


Figure 4-21: (A) DPV detection of 100, 200, 300, 400, 500, 600, 700, 800, 900 and 1000 μM ETH at Au|CuPPI and (B) linear calibration plot of I_{pa} vs concentration of ETH in 10 % human plasma

4.4.3 Pyrazinamide

The detection of pyrazinamide was carried out in the two complex media with both resulting in calibration curves in the range of 10 to 100 μM PYR as shown in Figure 4-22. The oxidation peak at -800 mV was monitored upon an increase in concentration of PYR in both media. The peak current increases in direct proportion to an increase in concentration. The sensitivity of the sensor was found to be higher in synthetic urine than plasma with values of 0.02165 $\mu\text{A}/\mu\text{M}$ and 0.00971 $\mu\text{A}/\mu\text{M}$ respectively. The sensor was thus able to obtain a LOD of 4.19 μM and LOQ of 13.98 μM in synthetic urine and a LOD of 3.55 μM and LOQ of 11.84 μM in plasma.



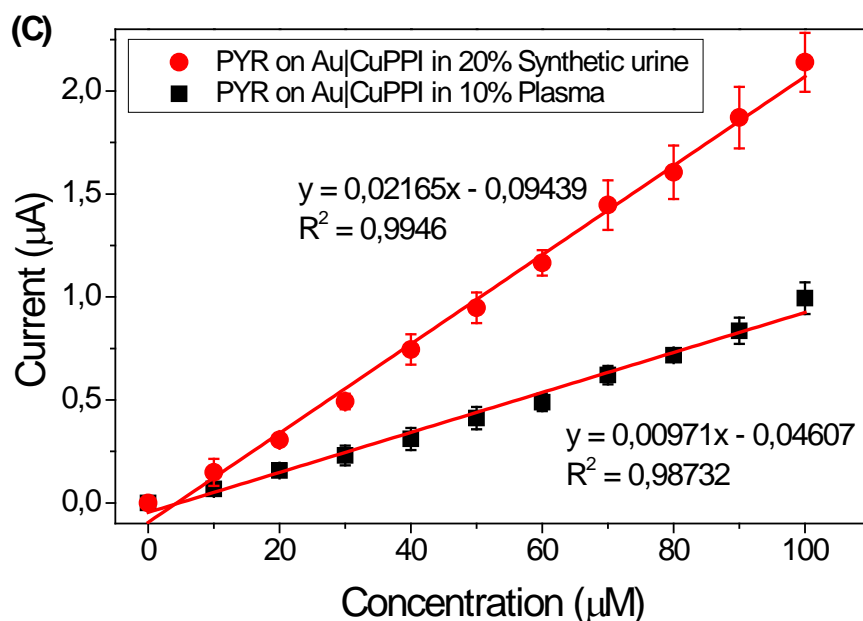


Figure 4-22: DPV detection of 10, 20, 30, 40, 50, 60, 70, 80, 90 and 100 µM PYR in (A) 20 % synthetic urine and (B) 10 % plasma and (C) calibration plot of I_{pa} vs concentration of PYR

4.4.4 Rifampicin

Rifampicin was found to have similar issues as ETH when carrying out the detections in both synthetic urine and plasma. The peaks attributed to RIF were masked by the effect of the matrices. In synthetic urine, the RIF interacted with the components of the synthetic urine in such a fashion that it caused the peak at 1000 mV to increase upon additions of 0.5 µM RIF as shown in Figure 4-23 (A). This current response increased linearly up until 2.5 µM after which the electrode was saturated and the calibration curve plateaued in Figure 4-23 (B). The LOD in synthetic urine was found to be 0.153 µM with an LOQ of 0.511 µM.

The matrix effects in plasma were again limiting the detection of RIF. The usual peaks attributed to this complex molecule was not visible except for one around 1100 mV. RIF was successfully detected by adding increments of 100 µM to the 10 % plasma matrix with a LOD of 21.35 µM and LOQ of 71.19 µM achieved. The sensitivity of the sensor was much greater in synthetic urine than plasma as previously stated. The detection of RIF calibration curves in 10 % plasma are as shown in Figure 4-24 (A) and (B). Electrochemical sensing has previously been completed in real samples, however most cases analyse the tablet form which is diluted in water and then detected in

buffer [65]. Not many instances have been found in which the calibrations are carried out in the complex media as well as the recovery, which is what is covered in the next section.

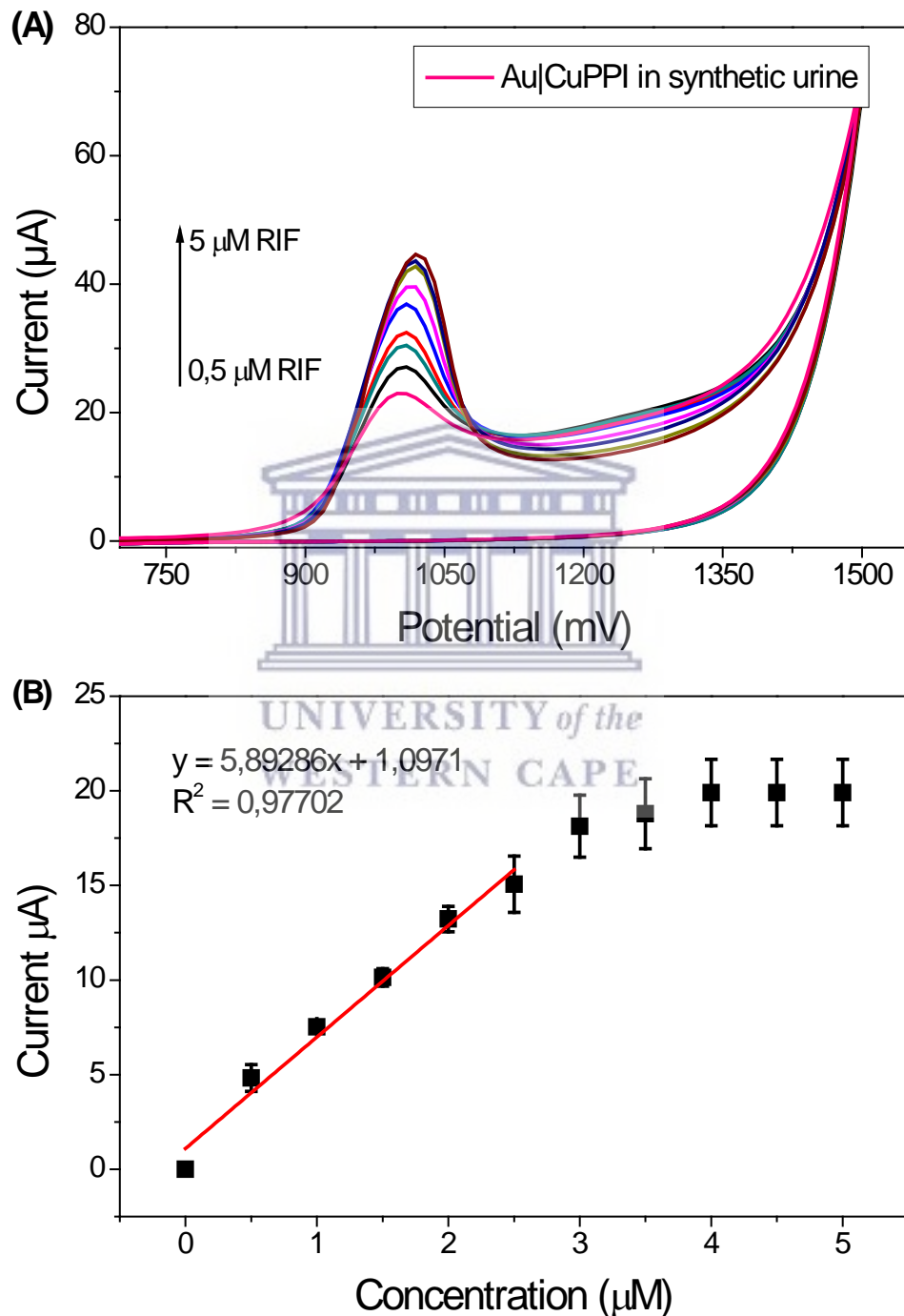


Figure 4-23: (A) CV detection of concentrations of 0.5, 1, 1.5, 2, 2.5, 3, 3.5, 4, 4.5 and 5 μM RIF at Au|CuPPI and (B) linear calibration plot of I_{pa} vs concentration of RIF in 20 % synthetic urine

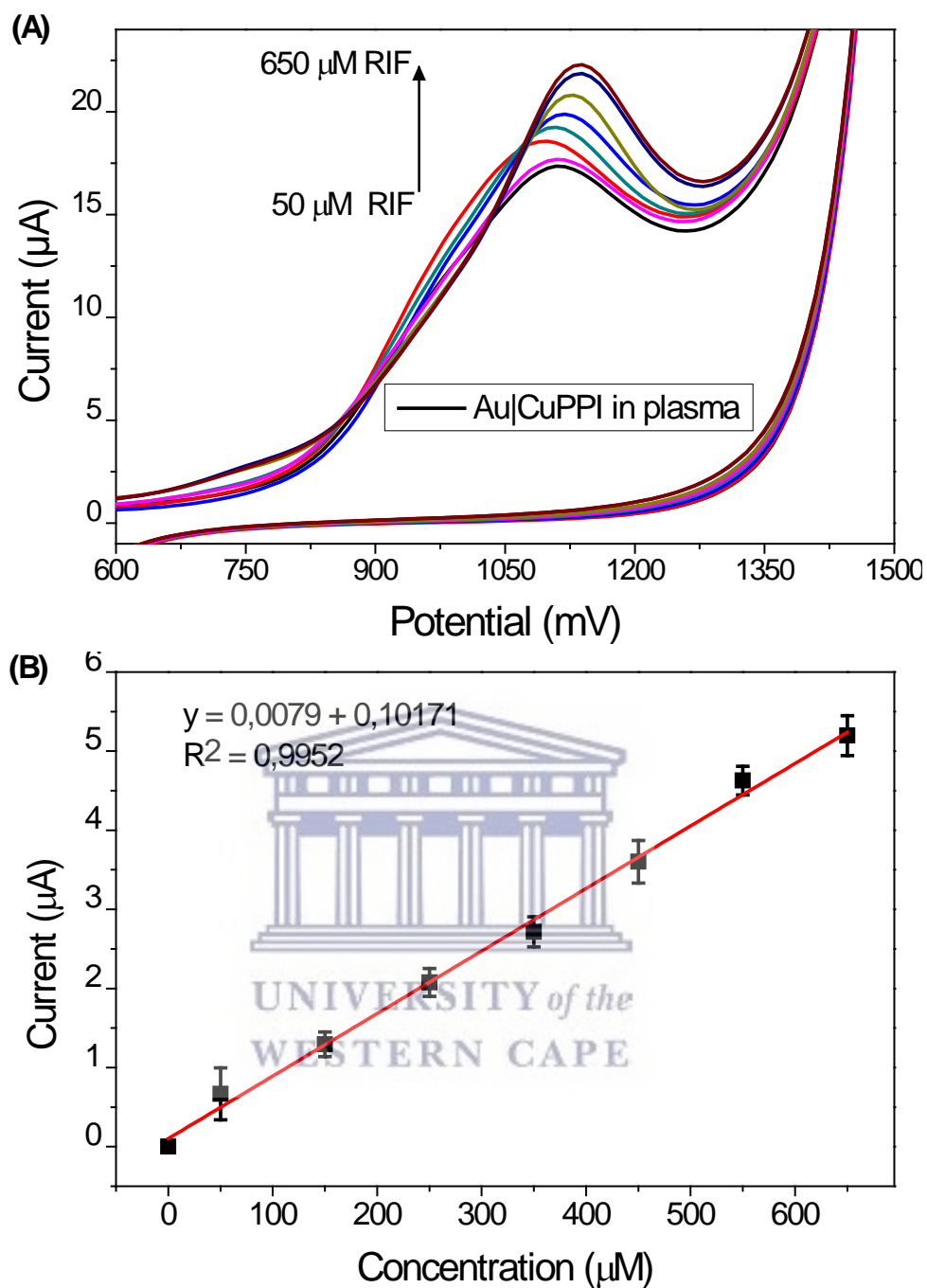


Figure 4-24: (A) CV detection of concentrations of 50, 150, 250, 350, 450, 550 and 650 μM RIF at Au|CuPPI and (B) linear calibration plot of I_{pa} vs concentration of RIF in 10 % human plasma

4.4.5 Recovery Studies of Au|CuPPI electrode

Each of the anti-TB drugs were also studied using a recovery experiment. In this case each of the tablet forms of the drug were dissolved in either 20 % synthetic urine or 10 % plasma, and detected using the Au|CuPPI modified electrode. The concentrations

of the tablets were then determined using the calibration curves above with the results of these shown in Table 4-4.

Table 4-4: Analytical efficiencies of the Au|CuPPI sensor towards of anti-TB drugs in 20 % synthetic urine and 10 % plasma

		LOD (μM)	LOQ (μM)	Sensitivity ($\mu\text{A}/\mu\text{M}$)	Spiked (μM)	Detected (μM)	Recovery (%)
INH	Synthetic urine	3.23	10.78	0.00787	20	18.5	92.5
					40	43	107.5
					60	63	105
	Plasma	3.3	10.99	0.1173	20	22.6	113
					40	39.78	99.45
					0	60.97	101.61
ETH	Synthetic urine	0.811	2.704	6.434	2	2.16	108
					4	3.91	94.75
					6	-	Out of linear range
	Plasma	48.52	161.76	0.00765	200	178.54	89.27
					400	435.56	108.89
					600	622.02	103.67
PYR	Synthetic urine	4.19	13.98	0.02165	20	20.236	101.18
					40	41.93	104.83
					60	57.44	95.74
	Plasma	3.55	11.84	0.00971	20	21.73	108.66
					40	38.96	97.39
					60	55.57	92.62
RIF	Synthetic urine	0.153	0.511	5.892	1	1.08	107.85
					2	2.05	102.46
					4	-	Out of linear range
	Plasma	21.35	71.19	0.0079	150	160	106.724
					350	360.88	103.11
					550	571.78	103.96

The recovery of each of these drugs was successful in both of the matrices shown. The lowest value of recovery is 89.27 %, which is for the detection of 200 μM ETH in plasma, while the highest value is 113 % for 20 μM INH in plasma. These values have

the highest error due to the many components present in plasma which interfere with detection through fouling of the electrode surface. The results for the sensor in the complex matrices are excellent with an average error of less than 9%. The Au|CuPPI has been proven to be an easy-to-assemble, stable and selective sensor which is able to detect all four anti-TB drugs in both synthetic urine and plasma with LOD in the 0.153 μM to 45.82 μM concentration range.



4.5 **Conclusions**

After diagnosis, tuberculosis is treated using a combination of four anti-TB drugs over the course of six months. These drugs are named isoniazid, ethambutol, rifampicin and pyrazinamide. These four drugs each have their own mechanism of fighting the *Mycobacterium Tubercle*, which is responsible for this deadly disease. There are currently many laboratory techniques that are used to detect these drugs for analytical purposes. These techniques are however very expensive, require sample preparation, time and a skilled technician to run the instruments. Here a simple, metallodendrimer based electrochemical sensor consisting of the copper based metallodendrimer (Au|CuPPI) was developed for anti-TB drug detection. This sensor was then applied to the detection of the anti-TB drugs and compared to a well-established technique such as UV-Vis. The limit of detection of the electrochemical sensor ranged from 0.022 nM to 1.16 nM and the UV-Vis technique had an LOD between 24.3 nM and 54.7 nM for all four of the anti-TB drugs. Not only is the limit of detection better for the electrochemical sensor better, but the fact that the molecules do not have to be UV-vis active or undergo pre-treatments give this sensor the advantage here. Electrochemical analysis of samples also allows for a portable and easy to use mode of detection, allowing for point of care analysis and rapid response time. This sensor can thus be successfully applied as a form of therapeutic drug monitoring during TB-treatment in order to minimise the adverse drug reactions brought on by the treatment of the disease [66]. The dendritic electrochemical sensor was then applied towards the detection of anti-TB drugs in synthetic urine and plasma. The sensor was successful and obtained very good results in terms of linear range, regression and limits of detection. The LOD in these media ranged from 0.153 μ M to 45.82 μ M in concentration and the recovery values from 89.27 % to 113 %. The dynamic linear range of each of the drugs in the real samples were at a higher concentration range compared to when the detection is carried out in buffer. This is due to the interferences of the compounds present in the synthetic urine as well as fouling of the electrode surface with plasma proteins. However, the results obtained are well within the therapeutic range for detection as discussed in the next chapter.

The simple Au|CuPPI chemical sensor has thus proven to be a viable candidate for real life application in selectively determining the concentration of towards four anti-TB drugs leftover in both plasma and urine.



4.6 **References**

- [1] W. Zhang, R. Wang, F. Luo, P. Wang, and Z. Lin, "Miniaturized electrochemical sensors and their point-of-care applications," *Chinese Chemical Letters*, **2019**.
- [2] L. Xue, W. Wang, Y. Guo, G. Liu, and P. Wan, "Flexible polyaniline/carbon nanotube nanocomposite film-based electronic gas sensors," *Sensors and Actuators, B: Chemical*, vol. 244, pp. 47–53, **2017**.
- [3] G. Matzeu, L. Florea, and D. Diamond, "Advances in wearable chemical sensor design for monitoring biological fluids," *Sensors and Actuators, B: Chemical*, vol. 211, pp. 403–418, **2015**.
- [4] C. Rassie, R. a Olowu, T. T. Waryo, L. Wilson, A. Williams, P. G. Baker, and E. I. Iwuoha, "Dendritic 7T-Polythiophene Electro-Catalytic Sensor System for the Determination of Polycyclic Aromatic Hydrocarbons," *International Journal of Electrochemical Science*, vol. 6, pp. 1949–1967, **2011**.
- [5] K. Pokpas, N. Jahed, P. G. Baker, and E. I. Iwuoha, "Complexation-based detection of nickel(II) at a graphene-chelate probe in the presence of cobalt and zinc by adsorptive stripping voltammetry," *Sensors (Switzerland)*, vol. 17, p. 1711, **2017**.
- [6] E. Bakker and M. Telting-Diaz, "Electrochemical Sensors," *Analytical Chemistry*, vol. 74, pp. 2781–2800, **2002**.
- [7] C. Dejous, H. Hallil, V. Raimbault, R. Rukkumani, and J. V. Yakhmi, "Using microsensors to promote the development of innovative therapeutic nanostructures," in *Nanostructures for Novel Therapy: Synthesis, Characterization and Applications*, Elsevier, **2017**, pp. 539–566.
- [8] World Health Organisation (WHO), "Global Tuberculosis Report 2019," **2019**.
- [9] G. S. Timmins and V. Deretic, "Mechanisms of action of isoniazid," *Molecular Microbiology*, vol. 62, pp. 1220–1227, **2006**.
- [10] F. G. Winder, P. Collins, and S. A. Rooney, "Effects of isoniazid on mycolic acid synthesis in Mycobacterium tuberculosis and on its cell envelope.," *The Biochemical journal*, vol. 117, p. 27P, **1970**.
- [11] A. N. Unissa, S. Subbian, L. E. Hanna, and N. Selvakumar, "Overview on mechanisms of isoniazid action and resistance in Mycobacterium tuberculosis," *Infection, Genetics and Evolution*, vol. 45, pp. 474–492, **2016**.
- [12] A. C. Pettit, J. Bethel, Y. Hirsch-Moverman, P. W. Colson, and T. R. Sterling, "Female sex and

- discontinuation of isoniazid due to adverse effects during the treatment of latent tuberculosis,” *The Journal of Infection*, vol. 67, pp. 424–32, **2013**.
- [13] S. Wu, L. Lan, J. Jiang, X. Ding, C. M. Ho, Y. Lou, and G. Fan, “Simultaneous determination of the potent anti-tuberculosis regimen—Pyrazinamide, ethambutol, protionamide, clofazimine in beagle dog plasma using LC–MS/MS method coupled with 96-well format plate,” *Journal of Pharmaceutical and Biomedical Analysis*, vol. 168, pp. 44–54, **2019**.
- [14] S. Chakraborty and K. Y. Rhee, “Tuberculosis drug development: History and evolution of the mechanism-based paradigm,” *Cold Spring Harbor Perspectives in Medicine*, vol. 5, pp. 1–11, **2015**.
- [15] L. F. Diniz, P. S. Carvalho, C. C. De Melo, and J. Ellena, “Reducing the Hygroscopicity of the Anti-Tuberculosis Drug (S,S)-Ethambutol Using Multicomponent Crystal Forms,” *Crystal Growth and Design*, vol. 17, pp. 2622–2630, **2017**.
- [16] L. D. Ghiraldi-Lopes, P. A. Z. Campanerut-Sá, G. P. C. Evaristo, J. E. Meneguello, A. Fiorini, V. P. Baldin, E. M. de Souza, R. B. de Lima Scodro, V. L. D. Siqueira, and R. F. Cardoso, “New insights on Ethambutol Targets in Mycobacterium tuberculosis,” *Infectious Disorders - Drug Targets*, vol. 19, pp. 73–80, **2018**.
- [17] N. Singh and L. Sharma, “Enantioseparation of D-and L-isomers of chiral drugs for improving their bioavailability: Some techniques including micellization with gemini surfactants,” *Indian Journal of Pharmaceutical Education and Research*, vol. 52, pp. 334–341, **2018**.
- [18] R. Yendapally and R. E. Lee, “Design, synthesis, and evaluation of novel ethambutol analogues,” *Bioorganic & medicinal chemistry letters*, vol. 18, pp. 1607–11, **2008**.
- [19] S. N. Holla, V. Mohan Babu Amberkar, P. Rajeshkrishna Bhandary, K. Meena Kumari, and M. Janardhanan, “Cycloserine induced late onset psychosis and ethambutol induced peripheral neuropathy associated with MDR-TB treatment in an Indian patient- A rare case report,” *Journal of Clinical and Diagnostic Research*, vol. 9, pp. FD01–FD03, **2015**.
- [20] N. Thapliyal, R. V. Karpoornath, and R. N. Goyal, “Electroanalysis of antitubercular drugs in pharmaceutical dosage forms and biological fluids: A review,” *Analytica Chimica Acta*, vol. 853, pp. 59–76, **2015**.
- [21] B. D. T. Pokam, J. E. Enoh, A. A. O. Eyo, N. O. Umoh, and P. W. Guemdjom, “Uric acid levels in patients on antituberculosis drugs in the southwest Region of Cameroon,” *International Journal of Mycobacteriology*, vol. 7, pp. 89–91, **2018**.
- [22] W. Song and S. Si, “The rare ethambutol-induced optic neuropathy: A case-report and literature review,” *Medicine (United States)*, vol. 96, pp. 1–4, **2017**.

- [23] Y. Zhang, M. M. Wade, A. Scorpio, H. Zhang, and Z. Sun, "Mode of action of pyrazinamide: disruption of Mycobacterium tuberculosis membrane transport and energetics by pyrazinoic acid.," *The Journal of antimicrobial chemotherapy*, vol. 52, pp. 790–5, **2003**.
- [24] S. Bavbek, N. Yilmaz, Ö. Aydın, and S. K. Ozdemir, "Pyrazinamide," *Tuberculosis*, vol. 88, pp. 141–144, **2008**.
- [25] F. Ajayi, U. Sidwaba, U. Feleni, S. Douman, E. Mxusani, L. Wilson, C. Rassie, O. Tovide, P. Baker, S. Vilikazi, R. Tshikhudo, and E. Iwuoha, "A Nanosensor System Based On Disuccinimydyl – CYP2E1 for Amperometric Detection of the Anti-Tuberculosis Drug , Pyrazinamide," *International Journal of Medical, Health, Biomedical, Bioengineering and Pharmeceutical Engineering*, vol. 8, pp. 67–71, **2014**.
- [26] G. Colucci, T. Silzle, and M. Solenthaler, "Pyrazinamide-induced sideroblastic anemia," *American Journal of Hematology*, vol. 87, pp. 305–305, **2012**.
- [27] A. M. O. Balaji, T. Sreen Rose, K. Laxminarayana Bairy, "Pyrazinamide induced maculopapular rash: A rare case report," *Research Journal of Pharmaceutical, Biological and Chemical Sciences*, vol. 7, pp. 2601–2604, **2016**.
- [28] K. U. Khayyam, F. Imam, M. Sharma, K. K. Pillai, and D. Behera, "Pyrazinamide-induced maculopapular rash.," *Indian journal of dermatology*, vol. 55, pp. 384–6, **2010**.
- [29] T. Schaberg, K. Rebhan, and H. Lode, "Risk factors for side-effects of isoniazid, rifampin and pyrazinamide in patients hospitalized for pulmonary tuberculosis.," *The European respiratory journal*, vol. 9, pp. 2026–30, **1996**.
- [30] S. Agrawal and R. Panchagnula, "Implication of biopharmaceutics and pharmacokinetics of rifampicin in variable bioavailability from solid oral dosage forms," *Biopharmaceutics & Drug Disposition*, vol. 26, pp. 321–334, **2005**.
- [31] S. Rastgar and S. Shahrokhian, "Nickel hydroxide nanoparticles-reduced graphene oxide nanosheets film: Layer-by-layer electrochemical preparation, characterization and rifampicin sensory application," *Talanta*, vol. 119, pp. 156–163, **2014**.
- [32] M. Grobbelaar, G. E. Louw, S. L. Sampson, P. D. van Helden, P. R. Donald, and R. M. Warren, "Evolution of rifampicin treatment for tuberculosis," *Infection, Genetics and Evolution*, vol. 74, p. 103937, **2019**.
- [33] S. Mani, S. Cheemalapati, S. Chen, and B. Devadas, "Anti-tuberculosis Drug Pyrazinamide Determination at Multiwalled Carbon Nanotubes / Graphene Oxide Hybrid Composite Fabricated Electrode," *International Journal of Electrochemical Science*, vol. 10, pp. 7049–7062,

2015.

- [34] J. Soloducho and J. Cabaj, "Conducting Polymers in Sensor Design," in *Conducting Polymers*, InTech, 2016, pp. 27–47.
- [35] B. K. Jena and C. R. Raj, "Au nanoparticle decorated silicate network for the amperometric sensing of isoniazid.," *Talanta*, vol. 80, pp. 1653–6, 2010.
- [36] D. A. Tomalia, A. M. Naylor, and W. A. Goddard, "Starburst Dendrimers: Molecular-Level Control of Size, Shape, Surface Chemistry, Topology, and Flexibility from Atoms to Macroscopic Matter," *Angewandte Chemie International Edition in English*, vol. 29, pp. 138–175, 1990.
- [37] M. Jędrych, K. Borowska, R. Galus, and B. Jodłowska-Jędrych, "The evaluation of the biomedical effectiveness of poly(amido)amine dendrimers generation 4.0 as a drug and as drug carriers: a systematic review and meta-analysis.," *International journal of pharmaceutics*, vol. 462, pp. 38–43, 2014.
- [38] R. G. Bellini, A. P. Guimarães, M. A. C. Pacheco, D. M. Dias, V. R. Furtado, R. B. de Alencastro, and B. A. C. Horta, "Association of the anti-tuberculosis drug rifampicin with a PAMAM dendrimer.," *Journal of molecular graphics & modelling*, vol. 60, pp. 34–42, 2015.
- [39] K. Scott, "Electrochemical Principles and Characterization of Bioelectrochemical Systems," in *Microbial Electrochemical and Fuel Cells: Fundamentals and Applications*, Elsevier Inc., 2016, pp. 29–66.
- [40] Y. Yi, G. Weinberg, M. Prenzel, M. Greiner, S. Heumann, S. Becker, and R. Schlögl, "Electrochemical corrosion of a glassy carbon electrode," *Catalysis Today*, vol. 295, pp. 32–40, 2017.
- [41] X. Xu, A. Makaraviciute, J. Pettersson, S. L. Zhang, L. Nyholm, and Z. Zhang, "Revisiting the factors influencing gold electrodes prepared using cyclic voltammetry," *Sensors and Actuators, B: Chemical*, vol. 283, pp. 146–153, 2019.
- [42] Q. L. Zhao, Z. L. Zhang, L. Bao, and D. W. Pang, "Surface structure-related electrochemical behaviors of glassy carbon electrodes," *Electrochemistry Communications*, vol. 10, pp. 181–185, 2008.
- [43] M. A. Karimi, A. Hatefi-Mehrjardi, M. Mazloum-Ardakani, R. Behjatmanesh-Ardakani, M. H. Mashhadizadeh, and S. Sargazi, "Study of electrocatalytic oxidation of isoniazid drug using Alizarin Red S as A mediator on the glassy carbon electrode," *International Journal of Electrochemical Science*, vol. 5, pp. 1634–1648, 2010.

- [44] Z. Sepehri, H. Bagheri, E. Ranjbari, M. Amiri-Aref, S. Amidi, M. R. Rouini, and Y. H. Ardakani, "Simultaneous electrochemical determination of isoniazid and ethambutol using poly-melamine/electrodeposited gold nanoparticles modified pre-anodized glassy carbon electrode," *Ionics*, vol. 24, pp. 1253–1263, **2018**.
- [45] A. E. B. Lima, G. E. Luz, N. C. Batista, E. Longo, L. S. Cavalcante, and R. S. Santos, "Determination of Ethambutol in Aqueous Medium Using an Inexpensive Gold Microelectrode Array as Amperometric Sensor," *Electroanalysis*, vol. 28, pp. 985–989, **2016**.
- [46] M. F. M. F. Bergamini, D. P. Santos, M. V. B. Zanoni, M. Valnice, and B. Zanoni, "Electrochemical behavior and voltammetric determination of pyrazinamide using a poly-histidine modified electrode," *Journal of Electroanalytical Chemistry*, vol. 690, pp. 47–52, **2013**.
- [47] B. Devadas, S. Cheemalapati, S. M. Chen, M. A. Ali, and F. M. A. Al-Hemaid, "Highly sensing graphene oxide/poly-arginine-modified electrode for the simultaneous electrochemical determination of buspirone, isoniazid and pyrazinamide drugs," *Ionics*, vol. 21, pp. 547–555, **2015**.
- [48] S. Amidi, Y. H. Ardakani, M. Amiri-Aref, E. Ranjbari, Z. Sepehri, and H. Bagheri, "Sensitive electrochemical determination of rifampicin using gold nanoparticles/poly-melamine nanocomposite," *RSC Advances*, **2017**.
- [49] K. R. Ward, N. S. Lawrence, R. S. Hartshorne, and R. G. Compton, "Cyclic Voltammetry of the EC' Mechanism at Hemispherical Particles and Their Arrays: The Split Wave," *The Journal of Physical Chemistry C*, vol. 115, pp. 11204–11215, **2011**.
- [50] P. Balasubramanian, T. S. T. Balamurugan, S. M. Chen, T. W. Chen, and P. H. Lin, "A novel, efficient electrochemical sensor for the detection of isoniazid based on the B/N doped mesoporous carbon modified electrode," *Sensors and Actuators, B: Chemical*, vol. 283, pp. 613–620, **2019**.
- [51] Y.-C. Hsieh and C.-W. Whang, "Analysis of ethambutol and methoxyphenamine by capillary electrophoresis with electrochemiluminescence detection," *Journal of Chromatography A*, vol. 1122, pp. 279–282, **2006**.
- [52] S. Chen, W. Yingliang, L. Shumian, and L. Chao, "Determination of ethambutol at glassy carbon electrode modified with multiwall carbon nanotubes," *Chemia Analityczna*, vol. 53, pp. 511–521, **2008**.
- [53] S. Cheemalapati, B. Devadas, and S.-M. Chen, "Highly sensitive and selective determination of pyrazinamide at poly-L-methionine/reduced graphene oxide modified electrode by differential

- pulse voltammetry in human blood plasma and urine samples,” *Journal of Colloid and Interface Science*, vol. 418, pp. 132–139, **2014**.
- [54] Y. Yan, J. Ma, X. Bo, and L. Guo, “Rod-like Co based metal-organic framework embedded into mesoporous carbon composite modified glassy carbon electrode for effective detection of pyrazinamide and isonicotinyl hydrazide in biological samples,” *Talanta*, vol. 205, p. 120138, **2019**.
- [55] P. R. Oliveira, A. F. Schibelbain, E. G. C. Neiva, A. J. G. Zarbin, L. H. Marcolino, and M. F. Bergamini, “Nickel hexacyanoferrate supported at nickel nanoparticles for voltammetric determination of rifampicin,” *Sensors and Actuators, B: Chemical*, vol. 260, pp. 816–823, **2018**.
- [56] K. Asadpour-Zeynali and F. Mollarasouli, “Novel electrochemical biosensor based on PVP capped CoFe₂O₄@CdSe core-shell nanoparticles modified electrode for ultra-trace level determination of rifampicin by square wave adsorptive stripping voltammetry,” *Biosensors and Bioelectronics*, vol. 92, pp. 509–516, **2017**.
- [57] S. Arifa Begum, D. Basava Raju, and N. Rama Rao, “Simultaneous estimation of rifampicin and isoniazid in combined dosage form by a simple UV spectrophotometric method,” *Der Pharmacia Lettre*, vol. 5, pp. 419–426, **2013**.
- [58] A. M. I. Mohamed, F. A. F. Mohamed, N. N. Atia, and S. M. Botros, “Ethambutol-Cobalt (II) ions complexation spectral characteristics and applications for quantitative analysis,” *Pakistan Journal of Pharmaceutical Sciences*, vol. 28, pp. 603–609, **2015**.
- [59] M. A. M. Hagga and S. Sultana, “A novel quantitative method for the simultaneous assay of rifampicin (RIF), isoniazid (INH), ethambutol (EMB), and pyrazinamide (PYP) in 4-FDC tablets,” *Oriental Journal of Chemistry*, vol. 32, pp. 3081–3087, **2016**.
- [60] E. A. Illarionova, A. I. Illarionov, and O. L. Nikonovich, “Definition of electronic transitions in the UV and visible spectral regions in rifampicin molecules,” *Bulletin of the Russian Academy of Sciences: Physics*, vol. 80, pp. 40–43, **2016**.
- [61] M. Sayana, T. Jyothi, T. Veeraiah, and V. Reddy, “Spectrophotometric determination of ethambutol in pure and pharmaceutical forms using triphenyl methane dyes,” *International journal of pharmaceutical sciences and research*, vol. 7, pp. 4191–4199, **2016**.
- [62] I. Zentner, H. P. Schlecht, L. Khensouvann, N. Tamuhla, M. Kutzler, V. Ivaturi, J. G. Pasipanodya, T. Gumbo, C. A. Peloquin, G. P. Bisson, and C. Vinnard, “Urine colorimetry to detect Low rifampin exposure during tuberculosis therapy: A proof-of-concept study,” *BMC Infectious Diseases*, vol. 16, **2016**.

- [63] N. Bunyakul and A. J. Baeumner, "Combining electrochemical sensors with miniaturized sample preparation for rapid detection in clinical samples," *Sensors (Switzerland)*, vol. 15, pp. 547–564, **2015**.
- [64] J. E. Contreras-Naranjo and O. Aguilar, "Suppressing non-specific binding of proteins onto electrode surfaces in the development of electrochemical immunosensors," *Biosensors*, vol. 9, pp. 1–23, **2019**.
- [65] P. K. Sonkar, M. Yadav, K. Prakash, V. Ganesan, M. Sankar, D. K. Yadav, and R. Gupta, "Electrochemical sensing of rifampicin in pharmaceutical samples using meso-tetrakis(4-hydroxyphenyl)porphyrinato cobalt(II) anchored carbon nanotubes," *Journal of Applied Electrochemistry*, vol. 48, pp. 937–946, **2018**.
- [66] I. Zentner, H. P. Schlecht, L. Khensouvann, N. Tamuhla, M. Kutzler, V. Ivaturi, J. G. Pasipanodya, T. Gumbo, C. A. Peloquin, G. P. Bisson, and C. Vinnard, "Urine colorimetry to detect Low rifampin exposure during tuberculosis therapy: A proof-of-concept study," *BMC Infectious Diseases*, vol. 16, p. 242, **2016**.

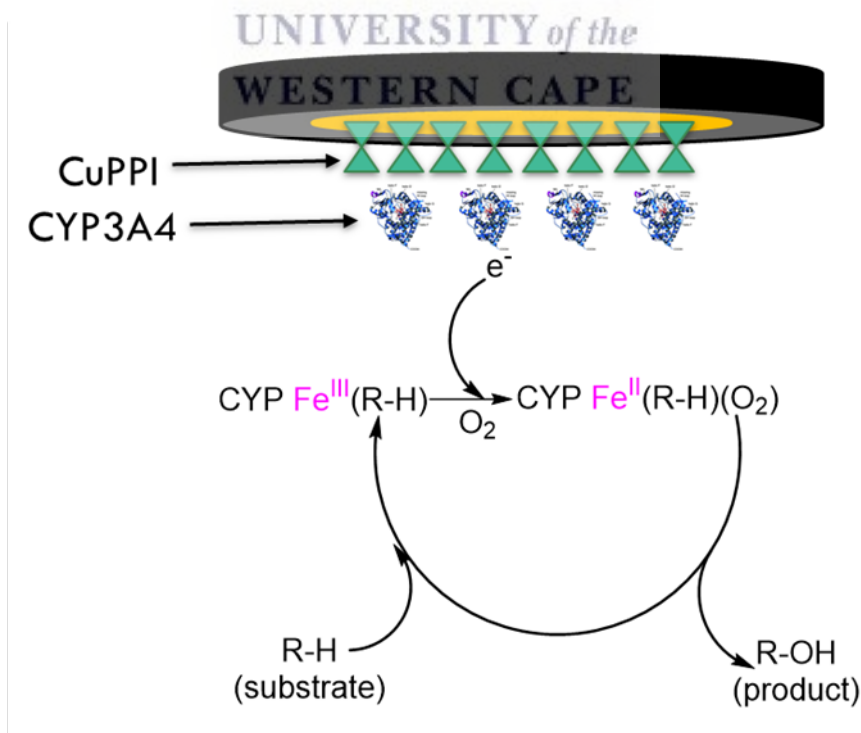


Chapter 5

5 CYP3A4 biosensor system for anti-TB drugs

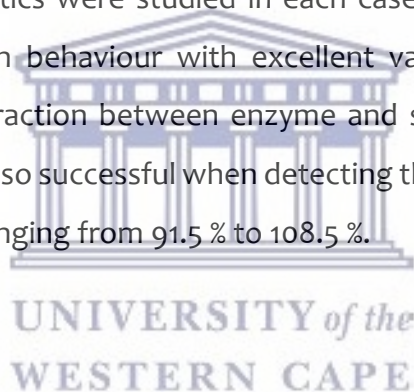
Abstract

Cytochrome P450's are responsible for the metabolism of a large variety of substances, including carcinogens, drugs and many others. CYP3A4, a part of this group of enzymes, is responsible for metabolising 50 % of all known drugs. Enzymes are perfect for use as recognition elements in biosensors since they have the advantage of being highly specific and sensitive. This enzyme was combined with first generation metallodendrimers, CuPPI for the detection of four first line anti-TB drugs. The method of action is summarised in the graphical abstract in Scheme 5-1 below:



Scheme 5-1: Graphical abstract for Chapter 5

This simple biosensor was successful in detecting all four anti-TB drugs i.e. isoniazid, ethambutol, pyrazinamide and rifampicin with limits of detection ranging from 0.02244 to 0.1072 nM. The sensor system was compared to a well-established technique such as UV-Vis which was found not to be a viable option. The observed UV-Vis limitations in this study include a very long reaction time of 24 hours as well as the added inability to clearly distinguish between the spectra of the enzyme and substrate. Electrochemistry has the added benefits of providing electrons for these reactions without the necessity of an additional redox partner such as CYP reductase and NADPH. The developed biosensor was then applied towards “real samples” in the form of spiked synthetic urine and plasma. Calibration curves were carried out in the complex matrices which were diluted with 0.1 M PB. These yielded good LOD in the range of ultra-low micromolar concentration i.e. 0.165 μ M to 0.884 μ M across all drugs. The enzyme kinetics were studied in each case and the reaction showed a typical Michaelis-Menten behaviour with excellent values for Michaelis constant proving the strong interaction between enzyme and substrate in complex media. Recovery studies were also successful when detecting the real tablets in both plasma and urine with results ranging from 91.5 % to 108.5 %.



5.1 **Introduction**

5.1.1 **Cytochrome P450 enzymes**

Cytochrome P450 (CYP) enzymes are considered as one of the major groups of enzymes responsible for drug metabolism [2]. CYP's are classified as heme-enzymes since they contain a heme prosthetic group. The heme group consists of a central iron cation (Fe^{2+} or Fe^{3+}) bound to the conjugate base of a porphyrin with various ligands attached to the iron centre at the axial positions [3]. The simplified structure of the heme centre of CYP enzymes is shown in Figure 5-1 .

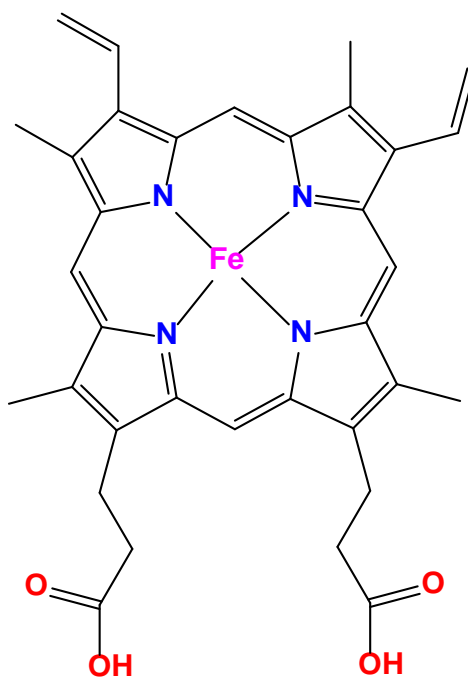


Figure 5-1: Simplified structure of a heme centre i.e. iron protoporphyrin IX [4]

The crystal structure of CYP3A4 was discovered in 2004 by two separate groups with very similar results. CYP3A4 has a general tertiary structure previously reported for P450 enzymes with variations in the B-C and F-G helices compared to other members of the family 3 group. There is a discrepancy between the structures reported by the two groups in the Arg212 side chain. The structure determined by Yano et al [5] shows the residue pointing towards the heme iron whereas Williams et al [6] has the side chain rotated by roughly 120° away from the proton pathway. This difference could be indicative of the flexibility of the enzyme to accommodate the various substrates which the enzyme metabolizes. The active site is adjacent to the heme moiety and has a relatively large volume according to Yano et al. This structure of CYP3A4 is as shown in Figure 5-2.

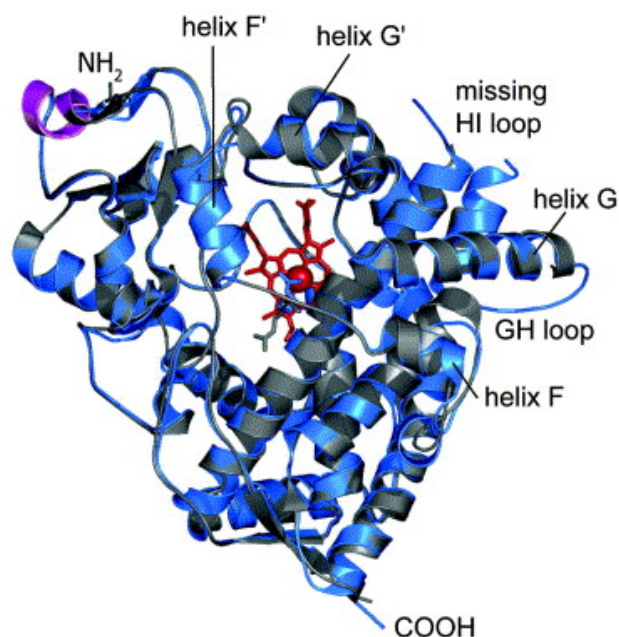
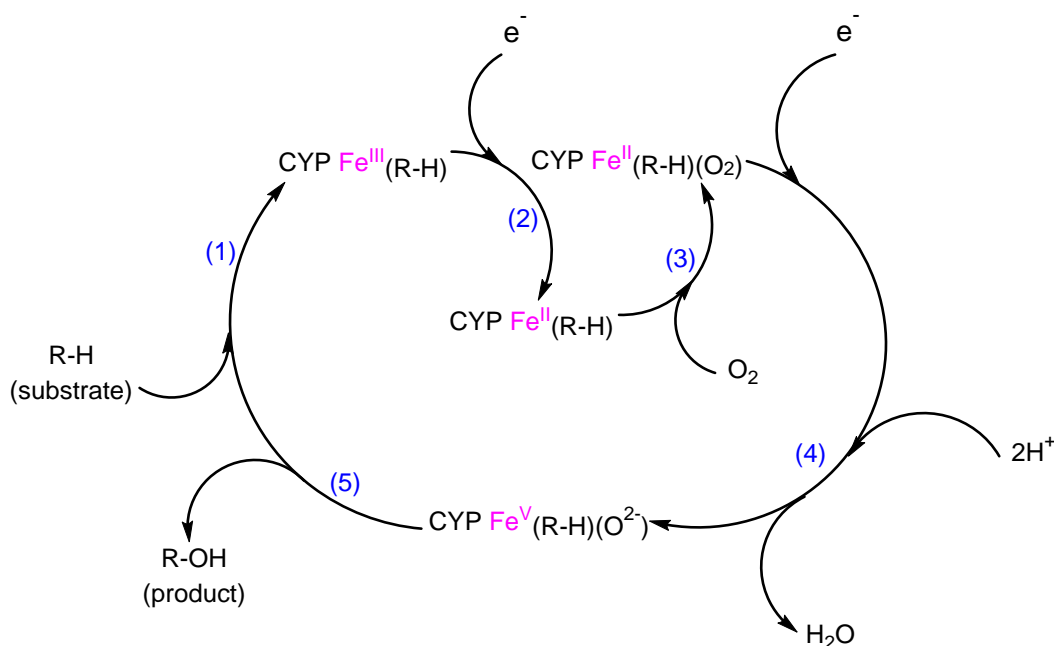


Figure 5-2: Crystal structure of Cytochrome P450 3A4 [7]

5.1.2 CYP3A4 drug metabolism

Heme-enzymes are capable of both oxidative as well as reductive chemistry with the most common forms being oxygenases and peroxidases [8]. CYP3A4 is a monooxygenase enzyme that incorporates one hydroxyl group into substrates during metabolism as well as producing one water molecule by reducing one dioxygen atom [9]. CYP3A4 follows the general mechanism of drug metabolism described in this section. A summary of the catalytic cycle and metabolism of substrates carried out by CYP enzymes is shown in Scheme 5-2 below:



Scheme 5-2: CYP450 enzyme mechanism of action

The substrate will bind in the same region as the heme group, which is called the active site (step 1). This binding causes the active site to change its conformation and reduces the heme iron centre from low spin to high spin i.e. Fe(III) to Fe(II) in step 2. This process is assisted by monooxygenation where molecular oxygen binds to the high spin complex as shown in step 3. Water is then expelled from the active site, resulting in a Fe(V) complex. Subsequent hydroxylation of the substrate takes place with the product being released from the active site and a water molecule returning to its original position close to the heme centre. The enzyme is therefore transformed back to its original state. The electrons transferred originate from other catalytic cycles and redox partners in the body, such as cytochrome P450 reductase (CPR) and cytochrome b5 [10] [11].

CYP3A4 alone has been reported to be responsible for the metabolism of 50 % of all drugs prescribed [12] and is thus one of the most important members of the CYP class of enzymes. CYP metabolises 1900 drugs, 1033 substrates, 696 inhibitors and 241 inducers [13], a list of 7 of the most common drugs in each category is shown in Table 5-1 below:

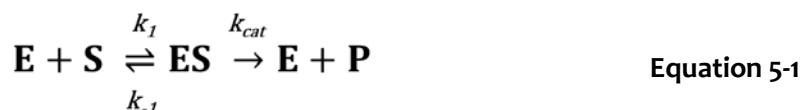
Table 5-1: A list of 7 substrates, inhibitors and inducers of the CYP3A4 enzyme [14], [15]

Substrates	Strong Inhibitors	Inducers
Tamoxifen	Ritonavir	Rifabutin
Tramadol	Erythromycin	Rifampicin
Codeine	Nelfinavir	Nevirapine
Warfarin	Sequinavir	St John's Wort
Caffeine	Telithromycin	Enzalutamide
Indinavir	Indinavir	Phenytoin
Fentanyl	Clarithromycin	Efavirenz

As can be seen from the table above, CYP3A4 metabolises drugs in various categories, from pain medication like tramadol to caffeine. Inhibitors like ritonavir on the other hand decrease the activity of CYP3A4 which results in an increase in the levels of substrates in plasma. It is thus very important to avoid consuming any of these inhibitors in conjunction with a substrate to avoid this toxicity as well as ineffective treatment. In contrast, inducers like rifampicin increase the activity of CYP3A4, sometimes resulting in up to 90% clearance of CYP3A4 substrates present in plasma. The degree to which each of these drugs induce or inhibit CYP3A4 varies and is not dependant on the classification of drugs at all [16], [17].

5.1.3 CYP enzyme kinetics

Enzymes are considered natural catalysts, which act on substrates to form products via a specific mechanism. This mechanism describes the kinetics of the substrate (S) binding to the enzyme (E) to form a complex denoted as ES, as described by G. Briggs and J. Haldane as described by Equation 5-1.



The reaction rate constants k_1 is applicable to the formation of the ES complex, k_{-1} is applicable to the dissociation of the complex and k_{cat} is applicable to the release of the product. The Michaelis constant, K_m , is defined as the ratio of complexation to dissociation of a particular reaction. A low value indicates a strong binding whereas a higher value indicates weak binding. K_m is denoted by Equation 5-2 [18]

$$K_m = \frac{k_{-1} + k_{cat}}{k_1} \quad \text{Equation 5-2}$$

The key formula which represents the relationship between the activity of the enzyme (v) and the concentration of substrate $[S]$ is shown Equation 5-3. In this equation v_{max} is the maximal activity and K_m is the Michaelis constant relative to the steps described in Equation 5-1 [19].

$$v = \frac{v_{max}[S]}{K_m + [S]} \quad \text{Equation 5-3}$$

The value of the Michaelis constant can thus be interpreted as the substrate concentration at which the rate of this reaction is half of the maximum enzyme activity. A figure representing the typical Michaelis-Menten dependence of reaction rate on substrate concentration is shown in Figure 5-3.

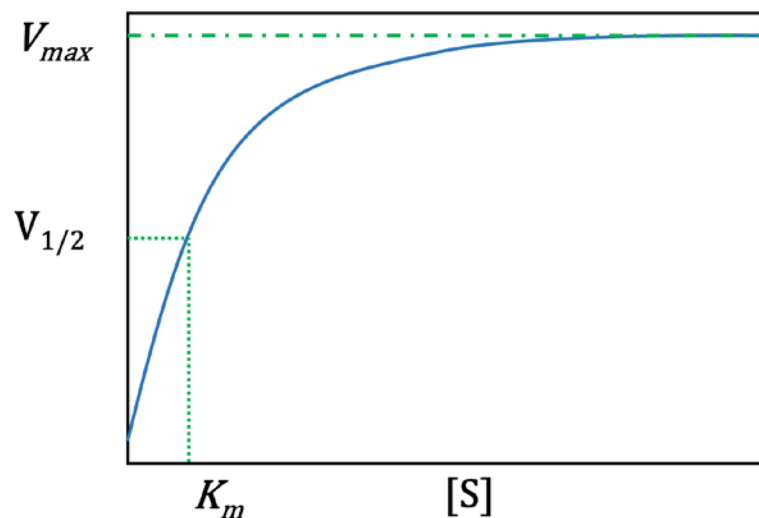


Figure 5-3: Michaelis-Menten kinetics indicating the dependence of reaction rate on substrate concentration

5.1.4 CYP3A4 in biosensors

Because of the wide variety of substrates that this enzyme metabolises, CYP3A4 has been used in very many applications in biosensors [20]. The benefit of electrochemical biosensors is that it eliminates the need for electron donors such as NADPH and cytochrome P450 reductase (CPR) [21]. The development of this type of CYP3A4 biosensor also allows for the determination of metabolic profile, considered a phenotype biosensor as described in Chapter 1. The development of phenotype biosensors will minimise the various adverse drug reactions associated with treatment of TB which include nausea, vomiting, seizures, clinical hepatitis, exanthema and many others [22]. The enzymatic biosensor thus mimics the body's natural metabolism of these drugs or substrates, allowing treatment to be tailored for different patients, minimising the ADR's mentioned above.

CYP3A4 has been combined with multi-walled carbon nanotubes to form a biosensor for detection of an inhibitor such as abiraterone [23]. Another inhibitor indinavir was also detected with the aid of didodecyldimethylammonium bromide (DDAB) vesicular system [24]. It has also been used in conjunction with a fourth generation PAMAM (polyamidoamine) dendrimer for the detection of caffeine, a substrate of CYP3A4 [25]. All of these biosensors mentioned exhibited excellent sensitivity and selectivity towards their substrates with the enzyme as a biological recognition element.

The smart materials incorporated into biosensors vary, since electrochemistry is capable of accommodating all sorts of favourable characteristics of these materials. The most important characteristic these materials possess is the ability to act as an electron mediators between enzyme-substrate interaction and the electrode surfaces. It would be preferable for these to have fast, reversible oxidation-reduction reaction couples to allow this transfers to be reproducible and quick [26]. These processes occurring at the electrode surface allows for the calculation of kinetic parameters in order to construct devices as analytical tools [21], [27]. The smart material i.e. CuPPI metallodendrimer, used in this work has been thoroughly described and characterised in Chapter 3. In this work, a CYP3A4 biosensor

incorporated with metallodendrimer (CuPPI) were used to detect isoniazid, ethambutol, rifampicin and pyrazinamide in both buffer and spiked real samples.

5.2 **Experimental**

5.2.1 **Materials**

Sodium dihydrogen phosphate (NaH_2PO_4), disodium hydrogen phosphate (Na_2HPO_4), sodium chloride (NaCl), ethanol and acetone were purchased from Sigma Aldrich, South Africa and used as received. 0.1 M Phosphate Buffer (PB) solution with pH of 7.4 was made using NaH_2PO_4 and Na_2HPO_4 . Anti-TB drugs (INH, ETH, PYR and RIF) were purchased from Sigma Aldrich, South Africa, and prepared by dissolving in 0.1 M PB pH 7.4. Ultra-pure water purified by a Milli-QTM system (Millipore) was used in all aqueous solutions and throughout the experiments, Synthetic urine was purchased from Sigma Aldrich, South Africa, containing calcium chloride, magnesium chloride, potassium chloride, sodium chloride, sodium phosphate, sodium sulfate, urea, and creatinine with sodium azide as a preservative. Human plasma was also purchased from Sigma Aldrich, South Africa. The CuPPI metallodendrimer used as electrocatalytic platform was synthesised as shown in Chapter 3. Cytochrome P450 3A4 enzyme was purchased from Biocom Africa (PTY) LTD, dissolved in 0.1 M PB to 100 μM stock solution and stored at -70°C until use. The enzyme was further diluted to the desired concentration with 0.1 M PB when needed.

5.2.2 **Instrumentation**

For the electrochemical analysis, a three electrode setup was used consisting of a platinum wire as counter electrode, Ag/AgCl (saturated KCl) reference electrode and gold working electrode (all purchased from BASi). A PalmSense potentiostat (Palm Instruments BV, Netherlands) was used for all electrochemical measurements. UV-

Vis was carried out on a Nicolett evolution 100 (Thermo Electron Corporation) instrument.

5.2.3 Preparation of electrodes

The gold working electrode was used for the preparation of the biosensor since the copper metallodendrimer better adheres to this surface. The Au has a working surface area of 1.6 mm in diameter and was cleaned before each experiment by polishing to a mirror like surface. The electrode was polished on polishing pads with alumina powder slurry of 1, 0.3 and 0.05 micron respectively. This process was then followed by sonication of the electrode in ethanol and water for 5 and 10 min respectively. Electrochemical cleaning of the gold electrode was also carried out by cycling in a 0.5 M solution of sulfuric acid. Ten cycles were done between the potentials of -400 mV and 1400 mV or until a reproducible voltammogram was obtained. A 5 mM solution of CuPPI metallodendrimer was prepared using 1:1 (v/v) acetone-ethanol. A volume of 8 μ L of the dendrimer solution was then drop-coated onto the surface of the clean gold electrode and left to dry for 45 min to allow for physical adsorption to take place. The surface of the electrode was then rinsed lightly with ethanol to remove any unbound dendrimer and dried under a stream of nitrogen gas. To form the biosensor, 10 μ M of CYP3A4 enzyme was drop-coated onto the surface of Au|CuPPI and allowed to electrostatically attach for 3 hours before use to produce an Au|CuPPI|CYP3A4 biosensing electrode.

5.2.4 Electrochemical protocol

All measurements were carried out with 0.1 M PB pH 7.4 as electrolyte. The cathodic sweep in the CV experiments were carried out first and the anodic scan second at a scan rate of 50 mV/s. The CV had an equilibration time of 5 s and E step of 10 mV. DPV was carried out at with a E step of 20 mV, an E pulse of 50 mV and t pulse of 0.02 s at a scan rate of 50 mV/s. DPV was the preferred method for detection of analytes since

it has an enhanced discrimination of Faradaic currents [28]. This allows for a clearer distinction between analytes whose electrochemical signatures have an E_{pa} or E_{pc} that are close to one another. Aerobic experiments were carried out under normal laboratory conditions in the presence of oxygen. Anaerobic experiments were carried out after bubbling the electrolyte solution with N_2 gas for 10 min, and maintaining a N_2 blanket over the solution thereafter.

5.2.5 UV-Vis spectroscopic protocol

Both the CYP3A4 enzyme as well as the anti-TB drugs were dissolved in 0.1 M PB at pH 7.4. The UV-Vis detection of samples were detected at a wavelength of 190 nm to 700 nm. UV-Vis spectra were captured at various time intervals from 0 min up to 24 hours.

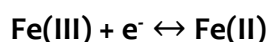


5.3 Results and Discussion

5.3.1 Characterisation of CYP3A4 biosensor

Since CYP3A4 is a monooxygenase, the overall reduction reaction is of highest interest in this system [29]. For this reason, the reduction/cathodic scan was always carried out first in any reactions involving the enzyme, followed by the oxidation/anodic scan when doing an electrochemical measurement. In order to determine the electrochemical activity of the CYP3A4 enzyme, the enzyme was initially characterised alone on a gold electrode under anaerobic conditions. The resulting voltammogram is as shown in Figure 5-4. The electrostatic attachment was found to be successful by linking the positively charged regions of the enzyme with the negatively charged gold electrode surface which occurs at the negative potential. Electrostatic attachment of enzymes is an easy and effective form of attachment of enzymes [30] [31].

Reaction of CYP3A4 at the gold electrode surface resulted in a redox couple with E_{pc} at 130 mV and E_{pa} at 270 mV. The peak separation, ΔE is 140 mV, which is what is expected since a one electron transfer resulted in ΔE of 60 mV. The multi-step electron transfer process occurring in the enzyme is the cause of the increase in this value. This redox couple responsible for these peaks is due to electron transitions at the heme centre of the CYP enzyme represented by the reaction equation below:



This is the dominant reaction, which occurs when there is no oxygen present in the system. The applied potential was sufficiently negative to reduce Fe^{3+} to Fe^{2+} . Similar reversible redox peaks have been found in literature with immobilized CYP and heme containing enzymes [32] [33] [34].

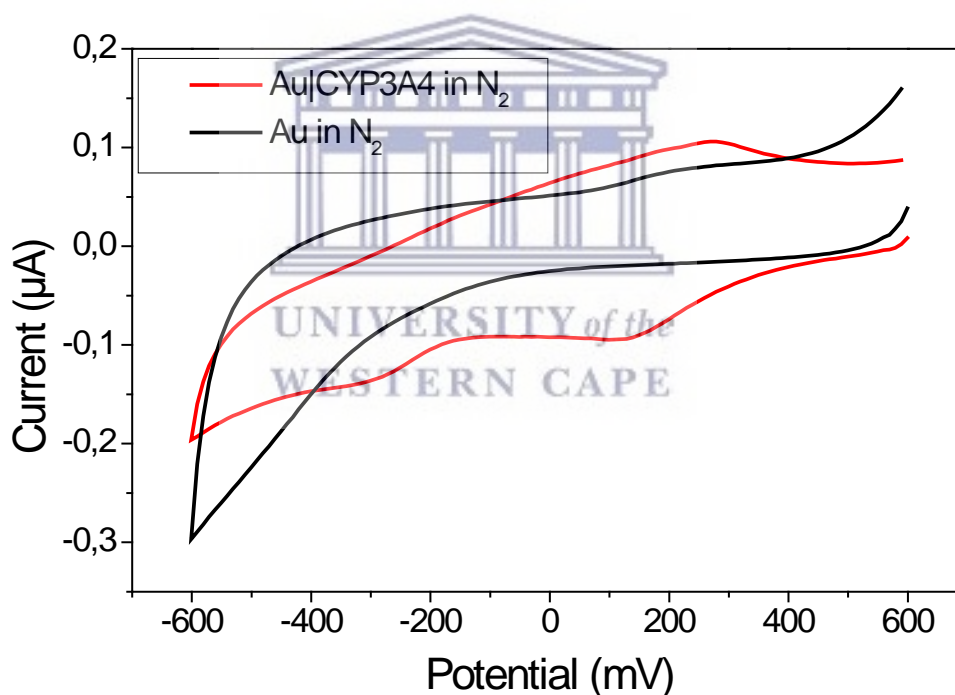


Figure 5-4: Electrochemical activity of Au|CYP3A4 under anaerobic conditions at 0.05 V/s

When oxygen is present in the system, a different reaction dominates and thus the same experiment was carried out in the presence of oxygen to investigate the reaction. The resulting cyclic voltammogram at 50 mV/s of the enzyme action is as shown below in Figure 5-5. The gold electrode has distinctive oxidation and reduction

peaks in the presence of oxygen. One notes that the gold oxidation peaks at around $E_{pa} = 430$ mV and 800 mV are greatly reduced when adding the CYP3A4 enzyme. This is due to the blocking effect of the amino acid chains of the enzyme structure. There are two reduction peaks present at $E_{pc} = -140$ mV and -510 mV. These are due to the reduction of oxygen at the gold electrode surface, and are in agreement with literature [35]. These peaks shift to a more negative potential of -290 mV and -620 mV respectively. This indicates an interaction of oxygen with the enzyme which is what is expected of CYP3A4 since it undergoes a monooxygenation reaction [21][36][37]. This response is caused by the CYP3A4 enzyme which catalyses the mass transport limited reduction of the dioxygen molecule [38].

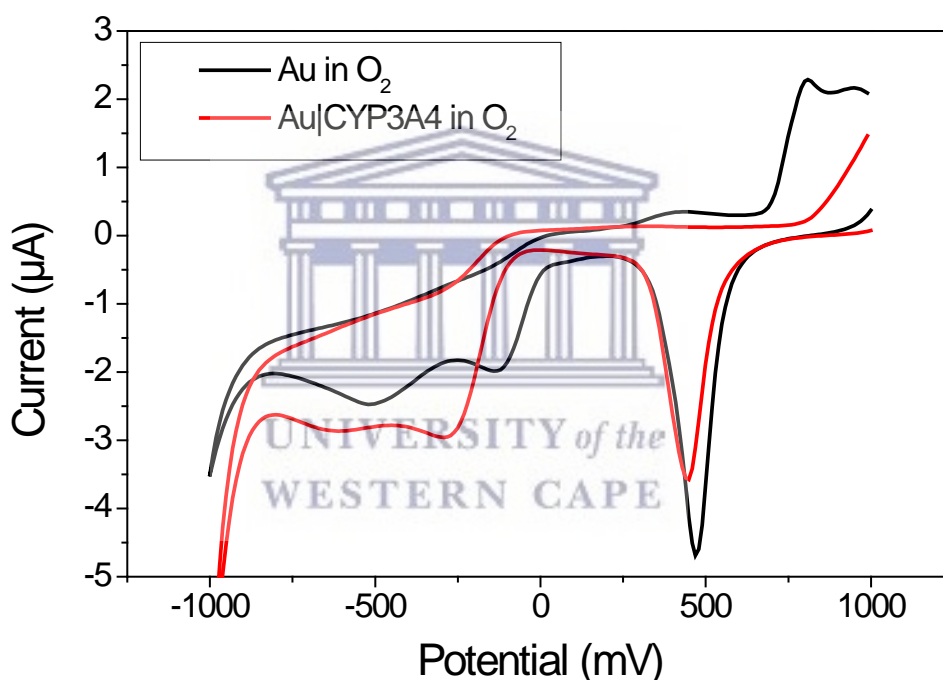


Figure 5-5: Electrochemical activity of Au and Au|CYP3A4 under aerobic conditions at 0.05 V/s

In order to validate the viability of the Au|CuPPI|CYP3A4 biosensor, the biosensor “building” was characterised in the presence of oxygen as shown in Figure 5-6. The CuPPI metallodendrimer on the gold electrode surface increased the conductivity of the gold electrode, with an additional anodic and cathodic peak as described in Chapter 3 at $E_{pa} = 210$ mV and $E_{pc} = 160$ mV. The cyclic voltammogram shows a higher current produced by the inherent gold peaks at $E_{pa} = 900$ mV and $E_{pc} = 500$ mV, which

is indicative of the electrocatalytic behaviour of the CuPPI metallodendrimer. Upon addition of the CYP3A4 to the Au|CuPPI, the outer enzyme structure blocks the surface of the electrode and stops electrons from reacting at the gold surface. The peaks attributed to gold as well as CuPPI thus reduce dramatically. This blocking of the electrode surface is commonly found in complex proteins such as enzymes [31]. The reduction peak for oxygen also shifts from -170 mV on Au|CuPPI to -270 mV on Au|CuPPI|CYP3A4. This peak, which is attributed to the monooxygenation reaction occurring within the enzyme will be the peak of interest in this study.

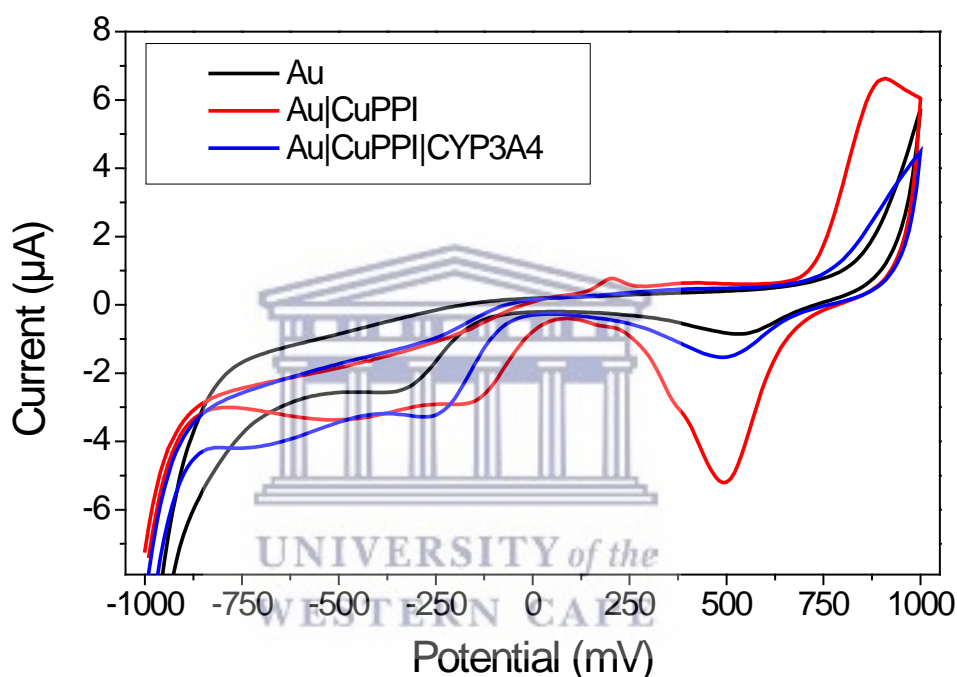


Figure 5-6: CV of Au, Au|CuPPI and Au|CuPPI|CYP3A4 electrode systems from -1 V to 1V at 0.1 V/s

5.3.2 Au|CuPPI|CYP3A4 biosensor detection of anti-TB drugs

The electrocatalytic ability of the Au|CuPPI|CYP3A4 biosensor was investigated using cyclic voltammetry and differential pulse voltammetry. The CV shown in Figure 5-7 shows the effect of the biosensor on 5 nM of isoniazid. It is clear that the reductive action of the enzyme on INH was successful as illustrated by the increase in the reduction potential upon addition of the substrate. The CV produced two peaks at -200 mV and -600 mV with the latter being due to the reduction of oxygen at the

electrode surface. The reduction peak around -200 mV in the CV was thus the peak of interest for the enzymatic reduction of analyte. The reduction peak is indicative of the reaction between substrate and enzyme in the presence of molecular oxygen.

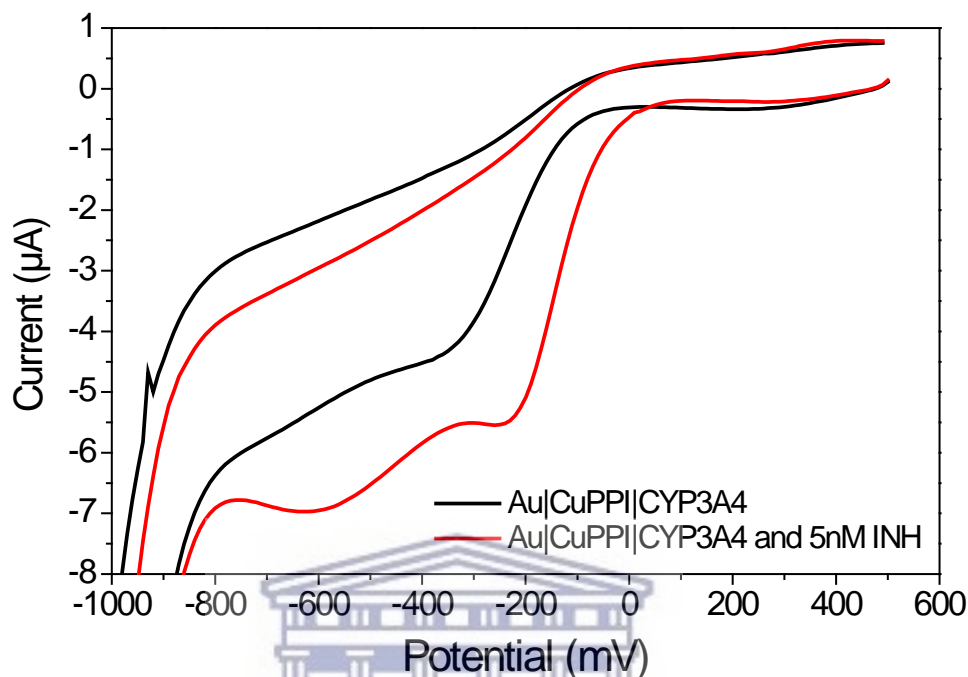


Figure 5-7: Enzymatic reduction of 5 nM INH at Au|CuPPI|CYP3A4 biosensor electrode in 0.1 M PB pH 7.4

The increase in peak current is due to the interaction of INH at the active site of the enzyme. INH binds to the Fe(III) ferric enzyme, causing the shift from high spin to low spin i.e. Fe(II). The low spin enzyme complex attracts molecular oxygen which binds and results in a Fe(V) complex. Water is then expelled from the complex and the hydroxylated product is released. The mechanism of INH metabolism is highly complex in the body and the intermediates and products associated with it are numerous. The first cycle of metabolism produces a diazo species i.e. **I5** in Figure 5-8 and the second metabolic cycle yields a 1-hydroxy diazo compound (**I11**). Recent studies revealed that the toxicity of INH is associated with the isonicotinoyl radical (**I10**) which is formed during the second catalytic cycle. A summary of the studies as shown in Figure 5-8 reveals that the major product of INH metabolism by CYPs is isonicotinic acid (**I12**) [39] [40].

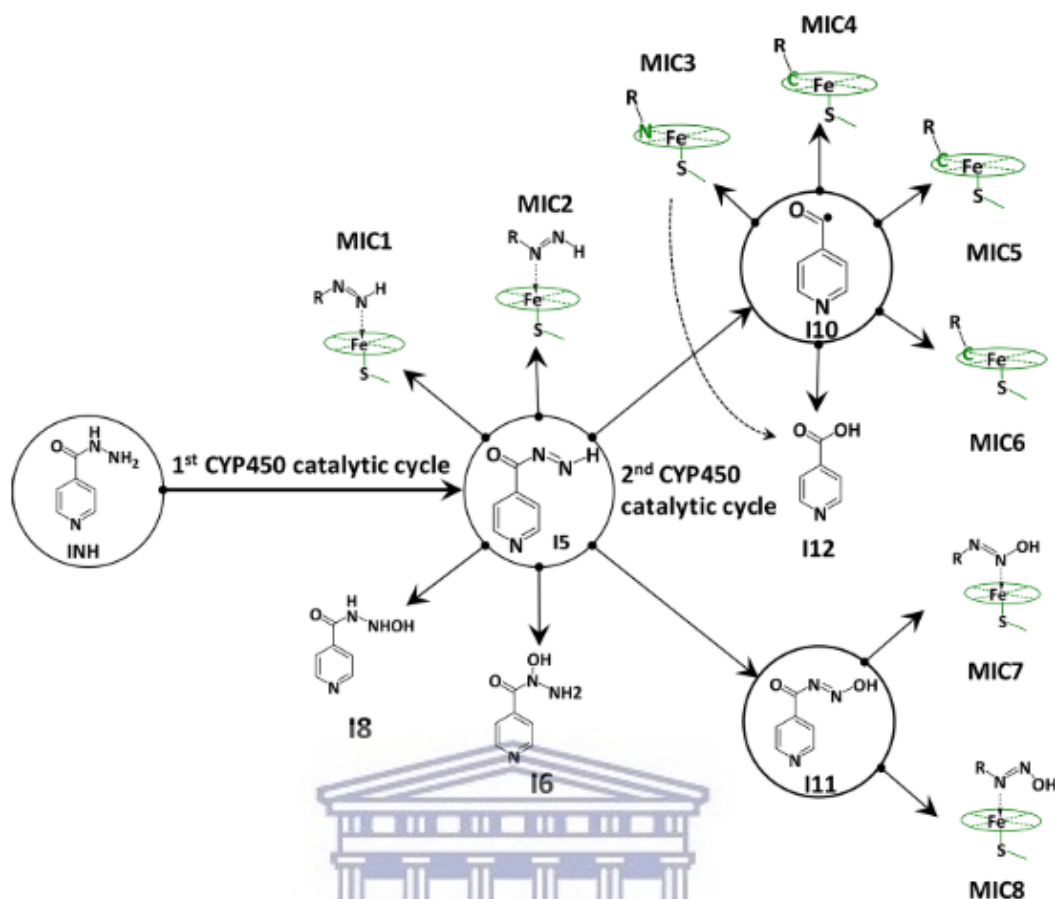


Figure 5-8: Most energetically favoured mechanistic pathway for the biocatalysis of INH by CYP's in the body [40]

UNIVERSITY of the
WESTERN CAPE

A more sensitive technique such as differential pulse voltammetry was used for the detection of four anti-TB drugs. The reduction peak of the biosensor was monitored for each drug since this is the one that represents the monooxygenation reaction associated with the action of the CYP3A4 enzyme on its substrates.

5.3.2.1 Isoniazid

The detection of isoniazid was carried out using the constructed biosensor under aerobic conditions. For each constructed biosensor, the monooxygenation peak was identified and then monitored upon addition of the different anti-TB drugs. The results are as shown in Figure 5-9 (A). Upon an addition of INH to the biosensor, the current of the reduction peak at -20 mV increased.

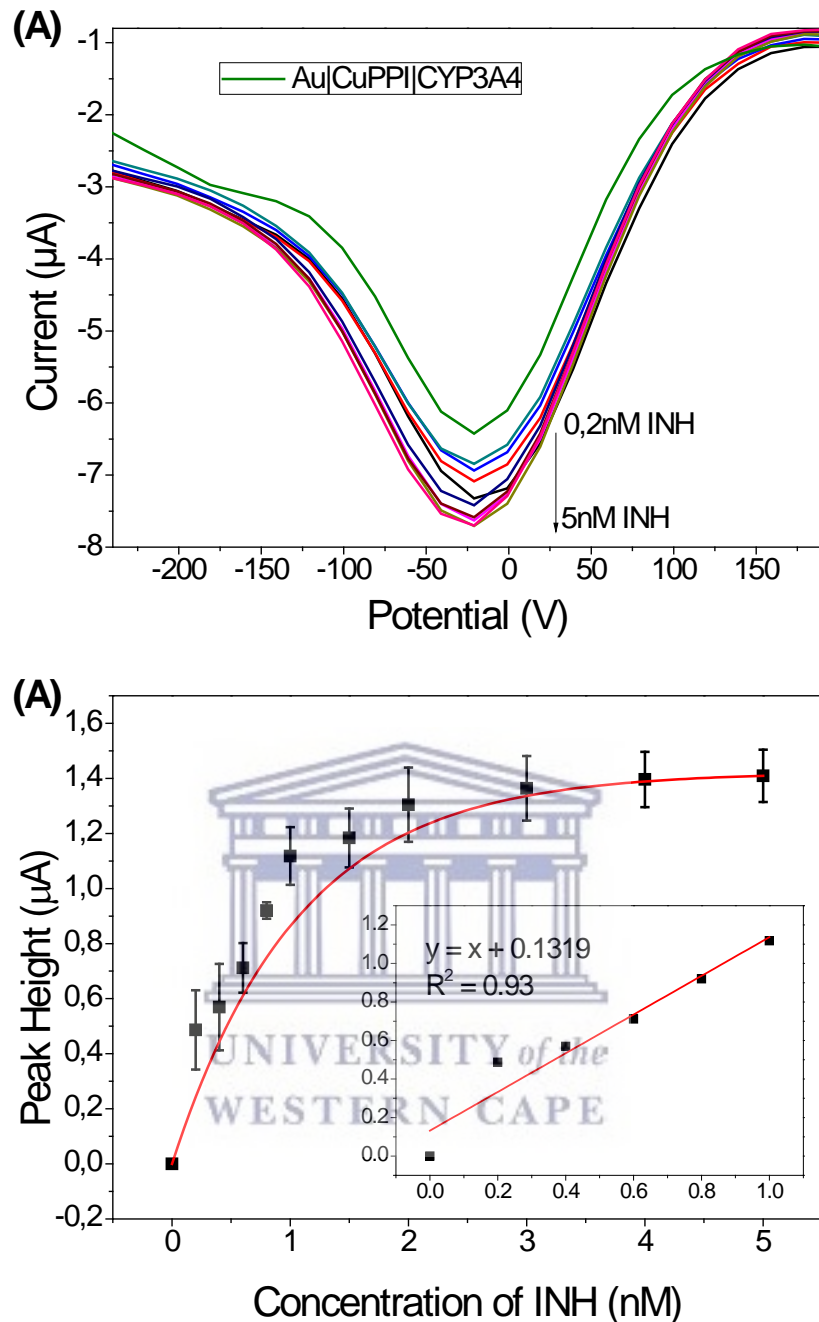


Figure 5-9: (A) DPV detection of 0.2, 0.4, 0.8, 1, 2, 3, 4 and 5 nM INH in 0.1 M PB pH 7.4 at Au|CuPPI|CYP3A4 (B) exponential calibration plot of I_{pc} vs concentration of INH in PB pH 7.4 from 0 to 5 nM with linear region inset from 0 to 1 nM

The concentration of isoniazid was detected in the concentration range from 0 to 5 nM. Upon each successive addition of INH the reduction peak at -20 mV increased. This is indicative of an electron transfer which has been confirmed to be due to the monooxygenation reaction of the enzyme on the substrate. The response of the biosensor to INH resulted in a Michaelis-Menten type profile from 0 to 5 nM INH.

There is a linear region ($R^2 = 0.93$) from 0 to 1 nM as shown in the inset (Figure 5-9 (B)), after which the enzyme becomes saturated and the graph forms a plateau. The calculated value for Michaelis constant, K_m was found to be 0.737 nM according to Equation 5-3. The limit of detection and quantification of the biosensor was calculated using Equations 5-4 and 5-5, where σ is standard deviation of blank samples and s is the slope of the regression equation. The LOD for detection of isoniazid was found to be 0.07259 nM and the LOQ was 0.2199 nM.

$$\text{LOD} = 3.3\sigma/s \quad \text{Equation 5-4}$$

$$\text{LOQ} = 10\sigma/s \quad \text{Equation 5-5}$$

5.3.2.2 Ethambutol

The dendritic biosensor was applied to the detection of ETH in 0.1 M PB in the concentration range of 0 to 5 nM. The cathodic peak (-60 mV) current increased upon an increase in concentration of ETH as can be seen in Figure 5-10 (A). This peak increased in a linear fashion from 0 to 0.8 nM, after which the peak current start plateauing in Figure 5-10 (B), which is typical of a Michaelis-Menten enzymatic reaction. This is indicative of enzyme saturation as shown before. The Michaelis constant K_m was calculated to be 0.565 nM. The LOD and LOQ for the detection of ETH was found to be 0.08642 nM and 0.2618 nM respectively according to Equations 5-3 and 5-4 respectively. It is interesting to note that the enzyme saturates with ETH quicker than with INH and has a lower value for K_m , which confirms that the CYP3A4-ETH complex is more tightly bound i.e. has a higher affinity, than the CYP3A4-INH complex.

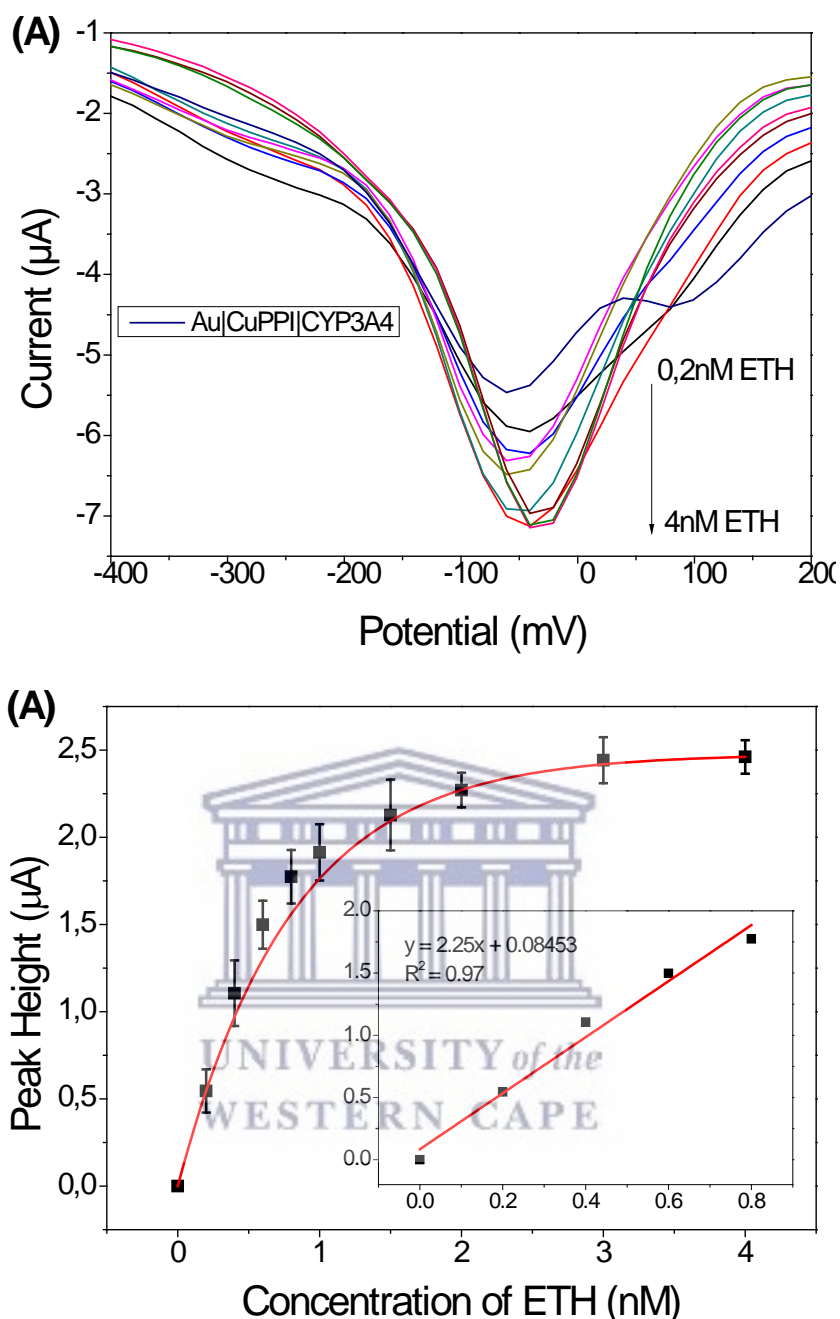


Figure 5-10: (A) DPV detection of 0.2, 0.4, 0.8, 1, 2, 3, 4 and 5 nM ETH in 0.1 M PB pH 7.4 at Au|CuPPI|CYP_{3A4} (B) exponential calibration plot of I_{pc} vs concentration of ETH in PB pH 7.4 from 0 to 5 nM with linear region inset from 0 to 0.8 nM

The metabolism of ETH is carried out in the general mechanism as shown in Scheme 5-2. The ETH binds to the CYP, reducing the hexa-coordinated low spin Fe(III) to a high spin Fe(II). The molecular oxygen binds to the complex to form the Fe(II)-O₂ complex. An aldehyde intermediate is formed which is followed by release of H₂O, resulting in

an oxoferryl intermediate of Fe(V). Finally the product of ETH metabolism is a dicarboxylic acid as shown in Figure 5-11 [41] [42].

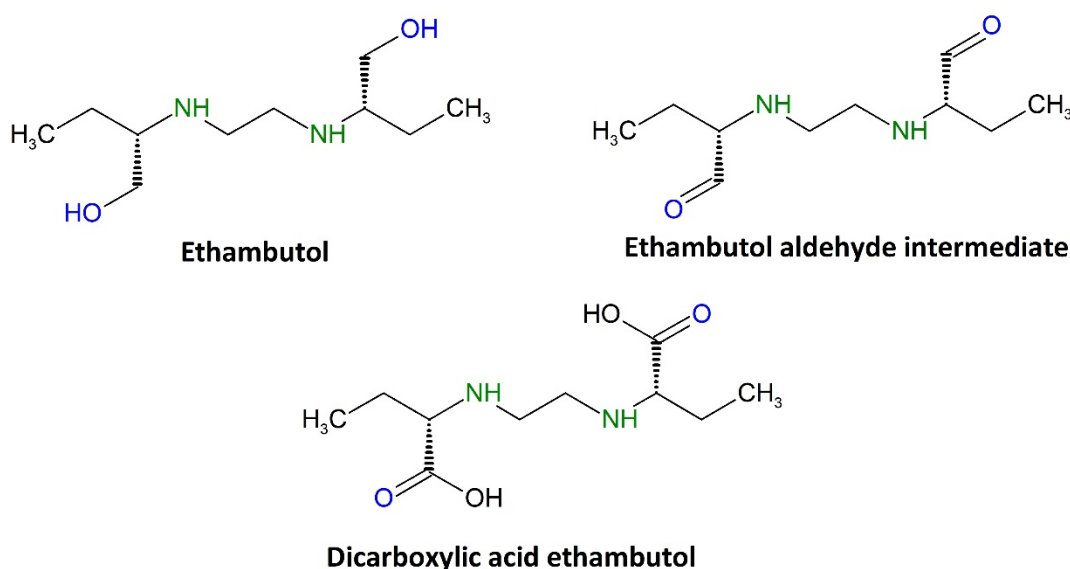


Figure 5-11: Structures of ethambutol, its aldehyde intermediate and dicarboxylic acid product of CYP metabolism

5.3.2.3 Pyrazinamide

Pyrazinamide was then detected using the Au|CuPPI biosensor. The monooxygenation peak was identified at -100 mV in this case. Upon the first addition of pyrazinamide to the system, the peak shifted to a more positive potential of -60 mV as shown in Figure 5-12 (A). The metabolism of PYR at the CYP enzyme occurs by PYR first binding to the enzyme causing the shift from low-spin to high-spin i.e. Fe(III) to Fe(II). The high-spin complex then attracts molecular oxygen while hydroxylating PYR to 5-hydroxypyrazinamide. The splitting of the O-O bond further hydroxylates the PYR intermediate, changing the enzyme to the Fe(V) state and yielding the 5-hydroxypyrazinoic acid product. The enzyme then returns back to its original state once the product is released for further reaction [43] [44] [45].

Subsequent additions increased the cathodic peak current and shifted the peak ever so slightly to a final potential of -40 mV at 4 nM PYR. The peak current increased linearly until 1 nM after which the biosensor saturates as can be seen in the calibration plot in Figure 5-12 (B). This Michaelis-Menten type of reactivity between CYP3A4 and

PYR yields a Michaelis constant K_m of 0.767 nM. The LOD and LOQ for PYR was found to be 0.02244 nM and 0.06801 nM respectively. The sensitivity of the sensor towards PYR is larger than the rest with a calibration plot slope of 3 $\mu\text{A}/\text{nM}$.

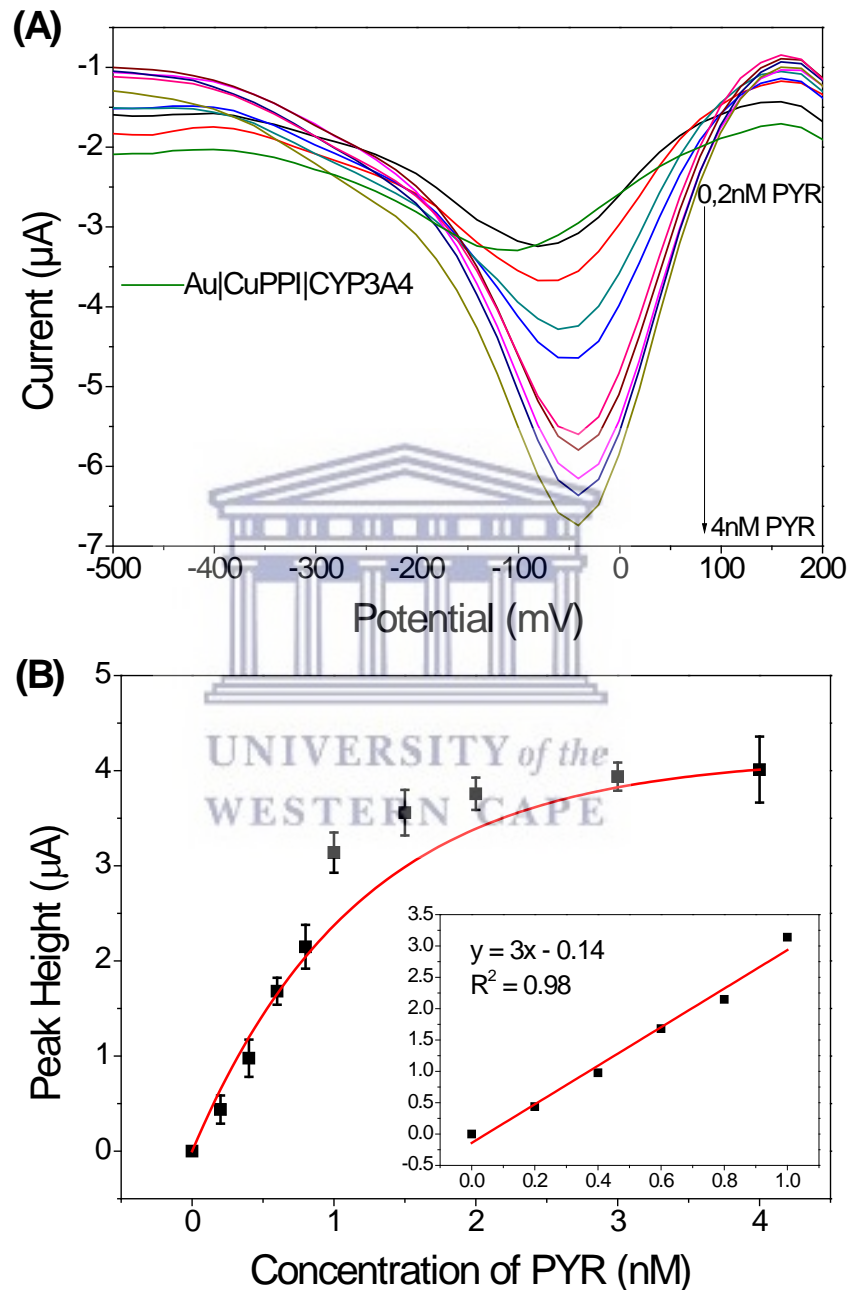


Figure 5-12: (A) DPV detection of 0.2, 0.4, 0.8, 1, 2, 3, 4 and 5 nM PYR in 0.1 M PB pH 7.4 at Au|CuPPI|CYP3A4 (B) Exponential calibration plot of I_{pc} vs concentration of PYR in PB pH 7.4 from 0 to 5 nM with linear region inset from 0 to 1 nM

5.3.2.4 Rifampicin

The biosensor was then applied for the detection of rifampicin, since it is a known substrate and inducer of CYP3A4 [46]. The metabolism of RIF via CYP begins with the formation of the CYP-Fe(II)-RIF high spin complex as described previously. The high spin Fe(II) attracts molecular oxygen which binds with the CYP and converts RIF to formylrifampicin. The expulsion of water results in the formation of a CYP-Fe(V) and the subsequent release of the carboxylic acid form of RIF. The structures of the product and intermediate associated with RIF metabolism is shown in Figure 5-13 [47]

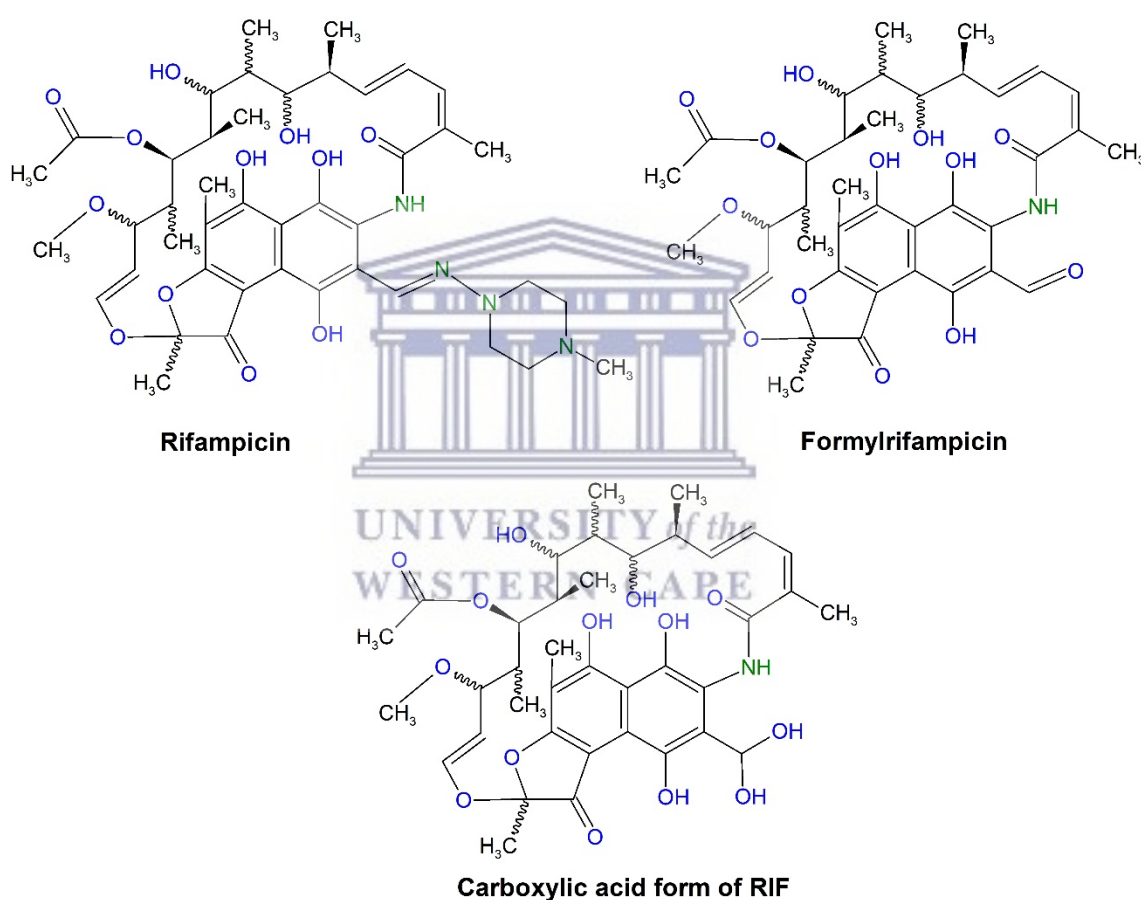


Figure 5-13: Structures of rifampicin, its formyl intermediate and carboxylic acid product of CYP metabolism

The electrochemical biosensor reacts to RIF in a similar way as it does to PYR, in the sense that the cathodic peak shifts to a more positive potential upon addition of more substrate. This peak was initially at -120 mV and shifted to -80 mV after 5 nM RIF was added as can be seen in Figure 5-14 (A). The cathodic peak increased linearly between

0.2 nM and 1 nM and thereafter the calibration curve shows typical Michaelis Menten behaviour up until 5 nM as shown in Figure 5-14 (B). The calculated value of the Michaelis constant, K_m was 0.75 nM. This low constant value is indicative of a strong interaction between substrate and enzyme as can be expected from RIF. The LOD and LOQ for the detection of RIF was found to be 0.1072 and 0.3249 nM respectively.

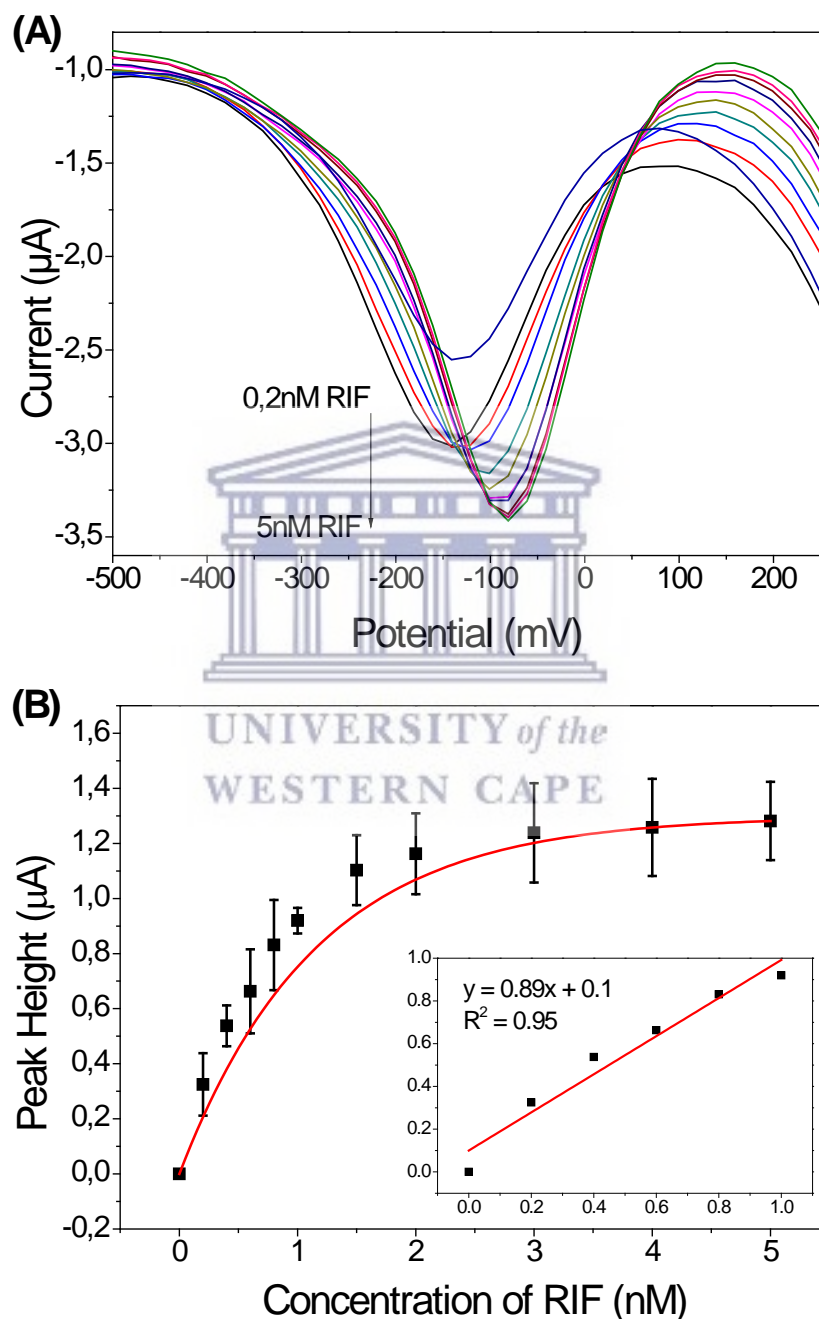


Figure 5-14: (A) DPV detection of 0.2, 0.4, 0.8, 1, 2, 3, 4 and 5 nM RIF in 0.1 M PB pH 7.4 at Au|CuPPI|CYP3A4 (B) exponential calibration plot of I_{pc} vs concentration of RIF in PB pH 7.4 from 0 to 5 nM with linear region inset from 0 to 1 nM

A table summarising the analytical efficiency of the Au|CuPPI|CYP3A4 biosensor is as shown in Table 5-2 indicating the LOD, LOQ and K_m values for the biosensor towards each anti-TB drug. The biosensor seems to be the best for the detection of PYR. It has the highest sensitivity towards this anti-TB drug and has the lowest limit of detection and quantification. In contrast, the lowest sensitivity and highest LOD and LOQ belong to rifampicin when using this sensor. The differences in these values are attributed to the various affinities towards each drugs as represented by the values of K_m . The interaction of the enzyme with each substrate differs, RIF is a much larger molecule than the other compounds and plays a role in how quickly the molecule can move into the active site of the CYP3A4 enzyme.

Table 5-2: Summary of analytical efficiency of Au|CuPPI|CYP3A4 biosensor in 0.1 M PB at pH 7.4

Anti-TB drug	Electrochemical Performance			
	Sensitivity ($\mu\text{A/nM}$)	LOD (nM)	LOQ (nM)	K_m (nM)
Isoniazid	1	0.07259	0.2199	0.75
Ethambutol	2.25	0.08642	0.2618	0.565
Pyrazinamide	3	0.02244	0.06801	0.767
Rifampicin	0.89	0.1072	0.3249	0.757

5.3.3 UV-Vis biosensor for detection of anti-TB drugs

The electrochemical biosensor was compared to a well-established technique such as UV-Vis spectroscopy in order to compare sensitivity and viability in terms of time taken for analysis and sample preparation. The UV-Vis spectra of the CYP3A4 enzyme and isoniazid was carried individually and together in order to determine the viability of UV-Vis as a detection method for the biosensor. The CuPPI metallodendrimer was not soluble in aqueous media and thus could not be used as a catalyst in the UV-Vis detection. CYP3A4 was suspended in phosphate buffer in which it is most stable. The spectrum of 5 μM of CYP3A4 enzyme on its own shows peaks at 212 and 262 nm. Isoniazid has a characteristic peak at the exact same wavelengths as the enzyme at

212 and 262 nm [48] [49]. Once the enzyme and substrate are placed together in the cuvette, these peaks have a noted increase in absorbance, with no new peaks appearing. The fact that the UV-spectra of these two compounds are basically identical poses a huge problem in assigning peaks to one or the other in a mixture as shown in Figure 5-15.

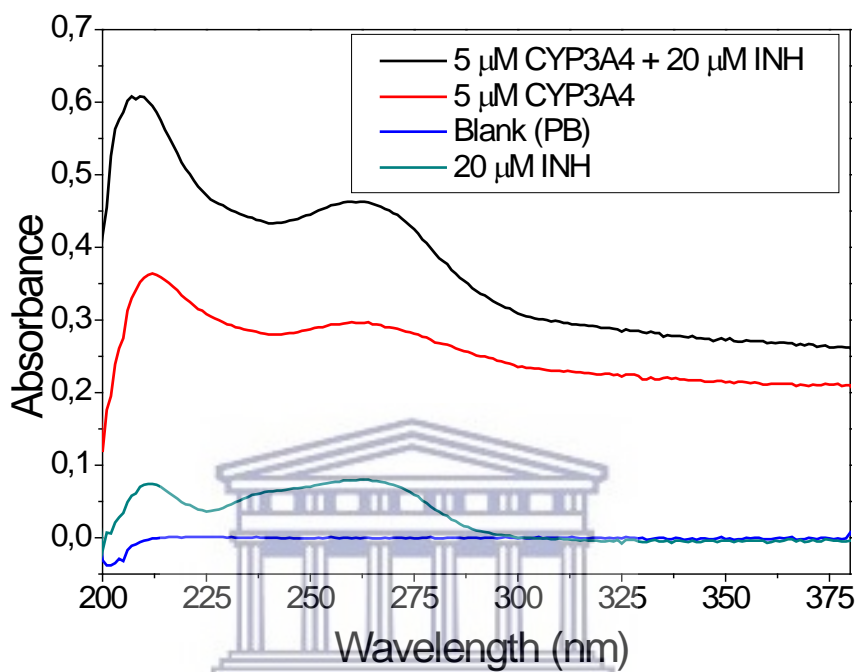


Figure 5-15: UV-Vis spectra of 5 μM CYP3A4 enzyme, 20 μM isoniazid and a combination of these in 0.1 M PB at pH 7.4

No new peaks were found in the spectra of the CYP3A4 and INH combined thus we can conclude that no reaction had taken place between enzyme and substrate to produce any new compounds. A time study was thus carried out to see if the reaction would complete after a certain period. A spectrum was taken every ten minutes up to 60 minutes. Very small changes were noted up until 40 minutes, when a distinct decrease in peak absorbance was noted in both peaks. Another spectrum was taken after 24 hours and a very notable decrease in absorbance at the 262 nm peak was noted as well as the appearance of a very small “bump” around 285 nm as shown in Figure 5-16 (A). This indicates that some isoniazid was metabolised by the enzyme and a new compound was formed via reaction with the enzyme to produce the new

peak. Another option is that the enzyme has denatured and caused the decrease in absorbance in the UV-Vis spectra.

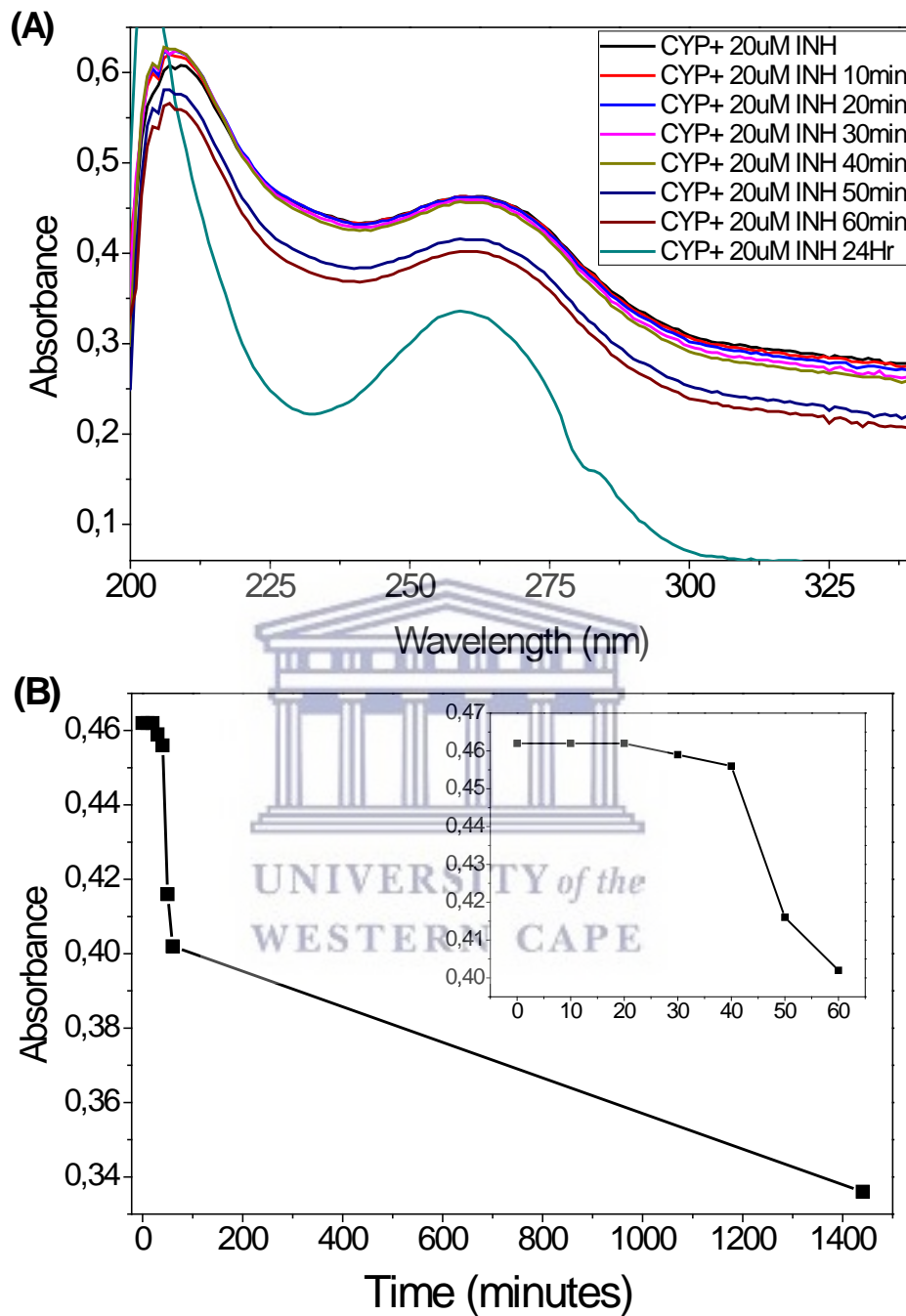


Figure 5-16: (A) Time study of 5 μM CYP3A4 enzyme reaction with 20 μM INH up to 24 hours (B) UV-Vis absorbance of CYP3A4 and INH mixture vs time from 0 to 24 h (inset) from 0 to 60 min

These initial tests and results prove that UV-Vis is not an efficient tool for monitoring the enzymatic metabolism of anti-TB drugs. The reaction takes too long to initiate

without an external stimuli such as an electron or additional redox partners. A new product is only produced after 24 hours which we could possibly attribute to the new peak appearing at 285 nm. Another reason that UV-Vis would not be a viable option for this sensor is the fact that some compounds are not optically active. Thus electrochemistry is a clear better alternative.

5.4 **Real Samples**

The superior electrochemical Au|CuPPI|CYP3A4 biosensor was then applied to spiked real samples as described in Chapter 4. The anti-TB drugs were detected in 20 % synthetic urine and 10% human plasma, which were both diluted with 0.1 M PB pH 7.4. The effect of the matrix was noticeable in these biosensors and resulted in the limit of detection being slightly higher than when using standard referencing materials. Factors contributing to these matrix effects include interfering substances (uric acid, salicylic acid, ascorbic acid etc.), fouling of the electrode (caused by plasma proteins), non-specific binding as well as pH [50] [51]. The mechanisms of each drugs metabolism is the same as discussed in previous sections (5.3.2.)

5.4.1 **Isoniazid**

The detection of INH was completed in 20 % synthetic urine with the DPV of successive additions of INH being shown in Figure 5-17 (A). The biosensor itself showed an E_{pc} of -280 mV which shifted to a more positive potential upon addition of INH to the system. A higher concentration of INH was necessary in order to obtain a response due to the interference of the compounds present in the sample matrices. The detection of INH was thus carried out in the range of 1 to 10 μM using the Au|CuPPI|CYP3A4 biosensor, which showed typical Michaelis-Menten behaviour. We found that a linear range of 1 to 7 μM was obtained, after which the calibration curve plateaued as shown in Figure 5-17 (B). A Michaelis constant of 3.888 μM was

obtained, along with LOD of 0.176 μM , LOQ of 0.586 μM and sensitivity of 0.13041 $\mu\text{A}/\mu\text{M}$ for the detection of INH in synthetic urine.

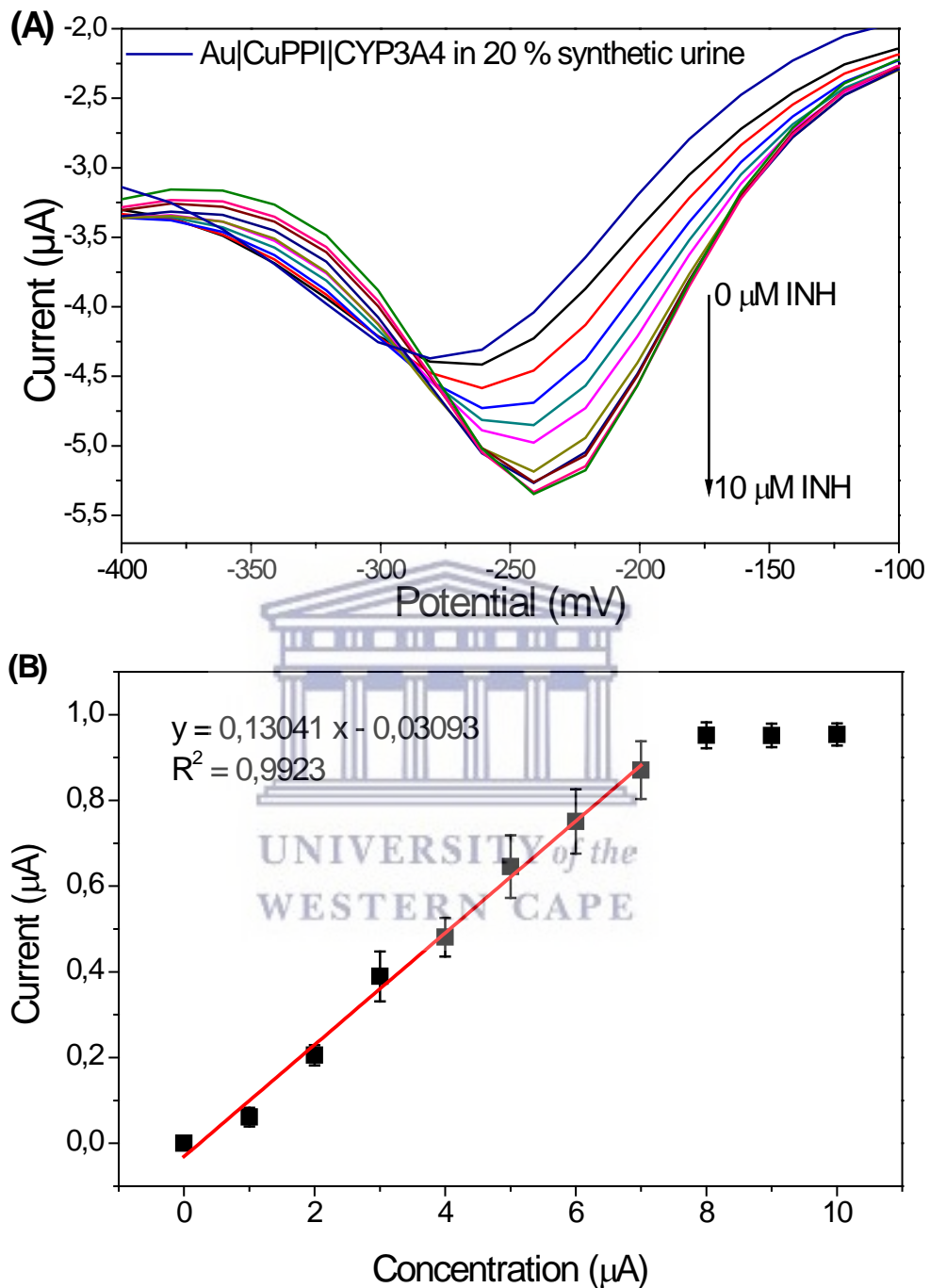


Figure 5-17: (A) DPV detection of 1, 2, 3, 4, 5, 6, 7, 8, 9 and 10 μM INH at Au|CuPPI|CYP3A4 (B) I_{pc} vs concentration of INH in 20 % synthetic urine

The Au|CuPPI|CYP3A4 biosensor in 10 % human plasma resulted in an E_{pc} of -240 mV. Upon addition of INH to the system the E_{pc} shifts to a more negative potential, up to -280 mV when 8 μM of INH is added as shown in Figure 5-18 (A). The linear range

obtained was from 1 to 6 μM after which the calibration curve plateaus in Figure 5-18 (B) in typical Michaelis-Menten behaviour. Carrying out any further additions to the plasma system was hindered by electrode fouling. The Michaelis constant, K_m was calculated to be 3.575 μM . The LOD and LOQ for INH in plasma was found to be 0.631 μM and 2.1 μM respectively. The sensitivity of the detection was found to be 0.0867 $\mu\text{A}/\mu\text{M}$. The therapeutic range for INH is 2.18 to 4.37 μM , which falls within the linear ranges obtained from the biosensor described here [52].

INH has been successfully detected in drug samples previously with 2,3-dichloro-5,6-dicyano-p-benzoquinone (DDQ) and reduced graphene oxide (rGO) which was immobilized in a nafion membrane. This sensor obtained a wide linear range of 0.5 μM to 380 μM and LOD of 0.15 μM when completing the detection of tablet forms of the drugs in PB. These values are comparable to the biosensor which was developed in this work in real sample matrices which are highly complex and contain many interferences [53]. Another method of detection of INH made use of metal nanoparticles. In one particular case a gold-platinum core-shell modified GCE was employed for quantification of the drug using amperometry. The detection was successful in determining INH in PB as well as spiked real samples in human blood serum and urine. The LOD of this nanoparticle based sensor was found to be 26 nM [54]. These types of studies however make use of expensive platinum and gold based nanoparticles which are made up of rare earth metals. The sensor developed in this work uses a material that is much cheaper to produce with similar results in terms of low detection limits.

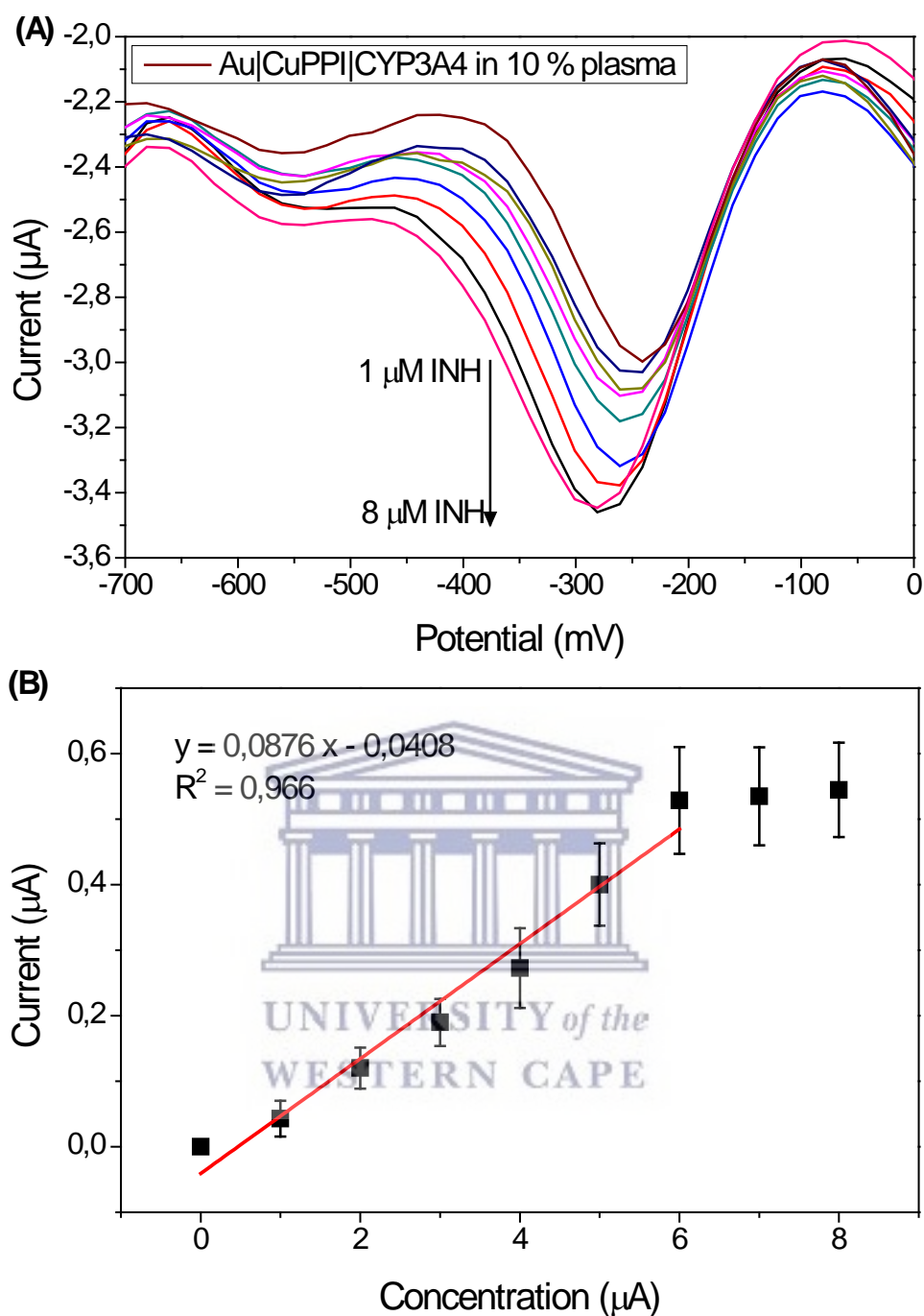


Figure 5-18: (A) DPV detection of 1, 2, 3, 4, 5, 6, 7 and 8 μM INH at Au|CuPPI|CYP3A4 (B) I_{pc} vs concentration of INH in 10 % plasma

5.4.2 Ethambutol

The detection of ETH in 20 % synthetic urine was successful from 1 to 10 μM with the lower linear range being from 1 to 4 μM and another linear range present from 5 to 8 μM as shown in Figure 5-19 (B). The E_{pc} in this case remained constant at -240 mV despite the increased concentration of ETH added to the system as shown in Figure

5-19 (A). The enzymatic biosensor reaches saturation after 8 μM as is typical Michaelis-Menten reaction kinetics, obtaining a Michaelis constant, K_m of 2.820 μM . The LOD and LOQ for ETH in synthetic urine was calculated at 0.386 μM and 1.288 μM respectively.

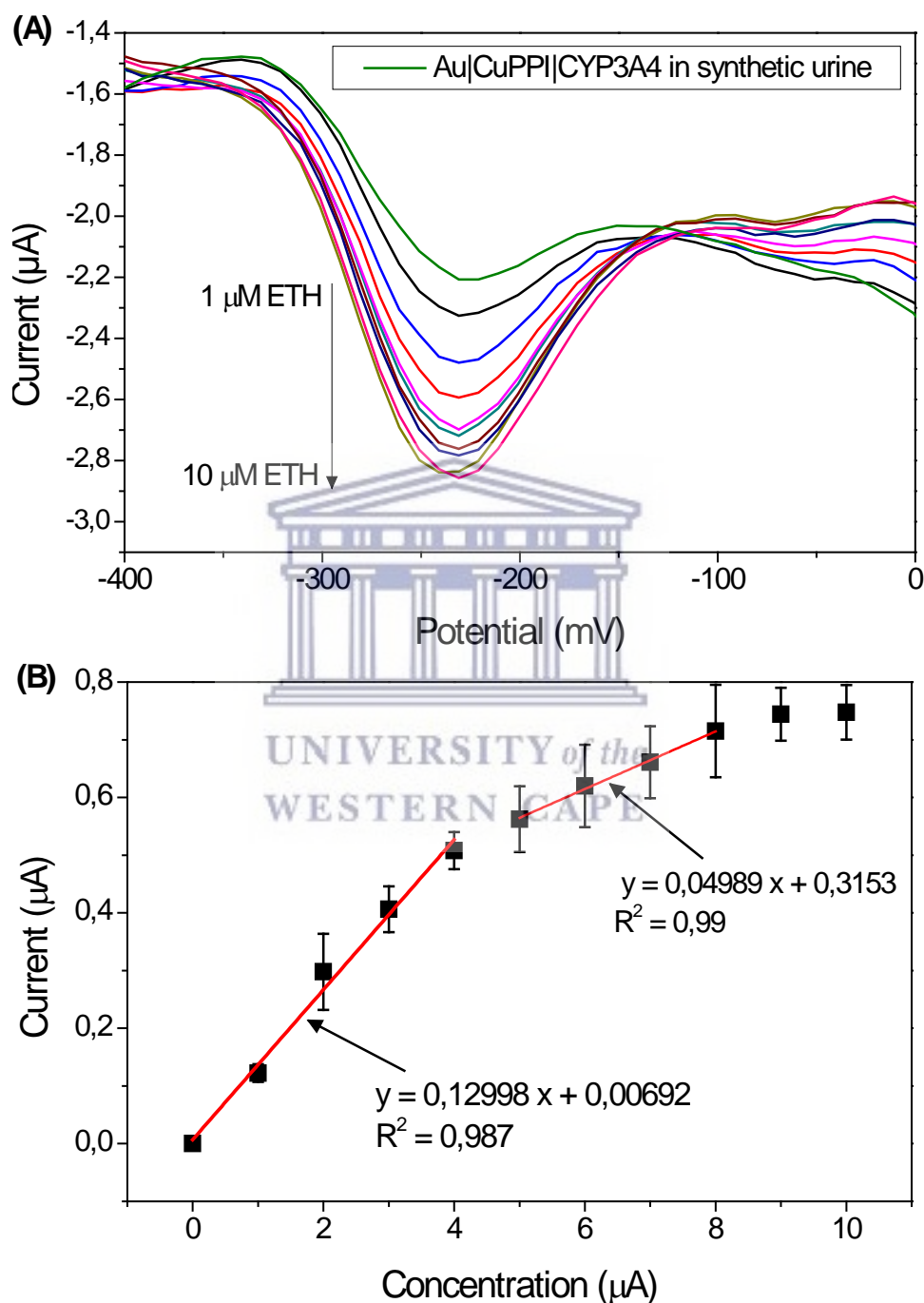


Figure 5-19: (A) DPV detection of 1, 2, 3, 4, 5, 6, 7, 8, 9 and 10 μM ETH at Au|CuPPI|CYP3A4
(B) I_{pc} vs concentration of ETH in 20 % synthetic urine

The detection of ETH in 10 % human plasma was found to be successful, with the E_{pc} shifting from -200 mV at zero concentration to -160 mV once 8 μM of ETH was added to the system in Figure 5-20. The linear range in this instance was 1 to 4 μM with a LOD and LOQ of 0.403 μM to 1.3646 μM respectively. The sensitivity of the sensor towards the detection of ETH in plasma was found to be 0.1195 $\mu\text{A}/\mu\text{M}$. The Michaelis constant, K_m was calculated to be 2.820 μM in the plasma matrix as well. Within 24 hours of ingesting ETH, roughly 50 % passes through urine un-metabolised and can be detected successfully using this method [52]. The serum peak levels of ETH in the body around 2 hours after taking the dosage is in the range of 2 to 6 $\mu\text{g}/\text{ml}$ i.e. 9 to 29 μM [52]. Although these levels are slightly out of the analytical range for the biosensor, delaying the time at which the samples are taken, would easily resolve this issue. Alternatively the chemical sensor described in Chapter 4 could be used.

Not many studies have taken place on the detection of ethambutol using electrochemistry in recent years. There has however been a study which detected ETH with the use of a competitive occupancy of two fluorescent probes that form complexes with CB[7] (cucurbit[7]uril). Once the complex forms with the probes the fluorescence intensity increases, while ETH competes to quench the fluorescence. The linear region of detection was found to be 5 to 1000 ng/ml and limit of detection of 1.7 ng/ml [55]. This method of detection of ETH is indirect, complicated and requires a more complex instrument for fluorescence detection. Another method of ETH detection was carried out electrochemically by Mekassa et al. This sensor consisted of a nickel nanoparticle decorated graphene oxide on a glassy carbon electrode. The sensor was successful in determining ETH in the linear range of 0.05 to 100 μM . A limit of detection of 0.023 μM was obtained when detecting using SWV in phosphate buffer. Recovery studies were carried out in this study using a spiked urine sample but no work has been found which detects ETH in human plasma [56]. The fact that ETH has been successfully detected in plasma in this work is hugely beneficial towards realistic application of the sensor towards real samples.

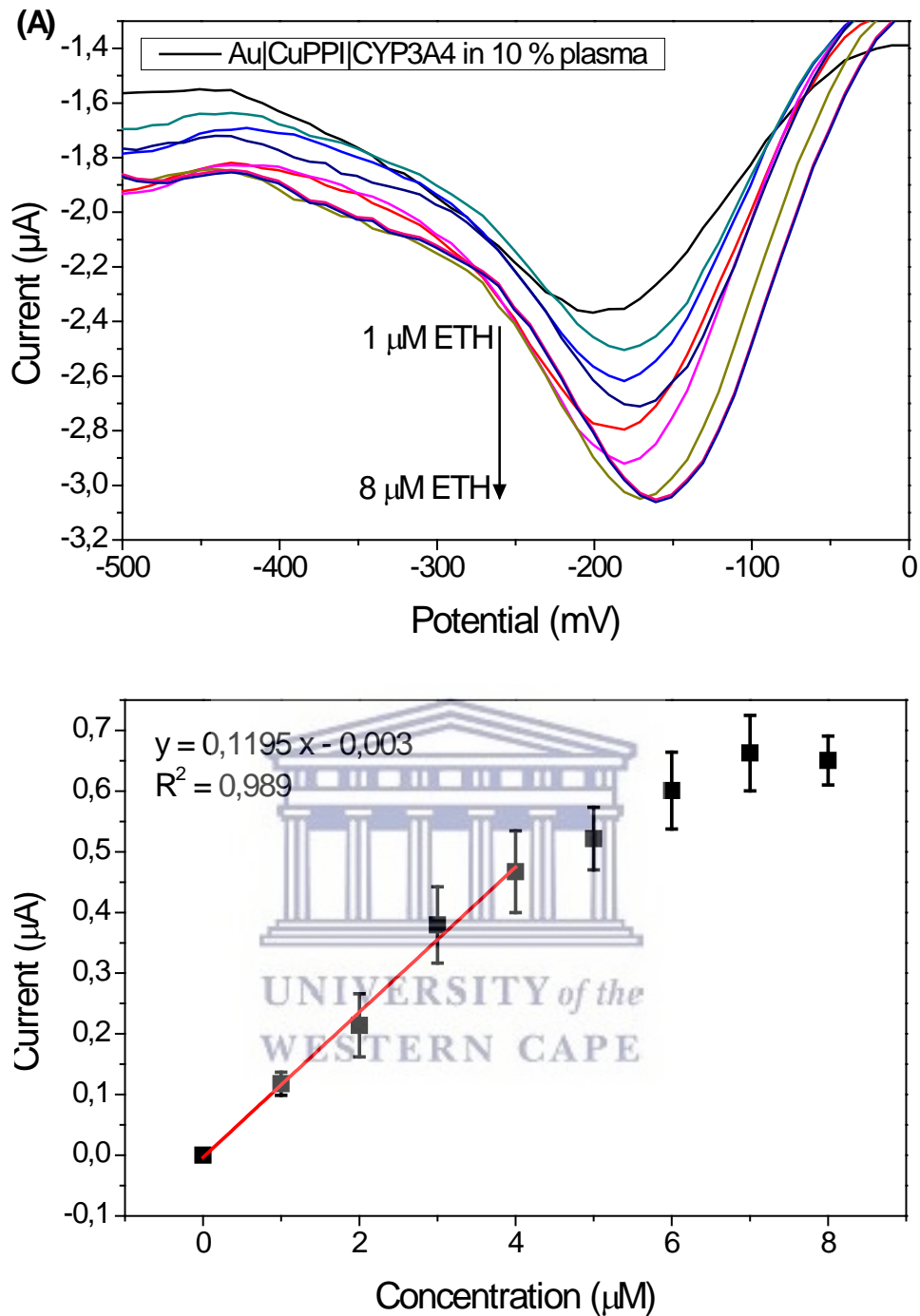


Figure 5-20: (A) DPV detection of 1, 2, 3, 4, 5, 6, 7 and 8 μM ETH at Au|CuPPI|CYP3A4 (B) I_{pc} vs concentration of ETH in 20% synthetic urine

5.4.3 Pyrazinamide

The detection of PYR using the Au|CuPPI|CYP3A4 biosensor was successful in 20% synthetic urine as shown by Figure 5-21 (A). The sensor showed a linear increase in cathodic peak current upon addition of PYR in the range of 1 to 10 μM . There was no noticeable shift in peak potential upon successive addition of PYR. This sensing

application showed a longer linear range than the other analytes with no enzyme saturation occurring in synthetic urine. This atypical Michaelis-Menten behaviour suggest that the enzyme saturation point has not yet been reached in this concentration range. Therefore, no Michaelis constant can be calculated from this graph. The LOD and LOQ was calculated to be 0.66 μM and 2.22 μM respectively with a sensitivity of 0.0677 $\mu\text{A}/\mu\text{M}$.

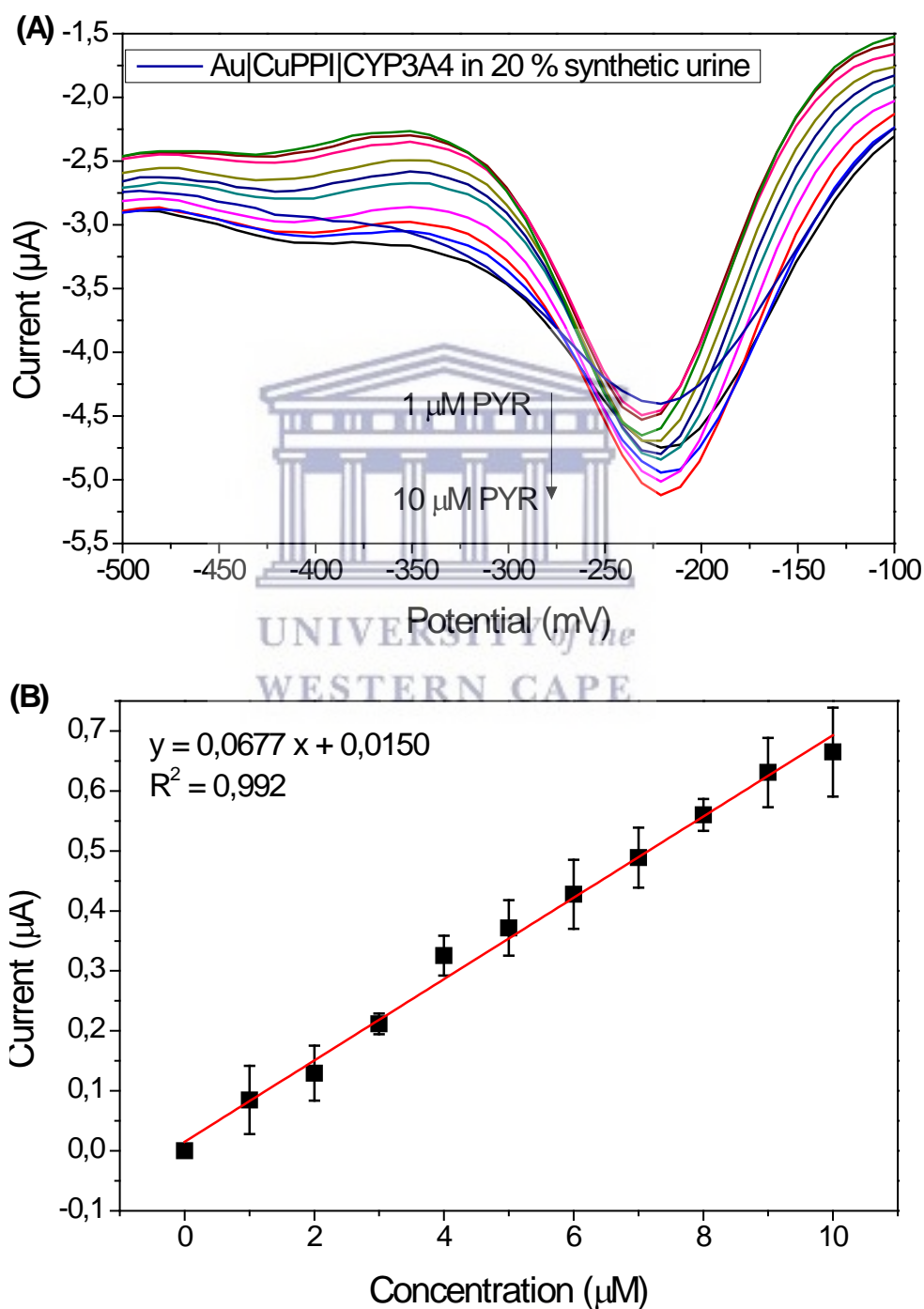


Figure 5-21: (A) DPV detection of 1, 2, 3, 4, 5, 6, 7, 8, 9 and 10 μM PYR at Au|CuPPI|CYP3A4
(B) I_{pc} vs concentration of PYR in 20 % synthetic urine

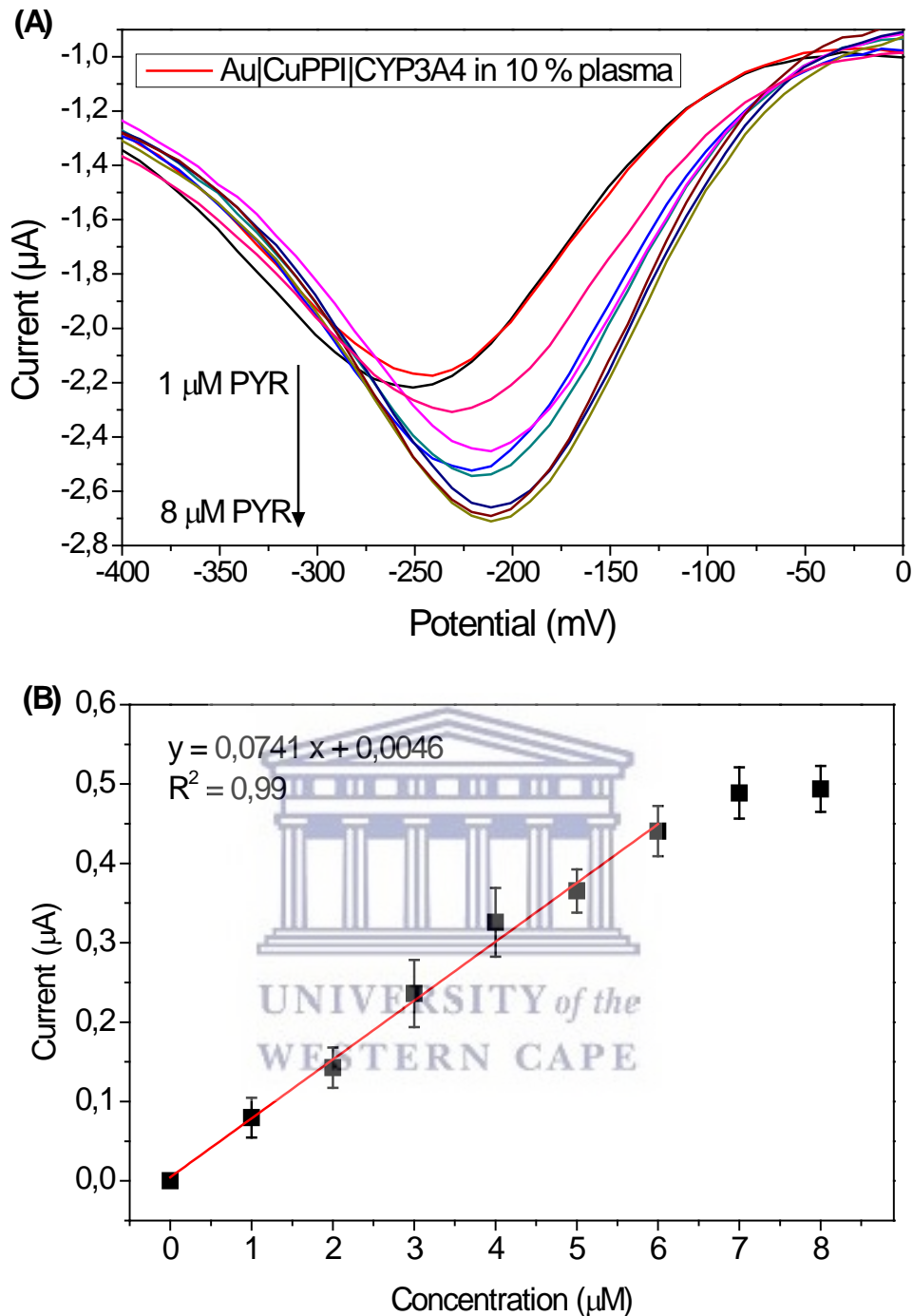


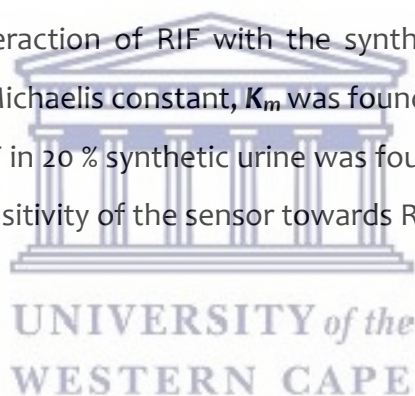
Figure 5-22: (A) DPV detection of 1, 2, 3, 4, 5, 6, 7 and 8 μM PYR at Au|CuPPI|CYP3A4 (B) I_{pc} vs concentration of PYR in 10% plasma

The metabolism of PYR at the biosensor was successful in 10% human plasma as shown in Figure 5-22 (A). This detection experiment resulted in a linear range of 1 μM to 6 μM , after which the enzyme saturate as shown in Figure 5-22 (B). The Michaelis constant, K_m calculated using Equation 5-3 was found to be 3.272 μM . As reported previously the plasma caused electrode fouling which hindered the detection on PYR

somewhat causing the electrode signals to not be analytically viable in some instances. This issue will have to be resolved in future work. The LOD and LOQ in this sensor was found to be 0.884 μM and 2.94 μM respectively, with a sensitivity of 0.0741 $\mu\text{A}/\mu\text{M}$.

5.4.4 Rifampicin

The final drug to be determined using the Au|CuPPI|CYP3A4 biosensor was rifampicin. This was the only drug which was capable of being determined at a lower concentration range of 0.5 μM to 5 μM which showed typical Michaelis-Menten behaviour since the saturation occurs at 3.5 μM . This behaviour is shown in Figure 5-23 (A) and (B). The reason for this is the fact that RIF is a known inducer of CYP3A4 [57], as well as the interaction of RIF with the synthetic urine constituents. The calculated value of the Michaelis constant, K_m was found to be 1.59 μM . The LOD and LOQ for detection of RIF in 20 % synthetic urine was found to be 0.165 μM and 0.552 μM respectively. The sensitivity of the sensor towards RIF was 0.181 $\mu\text{A}/\mu\text{M}$.



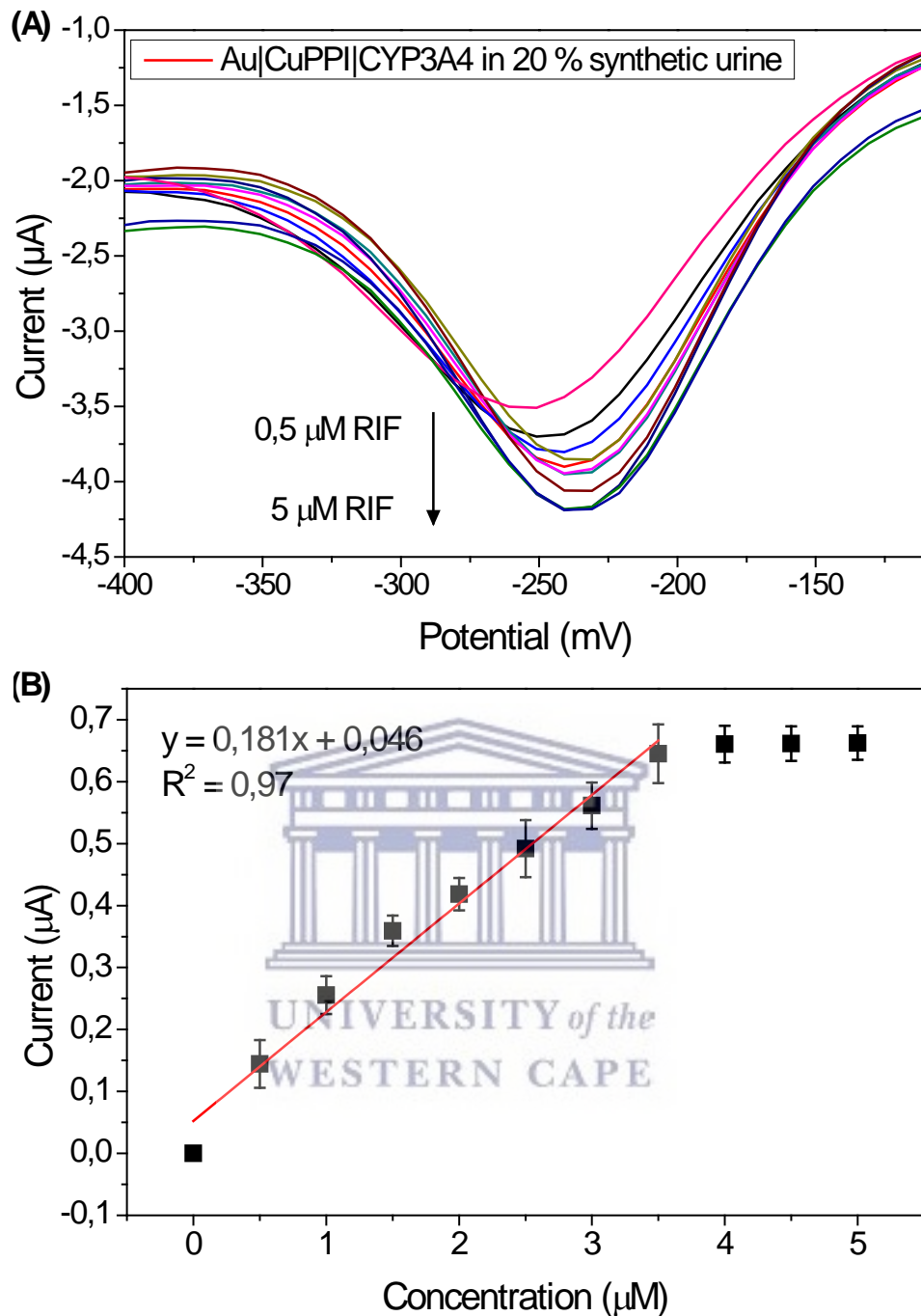


Figure 5-23: (A) DPV detection of 0.5, 1, 1.5, 2, 2.5, 3, 3.5, 4, 4.5 and 5 µM RIF at Au|CuPPI|CYP3A4 (B) I_{pc} vs concentration of RIF in 20 % synthetic urine

The detection of RIF in plasma resulted in the cathodic peak potential shifting slightly erratically upon addition of the substrate as can be seen in Figure 5-24 (A). The detection was carried out from 1 µM to 6 µM with the linear range being from 1 µM to 5 µM as shown in Figure 5-24 (B). The signals obtained after 6 µM were not analytically viable due to fouling of the electrode surface. The Michaelis constant for

this sensing application was calculated to be $2.67 \mu\text{M}$. A LOD and LOQ of $0.393 \mu\text{M}$ and $1.31 \mu\text{M}$ were obtained respectively with sensitivity of $0.04581 \mu\text{A}/\mu\text{M}$. This value is well within the therapeutic level for RIF, which is 2 to $6 \mu\text{g}/\text{ml}$ i.e. 2.43 to $7.3 \mu\text{M}$ [52].

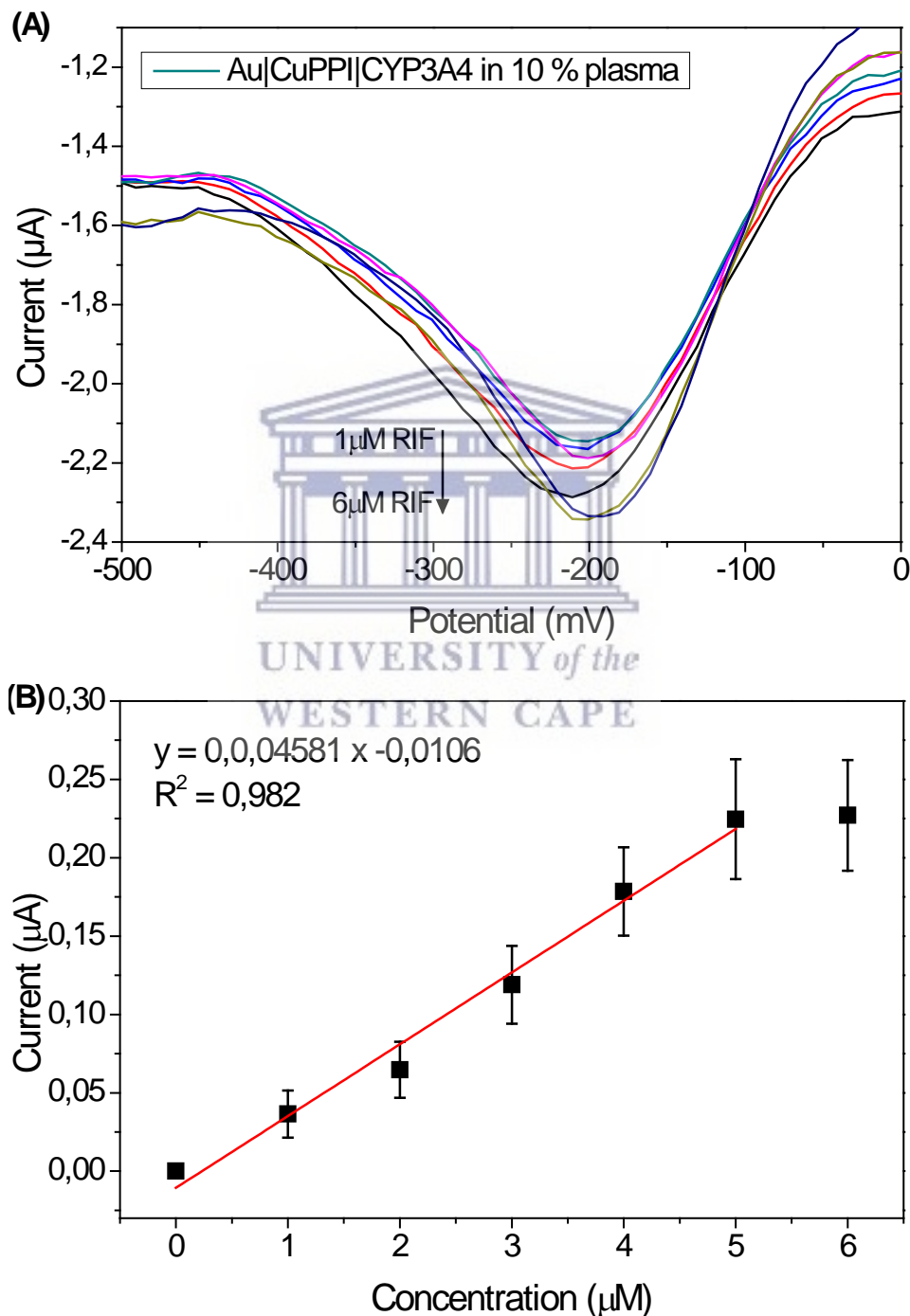
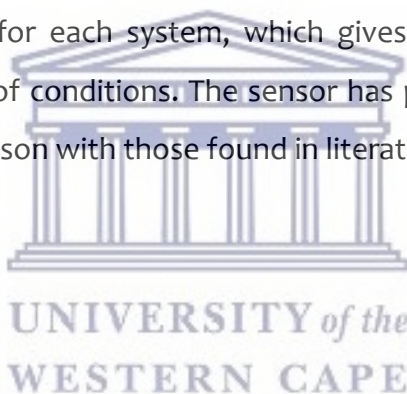


Figure 5-24: (A) DPV detection of 1, 2, 3, 4, 5 and 6 μM RIF at Au|CuPPI|CYP3A4 (B) I_{pc} vs concentration of RIF in 10% plasma

Quantification of INH and RIF via electrochemical sensing has been studied extensively as discussed by Farohki-Fard et al [58]. This review focuses on the types of materials used to detect INH and RIF and concluded that electrochemistry offers the most favourable characteristics in terms of sensitivity, LOD and ease of use. Many of the works discussed in this review suffered from at least one or more shortcomings. These included high detection limit and harsh pH conditions required. The Au|CuPPI|CYP3A4 biosensor minimises both of these factors by having optimum pH being neutral as well as having linear ranges that were well within the values for peak serum concentrations found in the body.

The results obtained from the calibration curves of the anti-TB drugs in 20 % synthetic urine and 10 % human plasma yielded very good results as well as limits of detection for all four analytes. A summary of these values can be found in Table 5-3 along with the Michaelis constant for each system, which gives information of the enzyme kinetics under each set of conditions. The sensor has proven to obtain results that are very good in comparison with those found in literature.



5.4.5 Recovery Studies

Recovery studies were completed by dissolving set concentrations of tablet forms of the anti-TB drugs in each of the two complex media. The results of the real tablet experiments were extrapolated from the calibration curves in synthetic urine and plasma accordingly and the percentage recovery calculated. The results are as shown in Table 5-3, including the limit of detection and limit of quantification for each calibration curve experiment. The LOD for these experiments ranged from 0.165 μM and 0.884 μM . The sensor was found to have the highest sensitivity towards RIF in synthetic urine and the lowest sensitivity toward RIF in plasma. The biosensor yielded good recovery results values as well ranging from 91.5 % to 108.5 %. This biosensor was thus proven to be a viable option for the determination of anti-TB drugs in both urine and plasma.

Table 5-3: Analytical efficiency of Au|CuPPI|CYP3A4 biosensor towards anti-TB drugs in 20 % synthetic urine and 10 % plasma

		LOD (μM)	LOQ (μM)	Sensitivity ($\mu\text{A}/\mu\text{M}$)	K_m (μM)	Spiked (μM)	Detected (μM)	Recovery (%)
Isoniazid	Synthetic urine	0.176	0.586	0.13041	3.888	2	2.17	108.5
						4	3.7	92.5
						6	5.8	96.6
	Plasma	0.631	2.1	0.0867	2.575	2	1.83	91.5
						4	3.87	96.75
						6	6.15	102.5
Ethambutol	Synthetic urine	0.386	1.288	0.12998	2.820	2	1.83	91.5
						4	3.78	94.5
						6	-	Out of linear range
	Plasma	0.403	1.364 6	0.1195	2.820	2	1.83	91.5
						4	3.86	96.5
						6	-	Out of linear range
Pyrazinamide	Synthetic urine	0.66	2.22	0.0677	N/A	2	2.07	103.5
						4	4.125	103.1
						6	5.78	96.3
	Plasma	0.884	2.94	0.0741	3.272	2	2.10	105.2
						4	4.32	108
						6	5.94	99
Rifampicin	Synthetic urine	0.165	0.552	0.181	1.590	1	0.97	97.6
						2	1.89	94.7
						3	2.97	99
	Plasma	0.393	1.31	0.04581	2.670	1	0.916	91.6
						2	1.89	94.7
						3	3.25	108.3

5.5 Conclusion

CYP450 enzymes are responsible for the majority of drugs being metabolised by the human body. It is thus an ideal group of enzymes for application in biosensors, which are analytical tools that are able to detect various chemicals and drugs with the help of a biological recognition element. CYP3A4 is a part of this diverse group of enzymes, which metabolises 50 % of all drugs prescribed. The metabolism of these drugs are carried out via a monooxygenation reaction, where molecular oxygen binds to the high spin heme centre and usually results in a hydroxylated product. CYP3A4 has been involved in various biosensors in literature and has now been applied towards the detection of four anti-TB drugs. The biosensor was constructed by drop-coating the CuPPI metallodendrimer and allowing it to physically adsorb onto the electrode surface. The CYP3A4 enzyme was then electrostatically attached to the Au|CuPPI electrode and used as is. The standard referencing material of each drug was detected successfully in the nanomolar range with LOD values ranging from 0.02244 nM to 0.08642 nM in 0.1 M phosphate buffer at pH 7.4. The enzyme kinetics of these reactions were also determined with Michaelis constant values that indicated a strong affinity between the enzyme and substrate in each case. These results were excellent in theory but the viability of the sensor was then tested in “real samples”. The two forms of real samples tested was synthetic urine and human plasma. These two matrices were chosen as the major forms of monitoring leftover drugs in the body for the phenotype sensor. Calibration curves were formed by adding successive additions of the anti-TB drug to a 20 % synthetic urine or 10 % human plasma, which was diluted with 0.1 M PB at pH 7.4. The limits of detection in the complex matrices was in the range of 0.165 μ M and 0.884 μ M. Recovery studies were also carried out by dissolving real tablet forms of each drug and carrying out the detection in both of the complex matrices. Each of these experiments yielded typical Michaelis-Menten behaviour with saturation of the enzyme taking place and favourable Michaelis constant values obtained. Results of the recovery were found to be in the range of 91.5 % to 108.5 %. These results showed that a cheap, simple and easy to produce material such as CuPPI was successful in being applied in an electrochemical

biosensor towards anti-TB drugs. The inclusion of the enzyme into the biosensor made it possible to mimic bodily functions in real samples such as those prepared in plasma and urine in this work. The only sample preparation step was dilution which is also quick, easy and possible to carry out at the point of care. This allows for the minimisation of matrix effects and creates a sample which would be conducive for electrochemical analysis. The sensor did not make use of any other form of modification such as blocking or pre-treatment. The biosensor thus affords a stable, cheap, easy to manufacture and easy to use biosensor, which yields excellent limit of detection and recovery in real samples.



5.6 **References**

- [1] S. C. Sim and M. Ingelman-Sundberg, "Update on Allele Nomenclature for Human Cytochromes P450 and the Human Cytochrome P450 Allele (CYP-Allele) Nomenclature Database," in *Methods in molecular biology (Clifton, N.J.)*, vol. 987, **2013**, pp. 251–259.
- [2] D. W. Nebert and D. W. Russell, "Clinical importance of the cytochromes P450," *The Lancet*, vol. 360, pp. 1155–1162, **2002**.
- [3] G. Gilardi, "Cytochromes P450 Redox Activity," in *Encyclopedia of Interfacial Chemistry*, Elsevier, **2018**, pp. 90–109.
- [4] T. L. Poulos, "Heme enzyme structure and function.," *Chemical reviews*, vol. 114, pp. 3919–62, **2014**.
- [5] J. K. Yano, M. R. Wester, G. A. Schoch, K. J. Griffin, C. D. Stout, and E. F. Johnson, "The Structure of Human Microsomal Cytochrome P450 3A4 Determined by X-ray Crystallography to 2.05Å Resolution," *Journal of Biological Chemistry*, vol. 279, pp. 38091–38094, **2004**.
- [6] P. A. Williams, J. Cosme, D. M. Vinkovic, A. Ward, H. C. Angove, P. J. Day, C. Vonrhein, I. J. Tickle, and H. Jhoti, "Crystal Structures of Human Cytochrome P450 3A4 Bound to Metyrapone and Progesterone," *Science*, vol. 305, pp. 683–686, **2004**.
- [7] E. E. Scott and J. R. Halpert, "Structures of cytochrome P450 3A4," *Trends in Biochemical Sciences*, vol. 30, pp. 5–7, **2005**.
- [8] E. G. Hrycay and S. M. Bandiera, "The monooxygenase, peroxidase, and peroxygenase properties of cytochrome P450," *Archives of Biochemistry and Biophysics*, vol. 522, pp. 71–89, **2012**.
- [9] L. Taylor, N. Krueger, O. Malysheva, J. Atkinson, and R. S. Parker, "ω-Hydroxylation of α-tocopheryl quinone reveals a dual function for cytochrome P450-4F2 in vitamin E metabolism," *Bioorganic and Medicinal Chemistry*, vol. 26, pp. 5555–5565, **2018**.
- [10] C. Barnaba, K. Gentry, N. Sumangala, and A. Ramamoorthy, "The catalytic function of cytochrome P450 is entwined with its membrane-bound nature," *F1000Research*, vol. 6, p. 662, **2017**.
- [11] M. Šrejber, V. Navrátilová, M. Paloncýová, V. Bazgier, K. Berka, P. Anzenbacher, and M. Otyepka, "Membrane-attached mammalian cytochromes P450: An overview of the membrane's effects on structure, drug binding, and interactions with redox partners," *Journal*

of *Inorganic Biochemistry*, vol. 183, pp. 117–136, **2018**.

- [12] K. E. Thummel and G. R. Wilkinson, “In vitro and in vivo drug interactions involving human CYP3A,” *Annual Review of Pharmacology and Toxicology*, vol. 38, pp. 389–430, **1998**.
- [13] R. Cacabelos, P. Cacabelos, and C. Torrellas, “Personalized Medicine of Alzheimer’s Disease,” in *Handbook of Pharmacogenomics and Stratified Medicine*, Elsevier Inc., **2014**, pp. 563–615.
- [14] U. M. Zanger and M. Schwab, “Cytochrome P450 enzymes in drug metabolism: Regulation of gene expression, enzyme activities, and impact of genetic variation,” *Pharmacology and Therapeutics*, vol. 138, pp. 103–141, **2013**.
- [15] S.-F. Zhou, “Drugs Behave as Substrates, Inhibitors and Inducers of Human Cytochrome P450 3A4,” *Current Drug Metabolism*, vol. 9, pp. 310–322, **2008**.
- [16] S. Rendic and F. J. Di Carlo, “Human cytochrome P450 enzymes: A status report summarizing their reactions, substrates, inducers, and inhibitors,” *Drug Metabolism Reviews*, vol. 29, pp. 413–580, **1997**.
- [17] C. for D. E. and Research, “Draft Guidance, Clinical Drug Interaction Studies–Study Design, Data Analysis, and Clinical Implications Guidance for Industry, U.S. Department of Health and Human Services, Food and Drug Administration, Center for Drug Evaluation and Research (CDER),” **2017**.
- [18] D. Y. Murzin and T. Salmi, “Enzymatic Kinetics,” in *Catalytic Kinetics*, Elsevier, **2016**, pp. 281–343.
- [19] E. I. Canela, G. Navarro, J. L. Beltrán, and R. Franco, “The meaning of the Michaelis-Menten constant: Km describes a steady-state,” *bioRxiv*, p. 608232, **2019**.
- [20] A. Yarman, U. Wollenberger, and F. W. Scheller, “Sensors based on cytochrome P450 and CYP mimicking systems,” *Electrochimica Acta*, vol. 110, pp. 63–72, **2013**.
- [21] V. V. Shumyantseva, A. V. Kuzikov, R. A. Masamrekh, T. V. Bulko, and A. I. Archakov, “From electrochemistry to enzyme kinetics of cytochrome P450,” *Biosensors and Bioelectronics*, vol. 121, pp. 192–204, **2018**.
- [22] M. A. Arbex, M. de C. L. Varella, H. R. de Siqueira, and F. A. F. de Mello, “Antituberculosis drugs: Drug interactions, adverse effects, and use in special situations.,” *Jornal Brasileiro de Pneumologia*, vol. 36, pp. 626–640, **2010**.
- [23] N. Aliakbarinodehi, G. De Micheli, and S. Carrara, “Enzymatic and Nonenzymatic Electrochemical Interaction of Abiraterone (Antiprostata Cancer Drug) with Multiwalled

- Carbon Nanotube Bioelectrodes,” *Analytical Chemistry*, vol. 88, pp. 9347–9350, **2016**.
- [24] A. Ignaszak, N. Hendricks, T. Waryo, E. Songa, N. Jahed, R. Ngece, A. Al-Ahmed, B. Kgarebe, P. Baker, and E. I. Iwuoha, “Novel therapeutic biosensor for indinavir-A protease inhibitor antiretroviral drug,” *Journal of Pharmaceutical and Biomedical Analysis*, vol. 49, pp. 498–501, **2009**.
- [25] M. Müller, N. Agarwal, and J. Kim, “A Cytochrome P450 3A4 Biosensor Based on Generation 4.0 PAMAM Dendrimers for the Detection of Caffeine.,” *Biosensors*, vol. 6, **2016**.
- [26] N. R. Hendricks, T. T. Waryo, O. Arotiba, N. Jahed, P. G. L. Baker, and E. I. Iwuoha, “Microsomal cytochrome P450-3A4 (CYP3A4) nanobiosensor for the determination of 2,4-dichlorophenol-An endocrine disruptor compound,” *Electrochimica Acta*, vol. 54, pp. 1925–1931, **2009**.
- [27] E. I. Iwuoha, S. Joseph, Z. Zhang, M. R. Smyth, U. Fuhr, and P. R. Ortiz de Montellano, “Drug metabolism biosensors: electrochemical reactivities of cytochrome P450cam immobilised in synthetic vesicular systems,” *Journal of Pharmaceutical and Biomedical Analysis*, vol. 17, pp. 1101–1110, **1998**.
- [28] K. Scott, “Electrochemical Principles and Characterization of Bioelectrochemical Systems,” in *Microbial Electrochemical and Fuel Cells: Fundamentals and Applications*, Elsevier Inc., **2016**, pp. 29–66.
- [29] E. Iwuoha and M. R. Smyth, “Reactivities of organic phase biosensors: 6. Square-wave and differential pulse studies of genetically engineered cytochrome P450cam (CYP101) bioelectrodes in selected solvents,” *Biosensors and Bioelectronics*, vol. 18, pp. 237–244, **2003**.
- [30] P. Pinyou, V. Blay, L. M. Muresan, and T. Noguer, “Enzyme-modified electrodes for biosensors and biofuel cells,” *Materials Horizons*, vol. 6, pp. 1336–1358, **2019**.
- [31] N. D. J. Yates, M. A. Fascione, and A. Parkin, “Methodologies for ‘Wiring’ Redox Proteins/Enzymes to Electrode Surfaces,” *Chemistry - A European Journal*, vol. 24, pp. 12164–12182, **2018**.
- [32] S. Y. Rhiu, D. R. Ludwig, V. S. Siu, and G. T. R. Palmore, “Direct electrochemistry of cytochrome P450 27B1 in surfactant films,” *Electrochemistry Communications*, vol. 11, pp. 1857–1860, **2009**.
- [33] B. D. Fleming, Y. Tian, S. G. Bell, L. L. Wong, V. Urlacher, and H. Allen O Hill, “Redox properties of cytochrome P450 BM3 measured by direct methods,” *European Journal of Biochemistry*, vol. 270, pp. 4082–4088, **2003**.
- [34] H. Wu, B. Sun, D. Huang, Y. Liu, and H. Zhang, “Characterization, Direct Electrochemistry, and

- Electrocatalysis of Immobilized Hemoglobin on a Platinum Nanoparticle–Didodecyldimethylammonium Bromide Composite Film,” *Analytical Letters*, vol. 49, pp. 556–567, **2016**.
- [35] I. Srejić, M. Smiljanić, Z. Rakočević, and S. Štrbac, “Oxygen Reduction on Au(100)-like Polycrystalline Gold Electrode in Alkaline Solution,” *Int. J. Electrochem. Sci*, vol. 11, pp. 10436–10448, **2016**.
- [36] E. Schneider and D. S. Clark, “Cytochrome P450 (CYP) enzymes and the development of CYP biosensors,” *Biosensors and Bioelectronics*, vol. 39, pp. 1–13, **2013**.
- [37] E. V. Suprun, V. V. Shumyantseva, and A. I. Archakov, “Protein Electrochemistry: Application in Medicine. A Review,” *Electrochimica Acta*, vol. 140, pp. 72–82, **2014**.
- [38] M. Honeychurch, “The direct electrochemistry of cytochrome P450. What are we actually measuring?,” **2003**.
- [39] P. Wang, K. Pradhan, X. bo Zhong, and X. Ma, “Isoniazid metabolism and hepatotoxicity,” *Acta Pharmaceutica Sinica B*, vol. 6, Chinese Academy of Medical Sciences, pp. 384–392, **01-Sep-2016**.
- [40] C. K. Jaladanki, A. Shaikh, and P. V. Bharatam, “Biotransformation of Isoniazid by Cytochromes P450: Analyzing the Molecular Mechanism using Density Functional Theory,” *Chemical Research in Toxicology*, vol. 30, pp. 2060–2073, **2017**.
- [41] F. P. Guengerich, “Mechanisms of cytochrome P450 substrate oxidation: MiniReview,” *Journal of Biochemical and Molecular Toxicology*, vol. 21, pp. 163–168, **2007**.
- [42] S. Prasad and S. Mitra, “Structure and Mechanism of Function of Cytochrome P450,” *Proceedings of the Indian National Science Academy*, vol. 70, pp. 283–291, **2004**.
- [43] S. Sarkar and A. Ganguly, “Current Overview of Anti-Tuberculosis Drugs: Metabolism and Toxicities,” *Mycobacterial Diseases*, vol. 6, **2016**.
- [44] M. T. Chirehwa, H. McIlIeron, R. Rustomjee, T. Mthiyane, P. Onyebujoh, P. Smith, and P. Denti, “Pharmacokinetics of pyrazinamide and optimal dosing regimens for drug-sensitive and -resistant tuberculosis,” *Antimicrobial Agents and Chemotherapy*, vol. 61, **2017**.
- [45] T. Y. Shih, C. Y. Pai, P. Yang, W. L. Chang, N. C. Wang, and O. Y. P. Hu, “A novel mechanism underlies the hepatotoxicity of pyrazinamide,” *Antimicrobial Agents and Chemotherapy*, vol. 57, pp. 1685–1690, **2013**.
- [46] N. R. Srinivas, “Pharmacokinetic Interaction of Rifampicin with Oral Versus Intravenous

Anticancer Drugs: Challenges, Dilemmas and Paradoxical Effects Due to Multiple Mechanisms,” *Drugs in R and D*, vol. 16, pp. 141–148, **2016**.

- [47] R. Ajayi, U. Sidwaba, U. Feleni, S. Douman, O. Tovide, S. Botha, P. Baker, X. Fuku, S. Hamid, T. Waryo, S. Vilakazi, R. Tshihkudo, and E. Iwuoha, “Chemically amplified cytochrome P450-2E1 drug metabolism nanobiosensor for rifampicin anti-tuberculosis drug,” *Electrochimica Acta*, vol. 128, pp. 149–155, **2014**.
- [48] K. Asadpour-Zeynali and E. Saeb, “Simultaneous Spectrophotometric Determination of Rifampicin, Isoniazid and Pyrazinamide in a Single Step,” *Iranian Journal of Pharmaceutical Research : IJPR*, vol. 15, p. 713, **2016**.
- [49] C. Rassie, J. Van Wyk, L. Wilson, N. Ntshongontshi, A. Jonnas, U. Feleni, R. F. R. F. Ajayi, P. Baker, and E. Iwuoha, “Electrochemical Ultra-Low Detection of Isoniazid Using a Salicylaldamine Functionalised G1-DAB-(NH₂)₄ Dendritic Sensor vs. UV-VIS Spectrophotometric Detection,” *Journal of Nano Research*, vol. 45, pp. 164–174, **2017**.
- [50] N. Bunyakul and A. J. Baeumner, “Combining electrochemical sensors with miniaturized sample preparation for rapid detection in clinical samples,” *Sensors (Switzerland)*, vol. 15, pp. 547–564, **2015**.
- [51] J. E. Contreras-Naranjo and O. Aguilar, “Suppressing non-specific binding of proteins onto electrode surfaces in the development of electrochemical immunosensors,” *Biosensors*, vol. 9, pp. 1–23, **2019**.
- [52] J. S. Park, J. Y. Lee, Y. J. Lee, S. J. Kim, Y. J. Cho, H. Il Yoon, C. T. Lee, J. Song, and J. H. Lee, “Serum levels of antituberculosis drugs and their effect on tuberculosis treatment outcome,” *Antimicrobial Agents and Chemotherapy*, vol. 60, pp. 92–98, **2016**.
- [53] K. C. M. S. Lima, A. C. F. Santos, R. N. Fernandes, F. S. Damos, and R. de Cássia Silva Luz, “Development of a novel sensor for isoniazid based on 2,3-dichloro-5,6-dicyano-p-benzoquinone and graphene: Application in drug samples utilized in the treatment of tuberculosis,” *Microchemical Journal*, vol. 128, pp. 226–234, **2016**.
- [54] N. S. K. Gowthaman, S. Kesavan, and S. A. John, “Monitoring isoniazid level in human fluids in the presence of theophylline using gold@platinum core@shell nanoparticles modified glassy carbon electrode,” *Sensors and Actuators, B: Chemical*, vol. 230, pp. 157–166, **2016**.
- [55] W. Y. Wu, J. Y. Yang, L. M. Du, H. Wu, and C. F. Li, “Determination of ethambutol by a sensitive fluorescent probe,” *Spectrochimica Acta - Part A: Molecular and Biomolecular Spectroscopy*, vol. 79, pp. 418–422, **2011**.

- [56] B. Mekassa, P. G. L. Baker, B. S. Chandravanshi, and M. Tessema, "Sensitive electrochemical determination of ethambutol in pharmaceutical formulation and human urine at nickel nanoparticles/electrochemically reduced graphene oxide modified electrode," *Bulletin of the Chemical Society of Ethiopia*, vol. 33, p. 215, **2019**.
- [57] R. Negoro, K. Takayama, Y. Nagamoto, F. Sakurai, M. Tachibana, and H. Mizuguchi, "Modeling of drug-mediated CYP3A4 induction by using human iPS cell-derived enterocyte-like cells," *Biochemical and Biophysical Research Communications*, vol. 472, pp. 631–636, **2016**.
- [58] A. Farokhi-Fard, B. Golichenari, M. M. Ghanbarlou, S. Zanganeh, and F. Vaziri, "Electroanalysis of isoniazid and rifampicin: Role of nanomaterial electrode modifiers," *Biosensors and Bioelectronics*, p. 111731, **2019**.



Chapter 6

6 Conclusion

Tuberculosis is a disease which has plagued people all over the globe since the 1600's. It is a highly contagious disease caused by *Mycobacterium tuberculosis* (MTB) and mostly infects the lungs of people who are infected with it. Symptoms of TB include shortness of breath, weight loss, persistent cough and even death when left untreated. This microorganism is passed from person to person via coughs, droplets, sputum and sneezes. It is thus highly prevalent in rural and impoverished areas where people live in small, confined spaces in close proximity to one another. People in these areas also do not have adequate access to treatment which allows for this disease to spread easily and without treatment. In 2018, 1.5 million people have died due to TB related issues, which is an astounding amount seeing that treatment has been available for decades. The first line of defence against TB consists of four anti-TB drugs, namely isoniazid, ethambutol, pyrazinamide and rifampicin. These drugs have various modes of action against the tubercle and have been relatively successful until the emergence of drug resistant bacteria. The symptoms associated with TB can lead to death when untreated. The development of a phenotype sensor would aid largely in overcoming some of the issues surrounding the treatment of TB. If one could adjust the treatment of TB according to a patient's metabolic profile, the adverse drug reaction caused by drugs could be minimised and encourage patients to complete their treatment. This would also assist in minimising the development of drug resistant TB strains.

A method of monitoring the amount of drugs used up by the body can be done through bodily fluid sampling (blood or urine) at various time intervals. Quantification of these drugs are usually carried out in the laboratory setting using methods such as

titrimetry, spectroscopy and chromatography such as HPLC and GC. As accurate as these well-established methods might be, they require a laboratory setting and bulky equipment in order to get the results you require. These instruments require trained technicians and sometimes multiple sample pre-treatment steps with a long waiting time. A method which circumvents these downfalls is electrochemistry. Electrochemistry offers an easy to use alternative which gives instant results at the point of care. These analytical tools can be portable and require very little sample pre-treatment. The electrode system can also be modified with smart materials and biological recognition elements which increase the conductivity, selectivity, sensitivity and limits of detections of the devices. Various smart materials that have been incorporated into sensors and biosensors include nanoparticles, conducting polymers, carbon based nanomaterials and many others. One of interest to us are a type of conducting polymers called dendrimers. These hyper branched molecules have an open, spherical structure which makes it an ideal conductor of electricity and thus an ideal electrocatalyst. A first generation copper metallodendrimer was synthesised and its electrochemical behaviour investigated for application in electrochemical sensing. The G1-core consisted of polypropyleneimine (PPI) which was modified with a 3, 5-di-tert-butylsalicyldimino group along the periphery. This PPI ligand was characterised using various spectroscopic and microscopic techniques in order to monitor the effect of the inclusion of a metal centre into the branches of the structure. These included FTIR (fourier transform infrared spectroscopy), AFM (atomic force microscopy), HR-TEM (high resolution transmission electron microscopy), HR-SEM (high resolution scanning electron microscopy), EDS (energy dispersive X-ray spectroscopy) and SAXS (small angle X-ray scattering). A copper centre was added to the PPI which resulted in the CuPPI metallodendrimer. The inclusion of the metal centre largely changed the structure of the material from the amorphous PPI to a rough polycrystalline CuPPI. It also changed the conductivity of the material and increased the surface area as well. The surface concentration of PPI on Au was calculated to be $5.095 \times 10^{-8} \text{ mol.cm}^{-2}$ while this value increased to $9.014 \times 10^{-7} \text{ mol.cm}^{-2}$ for Au|CuPPI. The viability of CuPPI as a sensor was further investigated by carrying out experiments of a CuPPI modified gold electrode which was created by drop-coating the synthesised material and allowing it to physically adsorb onto the

Au. The voltammetric experiments were carried out in both aerobic and anaerobic conditions. The metallodendrimer performed well with and without the presence of oxygen which was favourable. The effect of oxygen was determined by calculating the diffusion coefficient of the Au|CuPPI electrode. This value slightly decreases from $4.124 \times 10^{-5} \text{ cm}^2 \text{ s}^{-1}$ in the absence of oxygen to $3.29 \times 10^{-5} \text{ cm}^2 \text{ s}^{-1}$ when oxygen was present.

The Au|CuPPI electrode was then used as a chemical sensor towards the quantification of four anti-TB drugs. As an initial point of investigation the drugs were characterised on a bare Au and GCE electrode surface to identify each ones electrochemical signatures. Once this was confirmed the detection was carried out at the appropriate window potential for each anti-TB drug and calibration curves were constructed. The detection was carried out in 0.1 M PB at pH 7.4 in order to mimic the conditions of real bodily fluids. Linear ranges in the low nanomolar concentration range were obtained for the chemical sensor towards INH, ETH, PYR and RIF. The limit of detection of the electrochemical sensor ranged from 0.022 nM to 1.16 nM. As a point of reference, the electrochemical sensor was compared to a relatively easy and well established technique such as UV-Vis. The detection of the drugs using UV resulted in a limit of detection between 24.3 nM and 54.7 nM. UV-vis had the added downside of not being able to detect ETH without an added label in order to make the optically active in the UV-vis region. The electrochemical sensor was very specific towards these four drugs as each of them have unique signatures, which separate them clearly from one another. The drugs were then detected in spiked “real samples” in the form of synthetic urine and plasma. The much more complex matrices caused some issues in the chemical sensor which resulted in the low nanomolar range not being able to be detected. The samples were diluted to 20 % synthetic urine and 10 % plasma in order to overcome some of these matrix effects. The LOD for this sensor in complex matrices were in the range of 0.153 μM to 48.52 μM . Recovery studies were also carried out by mimicking real sample i.e. dissolving the tablet form of the drugs in either 20 % synthetic urine of 10% plasma. These gave excellent results by obtaining recovery of 89.27 % to 113 %. There were some issues when determining the concentrations of RIF and ETH in synthetic urine due to

interactions between the analyte and the urine contents. This resulted in a shorter linear range which will have to be resolved in future work.

Since the CuPPI was largely successful as a chemical sensor, it was then applied as a biosensor using a CYP3A4 enzyme as biological recognition element. A thorough literature review on CYP450 enzymes in catalytic reactions and sensors was therefore carried out. Cytochrome P450 enzymes are a versatile group of enzymes found in most living organisms including mammals, plants, bacteria and other microorganisms. These enzymes contain an iron-heme centre and catalyse a variety of reactions. Enzymes typically require redox partners in order to carry out their reactions. For CYP's these come in the form of CYP reductase and NADPH. CYP enzymes in nature catalyse a wide variety of reactions dependant on where they are present. They have been found to be involved in reactions like C-C cleavage, epoxidation, sulfoxidation and demethylation amongst many others. CYP's have also been found to be easily modified using synthetic biology in order to have them used in industrial applications. These enzymes have the ability to act stereo- and regioselectively at otherwise inactive carbons which make them useful in synthetic organic chemistry. The involvement of CYP's in biosynthesis, bioremediation and biocatalysis has proven invaluable. Enzymes involved in these processes allow for a more environmentally friendly approach by making use of a catalyst that does not require harmful solvents and also is re-usable. CYP's have already been used on a large scale in the synthesis of indigo dyes as well as the synthesis of pharmaceutical drugs. CYP's have also been expressed in plants which were then planted in contaminated soil and used for bioremediation purposes. The flexibility of this group of enzymes make it an ideal candidate for biosensing as well.

CYP enzymes are ideal as biological recognition elements in biosensors since they metabolise majority of prescribed drugs. CYP3A4 specifically is responsible for the metabolism of 50 % and is thus an ideal candidate for the detection of all four anti-TB drugs. Biosensors act as analytical tools which are excellent for quantification of drugs since they enhance the sensitivity and selectivity of the sensor towards substrates, despite the other components present in the media in which they are being detected. CYP3A4 metabolises its substrates via a monooxygenation reaction

where molecular oxygen is used to aid in the hydroxylation of the substrate to form the metabolised product. The simple biosensor was constructed by first modifying a gold electrode with CuPPI via physisorption. After drying, the modified electrode was then drop coated with CYP3A4 which was allowed to electrostatically attach to the dendrimer surface. This Au|CuPPI|CYP3A4 biosensor was used for the detection of INH, ETH, PYR and RIF in 0.1 M PB at pH 7.4. The sensor was capable of excellent linear ranges in the low nanomolar concentration range and obtained a limit of detection as low as 0.02244 nM using pure standard referencing versions of the drugs. The biosensor was then applied in the detection of the drugs in real samples such as synthetic urine and human plasma. These matrices were chosen as two ways in which to confirm the amount of drug leftover in the patients system after a pre-determined time so that modelling of drug metabolism can be carried out. Calibration curves were obtained by adding successive amounts of drug into a system containing either 20 % synthetic urine or 10 % plasma and the monooxygenation peak being monitored, which is an overall reduction reaction. The limits of detection in the complex matrices was in the range of 0.165 μ M and 0.884 μ M. Recovery studies were also carried out by dissolving real tablet forms of each drug and carrying out the detection in both of the complex matrices. Results of the recovery were found to be in the range of 91.5 % to 108.5 %.

The results of this work have proven that a cheap, simple and easy to produce material such as CuPPI was successful in being used in the detection of all four anti-TB drugs in pure and real samples. The chemical sensor has an increased selectivity in comparison to the biosensor, this is due to the unique electrochemical signatures associated with each drug. The biosensor however improves largely on the sensitivity of the system in getting to a much lower limit of detection. This biosensor has huge application in real world testing, since it is capable of obtaining excellent recovery as well with little to no pre-treatment, blocking, or complex and expensive synthetic protocols being employed.